

ISSN 2071-4726
2071-0305

Magazine of Civil Engineering

94(2), 2020





ПОЛИТЕХ
Санкт-Петербургский
политехнический университет
Петра Великого

Инженерно-строительный институт
Центр дополнительных профессиональных программ
195251, г. Санкт-Петербург, Политехническая ул., 29,
тел/факс: 552-94-60, www.stroikursi.spbstu.ru,
stroikursi@mail.ru

**Приглашает специалистов организаций, вступающих в СРО,
на курсы повышения квалификации (72 часа)**

Код	Наименование программы	Виды работ*
Курсы по строительству		
БС-01-04	«Безопасность и качество выполнения общестроительных работ»	п.1,2, 3, 5, 6, 7, 9, 10, 11, 12, 13, 14
БС-01	«Безопасность и качество выполнения геодезических, подготовительных и земляных работ, устройства оснований и фундаментов»	1,2,3,5
БС-02	«Безопасность и качество возведения бетонных и железобетонных конструкций»	6,7
БС-03	«Безопасность и качество возведения металлических, каменных и деревянных конструкций»	9,10,11
БС-04	«Безопасность и качество выполнения фасадных работ, устройства кровель, защиты строительных конструкций, трубопроводов и оборудования»	12,13,14
БС-05	«Безопасность и качество устройства инженерных сетей и систем»	15,16,17,18,19
БС-06	«Безопасность и качество устройства электрических сетей и линий связи»	20,21
БС-08	«Безопасность и качество выполнения монтажных и пусконаладочных работ»	23,24
БС-12	«Безопасность и качество устройства мостов, эстакад и путепроводов»	29
БС-13	«Безопасность и качество выполнения гидротехнических, водолазных работ»	30
БС-14	«Безопасность и качество устройства промышленных печей и дымовых труб»	31
БС-15	«Осуществление строительного контроля»	32
БС-16	«Организация строительства, реконструкции и капитального ремонта. Выполнение функций технического заказчика и генерального подрядчика»	33
Курсы по проектированию		
БП-01	«Разработка схемы планировочной организации земельного участка, архитектурных решений, мероприятий по обеспечению доступа маломобильных групп населения»	1,2,11
БП-02	«Разработка конструктивных и объемно-планировочных решений зданий и сооружений»	3
БП-03	«Проектирование внутренних сетей инженерно-технического обеспечения»	4
БП-04	«Проектирование наружных сетей инженерно-технического обеспечения»	5
БП-05	«Разработка технологических решений при проектировании зданий и сооружений»	6
БП-06	«Разработка специальных разделов проектной документации»	7
БП-07	«Разработка проектов организации строительства»	8
БП-08	«Проектные решения по охране окружающей среды»	9
БП-09	«Проектные решения по обеспечению пожарной безопасности»	10
БП-10	«Обследование строительных конструкций и грунтов основания зданий и сооружений»	12
БП-11	«Организация проектных работ. Выполнение функций генерального проектировщика»	13
Э-01	«Проведение энергетических обследований с целью повышения энергетической эффективности и энергосбережения»	
Курсы по инженерным изысканиям		
И-01	«Инженерно-геодезические изыскания в строительстве»	1
И-02	«Инженерно-геологические изыскания в строительстве»	2,5
И-03	«Инженерно-гидрометеорологические изыскания в строительстве»	3
И-04	«Инженерно-экологические изыскания в строительстве»	4
И-05	«Организация работ по инженерным изысканиям»	7

*(согласно приказам Минрегионразвития РФ N 624 от 30 декабря 2009 г.)

**По окончании курса слушателю выдается удостоверение о краткосрочном повышении
квалификации установленного образца (72 ак. часа)**

Для регистрации на курс необходимо выслать заявку на участие, и копию диплома об образовании по телефону/факсу: 8(812) 552-94-60, 535-79-92, , e-mail: stroikursi@mail.ru.

Magazine of Civil Engineering

SCHOLAR JOURNAL

ISSN 2071-0305

Свидетельство о государственной регистрации:
Эл № ФС77-77906 от 19.02.2020,
выдано Роскомнадзором

Специализированный научный журнал. Выходит с
09.2008.

Включен в Перечень ВАК РФ

Индексируется в БД Scopus

Периодичность: 8 раз в год

Учредитель и издатель:

Санкт-Петербургский политехнический университет
Петра Великого

Адрес редакции:

195251, СПб, ул. Политехническая, д. 29

Главный редактор:

Екатерина Александровна Линник

Научный редактор:

Николай Иванович Ватин

Выпускающий редактор:

Анастасия Крупина

Редакционная коллегия:

д.ф.-м.н., доцент Р.А. Абдикаримов;
д.т.н., проф. В.В. Бабков;
к.т.н., проф. А.И. Боровков;
д.т.н., проф. А. Бородинец;
д.т.н., проф. Н.И. Ватин;
PhD, проф. М. Вельжкович;
к.т.н., М.Р. Гарифуллин;
д.т.н., проф. Э.К. Завадскас;
д.ф.-м.н., проф. М.Н. Кирсанов;
D.Sc., проф. М. Кнежевич;
д.т.н., проф. В.В. Лалин;
д.т.н., проф. Б.Е. Мельников;
д.т.н., академик М.М. Мирсаидов;
д.т.н., проф. Р.Б. Орлович;
Dr. Sc. Ing., professor Л. Пакрастиньш;
Dr.-Ing. Habil., professor X. Пастернак;
д.т.н., проф. А.В. Перельмутер;
д.т.н., проф. М.Р. Петриченко;
д.т.н., проф. В.В. Сергеев;
д.ф.-м.н., проф. М.Х. Стрелец;
д.т.н., проф. О.В. Тараканов;
д.т.н., проф. Б.Б. Телтаев;
д.т.н., проф. В.И. Травуш;
д.т.н., проф. Д. Унгерман;
д.т.н., проф. С.В. Федосов

Magazine of Civil Engineering

SCHOLAR JOURNAL

ISSN 2071-0305

Peer-reviewed scientific journal

Start date: 2008/09

8 issues per year

Publisher:

Peter the Great St. Petersburg Polytechnic University

Indexing:

Scopus, Russian Science Citation Index (WoS),
Compendex, EBSCO, Google Academia, Index
Copernicus, ProQuest, Ulrich's Serials Analysis System,
CNKI

Corresponding address:

29 Polytechnicheskaya st., Saint-Petersburg, 195251,
Russia

Editor-in-chief:

Ekaterina A. Linnik

Science editor:

Nikolay I. Vatin

Technical editor:

Anastasia Krupina

Editorial board:

R.A. Abdikarimov, D.Sc., associate professor
V.V. Babkov, D.Sc., professor
A.I. Borovkov, PhD, professor
A. Borodinecs, Dr.Sc.Ing., professor
M. Veljkovic, PhD, professor
M. Garifullin, PhD, postdoctorant
E.K. Zavadskas, D.Sc., professor
M.N. Kirsanov, D.Sc., professor
M. Knezevic, D.Sc., professor
V.V. Lalin, D.Sc., professor
B.E. Melnikov, D.Sc., professor
M.M. Mirsaidov, D.Sc., professor
R.B. Orlovich, D.Sc., professor
L. Pakrastinsh, Dr.Sc.Ing., professor
H. Pasternak, Dr.-Ing.habil., professor
A.V. Perelmuter, D.Sc., professor
M.R. Petrichenko, D.Sc., professor
V.V. Sergeev, D.Sc., professor
M.Kh. Strelets, D.Sc., professor
O.V. Tarakanov, D.Sc., professor
B.B. Teltayev, D.Sc., professor
V.I. Travush, D.Sc., professor
S.V. Fedosov, D.Sc., professor

Дата выхода: 27.03.2020

Date of issue: 27.03.2020

© Peter the Great St. Petersburg Polytechnic University.
All rights reserved.

© Coverpicture – Ilya Smagin

© ФГАОУ ВО СПбПУ, 2020

© Иллюстрация на обложке: Илья Смагин

Contacts:

E-mail: mce@spbstu.ru

Web: <http://www.engstroy.spbstu.ru>

Contents

Krishan, A.L., Narkevich, M.Yu., Sagadatov, A.I., Rimshin, V.I. The strength of short compressed concrete elements in a fiberglass shell	3
Rybakov, V.A., Ananeva, I.A., Pichugin, E.D., Garifullin, M. Heat protective properties of enclosure structure from thin-wall profiles with foamed concrete	11
Matveev, S.A., Martynov, E.A., Litvinov, N.N., Kadisov, G.M., Utkin, V.A., The geogrid-reinforced gravel base pavement model	21
Nejati, F., Zhian, M., Safar Mashaie, F., Edalatpanah, S.A. Computational modeling of yielding octagonal connection for concentrically braced frames	31
Gavrilov, T.A., Kolesnikov, G.N. Evolving crack influence on the strength of frozen sand soils	54
Maklakov, D.V., Posohin, V.N., Safiullin, R.G., Kareeva, J.R. Intake rate through openings in the side wall of the duct	65
Karaburc, S.N., Yildizel, S.A., Calis, G.C. Evaluation of the basalt fiber reinforced pumice lightweight concrete	81
Al-Rousan, R. Behavior of strengthened concrete beams damaged by thermal shock	93
Kristiawan, S.A., Supriyadi, A. Two-way patched RC slabs under concentrated loads	108
Zemitis, J., Bogdanovics, R. Heat recovery efficiency of local decentralized ventilation devices	120
Degtyarev, V.V., Finite element modeling of cold-formed steel deck in bending	129
Bily, P., Fladr, J., Chylik, R., Hrbek, V., Vrablik, L. Micromechanical characteristics of high-performance concrete subjected to modifications of composition and homogenization	145



DOI: 10.18720/MCE.94.1

The strength of short compressed concrete elements in a fiberglass shell

A.L. Krishan^a, M.Yu Narkevich^{a*}, A.I Sagadatov^a, V.I Rimshin^b

^a *Nosov Magnitogorsk State Technical University, Magnitogorsk, Russia*

^b *National Research Moscow State Civil Engineering University, Moscow, Russia*

* *E-mail: Narkevich_MU@mail.ru*

Keywords: columns (structural), concretes, elasticity, fiber reinforced plastics, fibers, filament winding, stress-strain curves, structural design, tubes (components)

Abstract. Experimental studies of short axially compressed cylindrical elements with various indirect concrete reinforcements – fiberglass shells, steel spirals, and the joint use of these two types of reinforcement – have been carried out. The results of the experiments performed confirm the positive effect of both the outer fiberglass shell and spiral reinforcement on the strength of such elements. The highest strength was achieved with the simultaneous use of both types of indirect reinforcement. The presence of two types of indirect reinforcement significantly increased the deformability of the compressed elements under study. The maximum recorded values of the longitudinal deformations of shortening of such samples amounted to about 1.7 %. Such a high deformability of the compressed elements will allow to use high – strength longitudinal reinforcement efficiently in them. We list the main premises and dependencies of the method of deformational calculation of the strength of compressed concrete structures with indirect reinforcements. A performed comparison of the calculation results with experimental data indicates that the proposed method is perfectly suitable for practical use.

1. Introduction

The relatively rapid degradation of the strength properties of traditional building materials operating in aggressive environments is one of the main problems in the operation of buildings and structures in industry and civilian infrastructure.

Traditional building materials (steel, concrete, wood, brick and stone) have significant drawbacks that noticeably increase the cost of their maintenance, and reduce their service life. For example, it was estimated that in the United States repair and replacement of supporting building structures (piles, bridge supports, etc.) costs more than \$ 1 billion annually [1].

We should also note that for load-bearing structures with external indirect reinforcement, such as concrete filled glass fiber-reinforced polymer tubes (CFGFT), the destruction of the external metal shell from corrosion can cause not only the destruction of the element, but also of the structure as a whole.

These circumstances force the search and use in building structures of modern, more advanced building materials with high physical and mechanical properties, low specific gravity, not subject to corrosion, rotting, warping; possessing chemical resistance, low combustibility, low coefficient of thermal linear expansion, a wide range of operating temperatures.

Some materials possess the required properties, namely, polymer composite materials (PCM) – polymer materials reinforced with fabrics, mats, strands or other forms of fibrous fillers (FRP). These materials are considered an attractive alternative for structures operating in marine and other aggressive environments, since they are resistant to the destruction mechanisms mentioned above.

Due to the advantages of FRP, researchers in many countries, including China, the USA, Canada, Japan, etc., are studying CFGFT with PCM shells. The strength and deformability of compressed CFGFT elements [2, 7, 8, 13–15, 17], as well as the use of compressed CFGFT elements in piles [3, 9–11], offshore platforms [4], sheet piling [5, 6], road constructions [12, 16]. In Russia, in connection with the adopted program for the introduction of composite materials, structures and products from them in the construction industry of

Krishan, A.L., Narkevich, M.Yu., Sagadatov, A.I., Rimshin, V.I. The strength of short compressed concrete elements in a fiberglass shell. Magazine of Civil Engineering. 2020. 94(2). Pp. 3–10. DOI: 10.18720/MCE.94.1



This work is licensed under a CC BY-NC 4.0

the Russian Federation (approved by the order of the Ministry of Regional Development of the Russian Federation No. 306 dated July 24, 2013), PCM production (pipes made of glass and carbon fiber, reinforcement for reinforcing reinforced concrete structures, woven materials, etc.) has grown significantly. However, today, there is a significant lag behind the USA, a number of European countries and China in the development of a regulatory framework for the design and calculation of building composite structures using PCMs, as well as noticeably less experience in the use of PCMs in building structures and the operation of such structures. The lack of domestic materials, technologies and equipment for the production of PCMs dictates a high price for the final product, thereby restraining their use.

However, increasing interest in the use of PCMs in construction, and a number of the above – mentioned measures of state support for manufacturers of composite materials, emphasize the relevance of the development and research of composite load – bearing building structures, such as, for example, CFGFTs.

In order to reduce the cost of compressed CFGFT elements, we propose to reduce the size of the outer fiberglass shell (wall thickness or pipe diameter), while maintaining the necessary bearing capacity through the use of high – strength concrete and (or) additional reinforcement of the concrete core. An analysis of the possible options for reinforcing the concrete core indicates that the use of spiral reinforcement will be most effective here [20, 21].

The purpose of this work is to evaluate the effectiveness of the spiral reinforcement of a high-strength concrete core of short compressed CFGFT elements.

2. Methods

In the course of laboratory studies, the strength of short CFGFT cylindrical samples under axial compression was evaluated. The cross – sectional diameter of the test samples was 109 mm; their length was 500 mm. In total, two series of sample elements were investigated. Each series consisted of 3 identical samples.

For the production of samples of series I, heavy concrete of class B80 was used. A fiberglass pipe was used as the outer shell for concrete. It had the following characteristics:

- section diameter of 109 mm;
- wall thickness of 4.5 mm;
- modulus of elasticity under axial tension (compression) $E_{pl} = 13.8$ GPa;
- modulus of elasticity at circumferential tension $E_{pt} = 22.8$ GPa;
- axial tensile strength $f_{pl} = 265$ MPa;
- tensile strength at circumferential tension $f_{po} = 303$ MPa;
- Poisson's ratio $\nu_{po} = 0.39$;
- volumetric weight $\gamma_p = 19.5$ kN/m³.

Series II differed from Series I only by the presence of spiral reinforcement of the concrete core. Before molding samples of this series, a reinforcing cage was placed inside the fiberglass pipe. A wire with a diameter of 5 Vr500 served as spiral reinforcement of the frame, which was wound with a pitch of 30 mm around four longitudinal rods made of wire of the same class – diameter 5 Vr500. The diameter of the cross section of the spiral was 90 mm. The yield strength of reinforcing wire is $\sigma_{ys} = 552$ MPa.

Series III consisted of reinforced concrete elements with a cross – sectional diameter of 100 mm. Prototypes of this series had indirect reinforcement similar to the series II, but they did not have fiberglass shells.

To obtain more objective data, when comparing the strength of samples of the structures under study, three samples of different series were simultaneously formed using concrete mix of one batch.

After manufacturing, all the prototypes were kept at a temperature of about 20 °C for 28 days. The tests were carried out on a 500 – ton hydraulic press with a short – term compressive load. The load was transmitted over the entire cross section of the structures. In this case, a standard technique was used, regulated by Russian State Standard GOST 8829.

3. Results and Discussion

The main results of the experiments are summarized in Table 1. It contains the following data for each sample:

- prismatic strength of the source concrete f_c ;
- percentage of fiberglass reinforcement μ_p ;
- percentage of spiral reinforcement μ_{sc} ;
- breaking load N_u^{exp} ;
- the force that the sample could withstand under conditions of uniaxial compression N_{cp} ;
- indirect reinforcement efficiency coefficient $m_{\text{eff}} = N_u^{\text{exp}} / N_{cp}$;
- relative limit of elastic work $n_{el} = N_{el}^{\text{exp}} / N_u^{\text{exp}}$, where N_{el}^{exp} is maximum effort corresponding to the stage of elastic work;
- limitary axial deformation of shortening $\varepsilon_u^{\text{exp}}$.

Table 1. Main laboratory test results.

Sample	f_c , MPa	μ_p , %	μ_{sc} , %	N_u^{exp} , kN	N_{cp} , kN	m_{eff}	n_{el}	$\varepsilon_u^{\text{exp}}$, %
I-1	82.9	18.8	0	967	651	1.48	0.49	0.65
I-2	84.6	18.8	0	1033	664	1.55	0.54	0.75
I-3	85.0	18.8	0	1000	667	1.50	0.52	0.80
II-1	82.9	18.8	1.45	1300	694	1.87	0.52	1.70
II-2	84.6	18.8	1.45	1300	708	1.84	0.58	1.57
II-3	85.0	18.8	1.45	1380	711	1.94	0.60	1.80
III-1	82.9	0	1.45	867	651	1.33	0.55	0.55
III-2	84.6	0	1.45	833	664	1.25	0.51	0.50
III-3	85.0	0	1.45	900	667	1.35	0.56	0.48

An analysis of the results indicates that indirect reinforcement (fiberglass shell and / or spiral reinforcement) had a significant effect on the strength of centrally compressed samples. Explicitly, the presence of just spiral reinforcement led to an increase in their strength compared to uniaxially compressed elements by an average of 1.31 times, the presence of a fiberglass shell – by 1.51 times, and the presence of both types of indirect reinforcement – by 1.88 times.

The relative limit of elastic work for the samples of series II turned out to be higher than for samples of other series, but not by much. Compared to the samples of series I, it is 5–10 % higher, and compared to the samples of series III, the difference in n_{el} values is even less.

The maximum recorded values of the longitudinal deformations $\varepsilon_u^{\text{exp}}$ of the samples under study significantly depended on the level of indirect reinforcement. The smallest value of these deformations was recorded in samples of series III. Their $\varepsilon_u^{\text{exp}}$, on average, amounted to 0.63 %, which is approximately two and a half times higher than similar deformations of uniaxially compressed concrete. The limit deformations of series I samples turned out to be 22 % higher. The highest deformability was demonstrated by samples in a fiberglass shell with spiral reinforcement of concrete. For them, the average value was 1.69 %. It should be noted here that the high deformability of the compressed elements makes it possible to use high – strength longitudinal reinforcement efficiently in them.

The nature of the destruction of the studied samples mainly depended on the presence of an outer shell. For reinforced concrete elements with spiral reinforcement, before reaching the maximum load, almost complete destruction of the protective layer was observed (Figure 1, c). With a further increase in load, the concrete core crushed inside the spiral.

The destruction process of samples of series I and II was different. Immediately before the destruction, a slight bulging of the outer shell was observed. The reason for this was the fragmentation of the concrete core in local zones, due to the beginning of the shift of its parts. With a further increase in load, a rupture of the fiberglass shell was observed (Figure 1, a, 1, b). The nature of the destruction of the samples of both series was fragile. Externally, the picture of the destroyed samples practically did not differ. However, the presence of spiral reinforcement in Series II samples slightly decreased fragility due to a significant increase in the limit of deformability.

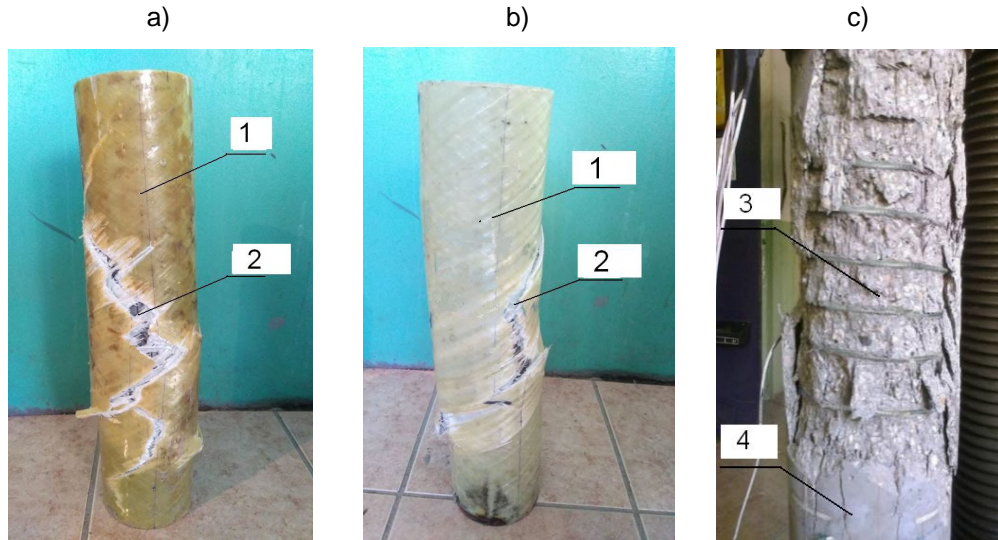


Figure 1. The nature of the destruction of samples from the series I (a), II (b) and III (c):
1 – not destroyed area; 2 – shell rupture at an angle of 30–60 degrees to the longitudinal axis;
3 – peeling of the protective layer of concrete; 4 – vertical cracks in the protective layer of concrete.

Strength calculation of test samples

In this paper, we study the force resistance of short samples of little flexibility. Their destruction occurs from a loss of compressive strength.

In modern publications, there are proposals for the calculation of such structures based on the breaking stress method [18]. In this case, the volumetric stress state of the materials is taken into account using empirical dependencies having a limited area of applicability. There are publications listing the results of calculations of compressed concrete elements based on finite element models [18–20]. Sadly, neither of the published works takes into account the actual nature of the force resistance of compressed elements with indirect reinforcement. In particular, they ignore the fact of a change in lateral pressure on the concrete core during a gradual increase in load, which causes a constant change in the stress state of the materials.

Considering this, we propose to calculate the strength of CFGFT using a different approach. The nature of their reinforcement involves the use of a deformation model for this purpose [21].

The essence of the proposed deformational calculation of the strength of centrally compressed elements is as follows. An element is considered, at the ends of which compressive load N with a random eccentricity e_a is applied. Before that, the concrete core and the outer shell (if applicable) of the element is divided into small ranges with areas A_{cj} and A_{pk} , within which the emerging stresses are averaged. The area of each rod of longitudinal reinforcement (if applicable) is indicated as A_{sn} .

In the calculation, the axial deformations of the most compressed fiber are increased step by step, starting from zero. In accordance with the Bernoulli hypothesis, a strain diagram is constructed in the cross section of an eccentric compressed element corresponding to the equilibrium conditions of internal forces in concrete, fiberglass, and forces from external load. To check the equilibrium conditions by the values of deformations in each section of concrete and fiberglass outer shell, into which the normal section of the element was previously divided, we calculate the stresses σ_{czj} , σ_{pzk} and σ_{szn} . The equilibrium conditions in the general case are written in the form of a system of equations:

$$N \cdot e_a = \sum_j \sigma_{czj} A_{cj} Z_{cj} + \sum_k \sigma_{pzk} A_{pk} Z_{pk} + \sum_n \sigma_{szn} A_{sn} Z_{sn}; \quad (1)$$

$$N = \sum_j \sigma_{czj} A_{cj} + \sum_k \sigma_{pzk} A_{pk} + \sum_n \sigma_{szn} A_{sn}, \quad (2)$$

where Z_{cj} , Z_{pk} and Z_{sn} are coordinates of the center of gravity of the j -th section of concrete, the k -th section of the fiberglass outer shell (if applicable) and the n -th rod of longitudinal reinforcement (if applicable).

When the equality of the left and right sides in Equations (1) and (2) is observed, the compressive force from the external load is fixed and the deformation build – up process continues $\varepsilon_{cz,max}$. The calculation continues until the compressive force reaches its maximum value N_u or until axial deformation reaches the maximum permissible value $\varepsilon_{cz,u}$, set by the researcher (see Figure 2).

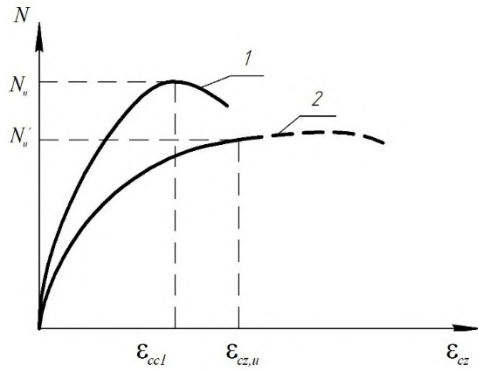


Figure 2. Dependencies « $N - \varepsilon_{cz}$ »: 1 is when N reaches its maximum value; 2 is when ε reaches its set value.

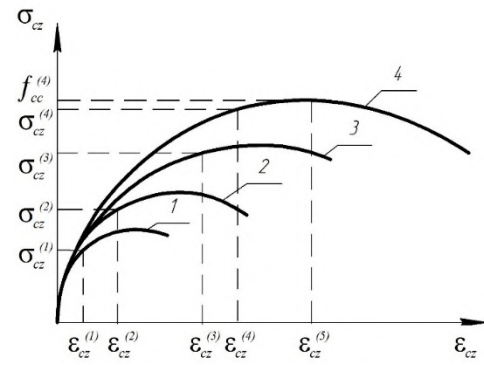


Figure 3. Concrete deformation diagrams for incremental longitudinal deformation: 1 – uniaxial compression, 2, 3 – volumetric compression at intermediate stages of deformation, 4 – volumetric compression in the limiting state.

The deformation calculation involves the use of deformation diagrams of the materials from which the structure under consideration is made. In our case, it is necessary to have diagrams reflecting the dependences between stresses and strains of axial direction for volumetrically stressed concrete and shell « $\sigma_{cz} - \varepsilon_{cz}$ » and « $\sigma_{pz} - \varepsilon_{pz}$ ». Longitudinal reinforcement deformation diagram « $\sigma_{sz} - \varepsilon_{sz}$ » can be adopted according to the recommendations of current standards. The accuracy of the calculations largely depends on the reliability of the adopted diagrams. In this case, the most difficult task is to build a diagram of concrete deformation.

Numerous proposals in publications on this subject [21, 22, 27–31] do not provide a reliable estimate of the strength resistance of a concrete core. They offer analytical dependences for describing the deformation diagrams of volumetrically compressed concrete when a lateral pressure of a certain value is applied to it. Pressure is most often taken for the limit state of the structure. In fact, the lateral pressure is constantly changing with increasing load level. To each side pressure $\sigma_{cr}^{(i)}$ at a particular i -th step of the calculation, there is a corresponding strain diagram. Taking into account the constant change in lateral pressure, we can obtain multiple diagrams « $\sigma_{cz}^{(i)} - \varepsilon_{cz}^{(i)}$ » (see Figure 3). This fact significantly complicates the deformation strength calculation, but it cannot be ignored.

To construct such strain diagrams, we propose to view the concrete core as a transversely isotropic body. The outline of each diagram is assumed to be curved with upward and downward sections. In this setting, for the analytical description of the diagrams, the most important task is to determine the coordinates of the vertices – the maximum stress $f_{cc}^{(i)}$ and corresponding deformation $\varepsilon_{cc1}^{(i)}$.

According to previously performed theoretical studies [32, 23], the maximum stress $f_{cc}^{(i)}$ and deformation $\varepsilon_{cc1}^{(i)}$ of volumetrically compressed concrete corresponding to lateral pressure is calculated using the following formulas:

$$f_{cc}^{(i)} = f_c \left(\frac{3\bar{\sigma}_i + 2}{4} + \sqrt{\left(\frac{\bar{\sigma}_i - 2}{4} \right)^2 + \frac{\bar{\sigma}_i}{b}} \right); \quad (3)$$

$$\varepsilon_{cc1}^{(i)} = \alpha_{ci} \left[\varepsilon_{c1} \alpha_{ci}^{1.5} - \frac{f_c}{E_c} (\alpha_{ci}^{1.5} - 1) \right], \quad (4)$$

where $\bar{\sigma}_i$ is a relative value of lateral pressure from the outer shell to the concrete core $\bar{\sigma}_i = \sigma_{cr}^{(i)} / f_c$;

b is material coefficient, which is an experimental value (for heavy concrete $b = 0.096$ [24]);

ε_{c1} is relative strain of uniaxially compressed concrete under stress f_c ;

α_{ci} is coefficient of strength growth of volumetrically compressed concrete ($\alpha_{ci} = f_{cc}^{(i)} / f_c$).

The relationship between stress and strain $\sigma_{cz}^{(i)} - \varepsilon_{cz}^{(i)}$ can be adopted according to the proposal of M. Attard and S. Setung [25], or a slightly modernized formula of D. Mander [16], which is written in the following form

$$\sigma_{cz}^{(i)} = f_{cc}^{(i)} \frac{\lambda^{(i)} \frac{\varepsilon_{cz}^{(i)}}{\varepsilon_{cc1}^{(i)}}}{\lambda^{(i)} - 1 + \left(\frac{\varepsilon_{cz}^{(i)}}{\varepsilon_{cc1}^{(i)}} \right)^{\lambda^{(i)}}}, \quad (5)$$

where $\lambda^{(i)}$ is a coefficient calculated by the following formula:

$$\lambda^{(i)} = \frac{E_c}{E_c - f_{cc}^{(i)} / \varepsilon_{cc1}^{(i)}}, \quad (6)$$

where E_c is initial modulus of elasticity of concrete.

To find the lateral pressure on concrete from the fiberglass shell, the following formula was proposed in [16]

$$\sigma_{cr}^{(i)} = \frac{v_{xr}^{(i)} - v_p^{(i)}}{\frac{d}{2E_{pc}t} + \frac{1 - v_{xr}^{(i)}}{v_{cz}^{(i)} E_c}} \cdot \varepsilon_{cz}^{(i)}. \quad (7)$$

where $v_{xr}^{(i)}$ and $v_p^{(i)}$ are lateral deformation coefficients of concrete and fiberglass;

$v_{cz}^{(i)}$ is the coefficient of elasticity of concrete;

E_{pc} is modulus of elasticity of the steel shell in compression;

d and t are external diameter and wall thickness of the steel shell

The coefficient of elasticity of concrete introduced into this formula to refine the calculation in the zone of large deformations is determined by the formula

$$v_{cz}^{(i)} = \frac{\sigma_{cz}^{(i)}}{E_c \varepsilon_{cz}^{(i)}}. \quad (8)$$

To simplify the calculations, the fiberglass shell can be considered as an elastic isotropic material. In this setting $v_p^{(i)} = v_{po}$, where v_{po} is Poisson's ratio of fiberglass.

The transverse strain coefficient of concrete varies. As the stress level increases, it increases from the Poisson's ratio $v_{co} = 0.18 \div 0.25$ to the limit value $v_{zru}^{(i)}$ at the stage of concrete destruction.

In [23], to determine the current values of $v_{jr}^{(i)}$ ($j = z, r$) by A.L. Krishan offered the following formula:

$$v_{zr}^{(i)} = v_{zru}^{(i)} - (v_{zru}^{(i)} - v_{co}) \left(\frac{v_{cz}^{(i)} - v_{czu}^{(i)}}{1 - v_{czu}^{(i)}} \right)^{0.5}. \quad (9)$$

The limit value of the coefficient of transverse deformation for a concrete core is determined by the formula

$$v_{zru}^{(i)} = v_{co} + (1 - \sqrt[3]{v_{czu}^{(i)}}), \quad (10)$$

where $v_{czu}^{(i)}$ is the coefficient of elasticity of the concrete core at the top of the diagram of its deformation, calculated by the formula (8) with $\sigma_{cz}^{(i)} = f_{cc}^{(i)}$ and $\varepsilon_{cz}^{(i)} = \varepsilon_{cc1}^{(i)}$.

Based on the proposed method of deformation calculation, an algorithm and a computer program «CFST-18» have been developed, which allow us to evaluate the stress-strain state and determine the

strength of compressed concrete elements. Table 2 shows a comparison of the new experimental values of strength and ultimate axial deformations of the samples studied by the authors of the article with the results of calculations using this program. Here, for analysis, calculated data are given on the total percentage of indirect reinforcement μ , the strength of volumetrically compressed concrete f_{cc}^{th} , as well as lateral pressure σ_{cr}^{th} in the limiting state of the element.

Table 2. Comparison of experimental data with calculation results.

Series	μ , %	f_c , MPa	σ_{cr}^{th} , MPa	f_{cc}^{th} , MPa	$\alpha_c = \frac{f_{cc}^{th}}{f_c}$	N_u^{th} , kN	$\frac{N_u^{exp}}{N_u^{th}}$	ε_u^{th} , %	$\frac{\varepsilon_u^{exp}}{\varepsilon_u^{th}}$
I-1	18.8	82.9	2.2	115.8	1.40	933	1.04	0.63	1.03
I-2	18.8	84.6	2.3	117.9	1.39	957	1.08	0.62	1.21
I-3	18.8	85.0	2.3	118.5	1.39	962	1.04	0.62	1.29
II-1	20.25	82.9	4.4	136.2	1.64	1440	0.90	1.92	0.88
II-2	20.25	84.6	4.4	138.9	1.64	1482	0.88	1.89	0.83
II-3	20.25	85.0	4.4	139.4	1.64	1490	0.93	1.88	0.96
III-1	1.45	82.9	4.0	126.7	1.53	826	1.05	0.44	1.25
III-2	1.45	84.6	4.0	129.1	1.53	845	0.98	0.42	1.19
III-3	1.45	85.0	4.0	129.6	1.52	850	1.06	0.42	1.14

Based on the comparison, we can state that the proposed calculation method allows to obtain quite reliable results on the strength and deformability of compressed elements with different options for indirect reinforcement. The maximum difference between the experimental and theoretical values of strength was 12 %. Moreover, such a discrepancy is observed for samples in which lateral deformations of concrete are restrained by both the outer shell and spiral reinforcement. Theoretical and experimental values of limit strains differ more significantly. The difference between them is in the range of +19 to –21 %. However, specialists know that such differences should be considered quite acceptable for deformations. Therefore, in general, we can state that the performed comparison confirmed the adequacy of the adopted calculation model.

4. Conclusions

1. The results of experimental studies indicate a positive effect on the strength of short compressed CFGFRT elements of both options used indirect reinforcement – the outer fiberglass shell and spiral reinforcement.

2. The high strength of such samples is due to a significant increase in concrete strength, which in samples with two types of indirect reinforcement increased by about 64 %.

3. The simultaneous presence of two types of indirect reinforcement significantly increased the deformability of the studied compressed elements. The maximum recorded values of longitudinal deformations of shortening of series II specimens amounted to about 1.7 %.

4. The high deformability of the compressed elements allows the efficient use of high-strength longitudinal reinforcement in them, which has economic feasibility.

5. The proposed calculation method allows obtaining reliable results on the strength and deformability of compressed elements with different options for indirect reinforcement.

References

- Lampo, R., Maher, A., Busel, J., Odello, R.. Design and development of FRP composite piling systems. Proceedings, International Composites Expo, 1997. Nashville. TN. Pp. 16–18.
- Fam, A.Z., Rizkalla, S.H. Concrete – filled FRP tubes for flexural and axial compression. Proceedings, 3rd International Conference on Advanced Composite Materials in Bridges and Structures. Ottawa. Canada, 2000. Pp. 315–322.
- Fam, A.Z., Pando, M.A., Filz, G., Rizkalla, S.H. Precast Piles for Route 40 Bridge in Virginia Using Concrete Filled FRP Tubes. PCI Journal, Precast/Prestressed Concrete Institute. 48(3), May – June 2003. Pp. 32–45.
- API. Recommended practice for planning, designing and constructing fixed offshore platforms – Working stress design. 20th Edition. American Petroleum Institute. Washington, DC, 1993.
- Ashford, S.A., Jakrapiyanun, W. Drivability of Glass FRP Composite Piling. Journal of Composites for Construction. 2001. 5(1). Pp. 58–60.
- Chin, J., Nguyen, T., Aouadi, K. Effects of environmental exposure on fiber – reinforced plastic (FRP) materials used in construction [Online]. Composites Technology & Research. URL: <https://doi.org/10.1520/CTR10120J>
- El – Tawil, S., Deierlein, G. Strength and ductility of concrete encased composite columns. Journal of Structural Engineering. 1999. 125(9), Pp. 1009–1019.
- Fardis, M., Khalili, H. Concrete encased in fiberglass plastic. ACI Proceedings, 78, Document JL78 – 38, 1981. Pp. 440–446.
- Iskander, M., Hassan, M. State of the practice review in FRP composite piling. Journal of Composites for Construction. ASCE. 1998. 2(3). Pp. 116–120.

10. Pando, M., Lesko, J., Case, S.. Preliminary Development of a Durability Model for concrete – filled FRP piles. Proceedings, 46th International Society for the Advancement of Material and Process Engineering (SAMPE) Conference. Long Beach. CA, 2001. Pp. 1597–1611.
11. Pando, M., Lesko, J., Fam, A., Rizkalla, S. Durability of Concrete-filled Tubular FRP Piles. Proceedings, 3rd International Conference on Composites in Infrastructure (CCI) [Online]. Conference. San Francisco. URL: <https://ru.scribd.com/document/335007153/Durability-of-Concrete-Filled-Tubular-FRP-Piles-Paper-12-pdf>
12. Ballinger, C. Composites poised to make inroads as highway structural materials. The Journal: Roads and Bridges, April 1994. Pp. 40–44.
13. Fam, A.Z., Rizkalla, S.H. Behavior, S.of axially loaded concrete – filled circular fiberreinforced polymer tubes. ACI Structural Journal. 2001. 98(3). Pp. 280–289.
14. Narkevich, M.Yu., Sagadatov, A.I. Study of the operation of centrally compressed steel – concrete elements with a core of high – strength concrete and thin – walledshell. BST: Bulletin of construction equipment. 2017. No. 11 (999). Pp. 14–15.
15. Krishan, A.L., Rimshin, V.I., Astafyeva, M.A., Narkevich, M.Yu. Determination of deformation characteristics of concrete. Natural and technical sciences. 2014. No. 9–10 (77). Pp. 367–369.
16. Krishan, A.L., Rimshin, V.I., Telichenko, V.I., Rakhmanov, V.A., Narkevich, M.Yu. The practical implementation of the calculation of concrete columns [Online]. Technology of the textile industry. 2017. 2(368). Pp. 227–232. URL: http://tftp.ivgpu.com/wp-content/uploads/2017/07/368_50.pdf
17. Fattah, A. Behaviour of concrete columns under various confinement effects. A dissertation doctor of philosophy. USA: Kansas State University. Kansas, 2012. 399 p.
18. Ahmed, M., Liang, Q., Patel, V., Hadi, M. Numerical analysis of axially loaded circular high strength concrete-filled double steel tubular short columns [Online]. Thin-Walled Structures. 2019. 138. Pp. 105–116. URL: <https://doi.org/10.1016/j.tws.2019.02.001>
19. Wang, G., Shen, Q., Jiang, H., Pan, X. Analysis and Design of Elliptical Concrete-Filled Thin-Walled Steel Stub Columns Under Axial Compression [Online]. International journal of steel structures. 2018. 18(2). Pp. 365–380. URL: <https://link.springer.com/article/10.1007/s13296-018-0002-5>
20. Wang, F., Han, L. Analytical behavior of special-shaped CFST stub columns under axial compression [Online]. Thin-Walled Structures. 2018. 129. Pp. 404–417. URL: <https://doi.org/10.1016/j.tws.2018.04.013>
21. Teng, J., Jiang, T., Lam, L., Luo, Y. Refinement of a design-oriented stress-strain model for FRP-Confined concrete [Online]. Journal Composites of Construction, ASCE. 2009. 13(4). Pp. 269–278. URL: [https://doi.org/10.1061/\(ASCE\)CC.1943-5614.0000012](https://doi.org/10.1061/(ASCE)CC.1943-5614.0000012)
22. Wei, Y., Wu, Y. Unified stress-strain model of concrete for FRP-confined columns [Online]. Journal of Construction and Building Materials. 2012. 26(1). Pp. 381–392. URL: <https://doi.org/10.1016/j.conbuildmat.2011.06.037>
23. Krishan, A.L., Astafyeva, M.A., Chernyshova, E.P. Strength Calculation of Short Concrete-Filled Steel Tube Columns [Online]. Journal of Concrete Structures and Materials. 2018. 84(12). URL: <https://doi.org/10.1186/s40069-018-0322-z>.
24. Karpenko, N.I., Karpenko, S.N., Petrov, A.N., Palyuvina, S.N. Model deformirovaniya zhelezobetona v prirashcheniyakh i raschet balok-stenok i izgibayemykh plit s treshchinami. Petrozavodsk: Izd-vo PetrGU, 2013. 156 p.
25. Attard, M., Setunge, S. Stress-strain relationship of confined and unconfined concrete [Online]. ACI Mater J. 1996. 93(5). Pp. 432–442. URL: <https://www.concrete.org/publications/internationalconcreteabstractsportal.aspx?m=details&ID=9847>
26. Krishan, A.L., Narkevich, M.Yu., Sagadatov, A.I. Experimental investigation of selection of warm mode for high-performance self-stressing self-compacting concrete [Online]. 7th International Symposium on Actual Problems of Computational Simulation in Civil Engineering (APCSCE). Russia, Novosibirsk, 2018. Pp. 1–6. URL: <https://doi.org/10.1088/1757-899X/456/1/012049>
27. Younesi, A., Rezaifar, O., Gholhaki, M., Esfandiari A. Structural health monitoring of a concrete-filled tube column. Magazine of Civil Engineering. 2019. No. 1(85). Pp. 136–145. DOI: 10.18720/MCE.85.11.
28. Snigireva, V.A., Gorynin, G.L. The nonlinear stress-strain state of the concrete-filled steel tube structures. Magazine of Civil Engineering. 2018. 83(7). Pp. 73–82. DOI: 10.18720/MCE.83.7.
29. Vatin, N.I., Barabanshchikov, Yu.G., Komarinskiy, M.V., Smirnov, S.I. Modification of the cast concrete mixture by air-entraining agents. Magazine of Civil Engineering. 2015. 56(4). Pp. 3–10. DOI: 10.5862/MCE.56.1. (rus)
30. Barabanshchikov, Yu.G., Arkharova, A.A., Ternovskii, M.V. Concrete with the lowered shrinkage and creep. Construction of Unique Buildings and Structures. 2014. 22(7). Pp. 152–165. DOI: 10.18720/CUBS.22.12. (rus)
31. Barabanshchikov, Yu.G., Komarinski, M.V. Superplasticized technological properties of concrete mixtures. Construction of Unique Buildings and Structures. 2014. 21(6). Pp. 58–69. DOI: 10.18720/CUBS.21.4. (rus)
32. Krishan, A.L., Troshkina, E.A., Chernyshova, E.P. Strength of Short Centrally Loaded Concrete-Filled Steel Tubular Columns [Online]. 18th IFAC Conference on Technology, Culture and International Stability TECIS 2018. Azerbaijan. Baku. 2018. Vol. 51. Iss. 30. Pp. 150–154. URL: <https://www.sciencedirect.com/science/article/pii/S2405896318329380?via%3Dihub>.

Contacts:

Anatolii Krishan, kris_al@mail.ru

Mikhail Narkevich, Narkevich_MU@mail.ru

Azat Sagadatov, azat0680@mail.ru

Vladimir Rimshin, v.rimshin@niisf.ru



DOI: 10.18720/MCE.94.2

Heat protective properties of enclosure structure from thin-wall profiles with foamed concrete

V.A. Rybakov^a, I.A. Ananeva^b, E.D. Pichugin^c, M. Garifullin^d

^a Peter the Great St. Petersburg Polytechnic University, St.-Petersburg, Russia

^b OTSK, Ltd, St.-Petersburg, Russia

^c «Airline», Moscow, Russia

^d Tampere University, Tampere, Finland

* E-mail: fishermanoff@mail.ru

Keywords: samples, non-autoclaved monolithic foamed concrete, rigid reinforcement, steel thin-wall profiles, cold-resisting properties, SOVBI technology, thermotechnical characteristics

Abstract. Receiving the qualitative, energy efficient and economic building is the main tendency in the civil engineering. One of the leading places is occupied by technology of frame-panel construction with use of new non-autoclaved, monolithic foamed concrete technology producing on a building site. On the example of the real samples there were determined the heat-shielding properties of foamed concrete in a condition of setting process and after attainment of strength with a practical and theoretical methods. The results were obtained for a non-autoclaved monolithic foamed concrete wall fragment (lightweight steel concrete structure – LSCS) for the areas with and without rigid reinforcement with steel thin-wall profiles (lightweight gauge steel structure – LGSS). Influence of the thermal bypass on cold-resisting properties of enclosure structures with technology “Intech LB” is revealed. On the basis of the received results, modernization of a design for improvement of its thermotechnical characteristics is made.

1. Introduction

Construction of residential country house or cottage is often associated with significant expenses; however, integration of new materials and modern technologies allows decrease them.

Technology that combines well known frame-panel construction technology (timber, plastic and thin-walled steel structures) with modern technology of construction site production of non-autoclave, cast in-situ, acoustic and thermal insulating, constructive foamed concrete can be considered as breakthrough in modern low-rise construction industry. Application of such concrete gives an opportunity to decrease shipping costs, construction period, materials consumption. Moreover, even thin foamed concrete walls possess sufficient thermal insulation properties. High mobility of this concrete type allows to effortlessly perform concrete mix distribution and to form building structures on any height.

There is a large variety of thermal insulating materials in modern construction industry; such as mineral wool, polystyrene and polyurethane foam. For example, M.V. Leshchenko and V.A. Semko proposes to use polystyrene concrete as an insulating material in wall panels made of light gauge studs. It should solve the problem of thermal bridges in such panels [1].

However, they possess significant disadvantages. For instance, mineral wool insulators are subjected to sitting and, also, moisturizing that causes in one hand decrease of insulating properties, in another cause increase in load that is crucial in rooftop insulation. Cellular concretes are well known as material for a long time and develop as foamed and aerated concretes. These branches are described in article [2–6].

Thermal insulation of building enclosing by cast in-situ foamed concrete is relatively modern way of cellular concrete application. This technology is developed and integrated in Russian Federation construction industry by group of V.D. Vasiliev [7, 8].

A.Y. Struchkova, Yu.G. Barabanshikov, K.S. Semenov, A.A. Shaibakova solved the problems of thermal cracking resistance of massive concrete and reinforced concrete structures during the building period are

Rybakov, V.A., Ananeva, I.A., Pichugin, E.D., Garifullin, M. Heat protective properties of enclosure structure from thin-wall profiles with foamed concrete. Magazine of Civil Engineering. 2020. 94(2). Pp.11–20.
DOI: 10.18720/MCE.94.2



considered. The calculation results of a research on the effect of hardening temperature on the process of heat dissipation process of concrete are given [9].

T.V. Krivaltzevich and E.V. Gurova conducted comparison of technical properties and basic characteristics of thermal insulation materials of different structure and considered advantages and disadvantages of non-autoclave foamed concrete in their work [10].

V.V. Bespalov, D. Ucer, I.D. Salmanov, I.N. Kurbamov, S.V. Kupavykh consider a problem whose purpose is determine the combined behavior of masonry walls and reinforcing meshes together, according to their deformation characteristics. The results obtained from the theoretical sample wall and the case study wall with plain and reinforced alternatives stated that the compatibility of deformation characteristics between the wall and the reinforcing mesh is the key for combined strength behavior of the wall [11].

V.V. Plotnikov and M.V. Bogatovsky demonstrated research results of development of energy and material saving technology of construction of interior multilayer cast in-situ walls with application of low density composite foamed concretes [12]. This technology provides ability to control formation of foamed concrete structure in process of its obtainment and on first stages of curing. For example, in articles [13–17] possibility of direction of pore structure of non-autoclave foam concrete is studied. Option of concrete performance characteristics increase by adding of different admixtures (colloidal suspension of silicon dioxide, cold-bonded fly ash, etc). Such admixture stabilizes and improves pore structure of material, developing properties of foamed concrete. Also, the article [18] proposes a numerical model for estimating the effect of composite reinforcement on the bearing capacity of a compressed-bent masonry wall which is constructed on the basis of experimental studies of walls from cellular concrete blocks.

Nowadays, there are technologies of enclosing structures construction based on combination of light steel framing and various thermal insulators. Lightweight metal framing is used for constructive purposes worldwide. However, it is applied in Russia for low rise construction only, since lack of production standards.

Major advantages of light steel framing constructions are demonstrated in articles [19–23].

D.V. Kuzmenko and N.I. Vatin [24] developed new type of enclosing structure based on light metal framing – thermal panel. Main components are thermal profile and efficient thermal insulator. Thermal panel is perspective modern energy-saving technology that can be applied in high-rise construction.

Based on LSTK M.K. Bronzova, N.I. Vatin, M.R. Garifullin were engaged in studying of a design in the work [25] and others in works [26–32].

Application of modern constructions is reasonable only if their superior thermal properties exploited properly. Results of reduced total thermal resistance calculation and heat transfer performance uniformity factor determination are demonstrated in work [33], performed by T.A. Karnilov and G.N. Gerasimov. They concluded that the most efficient method of thermal protection of two-layer walls is variation exterior layer along with constant width of inner layer that corresponds to minimal parameter of pillar cross section, determined by obtained value of bearing capacity.

Enclosing structure, applying in low-rise construction and in attic erection, is chosen as object of research. The structure consists from galvanized steel profile TS200-50-1.5, filled with non-autoclave cast in-situ foamed concrete in condition of natural moist contain (D200, 300 mm). Object was tested in climate chamber to determine thermal technical properties of construction.

Results of wall fragment thermal technical properties evaluation by climate chamber presented in article [34]. Temperature values on wall-slab joint (thermal conductive location) have been determined and compared to values calculated according to calculated values of temperature and dew point parameters.

There are developed three Standards that set regulations for design and construction cast in-situ, non-autoclave foamed concrete buildings. Saint-Petersburg Peter the Great Polytechnic University research group (N.I. Vatin, V.A. Rybakov, and A.O. Rodicheva) developed Company's Code

1) STO 83835311.001-2015. Reinforced concrete structures from heat-insulating non-autoclave monolithic foam concrete with rigid reinforcement from profile steel, with facing with asbestos-cement and glass-magnesite sheets. Design rules. ("Monplaisir", Ltd., Russia)

2) STO 06041112.001–2018 (changed 10.02.2019). Panels from steel concrete structures based on heat-insulating non-autoclave monolithic foam concrete, profile steel faced with fibrocement sheets. ("INTECH LB", Ltd., Russia)

3) STO 06041112.002–2018 (changed 10.02.2019). Steel concrete structures from heat-insulating non-autoclave monolithic foam concrete, profile steel with facing with fibrocement cement sheets. Design rules. ("INTECH LB", Ltd., Russia)

Requirements for cast in-situ foamed concrete are based on STO 83835311.001-2015, STO 06041112.001-2018, and STO 06041112.002-2018 and developed by Saint-Petersburg Peter the Great Polytechnic University research group.

Foamed concrete is a widely applicable material due to its economic efficiency. Main drawback of this material – low mechanical strength can be coped with framework for construction. Lightweight steel framing from thin wall profiles is one of the most convenient option for this purpose.

This research is focused on determination of thermal protecting properties of non-autoclave cast in-situ foamed concrete after strength gain in reinforced and unreinforced sections of enclosing structure, consisting of steel thin-wall profiles framing and cast in-situ foamed concrete.

Research process can be divided on solution of three goals:

1. Determination of physical and mechanical properties of foamed concrete- used in research;
2. Determination of thermal protecting properties of bearing enclosing structures, consisting of steel thin-walled profiles and cast in-situ foamed concrete;
3. Comparison of thermal resistance values in reinforced and unreinforced sections of structure.

2. Methods

2.1. Determination of thermal and mechanic parameters of thermal insulating constructive material

2.1.1. Determination of humidity

Humidity of foamed concrete is determined according to Russian State Standard GOST 12730.2–78. Twelve samples (100×100×100 mm) have been weighted in moist condition, put in low temperature experimental furnace SNOL 67/350 and being dried (+105 °C) until mass can be considered constant (approximately 48 hours). Then dry samples being weighted again and humidity being calculated by formula (1):

$$W_m = \frac{m_b - m_c}{m_c} \cdot 100 \%, \quad (1)$$

where W_m is samples humidity, %;

m_b is mass of samples before drying, kg;

m_c is mass of samples after drying, kg.

2.1.2. Determination of density

1. Density is found by formula (2):

$$\rho = \frac{m}{V}, \quad (2)$$

where ρ is density, kg/m³;

m is mass, kg;

V is volume, m³.

Results of density and humidity determination are presented in Table 1.

Table 1. Density and humidity of samples.

Samples number	Mass of moist samples, kg	Density, kg/m ³	Mass of dry samples, kg	Humidity, %
1	0.497	497	0.342	45
2	0.441	441	0.307	44
3	0.458	458	0.32	43
4	0.466	466	0.327	43
5	0.472	472	0.36	43
6	0.511	511	0.33	42
7	0.469	469	0.327	42
8	0.46	460	0.307	41
9	0.44	440	0.331	43
10	0.441	441	0.306	44
11	0.502	502	0.348	44
12	0.624	624	0.438	42
Average value	–	481.75	0.337	43

2.1.3. Determination of strength

Each specimen is being tested by compact experimental press MIP-25/50 to evaluate compressive strength. Samples 2, 4, 6, 11 have been put in plastic containers to conserve dehydrated condition after drying in SNOL 67/350 furnace. Samples 1, 3, 8, 12 were tested in conditions of natural humidity; mass of these Samples raised by 3–5 grams since furnace extraction. Results presented in Table 2.

Table 2. Compressive strength of specimens.

Samples number	Humidity, %	Mass, kg	Compressive strength, MPa
1	1	0.346	0.1
2	0.1	0.307	0.14
3	1	0.323	0.15
4	0.1	0.327	0.1
6	0.1	0.36	0.19
8	1	0.331	0.12
11	0.1	0.348	0.16
12	1	0.443	0.12
Average value			0.135

2.2. Determination of thermal protecting properties of enclosing structure based on thin-wall steel C-beams and cast in-situ foamed concrete.

Structure consists from non-autoclave cast in-situ foamed concrete D200 block (460×760×300 mm) with natural humidity (tests performed 37 days after casting) and two galvanized steel C-beams PS 200-50-1.5 (Figure 1).

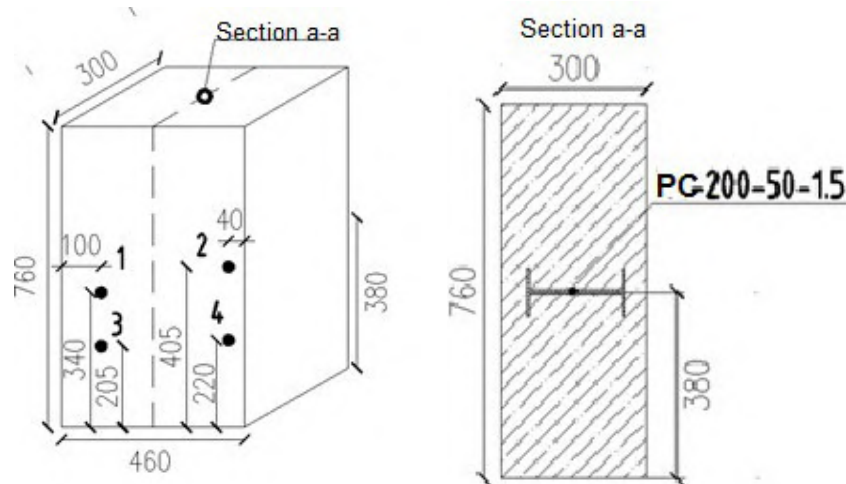


Figure 1. Geometric parameters of samples. Location of temperature sensors.

Goals of the experiment are determination of thermal resistance in points of reinforced and unreinforced foamed concrete, their comparison and analytic comparison of actual resistance to thermal transition to structure with theoretic calculation for the samples.

2.2.1. Determination of thermal technical properties of enclosing structure, climate chamber tests

Structure has been put in climate chamber TX-500, with following temperature conditions: temperature in cold (exterior) section is set on $-30\text{ }^{\circ}\text{C}$, temperature in warm (interior) section) set on $+24\text{ }^{\circ}\text{C}$. The sample was subjected to chamber tests until installation of thermal process balance, in this case – 3 days. Temperature sensors and sensors of heat flow were installed on surface of the sample (Figure 1). Results are formed in Table 2. Charts that represent dependence of surface temperature on time and dependence of heat flow on time presented on Figures 3, 4.

Coefficient of thermal conductivity is determined by formula (3):

Results of coefficient of thermal conductivity calculation put in Table 4. Approximate value is calculated for each point after installation of thermal balance, in this case balance was set on 4:57 07.06.2017.

Table 3. Temperature value sand heat flows values in interior and exterior points of wall samples.

Date		Time		Point 1		Point 2	
Day/ month/year	Hour/minute	Heat flow W/m ²	Interior temp., °C	Exterior temp., °C	Heat flow W/m ²	Interior temp., °C	Exterior temp., °C
05.05.	16:57	10.733	21.61	23.17	6.776	23.09	23.3
05.05.	19:57	34.892	18.01	-26.26	26.205	20.95	-25.8
05.05.	22:57	41.942	17.2	-26.53	41.693	20.14	-26.44
06.05.	1:57	46.919	17.02	-26.68	50.544	19.88	-26.72
06.05.	4:57	52.112	17.19	-26.69	54.82	20.02	-26.8
06.05.	7:57	52.868	17.77	-26.76	62.061	20.59	-26.87
06.05.	10:57	51.413	17.98	-26.9	62.293	20.75	-27.01
06.05.	13:57	53.769	18.58	-26.9	64.086	21.36	-27.03
06.05.	16:57	51.638	18.38	-26.96	62.781	21.06	-27.13
06.05.	19:57	50.962	17.96	-26.91	60.947	20.55	-27.1
06.05.	22:57	52.152	17.69	-26.94	65.48	20.29	-27.07
07.05.	1:57	49.82	17.65	-26.89	62.974	20.26	-27.06
07.05.	4:57	56.092	17.85	-26.93	64.895	20.37	-27.12
07.05.	7:57	57.965	20.93	-26.99	73.648	23.5	-27.1
07.05.	10:57	51.404	19.92	-27.11	68.787	22.42	-27.27
07.05.	13:57	49.483	19.75	-27.13	71.43	22.29	-27.22
07.05.	16:57	52.964	19.39	-27.02	68.723	21.85	-27.12
07.05.	19:57	49.829	18.72	-26.91	65.984	21.08	-27.02
07.05.	22:57	48.752	18.51	-26.99	71.406	20.93	-27.14
08.05.	1:57	49.941	18.62	-26.91	68.676	20.96	-27.06
08.05.	4:57	52.369	18.78	-27.03	68.26	21.05	-27.11
08.05.	7:57	58.463	21.09	-26.96	72.279	23.49	-27.09
08.05.	10:57	57.764	23.63	-27.15	77.732	26.05	-27.18
08.05.	13:57	60.24	20.84	-27.09	64.07	23.17	-27.13
08.05.	16:57	54.548	19.88	-27.09	67.018	22.26	-27.12
Date		Time		Point 3		Point 4	
Day/ month/year	Hour/minute	Heat flow W/m ²	Interior temp., °C	Day/ month/year	Hour/minute	Heat flow W/m ²	Interior temp., °C
05.05.	16:57	16.194	21.19	22.47	24.958	21.87	22.81
05.05.	19:57	19.387	19.43	-25.67	28.275	21	-24.48
05.05.	22:57	30.154	18.79	-26.09	35.133	20.89	-25.25
06.05.	1:57	31.402	18.5	-26.31	40.217	20.99	-25.53
06.05.	4:57	43.019	18.66	-26.34	41.656	21.32	-25.67
06.05.	7:57	38.47	19.19	-26.48	47.48	22.07	-25.79
06.05.	10:57	40.138	19.36	-26.68	44.839	22.32	-26.01
06.05.	13:57	39.028	19.92	-26.71	44.083	22.98	-26.08
06.05.	16:57	37.171	19.73	-26.8	42.373	22.69	-26.16
06.05.	19:57	44.586	19.3	-26.73	42.866	22.23	-26.13
06.05.	22:57	36.372	19.09	-26.74	42.126	22.03	-26.16
07.05.	1:57	35.581	19.09	-26.72	41.982	22.04	-26.09
07.05.	4:57	39.412	19.26	-26.76	41.021	22.22	-26.09
07.05.	7:57	41.009	22.19	-26.84	43.256	25.44	-26.23
07.05.	10:57	43.729	21.33	-27.04	42.644	24.39	-26.35
07.05.	13:57	35.995	21.2	-27.01	43.725	24.21	-26.35
07.05.	16:57	36.518	20.88	-26.91	41.227	23.76	-26.27
07.05.	19:57	34.021	20.2	-26.82	39.27	23.05	-26.17
07.05.	22:57	36.858	19.98	-26.88	40.256	22.95	-26.24
08.05.	1:57	40.124	20.1	-26.81	39.453	22.98	-26.18
08.05.	4:57	36.097	20.17	-26.98	38.776	23.09	-26.22
08.05.	7:57	40.893	22.58	-26.89	42.882	25.62	-26.25
08.05.	10:57	43.737	25.08	-27.04	46.096	28.25	-26.43
08.05.	13:57	37.199	22.36	-26.99	37.424	25.23	-26.31
08.05.	16:57	35.843	21.45	-26.98	38.999	24.34	-26.28

Used next formulas from ISO 7345:1987 Thermal insulation – Physical quantities and definitions (MOD), determine coefficient of thermal conductivity:

$$R = \frac{T_2 - T_1}{q};$$

$$\lambda = \frac{q \cdot d}{T_2 - T_1},$$
(3)

where λ is coefficient of thermal conductivity, W/(m·K);

q is heat flow, W/m²;

d is wall thickness, m;

T_1, T_2 are temperature of wall surfaces, °C

Table 4. Coefficient of thermal conductivity of surface.

Date Day/month/year	Time Hour/minute	Coefficient of thermal conductivity, W/(m·K)			
Date	Time	Point 1	Point 2	Point 3	Point 4
07.05.	4:57	0.376	0.41	0.257	0.255
07.05.	7:57	0.363	0.437	0.251	0.251
07.05.	10:57	0.328	0.415	0.271	0.252
07.05.	13:57	0.317	0.433	0.224	0.259
07.05.	16:57	0.342	0.421	0.229	0.247
07.05.	19:57	0.328	0.412	0.217	0.239
07.05.	22:57	0.321	0.446	0.236	0.246
08.05.	1:57	0.329	0.429	0.257	0.241
08.05.	4:57	0.343	0.425	0.23	0.236
08.05.	7:57	0.365	0.429	0.248	0.248
08.05.	10:57	0.341	0.438	0.252	0.253
08.05.	13:57	0.377	0.382	0.226	0.218
08.05.	16:57	0.348	0.407	0.222	0.231
Average value		0.344	0.422	0.24	0.244

Technical thermal resistance is calculated by formula (4) (For reinforced section is R_a , for unreinforced section is R_b).

$$R = \frac{d}{\lambda},$$
(4)

where R is thermal resistance, (m²·K)/W;

d is wall thickness, m;

λ is coefficient of thermal conductivity, W/(m·K)

$$R_a = \frac{0.3}{0.383} = 0.783 \frac{m^2 \cdot K}{W}; \quad R_b = \frac{0.3}{0.242} = 1.239 \frac{m^2 \cdot K}{W}.$$

Thermal resistance diagram for sample section is plotted to calculate thermal resistance for whole construction (Figure 2).

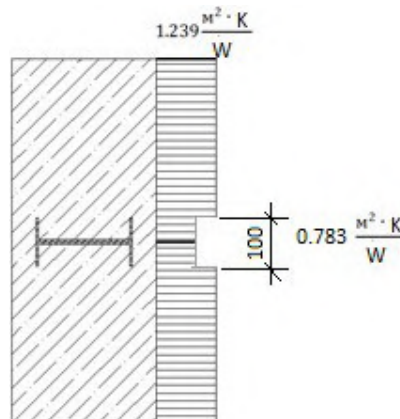


Figure 2. Thermal conductivity resistance for specimen cross section.

Average value of thermal resistance is calculated:

$$R = \frac{A_1 + A_2 + A_3 \dots + A_n}{\frac{A_1}{R_1} + \frac{A_2}{R_2} + \frac{A_3}{R_3} + \dots + \frac{A_n}{R_n}} = 1.209 \frac{\text{m}^2 \cdot \text{K}}{\text{W}}. \quad (5)$$

Formula (6) is applied to obtain thermal conductivity:

$$R_o = \frac{1}{\alpha_e} + R + \frac{1}{\alpha_i}, \quad (6)$$

where α_i is heat exchange coefficient for interior surface of enclosure structure by Set of Rules 50.13330.2012

$$(\alpha_i = 8.7 \frac{\text{m}^2 \cdot \text{K}}{\text{W}});$$

α_e is heat exchange coefficient for exterior surface of enclosure structure by Set of Rules 50.13330.2012

$$(\alpha_e = 23 \frac{\text{m}^2 \cdot \text{K}}{\text{W}});$$

R is thermal resistance, $(\text{m}^2 \cdot \text{K})/\text{W}$.

$$R_o = \frac{1}{8.7} + 1.209 + \frac{1}{23} = 1.367 \frac{\text{m}^2 \cdot \text{K}}{\text{W}}.$$

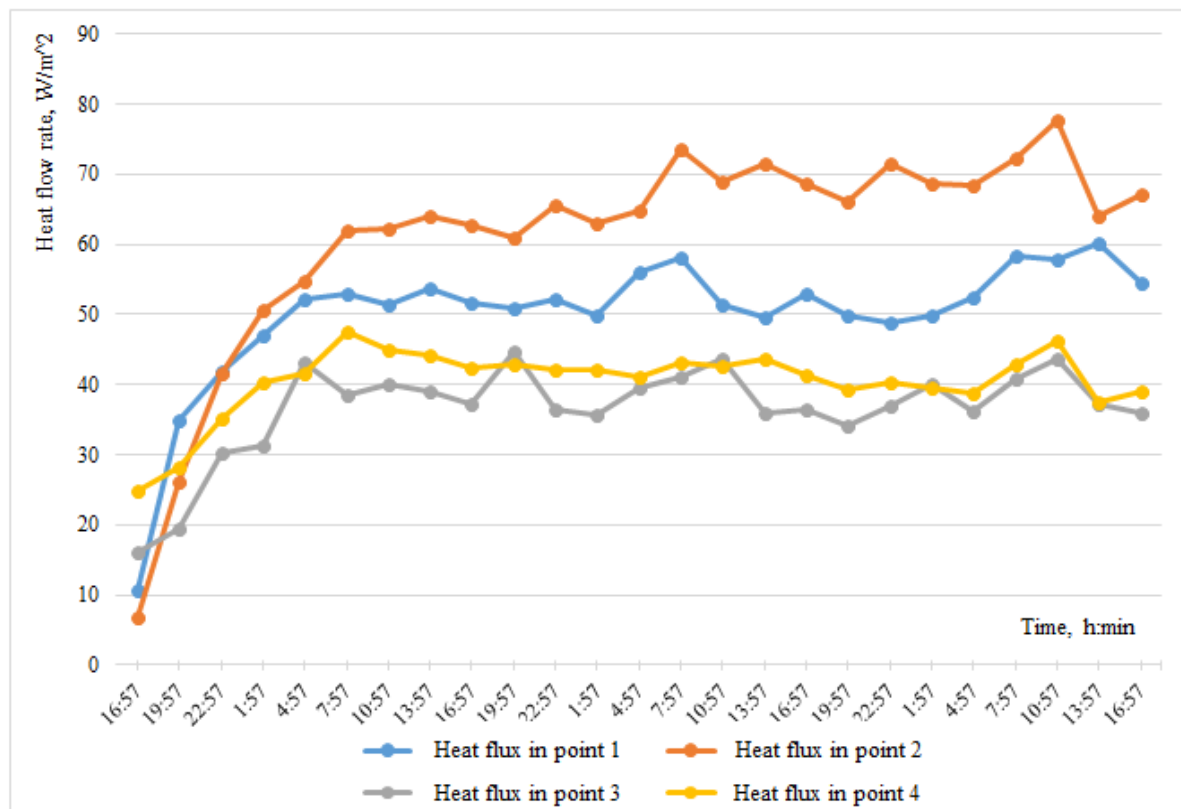


Figure 3. Heat flow chart.

3. Results and Discussion

Technologies of cast in situ non-autoclave foamed concrete buildings construction are lack in Russian industry in 2020. Thus, Business association "SOVBI" is a unique manufacturer of bearing enclosing structures, based on thin-wall profile metal framing and cast in situ foamed concrete. Therefore, research from this article does not have any analogue, and consideration of comparison of obtained results with others is premature. Researches of thermal-saving properties of this kind of structures are also lack abroad.

However, in order to evaluate adequacy of obtained results, method from ISO_06946–2007 can be applied.

3.1. Theoretical calculation of thermal conductivity resistance for non-uniform enclosing structure

Calculation of thermal conductivity resistance for non-uniform enclosing structure is performed according to following rules ISO_06946–2007.

The total thermal resistance R_o , of a component consisting of thermally homogeneous and thermally inhomogeneous layers parallel to the surface is calculated as the arithmetic mean of the upper and lower limits of the resistance:

$$R_o = \frac{R'_T + R''_T}{2}, \tag{7}$$

where R'_T is the upper limit of the total thermal resistance, is determined by formula:

$$\frac{1}{R'_T} = \frac{f_a}{R_{Ta}} + \frac{f_b}{R_{Tb}} + \frac{f_c}{R_{Tc}} + \frac{f_d}{R_{Td}} + \frac{f_e}{R_{Te}}. \tag{8}$$

$f_a; f_b; f_c; f_d; f_e$ are fractional area of each section (Figure 5).

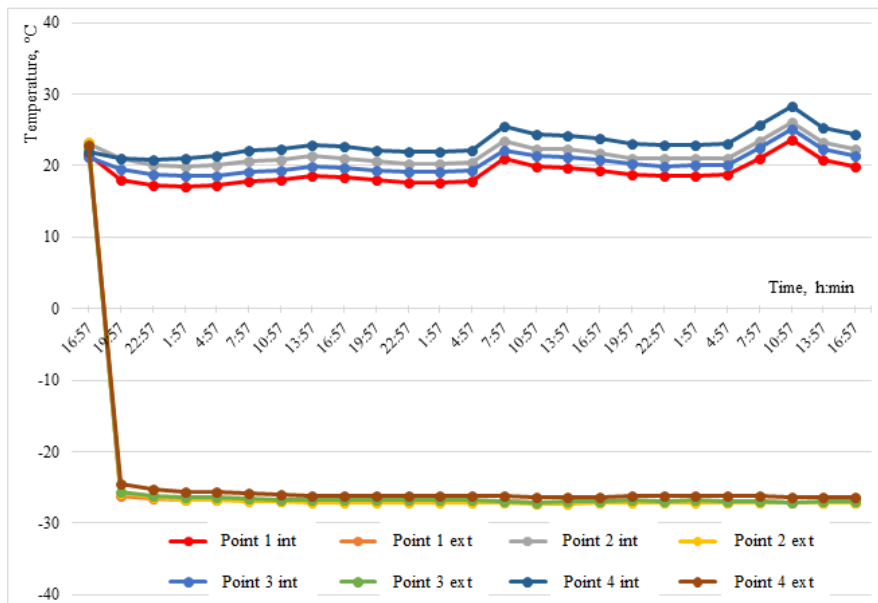


Figure 4. Surface temperature chart.

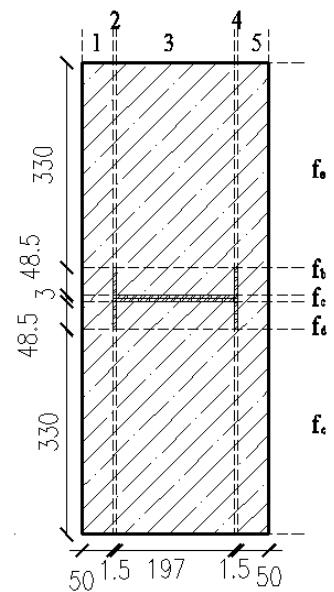


Figure 5 Division to planes.

$R_{Ta}; R_{Tb}; R_{Tc}; R_{Te}$ are the total thermal resistances from environment to environment for each section, calculated using Equation (4).

$$\frac{1}{R'_T} = 2 \cdot \frac{0.33}{\frac{0.3}{0.08}} + 2 \cdot \frac{0.0485}{2 \cdot \frac{0.05}{0.08} + 2 \cdot \frac{0.0015}{47} + \frac{0.197}{0.08}} + \frac{0.003}{2 \cdot \frac{0.05}{0.08} + \frac{0.2}{47}} = \frac{1}{0.44} \frac{m^2 \cdot K}{W}.$$

R''_T is the lower limit of the total thermal resistance:

Calculate an equivalent thermal resistance, R_j , for each thermally inhomogeneous layer using Equation (9):

$$\frac{1}{R_j} = \frac{f_a}{R_{aj}} + \frac{f_b}{R_{bj}} + \frac{f_c}{R_{cj}} + \frac{f_d}{R_{dj}} + \frac{f_e}{R_{ej}}. \tag{9}$$

The lower limit is then determined using Equation (10):

$$R''_T = R_1 + R_2 + R_3 + R_4 + R_5. \tag{10}$$

Determine $\frac{1}{R_j}$ for every layer with Equation (9):

$$\frac{1}{R_1} = \frac{0.33 + 0.0485 + 0.003 + 0.00485 + 0.33}{\frac{0.05}{0.08}} = 1.216 \frac{W}{m^2 \cdot K};$$

$$\frac{1}{R_2} = 2 \cdot \frac{0.33}{\frac{0.0015}{0.08}} + \frac{0.0485 + 0.003 + 0.0485}{\frac{0.0015}{47}} = 3168.2 \frac{W}{m^2 \cdot K};$$

$$\frac{1}{R_3} = 2 \cdot \frac{0.3785}{\frac{0.197}{0.08}} + \frac{0.003}{\frac{0.197}{47}} = 1.023 \frac{W}{m^2 \cdot K}.$$

$\frac{1}{R_1} = \frac{1}{R_5}$ and $\frac{1}{R_2} = \frac{1}{R_4}$ as the layers are similar, thus:

$$R''_T = 2.62 \frac{m^2 \cdot K}{W};$$

$$R_o = \frac{2.27 + 2.62}{2} = 2.44 \frac{m^2 \cdot K}{W}.$$

4. Conclusions

1. Research shows that strength properties of material do not allow to evaluate concrete with axial compression strength class, thus impact of foamed concrete on composite mechanical strength is negligibly. Major function of foamed concrete is thermal insulation.

2. Identified thermal protective properties of composite structure made of foamed concrete and steel thin-wall profiles have been determined experimentally in sections with/without reinforcement: reinforced sections – 0.783 (m²·K)/W; unreinforced sections – 1.239 (m²·K)/W

3. It's established that the heat resistance of the enclosing structure in reinforced section is 63 % of resistance in unreinforced one.

4. Shown comparison of thermal conductivity resistance of non-uniform enclosing structure has been performed by experimental and theoretical methodic :thermal conductivity resistance of enclosure, obtained experimentally – 1.367(m²·K)/W; thermal conductivity resistance of enclosure, obtained by calculation – 2.44(m²·K)/W.

5. It's established that the heat resistance of the thermal conductivity of non-uniform enclosure, obtained experimentally is two times less than resistance, calculated theoretically.

6. It is recommended to modify enclosure made of steel thin-wall profiles and foamed concrete with layer of mineral wool for optimal heating performance according to requirements for Province of Leningrad.

7. Explanation of the discrepancies between the practical and theoretical values of the heat transmission resistance:

7.1 As we used monolithic foamed concrete on the site in the winter time, high probability that during the process of pouring of the sample, water or snow penetrated into the pores of sample and decrease heat transmission resistance.

7.2 Experimental accuracy.

5. Acknowledgment

Acknowledgment is expressed to Igor I. Pestryakov, CEO of «Vysota» certification center, for provided equipment, used for tests and to Anatoly V. Seliverstov, CEO of «Sovbi», Ltd, for structure specimens, provided for tests.

References

1. Leshchenko, M.V., Semko, V. Thermal characteristics of the external walling made of cold-formed steel studs and polystyrene concrete. Magazine of Civil Engineering. 2015. 60(8). Pp. 44–55. (rus). DOI: 10.5862/MCE.60.6.
2. Korniyenko, S.V., Vatin, N.I., Gorshkov, A.S. Thermophysical field testing of residential buildings made of autoclaved aerated concrete blocks. Magazine of Civil Engineering. 2016. 64(4). Pp. 10–25. DOI: 10.5862/MCE.64.2
3. Gorshkov, A.S., Pestryakov, I.I., Korniyenko, S.V., Vatin, N.I., Olshevskiy, V.Ya. Actual thermal insulation properties of cellular autoclave curing concretes, Construction of Unique Buildings and Structures. 2018. 68(5). Pp. 75–104. (rus) DOI: 10.18720/CUBS.68.7
4. Korniyenko, S. Complex analysis of energy efficiency in operated high-rise residential building: case study. E3S Web of Conferences. 2018. No. 33. Pp. 02005.

5. Korniyenko, S.V. The experimental analysis and calculative assessment of building energy efficiency. *Applied Mechanics and Materials*. 2014. Vol. 618. Pp. 509–513.
6. Barabanshchikov, Y., Fedorenko, I., Kostyrya, S., Usanova, K. Cold-Bonded Fly Ash Lightweight Aggregate Concretes with Low Thermal Transmittance. *Advances in Intelligent Systems and Computing*. 2019. 983. Pp. 858–866.
7. Lundyshev, I.A. Karkasnyye sistemy, primenyayemyye v ograzhdayushchikh konstruksiyakh pri stroitel'stve iz monolitnogo penobetona [Frame systems used in enclosure structure in construction from monolithic autoclaved aerated concrete]. *Magazine of Civil Engineering*. 2009. 3(1). Pp. 13–16. (rus)
8. Vasilyev, V.D. Monolitnyy penobeton po tekhnologii «SOVBI» [Monolithic foam concrete according to the "Svbi" technology]. *Stroitelnyye materialy*. 2005. No. 12. Pp. 39–40. (rus)
9. Struchkova, A.Y., Barabanshchikov, Yu.G., Semenov, K.S., Shaibakova, A.A. Heat dissipation of cement and calculation of crack resistance of concrete massifs. *Magazine of Civil Engineering*. 2018. No. 78(2). Pp. 128–135. doi: 10.18720/MCE.78.10
10. Krivaltsevich, T.V., Gurova, Ye.V. Sravneniye neavtoklavnogo penobetona s drugimi teploizolyatsionnymi materialami [comparison of non-autoclave foam concrete with other heat-insulating materials]. *Arkhitektura, stroitelstvo, transport*. 2015. Pp. 508–512. (rus)
11. Bespalov, V.V., Ucer, D., Salmanov, I.D., Kurbanov, I.N., Kupavykh, S.V. Deformation compatibility of masonry and composite materials. *Magazine of Civil Engineering*. 2018. No. 78(2). Pp. 136–150. doi: 10.18720/MCE.78.11
12. Plotnikov, V.V., Botagovskiy, M.V. Povysheniye dolgovechnosti monolitnogo penobetona nizkoy plotnosti putem modifitsirovaniya tsementa aktivirovannymi kristallogidratami [Improving the durability of monolithic low-density foam concrete by modifying cement with activated crystalline hydrates]. *Promyshlennoye i grazhdanskoye stroitelstvo*. 2015. No. 10. Pp. 33–39. (rus)
13. Pertseva, O., Nikolskiy, S. Dependence of relative decreasing in strength by rate of strain for the new rapid method for determination of concrete frost resistance. *Applied mechanics and materials*. 2015. Pp. 505–510.
14. Korsun, V., Korsun, A. The influence of precompression on strength and strain properties of concrete under the effect of elevated temperatures. *Applied mechanics and materials*. 2015. Pp. 469–474.
15. Korsun, V., Vatin, N., Korsun, A., Nemova, D. Physical-mechanical properties of the modified fine-grained concrete subjected to thermal effects up to 200°s. *Applied mechanics and materials*. 2014. Pp. 1013–1017.
16. Usanova, K., Barabanshchikov, Yu., Fedorenko Yu., Kostyrya S. Cold-bonded fly ash aggregate as a coarse aggregate of concrete. *Construction of Unique Buildings and Structures*. 2018. 9(72). Pp. 31–45. DOI: 10.18720/CUBS.72.2
17. Bayev, M.N., Shchukina, Yu.V. Teploizolyatsionnyy neavtoklavnyy penobeton s povyshennymi kharakteristikami [Heat-insulating non-autoclave foam concrete with enhanced characteristics]. *Polzunovskiy vestnik*. 2011. No. 1. Pp. 35–37. (rus)
18. Orlovich, R.B., Bespalov, V.V., Derkach, V.N. Compressed-bent masonry walls reinforced with composite materials. *Magazine of Civil Engineering*. 2018. No. 79(3). Pp. 112–119. doi: 10.18720/MCE.79.12
19. Sovetnikov, D.O., Videnkov, N.V., Trubina, D.A. Light gauge steel framing in construction of multi-storey buildings. *Construction of Unique Buildings and Structures*. 2015. 30(3). Pp. 152–165. (rus). DOI: 10.18720/CUBS.30.11
20. Rybakov, V.A., Molchanova, N., Laptev, V., Suslova, A., Sivokhin, A. The effect of conjunction flexibility on the local stability of steel thin-walled slab beams. *MATEC Web of Conferences*. 2016. Pp. 01017.
21. Trubina, D., Abdulaev, D.A., Pichugin, E., Rybakov, V., Garifullin, M., Sokolova, O. Comprasion of the bearing capacity of I-st-profile depending on the thickness of its elements. *Applied mechanics and materials*. 2015. Pp. 752–757.
22. Trubina, D., Abdulaev, D., Pichugin, E., Rybakov, V. Geometric nonlinearity of the thin-walled profile under transverse bending. *Applied mechanics and materials*. 2014. Pp. 1133–1139.
23. Ariyanayagam, A.D., Poologanathan, K., Mahendran, M. Thermal modelling of load bearing cold-formed steel frame walls under realistic design fire conditions. *Advanced Steel Construction*. 2017. No. 2. Pp. 160–189.
24. Kuz'menko, D.V., Vatin, N.I. Ograzhdayushchaya konstruksiya «nulevoy tolshchiny» – termopanel' [Zero-thickness building envelope - thermopanel]. *Magazine of Civil Engineering*. 2008. 1(1). Pp. 13–21. (rus)
25. Bronzova, M.K., Vatin, N.I., Garifullin, M.R. Frame buildings construction using monolithic foamed concrete. *Construction of Unique Buildings and Structures*. 2015. 28(1). Pp. 74-90. (rus)
26. Vatin, N.I., Grinfeld, G.I., Okladnikova, O.N., Tulko, S.I. Soprotivleniye teploperedache ograzhdayushchikh konstruksiy iz gazobetona s oblitsovkoj iz silikatnogo kirpicha [Resistance to heat transfer of aerated concrete enclosures with silicate brick cladding]. *StroyPROFIL*. 2007. No. 5(59). Pp. 28–32. (rus)
27. Rybakov, V.A., Gamayunova, O.S. The stress-strain state of frame constructions' elements from thin-walled cores. *Construction of Unique Buildings and Structures*. 2013. 12(7). Pp. 79-123. (rus). DOI: 10.18720/CUBS.12.10
28. Lalin, V., Rybakov, V., Sergey, A. The finite elements for design of frame of thin-walled beams. *Applied mechanics and materials*. 2014. Pp. 858–863.
29. Stamatovic, B., Korsun, A. Local data flow principles in porosity of materials. *Applied mechanics and materials*. 2015. Pp. 371–376.
30. Korsun, V., Korsun, A. The influence of precompression on strength and strain properties of concrete under the effect of elevated temperatures. *Applied mechanics and materials*. 2015. Pp. 469–474.
31. Akimov, L.I., Ilenko, N., Mizharev, R., Cherkashin, A., Vatin, N.I., Chumadova, L.I. Composite concrete modifier cm 02-10 and its IMPA. *Matec web of conferences*. 2016. Pp. 01022.
32. Frolov, A., Chumadova, L., Cherkashin, A., Akimov, L. Prospects of use and impact of nanoparticles on the properties of high-strength concrete. *Applied mechanics and materials*. 2014. Pp. 1416–1424.
33. Kornilov, T.A., Gerasimov, G.N. Naruzhnyye steny maloetaznykh domov iz legkikh stalnykh tonkostennykh konstruksiy dlya usloviy kraynego severa [External walls of low-rise buildings made of light steel thin-walled structures for conditions of the far north]. *Zhilishchnoye stroitelstvo*. 2016. No. 7. Pp. 20–24. (rus)
34. Danilov, N.D., Doktorov, I.A., Ambrosyev, V.V., Fedotov, P.A., Semenov, A.A. Issledovaniye teplozashchitnykh svoystv fragmenta steny v klimaticheskoy kamere [Study of the heat-shielding properties of a wall fragment in a climate chamber]. *Promyshlennoye i grazhdanskoye stroitelstvo*. 2013. No. 8. Pp. 17–19. (rus)

Contacts:

Vladimir Rybakov, fishermanoff@mail.ru

Irina Ananeva, irina.ananeva94@yandex.ru

Egor Pichugin, pichugin_egor93@mail.ru

Marsel Garifullin, marsel.garifullin@tuni.fi

© Rybakov, V.A., Ananeva, I.A., Pichugin, E.D., Garifullin, M., 2020



DOI: 10.18720/MCE.94.3

The geogrid-reinforced gravel base pavement model

S.A. Matveev*, **E.A. Martynov**, **N.N. Litvinov**, **G.M. Kadisov**, **V.A. Utkin**

Siberian State Automobile and Highway University, Omsk, Russia

* E-mail: dfsibadi@mail.ru

Keywords: granular roadbed basis, geogrid reinforcement, stiffness, deflections, design model, multilayered plate

Abstract. The design model of reinforced crushed stone layer calculating as a multilayer plate on an elastic base using the technical theory of bending and the Bubnov-Galerkin method is proposed, which makes it possible to theoretically calculate and justify the effectiveness of using various types of geosynthetic materials for reinforcing pavement bases made of granular materials. The model is based on the hypothesis that the reinforced granular layer is deformed like a plate on an elastic base because of the mechanical connection with the geogrid. The calculating model is a multilayer plate consisting of an arbitrary number of solid homogeneous rigidly interconnected layers. The possibility of using this model for calculation of reinforced granular pavement base is confirmed experimentally. The results of the stamp tests showed satisfactory agreement with the results of theoretical studies. The discrepancy did not exceed 15 %.

1. Introduction

One of the main structural elements of flexible road pavement is a base of granular material – crushed stone or gravel. An effective way to increase the rigidity of such a base is to reinforce it with a geogrid or geocell material. This makes it possible to increase a load bearing capacity and the service life of the pavement. At the same time, research [1] shows that the reinforcement of road structures is economically advantageous, since the use of geogrids in the roads construction provides significant saving money.

Reinforcing geogrids are made of raw materials of various types: polymer and mineral. They have different dimensions and shape of the cell, that significantly affects the deformability of the reinforced layer, the mechanism of which is not fully understood. This is due to the lack of scientifically based, reliable, experimentally confirmed models of deformation of reinforced bases of granular material, and also of the theory of calculation of pavements with reinforced layers, including layers of granular material.

In paper [2] a one-dimensional mathematical model is proposed for modelling geosynthetic-reinforced granular fills over soft soils subject to a vertical surcharge load. The geosynthetic reinforcement consists of a membrane (geogrid, or geotextile) placed horizontally in engineered granular fill, which is constructed over soft soil. The proposed model is mainly based on the assumption of a Pasternak shearlayer. The results of full-scale accelerated load testing [3] demonstrate the benefits of using geosynthetics in terms of reducing the permanent deformation in the pavement structure. The authors [4, 5] were able to develop elastic solutions for geogrid-stabilized base courses over subgrade by considering lateral restraint and tensioned membrane effects. The analytical solutions were then employed to estimate the reduction of vertical stresses underneath the geogrid compared with the measured results.

The results of full-scale laboratory tests on geogrid reinforcements in unpaved roadway sections are presented in papers [6, 7]. The test sections were instrumented to measure geosynthetic deformation and to get information about the development of permanent strains in the geogrid during traffic loading. In addition, this study was performed to evaluate the integrity and performance requirements for geogrid junctions. An attempt to identify mechanical and physical properties of geogrids was made in the study Tang [8]. In works [9, 10], the elastic stiffness of a geogrid and its tensile rupture strength at a different temperature regimes were investigated. An empirical model of geogrid deformations under cyclic loading was proposed in [11]. The interaction features of a soil with geogrid at different loading rates, also under shear at cyclic loading, were studied in [12–14].

Matveev, S.A., Martynov, E.A., Litvinov, N.N., Kadisov, G.M., Utkin, V.A., The geogrid-reinforced gravel base pavement model. Magazine of Civil Engineering. 2020. 94(2). Pp. 21–30. DOI: 10.18720/MCE.94.3



This work is licensed under a [CC BY-NC 4.0](https://creativecommons.org/licenses/by-nc/4.0/)

A presence of significant structural deformations is a characteristic feature of a granular medium deformation. Due to these deformations, the grains of the lower row of the deformable granular layer are embedded in the base soil. In this case, there is a mutual penetration of the material of one layer into another. Professor Shestakov set the depth of individual crushed stone grain indentation approximately corresponds to its characteristic transverse dimension. Thus, the actual thickness of the upper layer is reduced. In order to preserve the design thickness of the upper layer in the absence of reinforcement, it is necessary to overspend the stone material. The geogrid, located at the level of the granular layer bottom, performs not only the functions of reinforcement, but also the separation of layers. It prevents the penetration of grains of gravel in the underlying sand layer. This makes it possible to prevent overspending of the stone material, and even to save it.

Ferellec and McDowell [15] created a model of ballast–geogrid interaction using the discrete-element method, studying the working properties of reinforced and non-reinforced gravel cushion on soft subsoil.

The soil reinforcement method, which consists of placing a geogrid at the bottom of granular layer, increases the load transfer on the underlying base distribution on top of subgrade layer [16]. In accordance with Abu-Farsakh and Chen [17] the inclusion of geogrid base reinforcement results in redistributing the applied load to a wider area, thus reducing the stress concentration and achieving an improved vertical stress. Alexandrov [18] has come to a similar conclusion, arguing that the presence of a reinforcing layer inside the granular medium changes the angle of distribution of vertical stresses in it.

Geogrid reinforcement of granular base layers of flexible pavements was carried out at the end of 80-th at the University of Waterloo. Reinforcing materials are incorporated into the base layer of flexible pavements so that the two materials act together. In summary, for optimum grid reinforcement of flexible pavements, the grid must be placed in a zone of moderate elastic tensile strain (i.e., 0.05 to 0.2 percent) beneath the load center, and maximum permanent strain in the grid over the design life should not exceed 1 to 2 percent, depending on the rut depth failure criteria [19].

Existing methods for reinforced granular pavement bases calculation are based on traditional methods for calculating flexible road pavements developed several decades ago. The difference between existing methods of calculation reinforced and unreinforced structure is the introduction of additional amplification factor obtained empirically.

New approach to reinforced granular base of pavement calculation is based on the model of a reinforced granular layer deformation like a multi-layer plate on an elastic base. The theoretical principles for the reinforced road structure calculating as a multilayer plate on an elastic foundation were developed by Matveev and Nemirovsky, further developed in [20] and experimentally confirmed in [21, 22]. The hypothesis that the reinforced granular layer works as a plate on an elastic base is confirmed in these studies, as well as in the works of other authors. The granular layer is actually a discrete medium and does not perceive tensile stresses. In the part of the granular layer adjacent to the geogrid reinforced granular material behaves like a continuous medium due to mechanical engagement with the geogrid, as well as due to friction forces between the individual grains. The reinforcing effect is achieved by the joint functioning of the geogrid with a granular material. In this case the geogrid ribs perceive horizontal tensile forces arising at the level of the reinforcing interlayer. The influence zone of the geogrid placed inside the granular layer as a reinforcing interlayer is extended to 15 cm up or down from the plane of reinforcement [23]. In this zone the additional shear resistance of the granular material caused by reinforcement is decreased with increasing distance from the geogrid. This phenomenon was experimentally confirmed in paper [24], where it was noted that the granular layer reinforcement makes the pseudo-plate effect.

From the analysis of the above sources, it follows that the development of a design model of a reinforced granular base in the form of a model of an equivalent in rigidity of a multilayer plate on an elastic base is actual. Therefore, the purpose of this study is to create a design model allowing setting the effect of geogrid parameters on the stiffness of the reinforced granular base of the pavement.

The problems of this study are to describe the stiffness characteristics of each of the layers, taking into account the basic properties and characteristics of the material constituting each layer; to describe the stiffness characteristics of the whole package of layers; to select a suitable method for calculating the multilayer plate; to perform the experimental studies in the form of stamp tests of the base of pavement structure.

The novelty of this work lies in the fact that the results of experimental studies of a crushed stone base reinforced with a geogrid with steel wires were obtained for the first time. Previously, bases with this type of geogrid have not been tested. The theory for calculating of flexible pavements bases has been developed. This theory allows us to determine the coefficient of decrease in the elastic deflections of reinforced bases for different types of reinforcement.

The results of this study can find practical application in the calculation of flexible pavements.

2. Methods

2.1. Theoretical solution

The object of the study is the base of pavement structure shown in Figure 1a. The upper layer is the crushed stone layer with thickness h_1 . The underlying soils are the sand with thickness of layer h_0 . The reinforcement in the form of a geogrid is located on the boundary between the crushed stone and the sand layer.

The geogrid is formed from flat metal-plastic strips connected at an angle of 90° and superimposed one upon the other in height. The geogrid cell size is $L \times L$. Metal-plastic strips consist of a bearing part and a covering. The bearing part of the strips is steel fibers of spring wire with a diameter of 0.6 mm, located at a certain distance from each other without interweaving. The number of wires inside one strip can change from 3 to 9. In the experiment there were used geogrids with number of wires 3, 6 and 9 in one strip respectively. A covering of strips is low pressure polyethylene. The connection of metal-plastic strips between themselves is carried out by thermal welding methods. The geogrid scheme is shown in Figure 1b.

In order to determine the deflections of the geogrid-reinforced granular layer, let us accept a hypothesis that a crushed stone layer will behave as a solid connected medium, provided that a geogrid is located at the base of the layer, similar to that shown in Figure 1a.

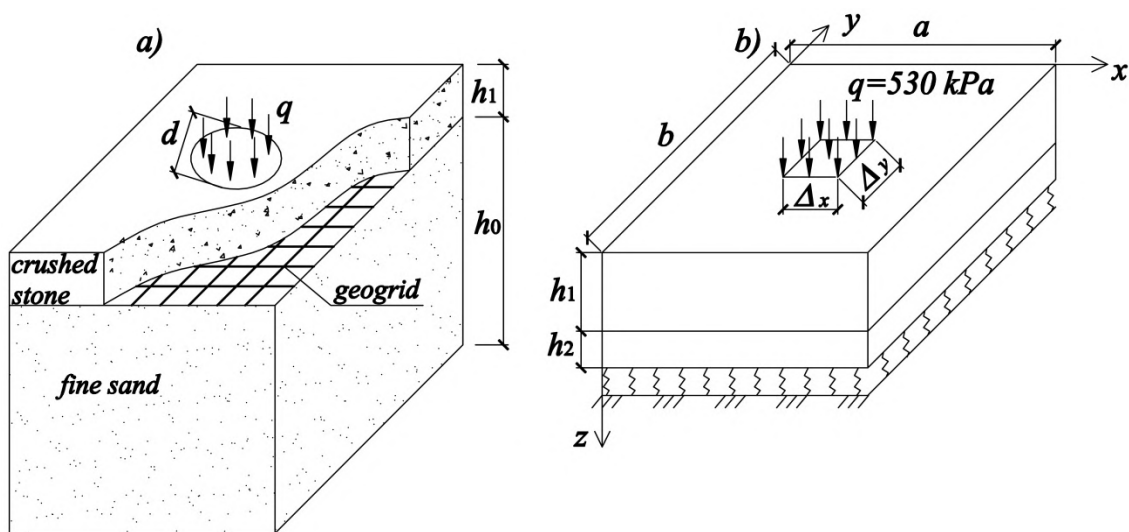


Figure 1. The reinforced base design: a) the base construction; b) the geogrid scheme.

A geogrid accepts tensile stresses and makes it possible to simulate a reinforced granular layer as plate on an elastic base [24]. In this case the technical theory of bending plate [20] can be used for reinforced granular base design. At small strains the internal forces in such plates arise from bending. In this case, both tensile and compressive stresses appear in the layer. Crushed stone as a discrete material is not able to perceive a tensile stresses. When reinforcing a crushed stone particle is caught by transverse ribs of a geogrid and cause tensile of the longitudinal ribs. It allows us to simulate a geogrid as a continuous composite layer or a thin plate with thickness h_2 (Figures 2, 3), working in tension. Such a plate does not have bending stiffness factor. But if it is included as an additional layer in the composition of the multi-layer plate, it will have a significant impact on the overall bending rigidity of the whole structure. In this way, the reinforced crushed stone layer can be simulated as a plate on an elastic base. The plate consists of two rigidly connected layers (Figure 2).

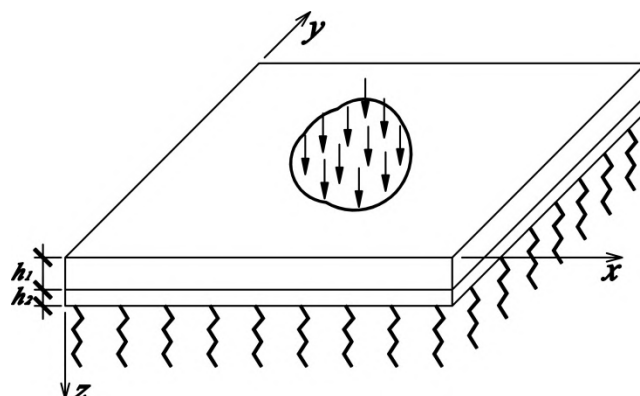


Figure 2. The model of two-layer plate located on an elastic base.

The physical and mechanical characteristics of layers will differ. Some layers of a multilayer plate may not work on bending, but they are formally included in the overall rigidity of the whole structure in accordance with the theory developed in the Siberian Branch of the Russian Academy of Sciences [2].

We accept the Kirchhoff-Love hypothesis, which will be valid for each layer of multilayer plate bending. The differential equation of bending plate is represented in the following form [20]:

$$D_{11} \frac{\partial^4 w}{\partial x^4} + 3D_{13} \frac{\partial^4 w}{\partial x^3 \partial y} + 2(D_{12} + D_{33}) \frac{\partial^4 w}{\partial x^2 \partial y^2} + 2D_{23} \frac{\partial^4 w}{\partial x \partial y^3} + D_{22} \frac{\partial^4 w}{\partial y^4} + C_z w + q = 0, \quad (1)$$

where C_z is the coefficient of soil reaction;

$q = q(x, y)$ is the intensity of the loads on the surface plate;

$w = w(x, y)$ is the deflection function;

$D_{11} \dots D_{33}$ are constants of the plate characterizing its elastic properties:

$$\begin{aligned} D_{11} &= d_{11} + c_{11} \cdot c_{11}^*; \\ D_{12} &= A_{12}^{(1)} g_1 + A_{12}^{(2)} g_2; \\ D_{22} &= A_{22}^{(1)} g_1 + A_{22}^{(2)} g_2; \\ D_{33} &= A_{33}^{(1)} g_1 + A_{33}^{(2)} g_2. \end{aligned} \quad (2)$$

Included the first Equation (2) constants d_{11} , C_{11} , c_{11}^* calculated by the formulas

$$\begin{aligned} d_{11} &= A_{11}^{(1)} g_1 + A_{11}^{(2)} g_2; \\ c_{11}^* &= \frac{(c_{21} b_{12} - c_{11} b_{22})}{(b_{11} b_{22} - b_{12} b_{21})}; \\ c_{11} &= A_{11}^{(1)} p_1 + A_{11}^{(2)} p_2; \\ c_{21} &= A_{21}^{(1)} p_1 + A_{21}^{(2)} p_2, \end{aligned} \quad (3)$$

where A_{kj} is the coefficient of proportionality between stress and strain accepted for the first (unreinforced) layer:

$$\begin{aligned} A_{11}^{(1)} &= A_{22}^{(1)} = \frac{E}{1-\nu^2}; \\ A_{33}^{(1)} &= \frac{E}{2(1+\nu)}; \\ A_{12}^{(1)} &= A_{21}^{(1)} = \frac{\nu E}{1-\nu^2}, \end{aligned} \quad (4)$$

Here E is the elasticity modulus of crushed stone layer;

ν is Poisson's ratio.

The constants included in the Equation (3) are determined by the formulas

$$g_1 = \frac{h_1^3}{3}; \quad g_2 = \frac{1}{3}(3h_1^2 + 3h_1 h_2 + h_2^2)h_2, \quad (5)$$

$$p_1 = \frac{h_1^2}{2}; \quad p_2 = \frac{1}{2}(2h_1 + h_2)h_2, \quad (6)$$

here h_1 , h_2 are thickness of the 1-st and 2-nd layers respectively;

$$\begin{aligned}
 b_{11} &= A_{11}^{(1)} h_1 + A_{11}^{(2)} h_2; \\
 b_{22} &= A_{22}^{(1)} h_1 + A_{22}^{(2)} h_2; \\
 b_{12} &= A_{12}^{(1)} h_1 + A_{12}^{(2)} h_2.
 \end{aligned} \tag{7}$$

The total cross-sectional area of the reinforcing fibers oriented along the x-axis, is

$$A_{ax} = n_x A_f, \tag{8}$$

where A_f is cross-sectional area of one fiber;

n_x is the number of reinforcing fibers parallel to the x-axis, perpendicular to the width b of the cross-section.

Accordingly, the total cross-sectional area of the reinforcing fibers oriented along the y-axis, perpendicular to the width a of the cross-section of the reinforcing layer normal to the y-axis, is

$$A_{ay} = n_y A_f, \tag{9}$$

where n_y is the number of reinforcing fibers parallel to the y-axis per width a of the cross section.

We replace separately located reinforcing fibers (Figure 3b) with a solid elastic composite layer of thickness h_2 (Figure 3c) with areas of cross-sections normal to the x and y axes, respectively

$$A_{2x} = b h_2; \quad A_{2y} = a h_2, \tag{10}$$

and coefficients of reinforcement

$$\omega_x = \frac{A_{ax}}{A_{2x}}; \quad \omega_y = \frac{A_{ay}}{A_{2y}} \tag{11}$$

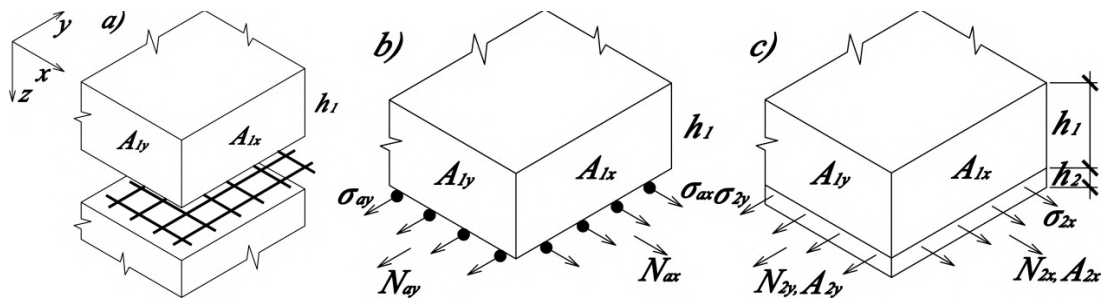


Figure 3. Reinforced plate: a) the structural scheme of a plate; b) forces and stresses in reinforcing fibers; c) forces and stresses in a continuous composite layer.

Such a replacement makes it possible to simplify and unify the design model of the reinforced layer (Figure 3a), by presenting it in the form of a two-layer system (Figure 3c) with different elastic characteristics constant within each layer.

We assume that the normal stresses σ_{2x} and σ_{2y} in a cross sections of the composite layer coinciding with the geogrid cell boundary are distributed evenly over the areas A_{2x} and A_{2y} respectively (Figure 3c) and their resultant ones are determined from the equalities

$$N_{2x} = \sigma_{2x} A_{2x}, \quad N_{2y} = \sigma_{2y} A_{2y}. \tag{12}$$

The tensile forces in reinforcing fibers N_{ax} and N_{ay} represent like expressions

$$N_{ax} = \sigma_a A_{ax}, \quad N_{ay} = \sigma_a A_{ay} \tag{13}$$

where σ_a is normal stress in reinforcing fiber.

Taking into account equalities (11)–(13), from conditions

$$N_{ax} = N_{2x}, \quad N_{ay} = N_{2y}, \tag{14}$$

we get

$$\sigma_{2x} = \omega_x \sigma_a, \quad \sigma_{2y} = \omega_y \sigma_a. \tag{15}$$

Assume that the Kirchhoff-Love hypothesis for a plate consisting of two elastic layers rigidly connected to each other is valid.

We use the Bubnov-Galerkin method [20] to calculate the multilayer plate located on an elastic base while bending. The design scheme of the plate is shown in Figure 4.

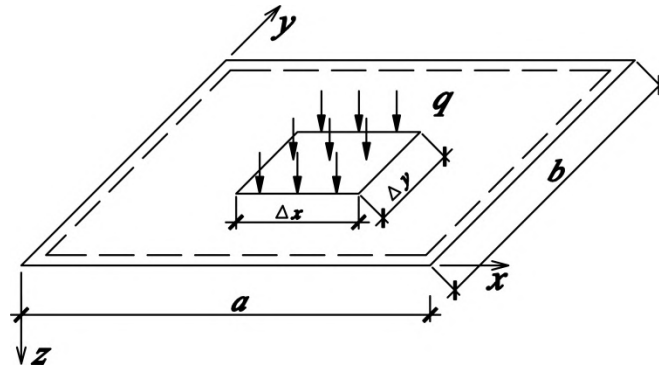


Figure 4. The design scheme of the plate located on an elastic base.

The loading area in the design scheme is taken in the rectangle form equal to area a circles stamp. The deflection function is given in the form of a double trigonometric row

$$w(x, y) = \sum_m \sum_n w_{mn} \cdot \sin \frac{m\pi x}{a} \cdot \sin \frac{n\pi y}{b} \quad (16)$$

where m and n are integers in the range $1 \dots m$ and $1 \dots n$;

a and b are plate dimensions, m ;

w_{mn} is the row coefficient, calculated by the formula

$$w_{mn} = \frac{q_{mn}}{(D_0 + C_z)}, \quad (17)$$

here D_0 is the total plate cylindrical stiffness:

$$D_0 = \left[\begin{array}{l} D_{11} \left(\frac{m\pi}{a} \right)^4 + 2(D_{12} + D_{33}) \cdot \\ \left(\frac{m\pi}{a} \right)^2 \left(\frac{n\pi}{b} \right)^2 + D_{22} \left(\frac{n\pi}{b} \right)^4 \end{array} \right]; \quad (18)$$

q_{mn} is the row coefficient of load:

$$q_{mn} = \frac{16q}{\pi^2 mn} \sin \frac{m\pi}{2} \sin \frac{m\pi \Delta x}{2a} \sin \frac{n\pi}{2} \sin \frac{n\pi \Delta y}{2a} \quad (19)$$

where Δx and Δy are dimensions of loading area (Figure 4).

2.2. Experiment

Experimental studies were carried out in the form of stamp tests of two layers base of pavement structure. The upper layer consists of crushed stone fraction 40–70 mm. The layer thick $h_1=0.2$ m. The lower layer of thickness $h_0=0.9$ m is made of fine sand. The reinforcement in the form of a geogrid is located on the boundary of the layers. The reinforced base design is shown in Figure1a.

The experiment was performed in the soil channel of the Siberian State Automobile and Highway University. The soil channel has dimensions in plan of 6×3.15 m and a depth of 1.2 m.

Crushed stone was distributed layer by layer with moistening and compaction onto a previously compacted layer of sand. The total thickness of the crushed stone in the compacted state was 0.2 m. The loading was carried out through a circular rigid stamp with a diameter of 0.33 m, which simulates the imprint of the car wheel. The load was applied through a hydraulic jack in steps of 10 kN and reached 50 kN. The test setup scheme is shown in Figure 5, where $B = 3.15$ m.

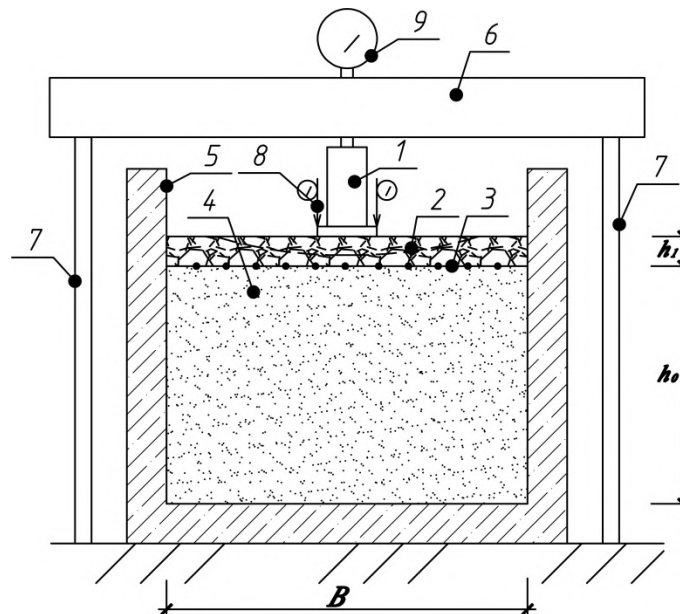


Figure 5. The test setup scheme: 1 – hydraulic cylinder of jack, 2 – crushed stone layer, 3 – geogrid, 4 – sand base, 5 – concrete tray, 6 – traverse, 7 – high rigidity rods connecting the traverse to the force floor, 8 – dial indicators with a scale value of 0,01 mm, 9 –pressure gauge of jack.

The deflections of investigated structure under the stamp were determined by the help of dial indicators with a division value of 0.01 mm mounted on the upper surface of the stamp. The indicators were attached to the reference beam to eliminate the effect of deformations of the experimental setup. The indicators rods are touched the stamp surface from opposite edges in order to eliminate the effect of a skew stamp under load (Figure 6).



Figure 6. Photograph of large-scale model experiment set-up: 1 – hydraulic cylinder of jack, 2 – rigid stamp, 3 – dial indicators with a scale, 4 – indicator mounting rods, 5 – bench mark beams, 6 – traverse.

The measurements were carried out both during loading and unloading the structure to select the elastic component of the deflection, which is used to calculate the modulus of elasticity. The value of the unreinforced structure deflection was determined as a control value.

The modulus of elasticity was determined from formula using the obtained values of elastic deflections [25]:

$$E_0 = \frac{Kd(1-\nu^2)\Delta q}{\Delta s}, \quad (20)$$

where K is the coefficient accepted for a rigid stamp equal of 0.79;

d is the stamp diameter, m;

$\nu = 0.3$ is Poisson's ratio for the soil structure;

Δq is the pressure difference under the stamp, kPa;

Δs is the difference of the stamp deflections, m.

There is proposed to estimate the effect of reinforcement using the coefficient C_w , which presents the percentage between deflections of reinforced and unreinforced structure;

$$C_w = \left(1 - \frac{w_2}{w_1}\right) \cdot 100\%, \quad (21)$$

where w_1 and w_2 are the maximum deflection of unreinforced and reinforced system respectively.

The results of the tests are presented in Figure 7.

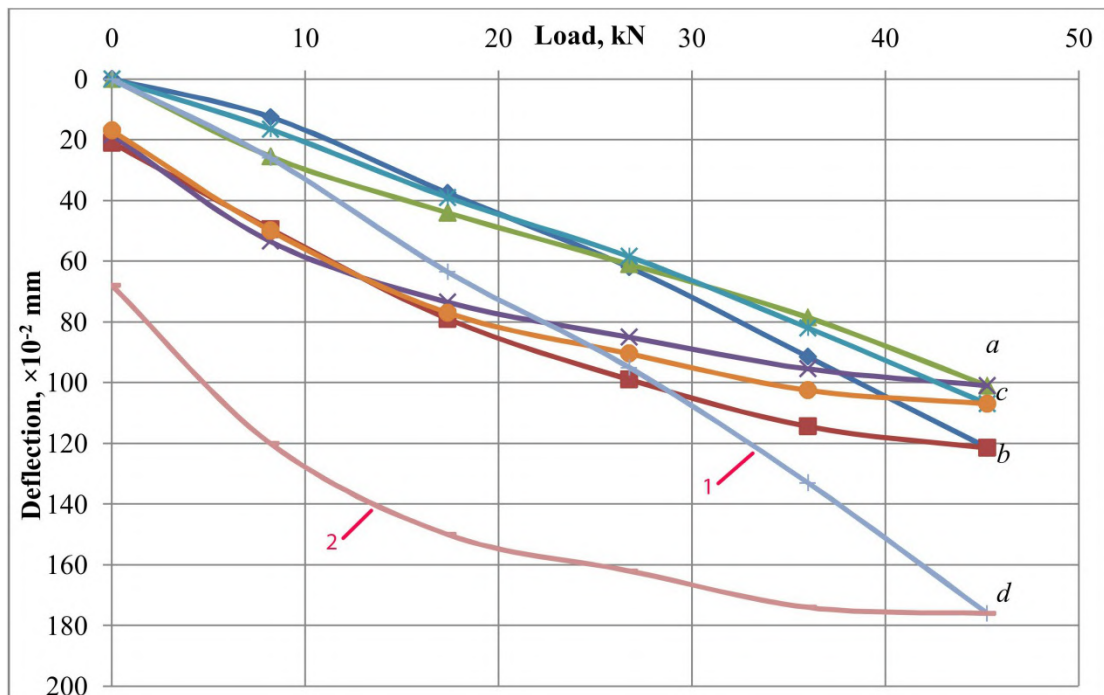


Figure 7. Load-unload diagram of reinforced (a, b, c) and unreinforced (d) structure: a) the number of wires inside one strip – 3; the cell size 100×100 mm; b) the number of wires inside one strip – 6; the cell size 75×75 mm; c) the number of wires inside one strip – 9; the cell size of 75×75 mm; 1) Load; 2) Unload.

According to the test results, there was a decrease in deflections for all reinforced structures. The greatest reinforcement effect was shown by a structure reinforced with a geogrid with a cell size of 100×100 mm and the number of wires inside one strip – 3. An almost linear increase in deflections is observed on the loading branches for all reinforced structures. The decrease in deflections shown on the unloading branch of the diagram occurs along a smooth curve. This type of deformation corresponds to the fact that the reinforcement of the base gives an increase in its elastic characteristics. The maximum effect of reinforcement on the deflection is 41 %, on the modulus of elasticity is 69 %.

3. Results and Discussion

An analysis of the experimental data shows that the crushed stone layer reinforcement by geogrid with steel fibers on a sandy base makes it possible to reduce the elastic deflection of the “crushed stone –sand” system by more than 40%. The results of theoretical and experimental studies are given in Table 1.

Table 1. The results of theoretical and experimental studies.

The size cells, mm	The number of reinforcing wires inside one strip	Elastic deflection, w , mm		Divergences, %
		theoretical	experimental	
50x50	3	0.930	0.947	1.83
	9	0.79	0.925	17.09
75x75	3	0.950	0.860	10.47
	6	0.900	0.998	10.89
	9	0.850	0.917	7.88
100x100	3	0.970	0.862	12.53
	9	0.890	0.995	11.78

The Table 1 presents the results of theoretical and experimental studies. Their analysis and comparison shows good convergence. This is a confirmation of the adequacy of the proposed calculation model. Its essence lies in the fact that a granular layer reinforced with a geogrid can be considered as a bending plate on an elastic base. The effect of reinforcement arises due to the fact that individual grains of granular materials are grasped by the geogrid while ensuring their joint deformation.

A direct comparison of the experimental results with the results of other authors is impossible, since the geogrid with steel wires used to reinforce the bases is made relatively recently and there are no published data on the results of stamp tests of such structures in the literature. The reinforcement effect of pavement base on deflection established in this work for all sizes of geogrids with steel wires was 30–40%. A similar result (31%) was obtained when testing the construction of crushed stone bases reinforced with polymer geogrids described Mikhaylin [26].

4. Conclusions

1. A design model of a reinforced granular base of the pavement structure was created in the form of an equivalent in rigidity two-layer bending plate on an elastic base.
2. The formulas of cylindrical stiffness of a two-layer plate are received. They describe the stiffness characteristics of each of the layers and the whole package of layers.
3. The Bubnov-Galerkin variation method is used to determine the deflections of a two-layer plate. It is characterized by fast convergence.
4. The results of experimental studies in the form of a stamp test of a reinforced crushed stone base of a pavement showed a satisfactory agreement with the results of calculations by the proposed method.

The proposed calculating method for the reinforced granular base of roadbed as a two-layer plate on an elastic foundation leads to a rapidly convergent series using the technical bending theory and the Bubnov-Galerkin method. This makes it possible to apply it in practical calculations of the bases of granular materials reinforced with geogrid.

References

1. Tabatabaei, S.A., Rahman, A. The Effect of Utilization of Geogrids on Reducing the Required Thickness of Unpaved Roads [Online]. *Advanced Materials Research*. 2013. Vol. 712–715. Pp. 937–941. URL: <https://doi.org/10.4028/www.scientific.net/AMR.712-715.937>
2. Yin, J.H. Modelling Geosynthetic-Reinforced Granular Fills Over Soft Soil. *Geosynthetics International*. 1997. No. 4(2). Pp. 165–185.
3. Chen, Q., Hanandeh, S., Abu-Farsakh, M., Mohammad, L. Performance evaluation of full-scale geosynthetic reinforced flexible pavement [Online]. *Geosynthetics International*. 2018. No. 25(1). Pp. 26–36. URL: <https://doi.org/10.1680/jgein.17.00031>
4. Sun, X., Han, J. Mechanistic-empirical analysis of geogrid-stabilized layered systems: Part I. Solutions [Online]. *Geosynthetics International*. 2019. No. 26(3). Pp. 273–285. URL: <https://doi.org/10.1680/jgein.19.00006>
5. Sun, X., Han, J. Mechanistic-empirical analysis of geogrid-stabilized layered systems: Part II. Analysis [Online]. *Geosynthetics International*. 2019. No. 26(3). Pp. 286–296. URL: <https://doi.org/10.1680/jgein.19.00007>
6. Christopher, B., Perkins, S. Full scale testing of geogrids to evaluate junction strength requirements for reinforced roadway base design, *Proceedings: The Forth European Geosynthetics Conference Eurogeo 4*: Editor: Neil Dixon, Edinburg, United Kingdom, 7–10 September 2008. 8 p.
7. Chen, Q., Hanandeh, S., Abu-Farsakh, M., Mohammad, L. Performance evaluation of full-scale geosynthetic reinforced flexible pavement [Online]. *Geosynthetics International*. 2018. No. 25(1). Pp. 26–36. URL: <https://doi.org/10.1680/jgein.17.00031>
8. Tang, X., Chehab, G.R., Palomino, A. Evaluation of geogrids for stabilising weak pavement subgrade. *International Journal of Pavement Engineering*. 2008. Vol. 9. No. 6. Pp. 413–429. DOI: 10.1080/10298430802279827
9. Kongkitkul, W., Tabsombut, W., Jaturapitakkul, C., Tatsuoka, F. Effects of temperature on the rupture strength and elastic stiffness of geogrids. *Geosynthetics International*. 2012. No. 19(2). Pp. 106–123. DOI: 10.1680/gein.2012.19.2.106.10
10. Chantachot, T., Kongkitkul, W., Tatsuoka, F. Effects of temperature rise on load-strain-time behaviour of geogrids and simulations [Online]. *Geosynthetics International*. 2018. No. 25(3). Pp. 287–303. URL: <https://doi.org/10.1680/jgein.18.00008>
11. Cardile, G., Moraci, N., Pisano, M. Tensile behaviour of an HDPE geogrid under cyclic loading: experimental results and empirical modeling [Online]. *Geosynthetics International*. 2016. No. 24(1). Pp. 95–112. URL: <https://doi.org/10.1680/jgein.16.00019>

12. Bathurst, R.J., Ezzein, F.M. Geogrid pullout load–strain behaviour and modelling using a transparent granular soil [Online]. *Geosynthetics International*. 2016. No. 23(4). Pp. 271–286. URL: <https://doi.org/10.1680/jgein.15.00051>
13. Liu, F.-Y., Wang, P., Geng, X., Wang, J., Lin, X. Cyclic and post-cyclic behaviour from sand–geogrid interface large-scale direct shear tests [Online]. *Geosynthetics International*. 2016. No. 23(2). Pp. 129–139. URL: <https://doi.org/10.1680/jgein.15.00037>
14. Ziegler, M. Application of geogrid reinforced constructions: history, recent and future developments. *Procedia Engineering*. 2017. No. 172. Pp. 42–51. DOI: 10.1016/j.proeng.2017.02.015
15. Ferrellec, J.-F., McDowel, G.R. Modelling of ballast–geogrid interaction using the discrete-element method [Online]. *Geosynthetics International*. 2012. No. 19(6). Pp. 470–479. URL: <https://doi.org/10.1680/gein.12.00031>
16. Blanc, M., Thorel, L., Girout, R., Almeida, M. Geosynthetic reinforcement of a granular load transfer platform above rigid inclusions: comparison between centrifuge testing and analytical modeling [Online]. *Geosynthetics International*. 2014. No. 21(1). Pp. 37–52. URL: <http://dx.doi.org/10.1680/gein.13.00033>
17. Abu-Farsakh, M.Y., Chen, Q. Evaluation of geogrid base reinforcement in flexible pavement using cyclic plate load testing [Online]. *International Journal of Pavement Engineering*. 2011. Vol. 12, No. 3. Pp. 275–288. URL: <https://doi.org/10.1080/10298436.2010.549565>
18. Aleksandrov, A.S., Kalinin, A.L., Tsyguleva, M.V. Distribution capacity of sandy soils reinforced with geosynthetics. *Magazine of Civil Engineering*. 2016. No. 6. Pp. 35–48. DOI: 10.5862/MCE.66.4
19. Haas, R., Walls, J., Carroll, R.G. Geogrid reinforcement of granular bases in flexible pavements. *Transportation Research Record*. 1988. No. 1188. Pp. 19–27.
20. Matveev, S.A., Martynov, E.A., Litvinov, N.N. Eksperimental'no-teoreticheskiye issledovaniya armirovannogo osnovaniya dorozhnoy odezhdy [Experimental and theoretical studies of the reinforced base of the pavement] [Online]. *Vestnik SIBADI*. 2015. No. 4(44). Pp. 77–83. URL: [https://doi.org/10.26518/2071-7296-2015-4\(44\)-80-86](https://doi.org/10.26518/2071-7296-2015-4(44)-80-86). (rus)
21. Matveev, S.A., Martynov, E.A., Litvinov, N.N. Effect of Reinforcing The Base of Pavement With Steel Geogrid [Online]. *Applied Mechanics and Materials*. 2014. Vol. 587–589. Pp. 1137–1140. URL: <https://doi.org/10.4028/www.scientific.net/AMM.587-589.1137>
22. Matveev, S.A., Martynov, E.A., Litvinov, N.N. Determine The Reinforcement Effect of Gravel Layer on a Sandy Foundation [Online]. *Applied Mechanics and Materials*. 2014. Vol. 662. Pp. 164–167. URL: <https://doi.org/10.4028/www.scientific.net/AMM.662.164>
23. Rakowski, Z. An attempt of the synthesis of recent knowledge about mechanisms involved in stabilization function of geogrids in infrastructure constructions [Online]. *Procedia Engineering*. 2017. No. 189. Pp. 166–173. URL: https://doi.org/10.1007/978-3-030-01908-2_14
24. Berestyaniy, Y.B., Valtseva, T.U., Mikhailin, R.G., Goncharova E.D. Motorway Structures Reinforced with Geosynthetic Materials in Polar Regions of Russia. The 24rd International Offshore (Ocean) and Polar Engineering Conference. Bussan, Korea. 2014. Pp. 502–506.
25. State standard GOST 20276-2012. Soils. Methods of field determination of durability and deformability's characteristics. Moscow, 2013. 32 p. (rus)
26. Mikhaylin, R.G. Sovershenstvovanie metodiki rascheta armirovaniya nezhestkix dorozhny`x odezhd georeshetkami [The improving of methodology for calculating of flexible pavement reinforcement with geogrids]: PhD Diss: 05.23.11. Khabarovsk, 2016. 114 p. (rus)

Contacts:

Sergey Matveev, dfsibadi@mail.ru

Evgeny Martynov, asp-evg@mail.ru

Nikolai Litvinov, niklitvinov_23@mail.ru

Grigoriy Kadisov, kadisov@rambler.ru

Vladimir Utkin, prof.utkin@mail.ru

© Matveev, S.A., Martynov, E.A., Litvinov, N.N., Kadisov, G.M., Utkin, V.A., 2020



DOI: 10.18720/MCE.94.4

Computational modeling of yielding octagonal connection for concentrically braced frames

*F. Nejati, M. Zhian, F. Safar Mashaie, S.A. Edalatpanah**

Ayandegan Institute of Higher Education, Tonekabon, Iran

** E-mail: saedalatpanah@gmail.com*

Keywords: finite element method, yielding octagonal connection, concentrically braced frames, non-linear time history analysis, near and far-field earthquakes

Abstract. Ductility is a feature which allows a structure to undergo large plastic deformations without any strength loss. Yield dampers are energy dissipation devices which increase the ductility and control the vibration of structures by absorbing earthquake input energy. If a structure is properly designed according to the standard, if a severe earthquake occurs, it will cause serious damage to the structure. If this happens in a massive city, thousands of people are homeless and need to evacuate the debris that it seems impossible to do. Therefore, the design of systems that lead the damage to a certain part of structures is required. Incorporating an energy-dissipater element in the braces is one of the novel approaches to increase the ductility of the braces. This study aims to assess the influence of design parameters related to the energy absorption device on the seismic response of CBFs. These factors include the yield strength, initial stiffness, and strain hardening ratio. Thus a regular octagonal-shaped energy absorption device is introduced, which enters the non-linear range by steel yielding in order to dissipate the earthquake input energy and prevent other structural members from entering the plastic region. The proposed device can be called Yielding Octagonal Connection (YOC), which is modeled using Abaqus finite element software and exposed to cyclic loading according to the ATC-24 code. A bilinear stress-strain curve for steel is used for the modeling. When the hysteresis and envelope curves are obtained, the structure equipped with YOCs is designed using SAP2000. To investigate the behavior of this energy absorption device, a non-linear time history analysis (NLTHA) is conducted for 16-storey steel structures with regular plans and concentrically braced frames (CBFs) under near- and far-field earthquakes. The results of analyses indicate 68 % and 65 % decrease in the maximum base reaction, 79 % and 82 % decrease in the maximum roof story acceleration, 60 % and 58 % decrease in the maximum displacement at roof level under near and far-field earthquakes, respectively.

1. Introduction

Seismic design codes are generally accepted to repair the structures after major earthquakes. Members of a structure deformed against earthquake forces and dissipate the energy of an earthquake. When the earthquake forces rise to an extent, causing important structural members to have plastic joints. Since the repair of the important members of the structure is very difficult and sometimes impossible after earthquake. In order to provide a repairable building, "Directed Damage Design" idea can be used, which means guiding damages to predetermined specific points of structure so that the damage of primary and secondary structural members is reduced by the concentration of plastic regions on these points. Yield dampers provide a suitable solution to focus damage on specific parts of the structural system. The mechanism of these dampers is based on increasing the energy absorption by concentrating a major part of plastic regions on them due to the nature of inelastic behavior, improving the seismic performance of the structure against ground motions. This paper proposes a new seismic damper based on the yielding of metals and compares its performance to a Special Concentrically Braced Frame «SCBF» through non-linear dynamic analyses. It can be easily installed like a conventional brace and strength and stiffness can be adjusted independently. To validate the applicability of the proposed damper design, a series of cyclic load tests on the damper were conducted. The cyclic behavior of the damper was determined by finite element method. The following researches have indicated a number of performance issues with respect to some of yielding dampers.

Nejati, F., Zhian, M., Safar Mashaie, F., Edalatpanah, S.A. Computational modeling of yielding octagonal connection for concentrically braced frames. Magazine of Civil Engineering. 2020. 94(2). Pp. 31–53. DOI: 10.18720/MCE.94.4



This work is licensed under a CC BY-NC 4.0

Added damping and stiffness (ADAS) and triangular added damping and stiffness (TADAS) dampers can be mentioned amongst these dampers. Franco et al. [1] proposed a yield damper whose performance mechanism was based on the plasticity properties of metals under twisting contact stress. This device comprised a tube of different cross-sections with lower thickness and diameter at middle parts. Hence the tube displacements were limited, and it would be allowed only to twist, improving the seismic resistance of structure by energy dissipation. In the same year, Mistakidis [2] numerically analyzed shear wall panels using low-yield-point (LYP) steel to retrofit and improve the seismic behavior of structures. Benavent-Climent [3] also introduced a brace-type damper consisted of a tube-in-tube assemblage of hollow sections. Its outer section comprised strips created by cutting a series of slits through the wall and the strips dissipated earthquake energy by flexural-shear yielding. Other studies were conducted by Ward et al. [4] investigated the Cast Modular Ductile Bracing System (CMDDB) is under development as an alternative to special concentrically braced frames. This system introduces cast components at the ends and center of the brace in an attempt to produce a system with reliable strength, stiffness, and deformation capacity. A cruciform cross-section has been chosen for the cast component geometry, which is specially detailed to enhance energy dissipation and increase low cycle fatigue life thereby reducing the likelihood of fracture. Gray et al. [5] proposed a new cast steel yielding brace system which was a type of high-ductility braces with unique characteristics. In this system, the fingers of a specially engineered cast steel connection dissipate seismic energy by yielding. In another research, Beheshti-Aval et al. [6] studied a combination of circular damper and friction connection installed in the center of X-bracing systems. Hong-Nan Li and Gang Li [7] presented a dual friction metallic damper experimentally that have appropriate energy dissipation capabilities. Nejati et al. [8] assessed the performance of yield dampers in a steel structure through rocking (see-saw) motion. The results suggested that it is possible to dramatically reduce the damage of the structure using the damper and hence the structural system can be easily repaired after major earthquakes. Hsu and Halim [9] introduced a new brace design that adopted curved steel dampers with amplified deformation mechanisms. Marco Baiguera et al [10] studied on a dual seismic-resistant steel frame, which consists of a moment-resisting frame equipped with high post-yield stiffness energy-dissipative braces for residual drift reduction. Tiyyari et al [11] proposed a new bracing system that consists of U-shaped elements as energy dissipation devices that can be considered as a hysteretic damper, which combines the advantages of the yielding dampers and the buckling resistant braces «BRB». Jarrah et al [12] introduced a new metallic damper which is comprised of a set of parallel hollow circular plates that can be installed in a structure within V-braces or diagonal braces.

The presented researches show the good performance of yield dampers as energy absorption devices that can reduce damage to other structural members by the concentration of failures on themselves. These systems can be used in both the design of new construction and retrofitting of existing buildings. In this paper, a regular octagonal energy absorption device is introduced, and its modeling process is described using Abaqus finite element software. The proposed device can be called Yielding Octagonal Connection (YOC). This damper is evaluated in the Concentrically Braced Frames system under the near- and far-field earthquakes by SAP2000 software [13].

2. Methods

2.1. Finite Element Simulation of YOCs

The proposed energy absorption device YOC is made of ST37 steel (equivalent to A283 in ASTM standard [14]), 15 cm in outer dimension, 1.5 cm in thickness and 15 cm in length. Two $20 \times 15 \times 1.5 \text{ cm}^3$ connection plates were also connected to the YOC with a fillet weld. The octagonal element and connection plates were merged together and the simulation of the weld is neglected in the current study assuming that failure does not occur in the welds. The geometric shape of the yield damper is illustrated in Figure 1(a). As shown in Figure 1(b), the YOC is located at the point where the brace is connected to the top gusset plate of the frame.

YOC is modeled as a deformable, 3-dimensional, solid and homogeneous element, indicating the homogeneity and constancy of density throughout the components, and assessed through general and static analyses. Non-linear geometric deformations (large deformations) are applied in all steps of the analysis. The specifications of the steel used are given in Table 1 according to A283 in ASTM standard [14]).

The YOC is modeled using an 8-node linear brick element with reduced integration and hour-glass control (C3D8R). The C3D8R is defined as three-dimensional, hexahedral, eight-node linear brick, with reduced integration with hourglass control and first-order (linear) interpolation. Reduced integration uses a lower-order integration to form the elements stiffness which greatly reduces computation time. The first-order element is highly suggested when large strains have happened. A mesh size of 4 mm was utilized in the finite element simulation. Figure 2 shows the mesh of YOC.

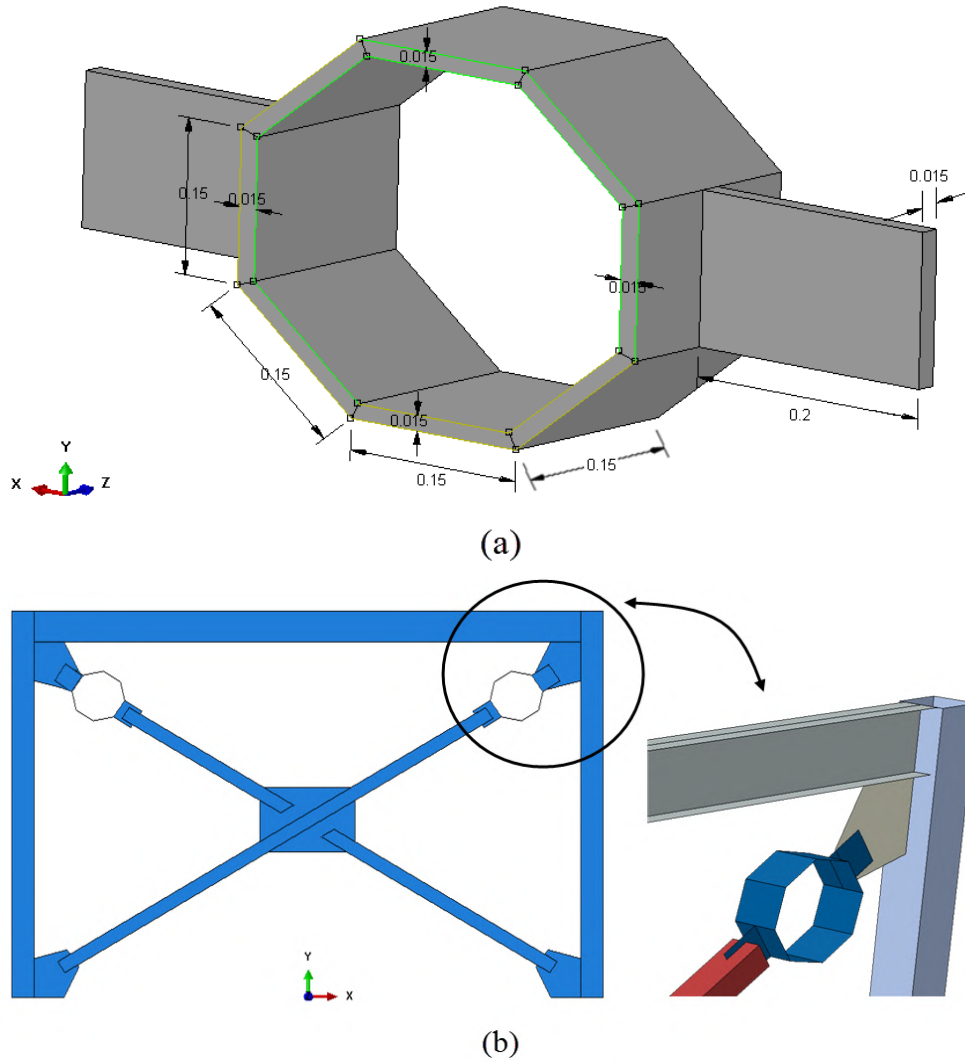


Figure 1. Geometric dimensions [m] of YOC (a), Position of YOC in the braced frame (b).

Table 1. Steel specifications.

Density (kg/m ³)	Modulus of Elasticity (GPa)	Poisson's Ratio	Yield Strength (MPa)	Ultimate Strength (MPa)	Ultimate Strain
7850	200	0.3	240	370	0.2

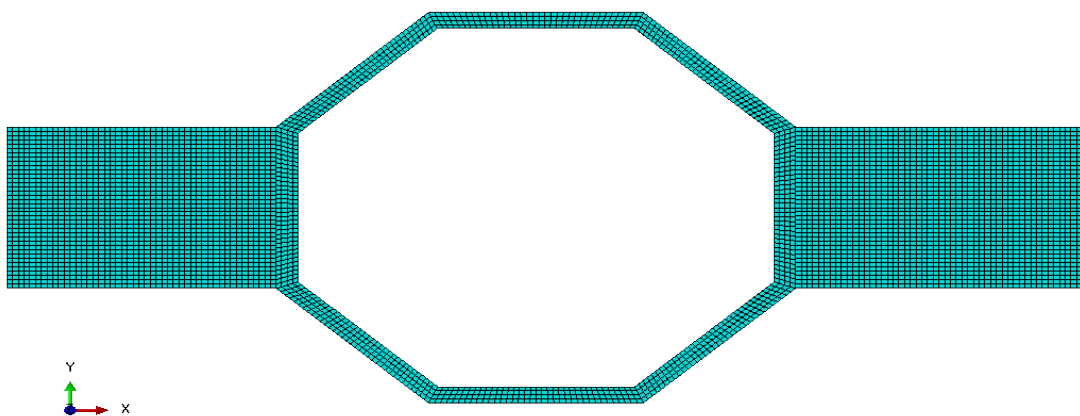


Figure 2. The meshing of YOC for Finite Element Analysis.

The cyclic loading protocol is applied according to the ATC-24 code [15] in order to examine the performance of YOC under cyclic loads. A displacement-controlled loading calculated based on the yielding displacement of the model is used in the current study. Figure 3 presents the loading sequence applied to the model, where δ_i is the maximum displacement at the i^{th} cycle of loading history and n_i is the number of cycles with the peak of δ_i and Δ is yielding displacement of the energy absorbing device. The fixed boundary conditions and cyclic loading are defined for both opposite sides of the octagonal device. Also, in Figure 4 the support conditions and loading direction are displayed.

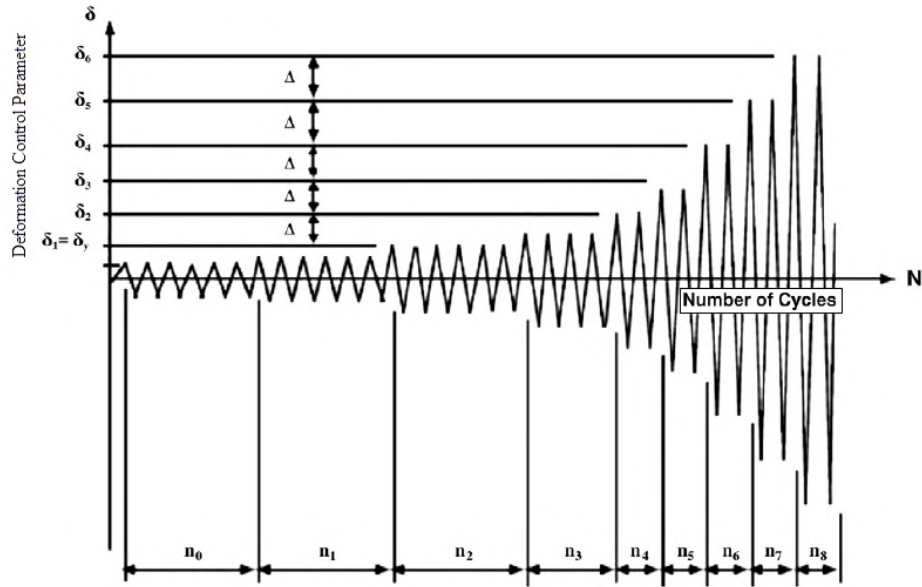


Figure 3. Loading protocol according to the ATC-24 code [15].

Figure 4 shows the loading and boundary condition of YOC. It should be mention that all degrees of freedom are restrained on boundary conditions.

Boundary Conditions

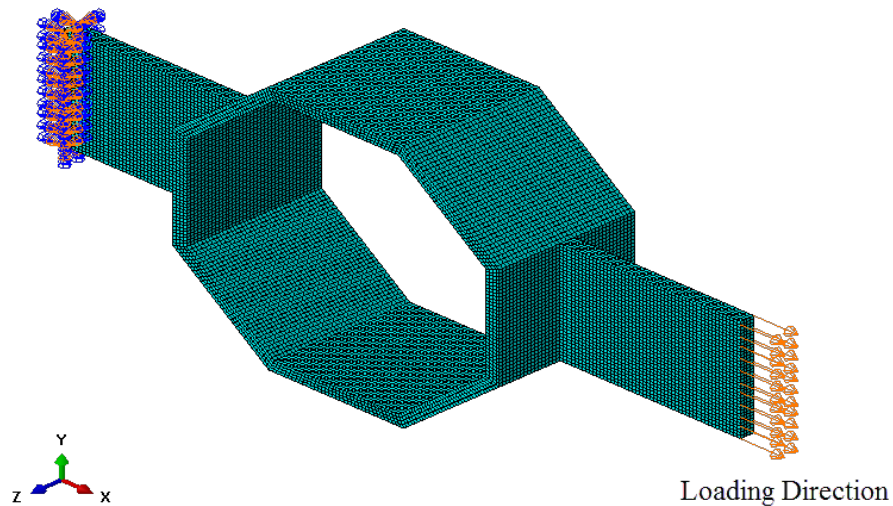


Figure 4. Boundary conditions and loading of YOC.

Figure 5 shows the von Mises stresses in YOC under the cyclic loading. The load-displacement diagram of the model is presented in Figure 6. The model was pushed until the peak strain reached the ultimate strain. The maximum tension and compression forces were 141.65 kN and 119.38 kN, respectively.

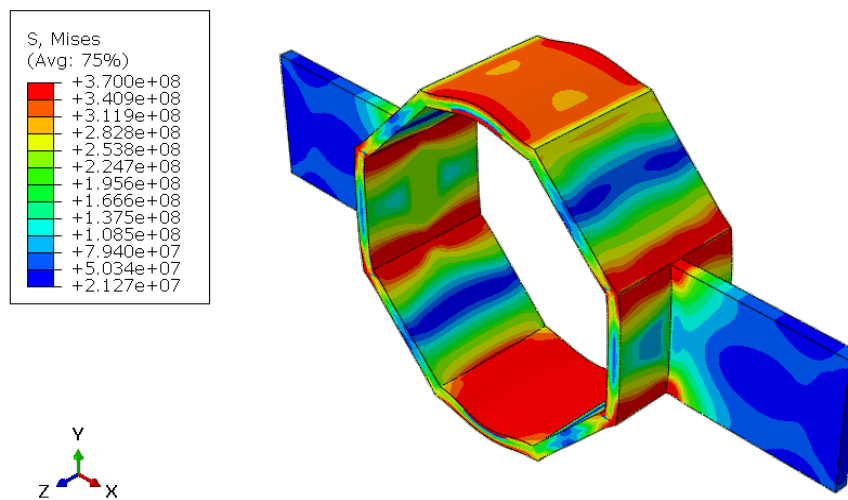


Figure 5. von Mises stress distribution in YOC (Pa).

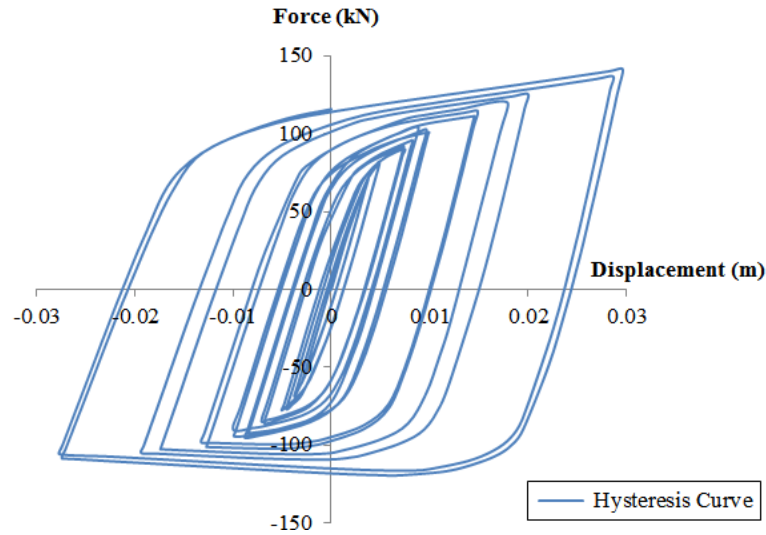


Figure 6. Force-displacement hysteresis curve of YOC.

The envelope of the hysteretic response of the YOC is presented in Figure 7. As can be seen in this figure, the maximum displacement and corresponding displacement of the system at the end of the tensile elastic limit are 29.6 mm and 4.9 mm, respectively, based on two linearization method of FEMA 356 [16]. Similarly, the aforementioned parameters under the compression force were 27.7 mm and 4.6 mm, respectively. Therefore, the ductility of the model (μ) in tension and compression can be calculated, where Δ_{max} is the maximum deformation at failure and Δ_y is the deformation when the material or member yields.

$$\mu_T = \frac{\Delta_{Max}}{\Delta_y} = \frac{29.6}{4.9} = 6.04; \quad (1)$$

$$\mu_C = \frac{\Delta_{Max}}{\Delta_y} = \frac{27.7}{4.6} = 6.02. \quad (2)$$

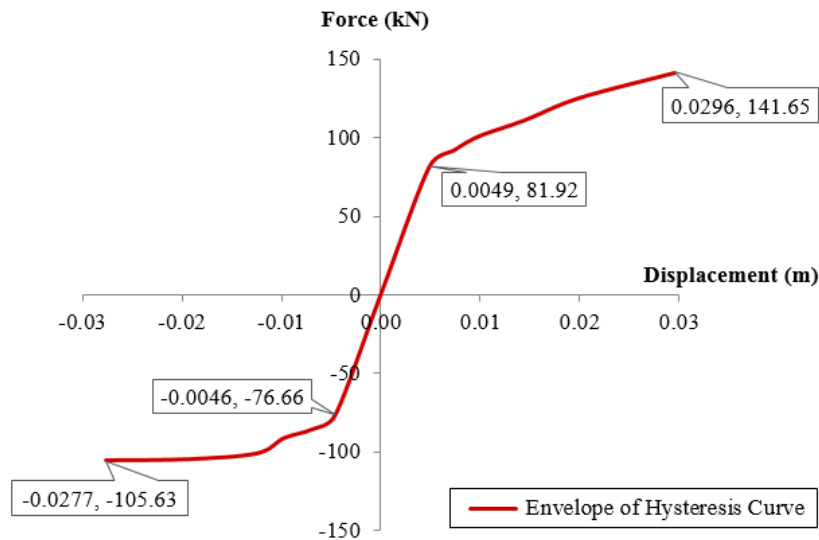


Figure 7. Hysteresis loop push of force-displacement plot for YOC.

2.2. Verification of the FE model

An experimental test performed by Abbasnia et al. [17] was used to verify the accuracy of the simulation. The specimen consisted of a steel ring with an outer diameter of 220 mm, the thickness of 12 mm, and a length of 100 mm. Two $200 \times 100 \times 12 \text{ mm}^3$ connection plates were also connected to the steel ring with a 7 mm fillet weld. Figure 8(a) presents the tested specimen and Figure 8(b) shows its Abaqus model.

In the first step, based on the experimental results, steel material properties were defined in the Abaqus software [18]. Figure 9 presents the steel stress-strain diagram for ring and plates. The steel rings and connection plates were merged together and simulation of the weld is neglected in the current study assuming that failure does not occur in the welds. Fixed boundary condition was applied to one end of the model while an axial force was applied to the other end to investigate the behavior of the model (Figure 10). A mesh size of 4 mm was utilized in the finite element simulation.

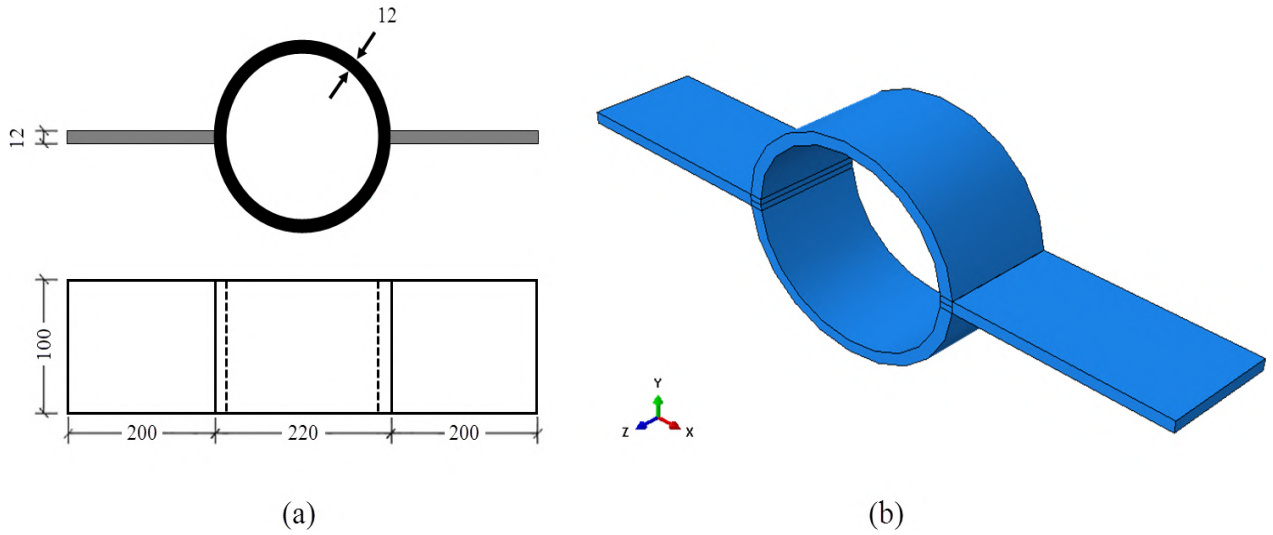


Figure 8. Dimensions [mm] of experimental specimen (a) analytical specimen (b).

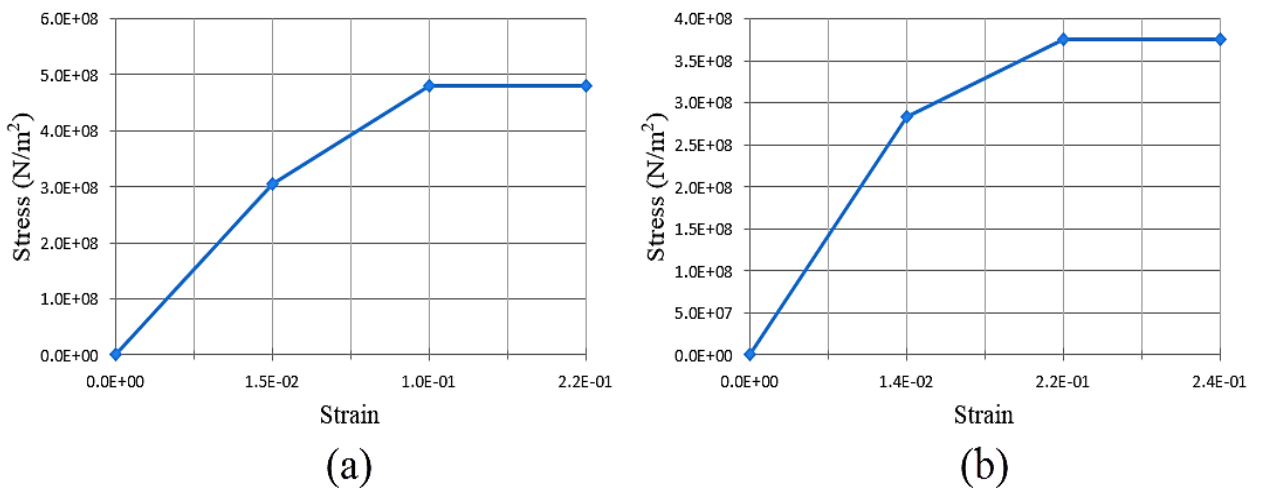


Figure 9. Steel Stress-strain diagram for the ring (a) and plates (b).

Boundary conditions



Figure 10. Boundary conditions and loading direction in Abaqus for analytical specimen.

Figure 11(a) illustrates how the steel ring was loaded by a hydraulic universal jack with a capacity of 700 kN of compressive and tensile strength. In addition to the applied axial force, the jacks measured the diameter of the ring. Figures 11(b) and 11(c) show the steel rings in pre-failure cycles in tensile and compression states, respectively.

Figure 12 shows von Mises stresses under a cyclic load for the steel ring in Abaqus.

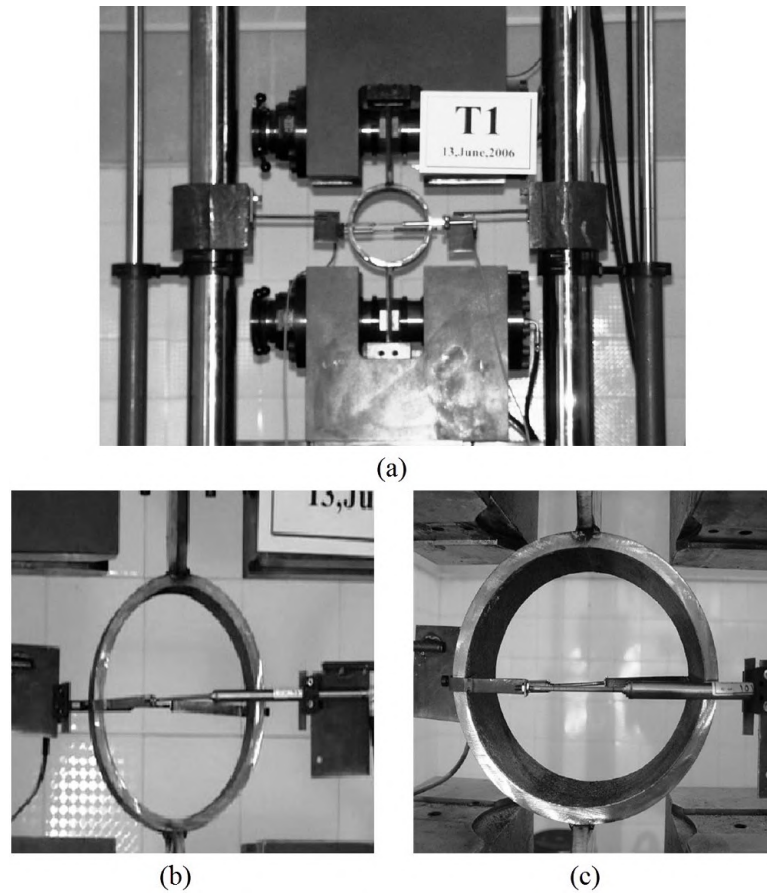


Figure 11. Hydraulic Universal Jack (a), Steel ring in tension (b), Steel ring in compression (c) [17].

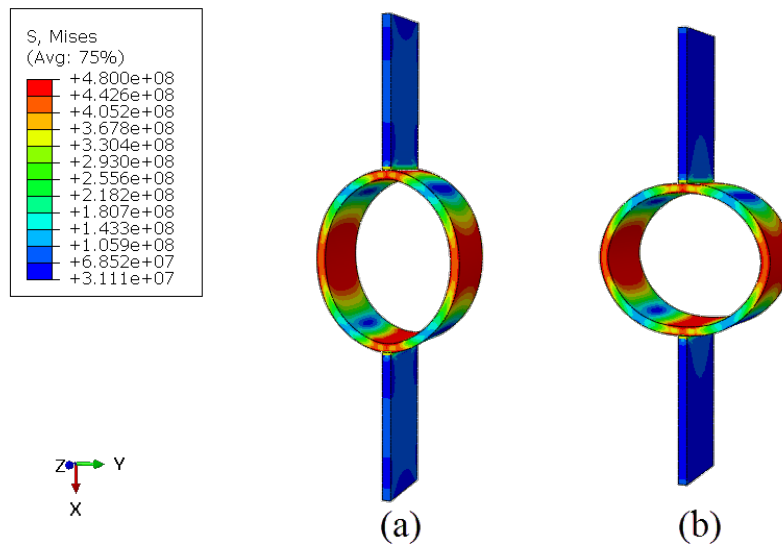


Figure 12. von Mises stress distribution [Pa] in the steel ring in tension (a) and compression (b).

The load-displacement in experimental analysis dependence of the simulated ring under cyclic loading is shown in Figure 13. The Model was pushed until the peak strain in the model reached the ultimate strain. The maximum displacement and corresponding displacement of the system at the end of the tensile elastic limit are 20.16 mm and 2.79 mm, respectively. On the other hand, the aforementioned parameters under the compression force were 19.93 mm and 3.09 mm, respectively. Also, the maximum tension and compression force sustained by the model was 87.74 kN and 73.39 kN, respectively. Therefore, the ductility of the model in tension and compression can be calculated. This value are expressing for simulation, such that:

$$\mu_T = \frac{\Delta_{Max}}{\Delta_y} = \frac{20.16}{2.79} = 7.23; \quad (3)$$

$$\mu_C = \frac{\Delta_{Max}}{\Delta_y} = \frac{19.93}{3.09} = 6.45. \quad (4)$$

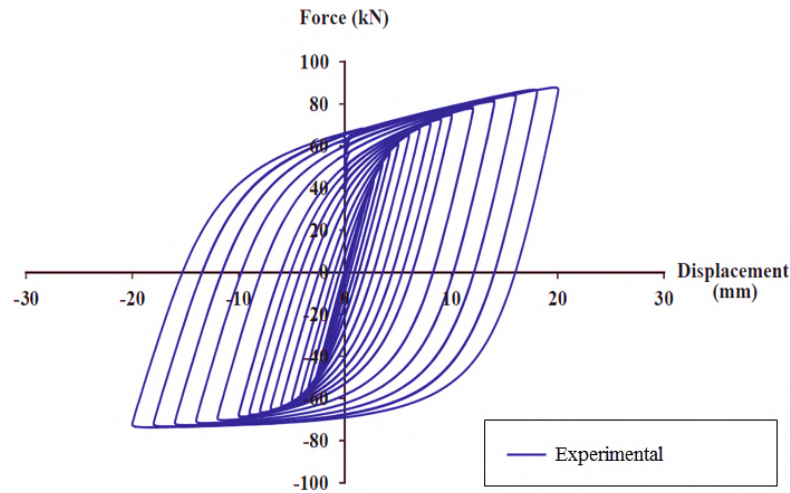


Figure 13. Force-displacement plot for experimental specimen [17].

The comparison between the numerical model and the experimental test, provided in Figure 14, demonstrated that the simulation can successfully predict the behavior of the tested steel ring and the results are in good agreement. Simulation results show that the maximum displacement and corresponding displacement of the system at the end of the tensile elastic limit are 20.37 mm and 2.53 mm, respectively. On the other hand, the aforementioned parameters under the compression force were 19.86 mm and 2.95 mm, respectively. Also, the maximum tension and compression force sustained by the model was 84.92 kN and 73.01 kN, respectively. Therefore, the ductility of the model in tension and compression can be calculated, such that:

$$\mu_T = \frac{\Delta_{\max}}{\Delta_y} = \frac{20.37}{2.53} = 8.05; \quad (5)$$

$$\mu_C = \frac{\Delta_{\max}}{\Delta_y} = \frac{19.86}{2.95} = 6.73. \quad (5)$$

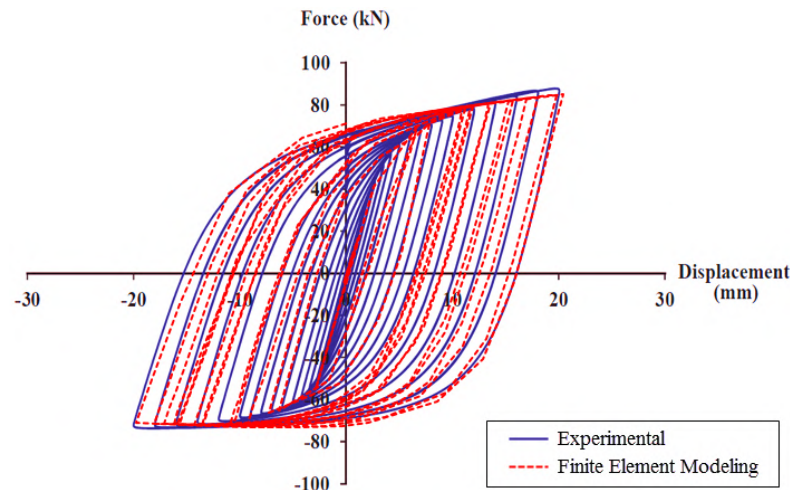


Figure 14. Comparative hysteresis plots for finite element modeling and experimental results.

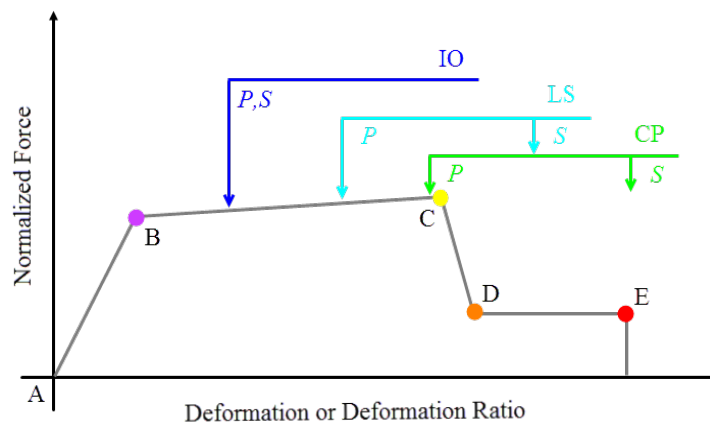
2.3. Specifications of the building

A 16-story steel structure with a regular plan and X-shaped bracing system is modeled 3-dimensionally in SAP2000 software to evaluate the performance of damper in the structure. The building was designed based on the conventional provisions (Iranian Standard No.2800 [19], which is very similar to the UBC). The plan of the floors along with the locating of the braces is shown in Figure16 (a). The beams, columns, and braces are connected using pinned connections and the base of the structure is connected to the foundation using fixed connections. Moreover, IPE sections for the beams and hollow structural section (HSS) for the columns and braces are determined. The gravity load is included in dead and live loads. According to the building executive plans, the dead and live load of the story floors are considered equal to 700 kg/m² and 200 kg/m². Also the dead and live load of the roof floor are considered equal to 650 kg/m² and 150 kg/m². The other types of loading including a wind load, a snow load, and also the load from soil–structure interaction have not been considered. The concrete deck compressive strength and thickness have been considered equal to 200 MPa and 15 cm, respectively. The cross-section specifications are summarized in Table 2.

Table 2. Specifications of cross-sections.

Number of stories	Column		Brace	Beam
	Other	Bay of bracing		
1	BOX 400×400×25	BOX 520×520×25		
2	BOX 400×400×25	BOX 450×450×25	BOX 160×160×10	IPE 240
3–6	BOX 400×400×25	BOX 400×400×25		
7, 8	BOX 340×340×20	BOX 340×340×20		
9, 10	BOX 280×280×16	BOX 280×280×16	BOX 140×140×10	IPE 220
11	BOX 200×200×16	BOX 200×200×16		
12	BOX 200×200×16	BOX 200×200×16	BOX 120×120×10	
13, 14	BOX 160×160×10	BOX 160×160×10		IPE 200
15, 16	BOX 120×120×10	BOX 120×120×10	BOX 100×100×10	

Plastic hinges are assigned in SAP2000 software as follows: for the columns of the braced span, force-controlled actions (brittle elements) and axial force type plastic hinges are defined and assigned. For the brace members, deformation-controlled actions (ductile elements) and axial force type plastic hinges are assigned. The plastic hinges are defined in accordance with the ASCE 41-13 [20]. Figure 15 shows the generalized force-deformation curves and acceptance criteria for deformation-controlled actions. Acceptance criteria for deformation or deformation ratios for primary components “P” and secondary components “S” corresponding to the target Building Performance Levels of Collapse Prevention “CP”, Life Safety “LS”, and Immediate Occupancy “IO” as shown in Figure 15. The portions of the hinge load-deformation curve from A to B are ignored by the SAP2000 software. In this range, the behavior of the element is linear and the hinge is colorless. After hinge yields at point B, plastic deformation is determined by the curve B-C-D-E with all plastic deformation measured relative to B. The hinge colors in the plastic region for ductile elements are shown in Table 3.

**Figure 15. Generalized Component Force-Deformation Relations for deformation-controlled actions.****Table 3. The hinge colors in the plastic region for ductile elements in SAP2000 software.**

Hinge Status	Hinge Color
Before point B	Colorless
B to < IO	Purple
IO to < LS	Blue
LS to < CP	Turquoise
CP to < C	Green
C to < D	Yellow
D to < E	Orange
After Point E	Red

The SAP2000 force-controlled tool was employed to check the “Force/Maximum Allowed Force Ratio” of the structural members. The values of these ratios are specified by the user. There is no plastic area for the force-controlled actions (Brittle elements), then it is not necessary to consider the acceptance criteria for the brittle elements; however, the SAP2000 has chosen the same three colors as the acceptance criteria colors. Therefore, the brittle elements can have blue, turquoise, green, and red colors.

2.4. Using the proposed device in building frames

In order to model the proposed connection at the end of the brace, multi-linear plastic kinematic is used in SAP2000 software. This behavioral model, based on the kinematic hardening behavior commonly observed in metals, presents a non-linear force-deformation relationship under monotonic loading provided by a multi-linear curve described by a set of user-defined points, as seen in Figure 16(a). The first slope on each side of the origin is elastic and the remaining portions of the curve define plastic deformation. Upon reversals of deformation, the hysteresis path follows the two elastic segments of the curve from each side of the origin before initiating plastic deformation in the reverse direction. To appropriately illustrate the behavior of load reversal paths under cyclic loading of increasing magnitude, Figure 16(b) defines the origin as point 0, the points on the positive axis as 1, 2, 3 from the origin, and the points on the negative axis as -1, -2, -3 from the origin. The displacement and force values obtained from the YOC hysteresis curve for these 7 points are presented in Table 4.

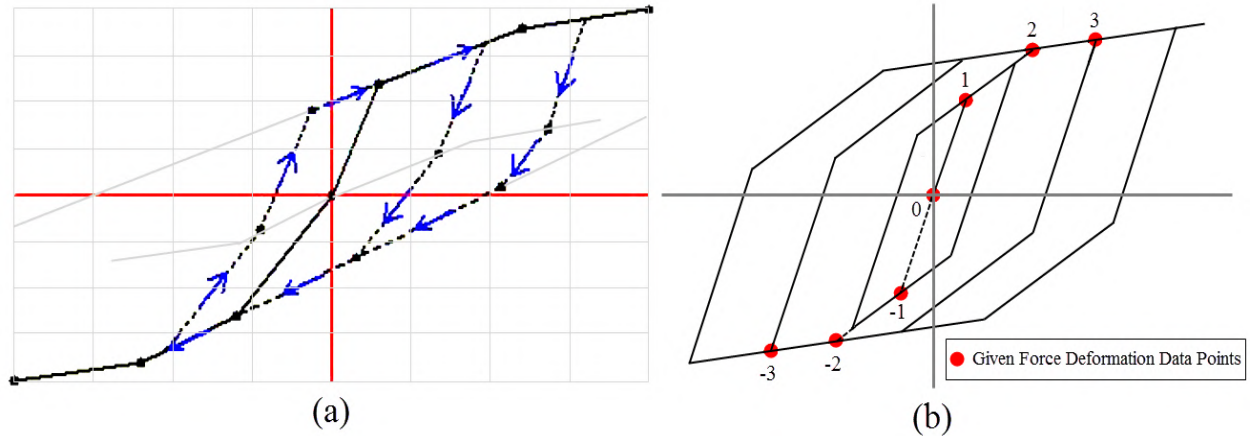


Figure 16. SAP2000 multi-linear kinematic plasticity property type for uniaxial deformation (a), SAP2000 behavior under cyclic loading of increasing magnitude for the multi-linear kinematic plasticity property type for uniaxial deformation (b).

Table 4. Defined envelop curves for the multi-linear plastic link elements in SAP2000.

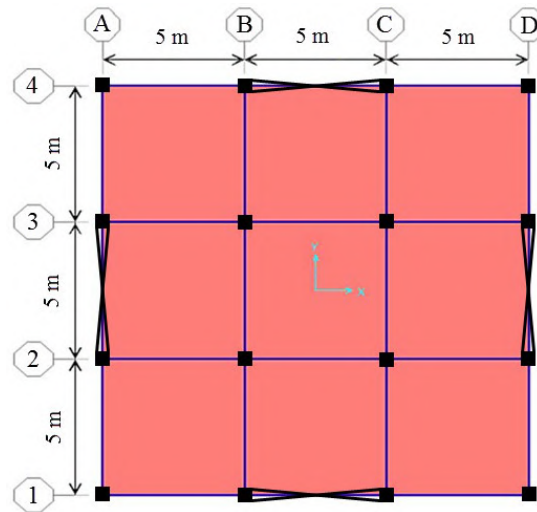
Point	Displacement (mm)	Force (kN)
3	29.6	141.65
2	14.5	111.46
1	4.9	81.92
0	0	0
-1	4.6	76.66
-2	12.4	101.18
-3	27.7	105.63

The hysteresis envelope curve for the proposed damper is located within a 16-story steel structure equipped with a CBF system in order to evaluate the seismic performance of the damper in braced frames under near- and far-field earthquakes. Figure 17 shows the plan and the 3D view of the 16-story structure equipped with and without YOC schematically.

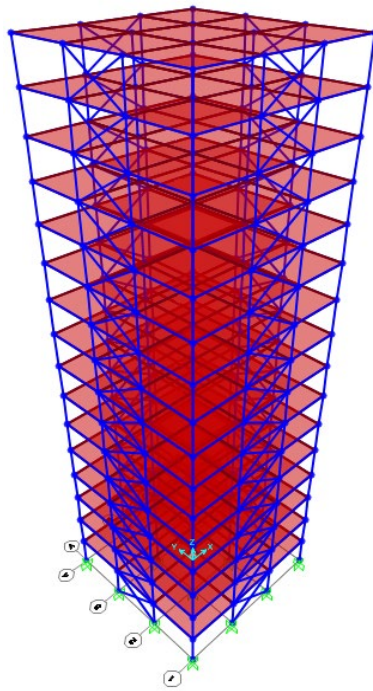
2.5. Specifications of applied earthquakes

Given the distance from a fault, recorded accelerations are classified as near-fault and far-fault earthquakes. If acceleration is recorded at a station within a distance of less than 15 km from the fault, it is generally called a near-fault motion, while that recorded within a further distance is called a far-fault motion. The distance from the fault is very important for selecting the acceleration, because it may lead to highly different responses of the structure. Thus three near-field and far-field accelerations are used for the Non-Linear Time History Analysis (NLTHA) in this study, whose specifications are given in Tables 5 and 6, respectively. The earthquake records have been scaled based on the method proposed by Section 2.4.2.2 ASCE 41-13 [20]. Therefore, the scale number obtained for the near- and far-field acceleration is equal to 0.4117 g and 0.4349 g, respectively. Ground motions used in this study were generated by PEER ground motion database [21]. Figure 18 shows the response spectra for the suite of ground motions. A Target response spectrum based on type II soil (The average shear wave shear rate $\langle\langle\bar{V}_s\rangle\rangle$, Average Standard

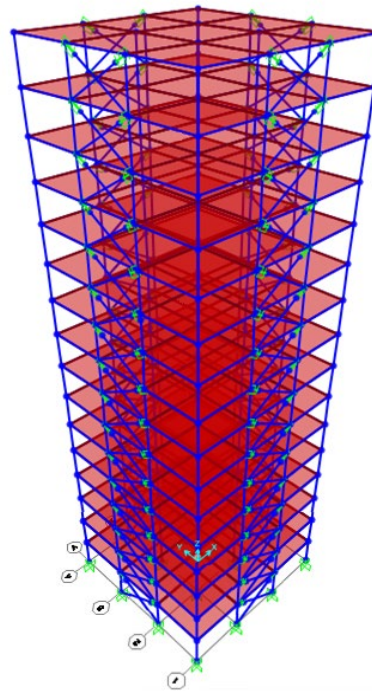
Penetration Resistance $\langle \bar{N}_{1(60)} \rangle$ and Average Undrained Shear Strength $\langle \bar{C}_u \rangle$ are 700 m/s, 60 and 275 kPa, respectively) and very high risk in seismic regions of Iran have been selected [19].



(a)



(b)



(c)

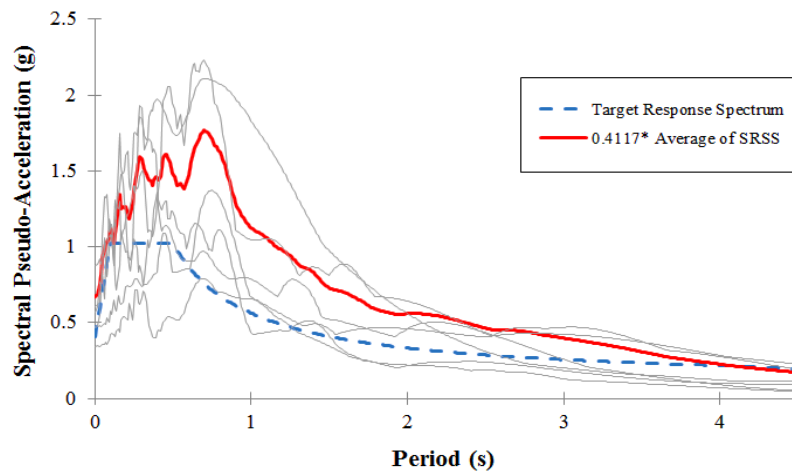
Figure 17. Plan (a) Structure without YOC (b) Structure with YOC (c).

Table 5. Specifications of near-field accelerations [21].

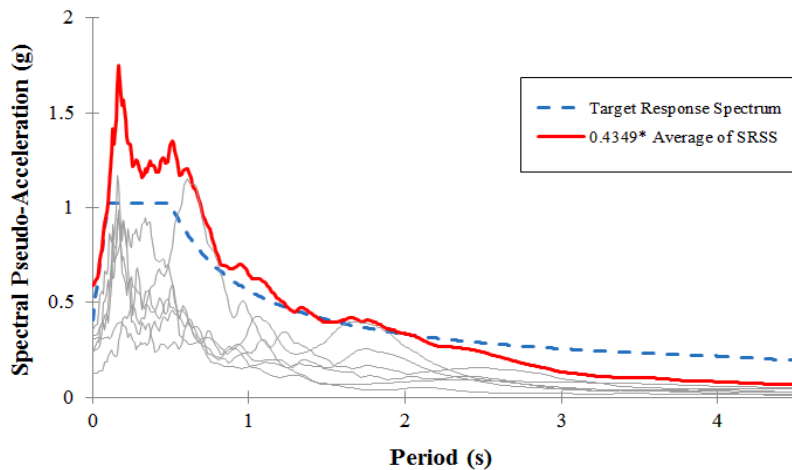
Earthquake Name	Station Name	Date	Magnitude (Richter)	Closest Distance to Fault Rupture (km)	Component	PGA (g)
Imperial Valley	El Centro Array	1979	6.53	0.56	Horizontal-X-axis	0.34
					Horizontal-Y-axis	0.46
					Vertical	0.57
Loma Prieta	LGPC	1989	6.93	3.88	Horizontal-X-axis	0.56
					Horizontal-Y-axis	0.60
					Vertical	0.89
Northridge	Rinaldi Receiving Sta	1994	6.69	6.50	Horizontal-X-axis	0.87
					Horizontal-Y-axis	0.47
					Vertical	0.95

Table 6. Specifications of far-field accelerations [21].

Earthquake Name	Station Name	Date	Magnitude (Richter)	Closest Distance to Fault Rupture (km)	Component	PGA (g)
Kobe	Kakogawa	1995	6.90	22.50	Horizontal-X-axis	0.24
					Horizontal-Y-axis	0.32
					Vertical	0.17
Darfield	LPCC	2010	7.00	25.67	Horizontal-X-axis	0.23
					Horizontal-Y-axis	0.35
					Vertical	0.15
Landers	Indio-Jackson Road	1992	7.28	48.84	Horizontal-X-axis	0.30
					Horizontal-Y-axis	0.12
					Vertical	0.08



(a)



(b)

Figure18. Spectral acceleration of the suite of ground motions: near-field (a) far-field (b).

3. Results and Discussion

To evaluate the effect of using YOC devices in reducing the seismic response, the selected building (Figure 17) equipped with- and without- YOCs is investigated through the non-linear time history analysis and its responses are compared with each other. The results related to the 16-story building are categorized as follows.

3.1. Formation of plastic hinges

Figures 19–24 show how plastic hinges form in the structure equipped with damper and the structure without damper during near- and far-field earthquakes. Evidently, in the structure without damper, plastic hinges are formed until the collapse of the structure. When the braced frame is equipped with the YOCs, no

plastic hinge is formed during the earthquakes; this indicates that the formation of plastic hinges is concentrated on the energy absorption devices and the plasticization of structural members is avoided, and there was no yielding or buckling in the braces.

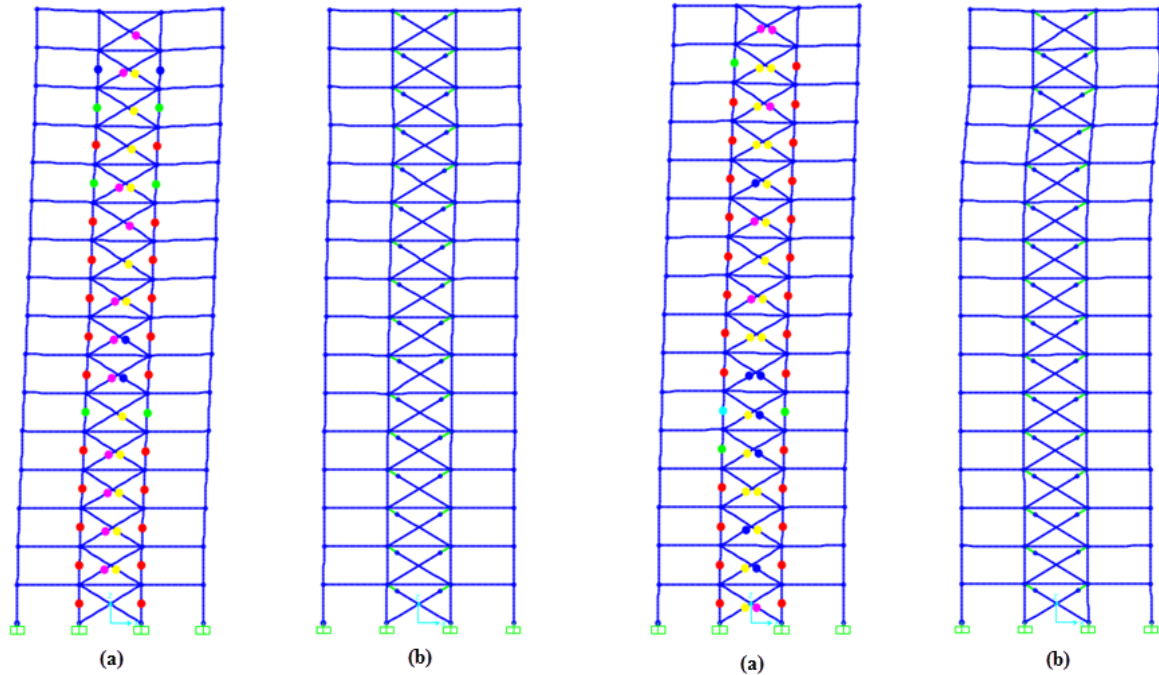


Figure 19. Plastic hinges formed subjected to Imperial Valley earthquake: (a) structure without damper; (b) structure equipped with YOCs.

Figure 20. Plastic hinges formed subjected to Loma Prieta earthquake: (a) structure without damper; (b) structure equipped with YOCs.

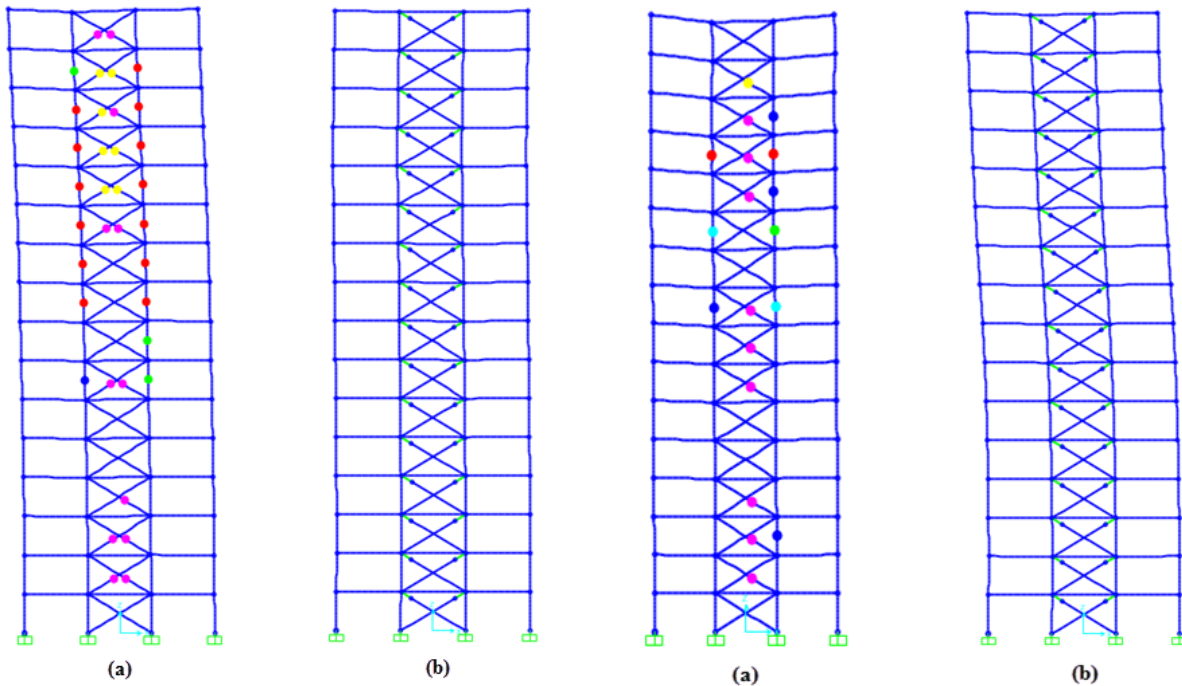


Figure 21. Plastic hinges formed subjected to Northridge earthquake: (a) structure without damper; (b) structure equipped with YOCs.

Figure 22. Plastic hinges formed subjected to Kobe earthquake: (a) structure without damper; (b) structure equipped with YOCs.

3.2. Effect of the damper on story drift ratio

The estimation of the maximum story drift ratio (defined as the ratio of the maximum story drift to the story height) and of the maximum roof displacement is appropriate measures of the global and local response of buildings under earthquakes, respectively. As demonstrated in Figures 25–30, the maximum story drift ratios have an ascending trend in the 16-story structure during the near- and far- field earthquakes. Although the maximum drift ratio in the middle stories increases, it decreases in the upper stories.

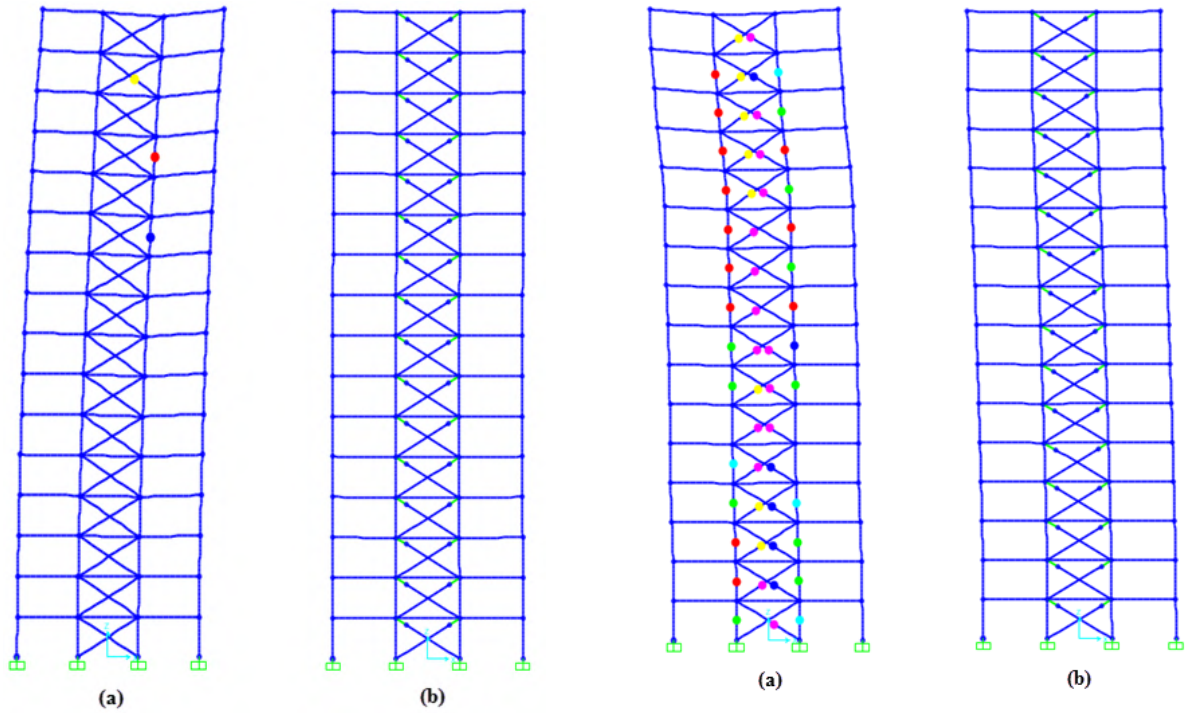


Figure 23. Plastic hinges formed subjected to Darfield earthquake: (a) structure without damper; (b) structure equipped with YOCs.

Figure 24. Plastic hinges formed subjected to Landers earthquake: (a) structure without damper; (b) structure equipped with YOCs.

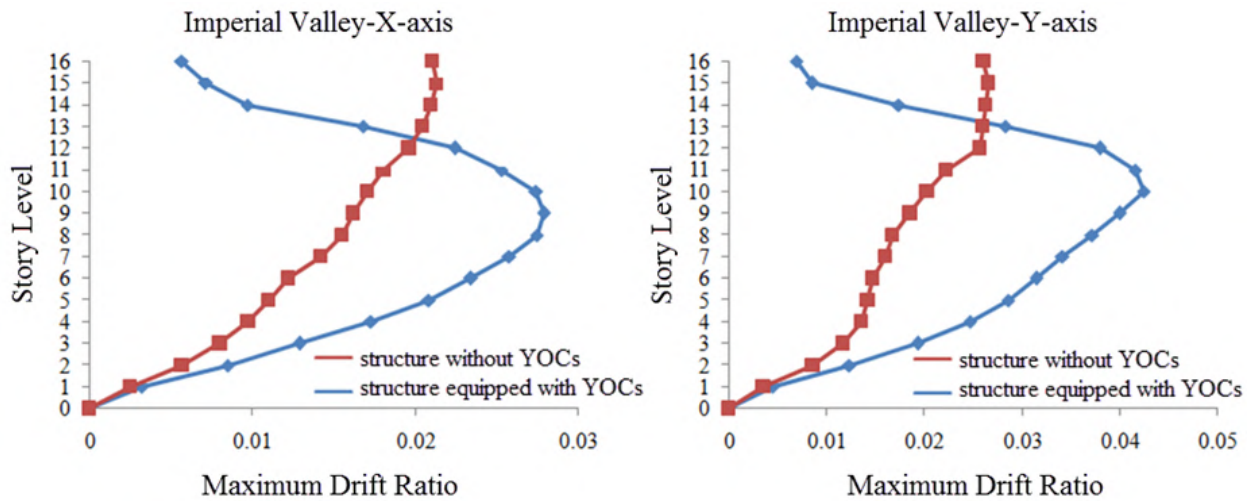


Figure 25. Maximum story drift ratio subjected to Imperial Valley earthquake along X- and Y- axes.

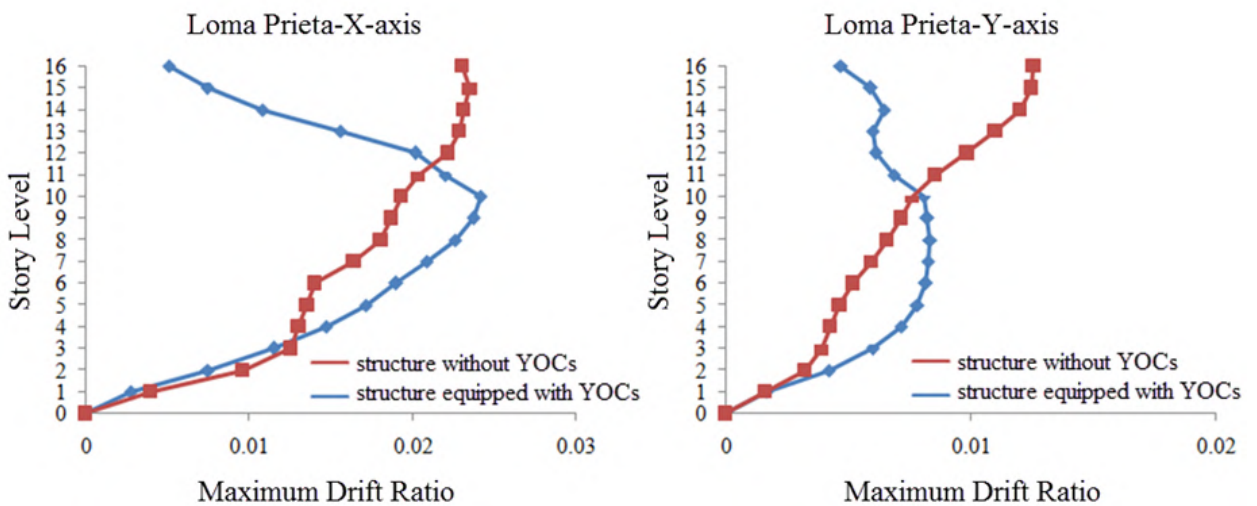


Figure 26. Maximum story drift ratio subjected to Loma Prieta earthquake along X- and Y- axes.

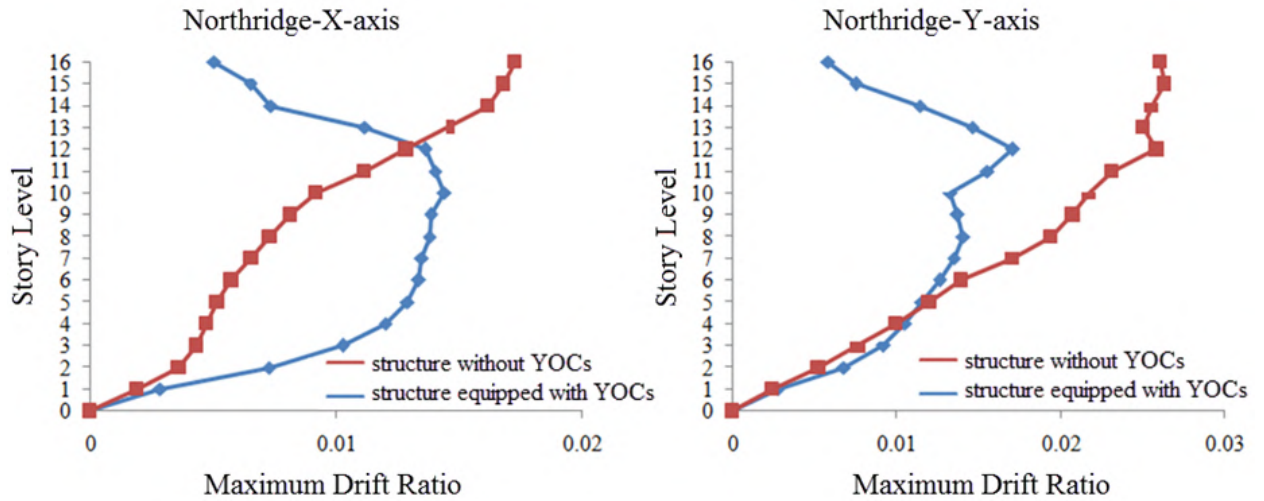


Figure 27. Maximum story drift ratio subjected to Northridge earthquake along X- and Y- axes.

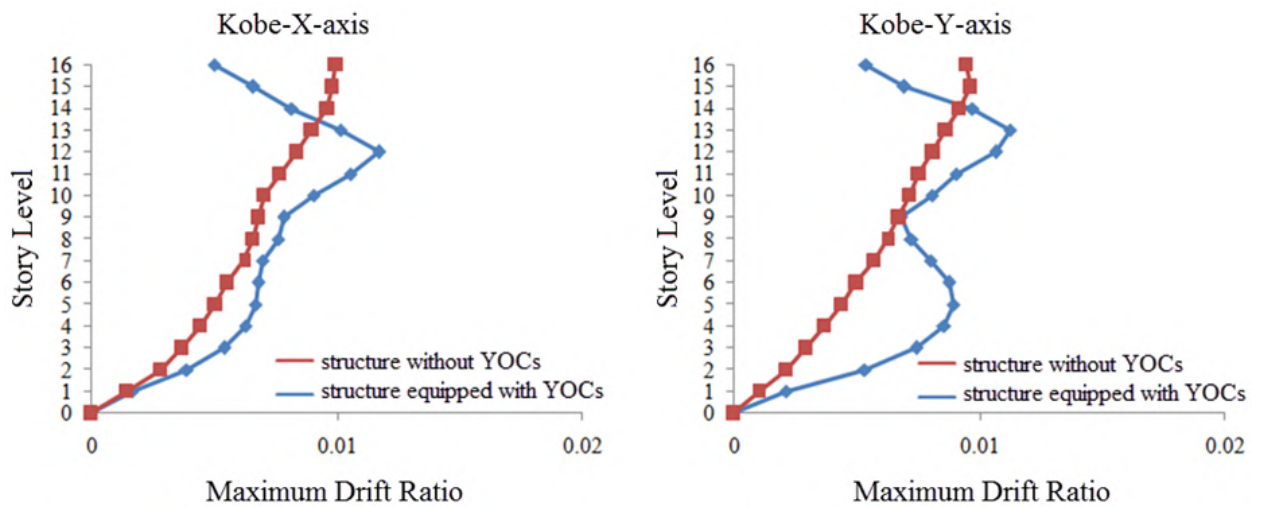


Figure 28. Maximum story drift ratio subjected to Kobe earthquake along X- and Y- axes.

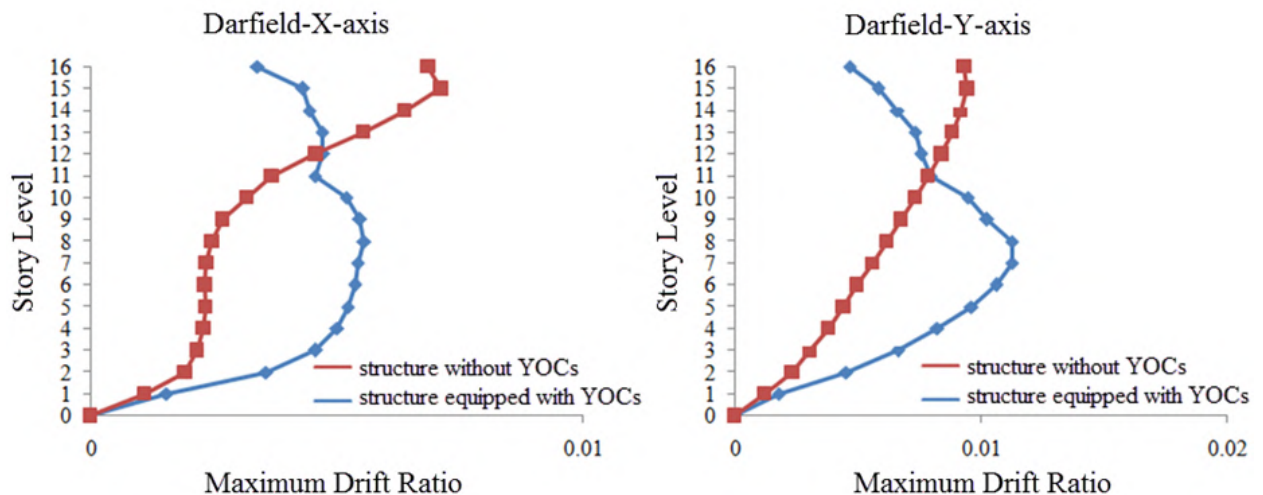


Figure 29. Maximum story drift ratio subjected to Darfield earthquake along X- and Y- axes.

Usually, the expected loss resulting from damage to acceleration-sensitive non-structural elements is somewhat higher than that in structural elements. Story accelerations are needed for determining forces for the design of non-structural components and equipment supported on the floors. As shown in Figures 31–36 for near- and far-field earthquakes, the peak floor accelerations at all floors of the structure equipped with YOCs are less than that of the structure without YOCs. These results indicate that the performance of non-structural members in the structure equipped with YOCs has improved.

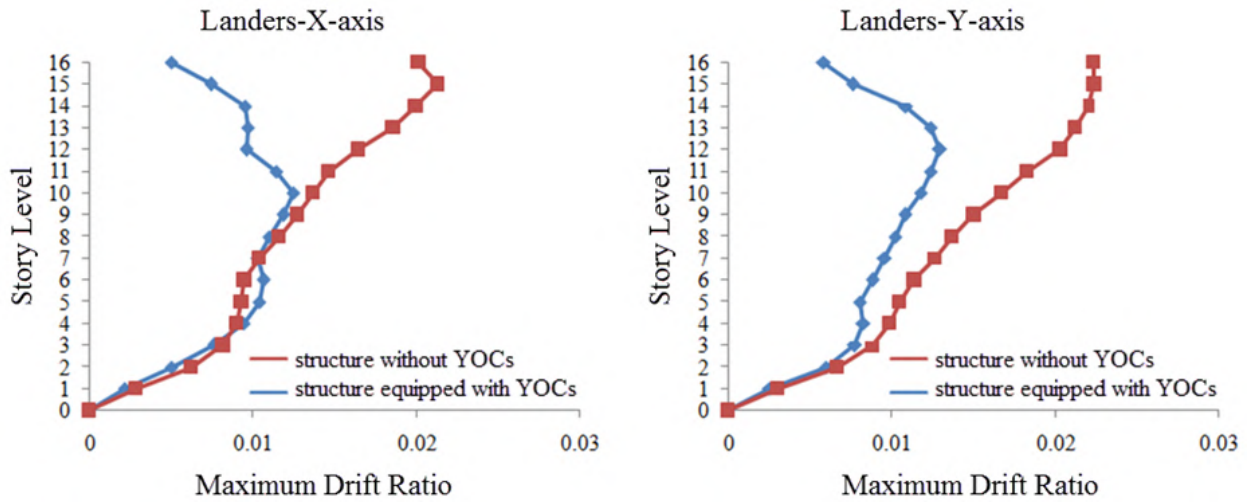


Figure 30. Maximum story drift ratio subjected to Landers earthquake along X- and Y- axes.

3.3. Effect of the damper on the peak floor acceleration

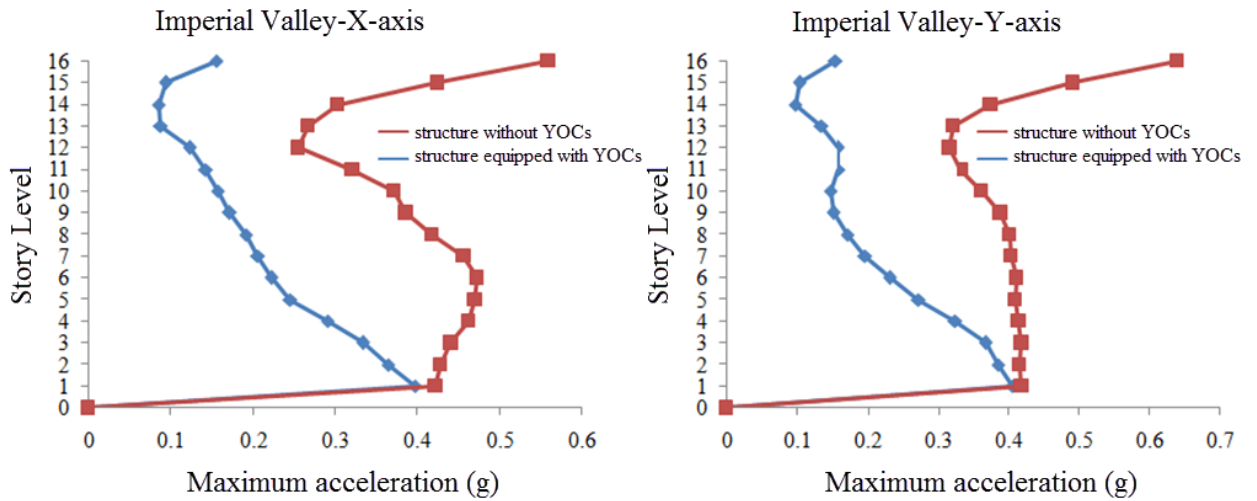


Figure 31. Peak floor acceleration ratio subjected to Imperial Valley earthquake along X- and Y- axes.

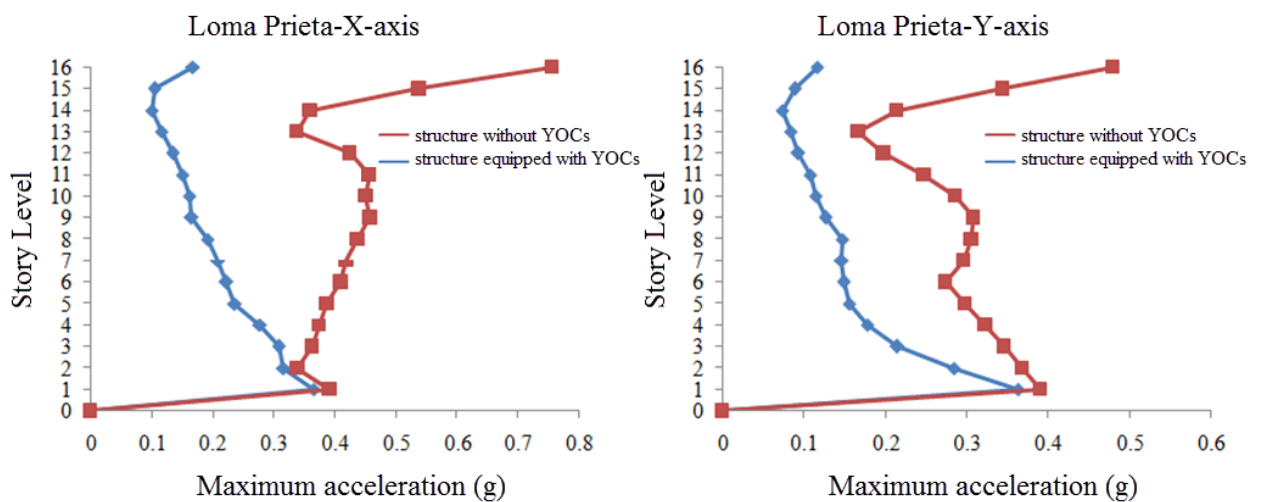


Figure 32. Peak floor acceleration ratio subjected to Loma Prieta earthquake along X- and Y- axes.

In Tables 7 and 8 a comparison of base reaction values in the structure without YOCs and the structure equipped with YOCs is presented and the variations are investigated. The application of YOC in the structure results in a 51–67 % decrease in the base reaction under near-field earthquakes and a 33–65 % decrease in the base reaction under far-field earthquakes. The maximum reduction in the amounts of base reaction for near- and far-field earthquake belongs to the Loma Prieta and Landers earthquakes, respectively.

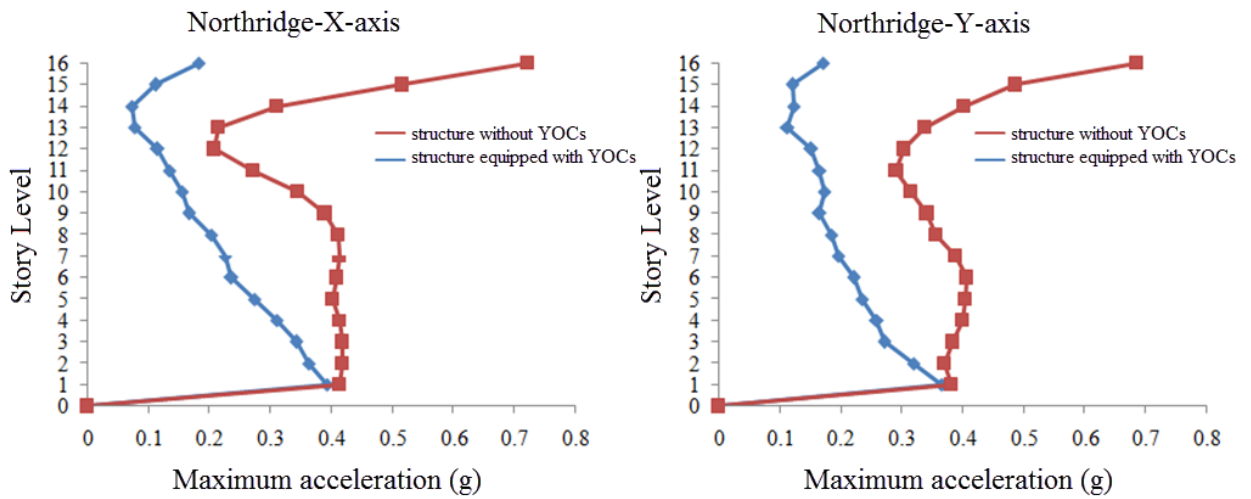


Figure 33. Peak floor acceleration ratio subjected to Northridge earthquake along X- and Y- axes.

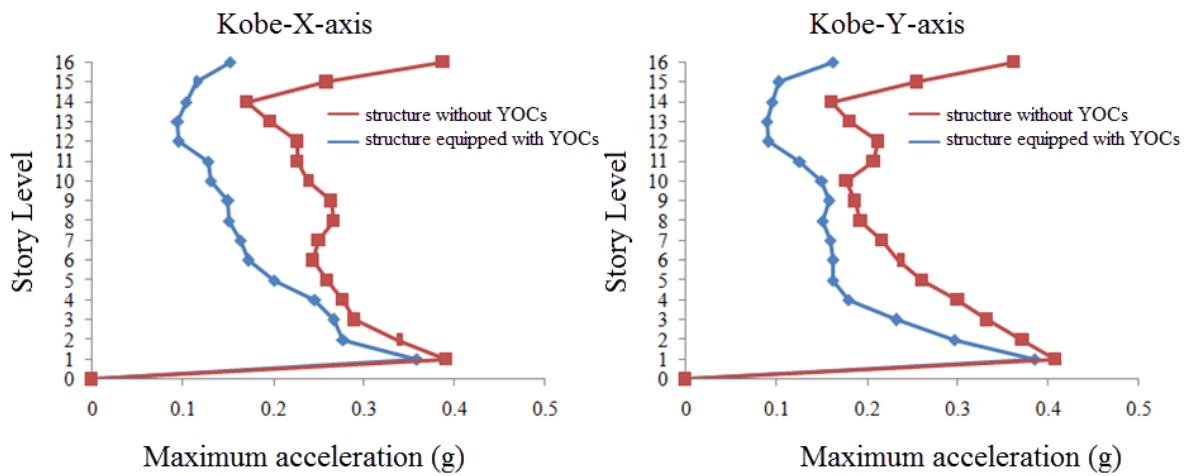


Figure 34. Peak floor acceleration ratio subjected to Kobe earthquake along X- and Y- axes.

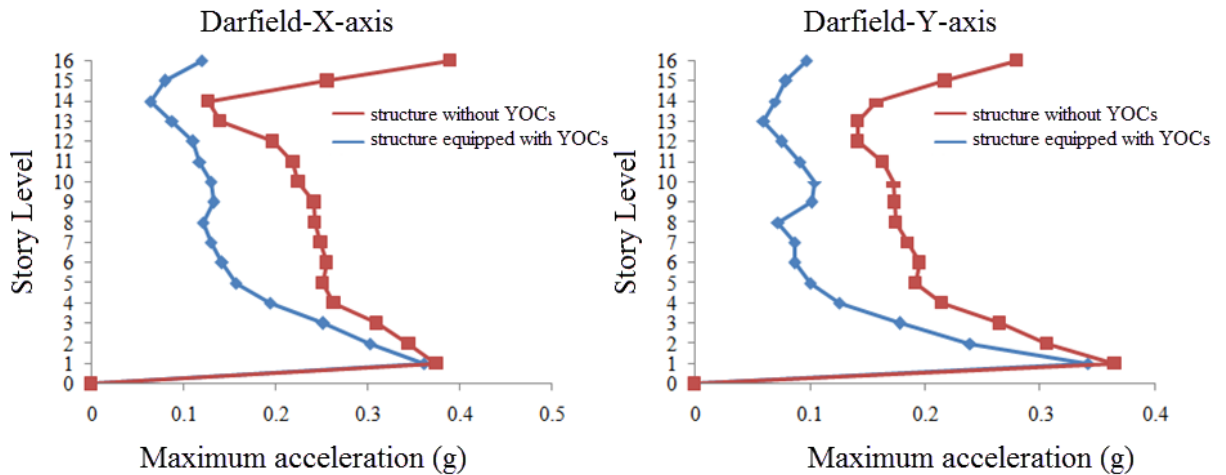


Figure 35. Peak floor acceleration ratio subjected to Darfield earthquake along X- and Y- axes.

3.4. Effect of the damper on maximum roof acceleration

In Figures 37–42, the time histories of the Peak floor acceleration at roof level during near- and far-field earthquakes are compared. As presented in the acceleration time history graphs, the octagonal damper leads to a significant decrease in the roof acceleration. The reduction of roof acceleration varies from 72 % to 78 % and from 55 % to 82 % under near- and far-field earthquakes, respectively.

3.4.1. Effect of the damper on maximum roof acceleration in near-field earthquakes

It is seen in Figures 37–39 that maximum roof acceleration of the structure equipped with YOCs has decreased by 77 %, 77 % and 75 % of the structure without YOCs under Imperial Valley, Loma Prieta, and Northridge earthquakes, respectively.

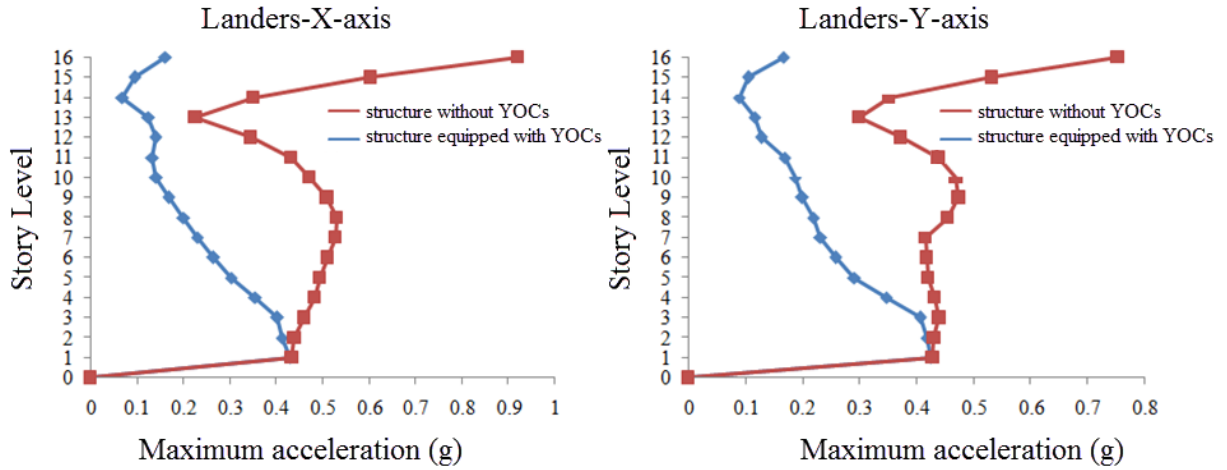


Figure 36. Peak floor acceleration ratio subjected to Landers earthquake along X- and Y- axes.

3.5. Effect of the damper on base reaction

Table 7. The base reaction of the 16-story building under near-field earthquakes.

Earthquake	Structure equipped with YOCs (ton)		Structure without YOCs (ton)		Difference (%)	
	X-axis	Y-axis	X-axis	Y-axis	X-axis	Y-axis
Imperial Valley	205.99	235.04	502.19	647.06	-58.98	-63.67
Loma Prieta	223.18	151.92	688.33	389.26	-67.57	-60.97
Northridge	237.56	231.81	485.12	540.95	-51.03	-57.14

Table 8. The base reaction of the 16-story building under far-field earthquakes.

Earthquake	Structure equipped with YOCs (ton)		Structure without YOCs (ton)		Difference (%)	
	X-axis	Y-axis	X-axis	Y-axis	X-axis	Y-axis
Kobe	163.35	159.34	357.69	238.60	-54.33	-33.21
Darfield	142.29	129.53	316.48	300.15	-55.03	-56.84
Landers	240.62	232.61	610.42	675.74	-60.58	-65.57

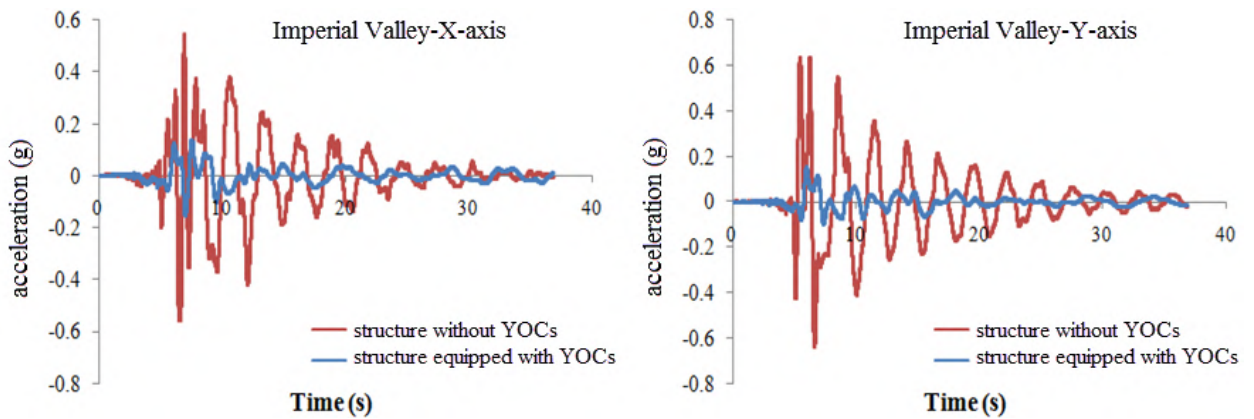


Figure 37. Roof acceleration histories of the building along X- and Y- axes subjected to Imperial Valley earthquake.

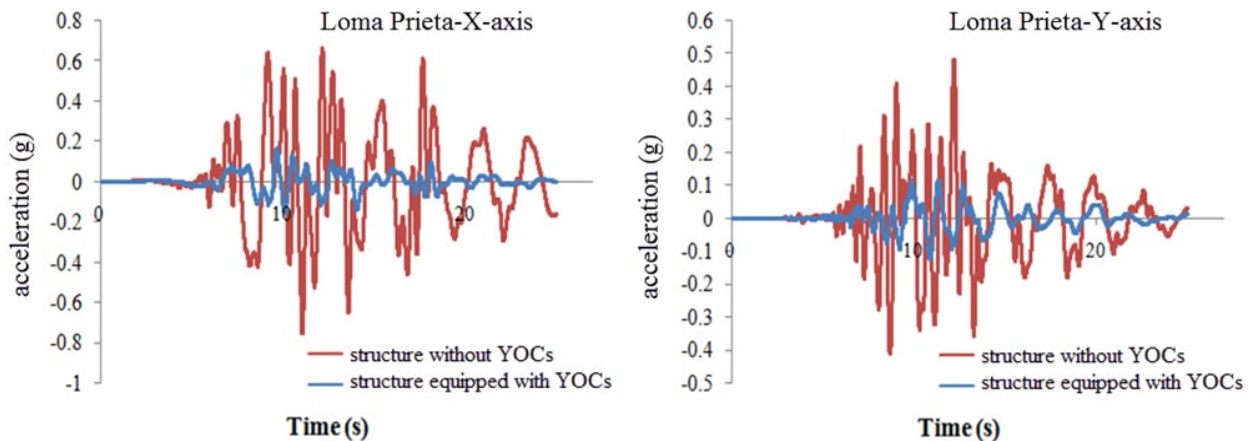


Figure 38. Roof acceleration histories of the building along X- and Y- axes subjected to Loma Prieta earthquake.

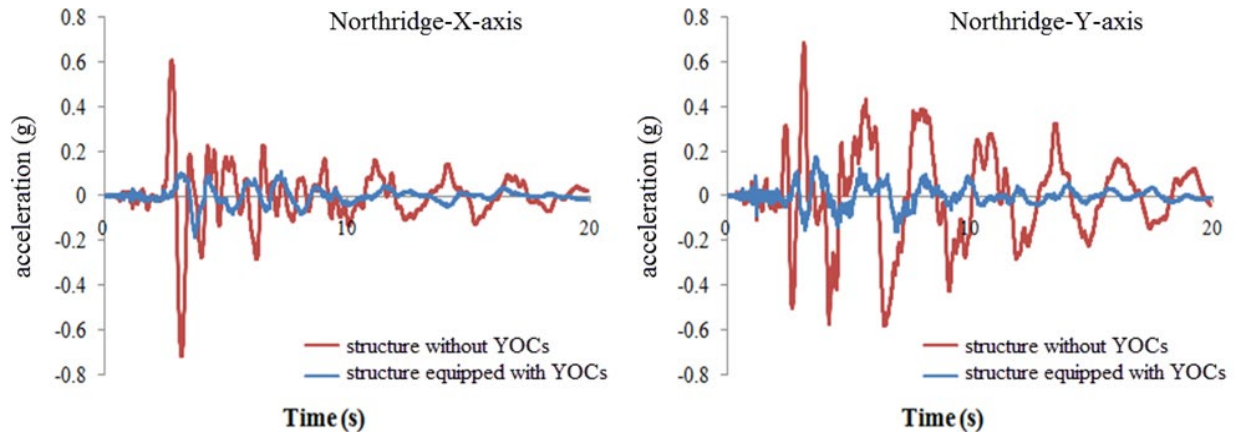


Figure 39. Roof acceleration histories of the building along X- and Y- axes subjected to Northridge earthquake.

3.5.1. Effect of the damper on maximum roof acceleration in far-field earthquakes

It is seen in Figures 40–42 that maximum roof acceleration of the structure equipped with YOCs has decreased by 62 %, 89 % and 83 % of the structure without YOCs under Kobe, Darfield and Landers earthquakes, respectively. In general, the results of the near- and far field earthquakes indicate that addition of YOC leads to a significant decrease in the maximum acceleration of the roof floor.

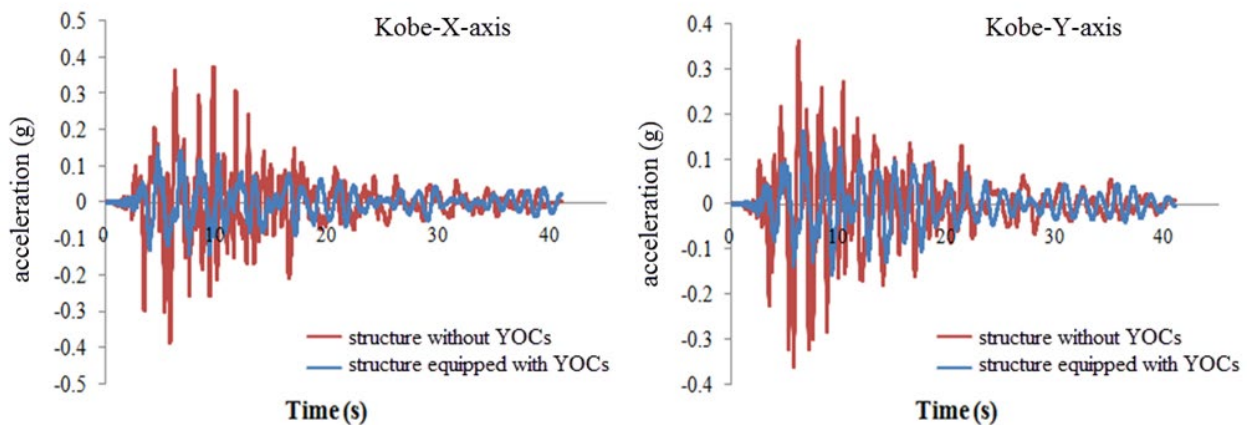


Figure 40. Roof acceleration histories of the building along X- and Y- axes subjected to Kobe earthquake.

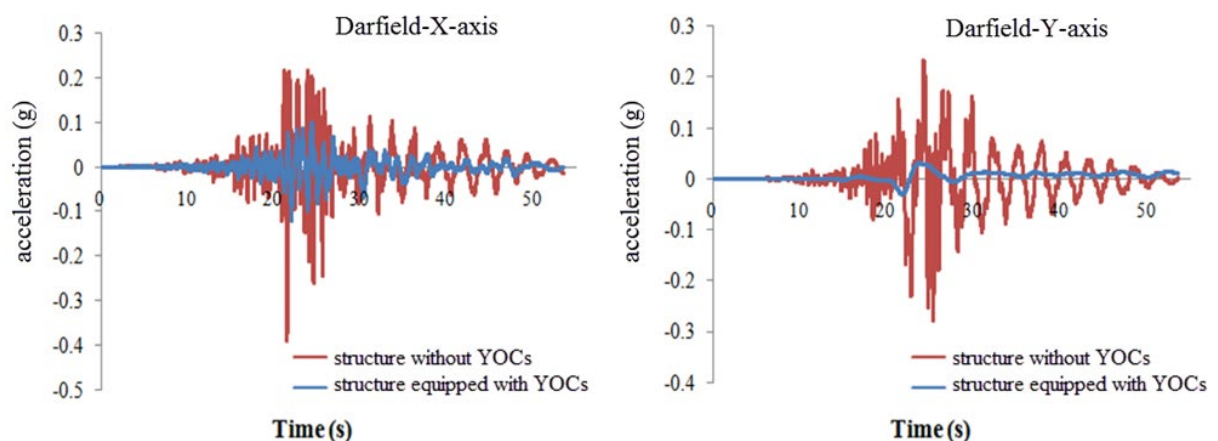


Figure 41. Roof acceleration histories of the building along X- and Y- axes subjected to Darfield earthquake.

3.6. Effect of maximum roof displacement

Figures 43–48 depict the effect of the damper on the time history of the maximum roof displacement during near- and far-field earthquakes. The 16-story structure equipped with the damper can reduce the maximum roof displacement by 61 % under the Northridge earthquake and 57 % under the Landers earthquake. However, an increase of 28 % and 8 % is observed under the Imperial Valley and the Darfield earthquakes, respectively. This difference is due to the fact that the structure shows different behavior under various records.

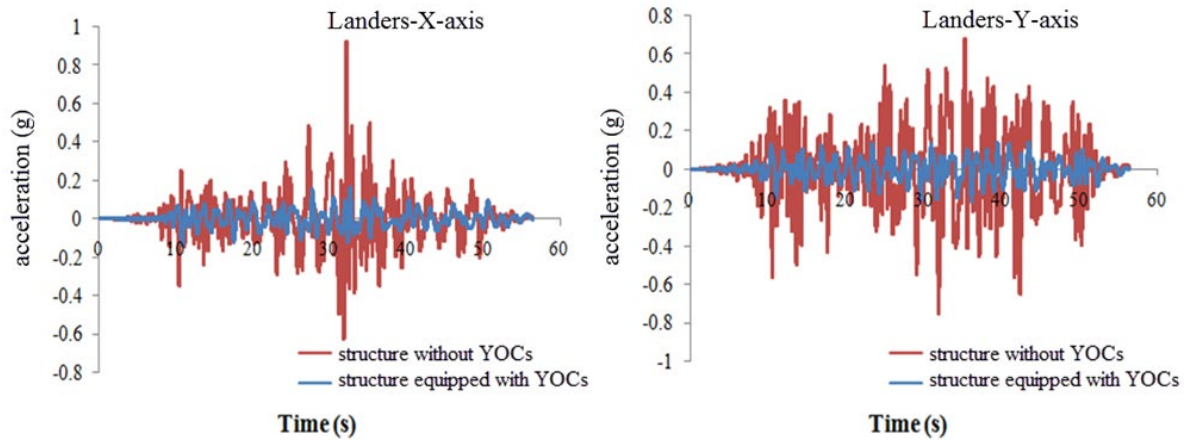


Figure 42. Roof acceleration histories of the building along X- and Y- axes subjected to Landers earthquake.

3.6.1. Effect of maximum roof displacement in near-field earthquakes

It can be seen in figures 43 to 45 that maximum roof displacement of the structure equipped with YOCs has decreased by 28 % and 61 % of the structure without YOCs under Loma Prieta and Northridge earthquakes, respectively. It has increased by 28 % under Imperial Valley earthquake.

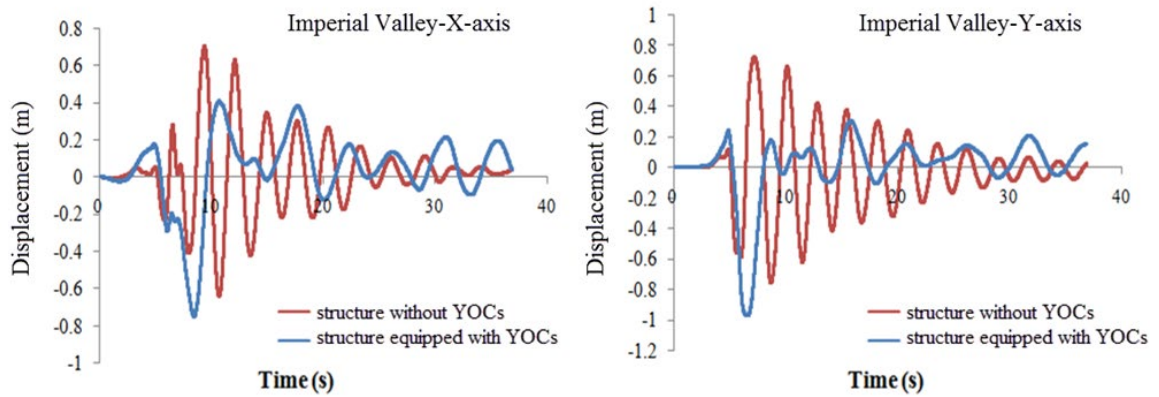


Figure 43. Roof displacement histories of the building along X- and Y- axes subjected to Imperial Valley earthquake.

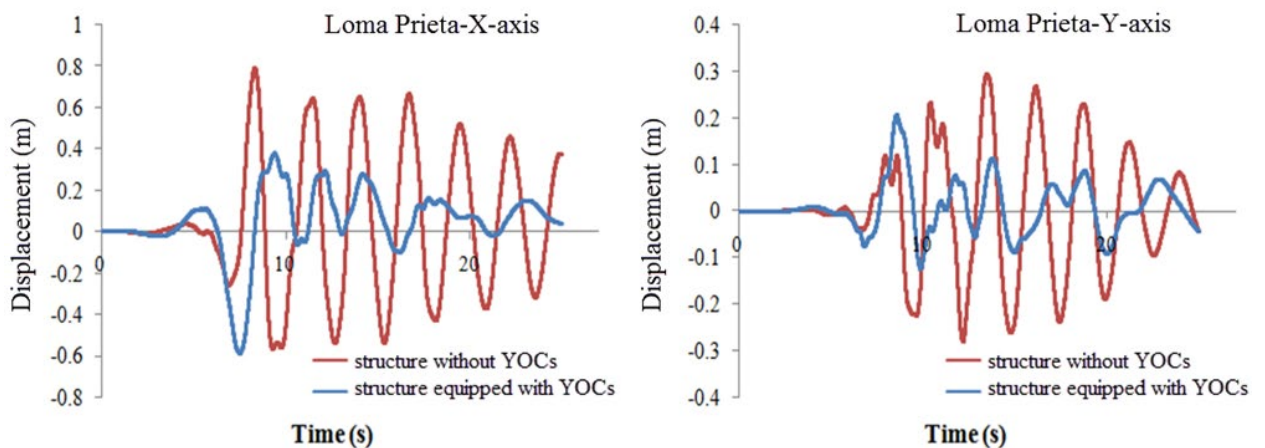


Figure 44. Roof displacement histories of the building along X- and Y- axes subjected to Loma Prieta earthquake.

3.6.2. Effect of maximum roof displacement in far-field earthquakes

It can be seen in Figures 46–48 that maximum roof displacement of the structure equipped with YOCs has decreased by 31 % and 58 % of the structure without YOCs under Kobe and Landers earthquakes, respectively. It has increased by 8 % under Darfield earthquake. In general, the results of the near- and far field earthquakes indicate that addition of YOC leads to a decrease in the maximum displacement of the roof floor.

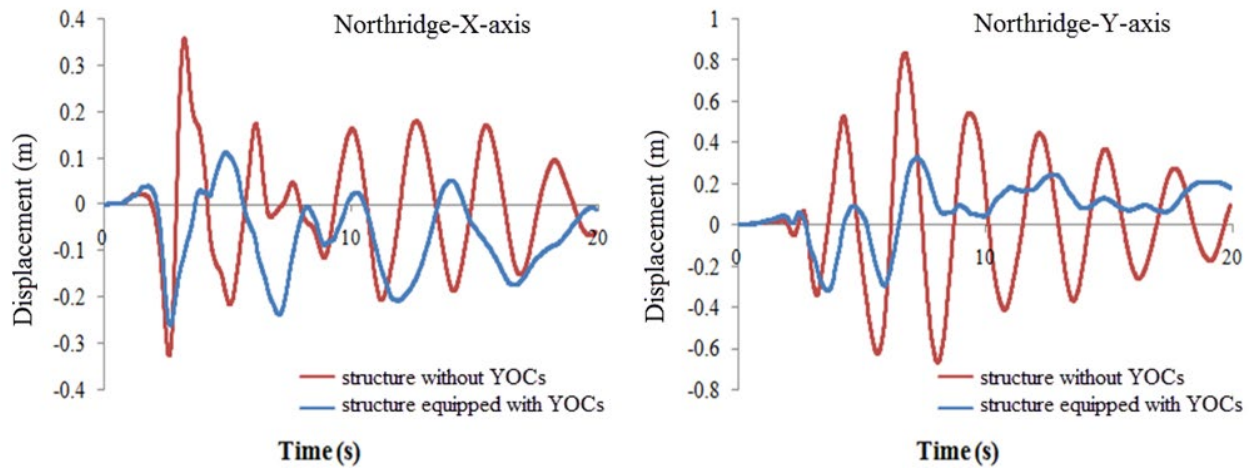


Figure 45. Roof displacement histories of the building along X- and Y- axes subjected to Northridge earthquake.

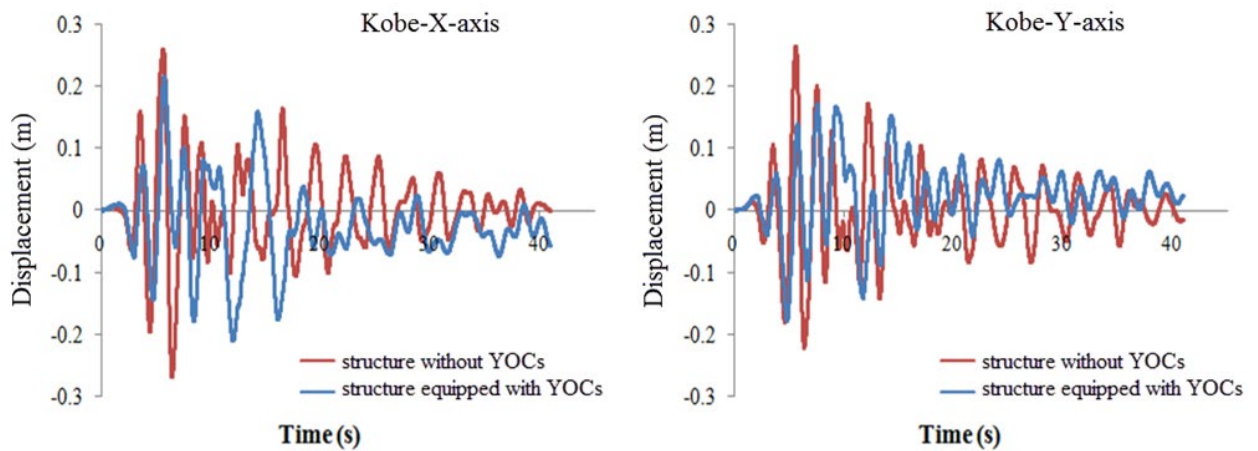


Figure 46. Roof displacement histories of the building along X- and Y- axes subjected to Kobe earthquake.

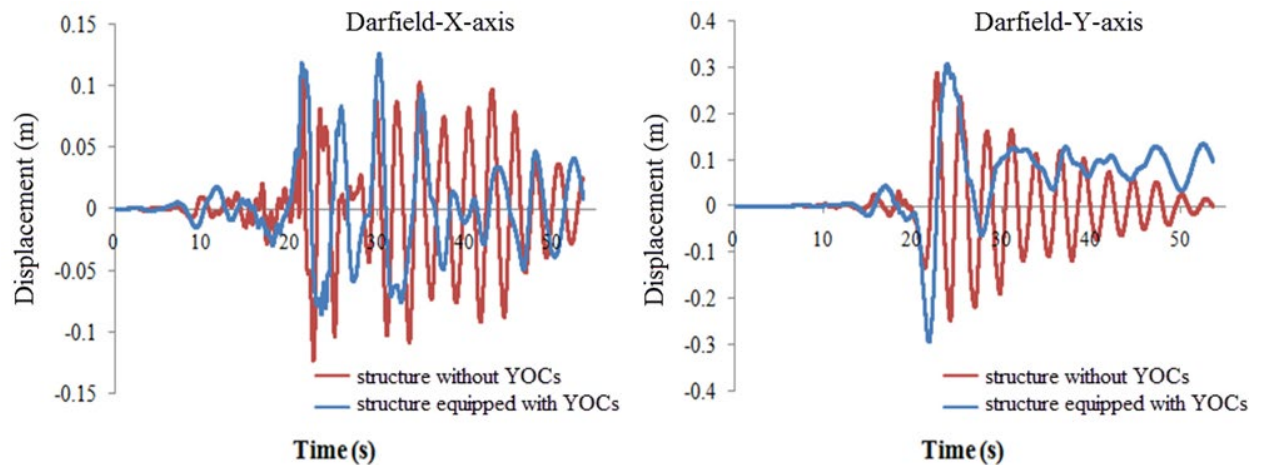


Figure 47. Roof displacement histories of the building along X- and Y- axes subjected to Darfield earthquake.

4. Conclusion

In this paper, by using numerical studies, the new energy absorption device on the seismic response of CBF called Yielding Octagonal Connection “YOC” has been introduced, which is modeled using Abaqus finite element software, and hysteresis curve were created for this element under cyclic loading. In order to evaluate the behavior of the YOC, a series of non-linear time history analyses are performed for the 16-story steel structure under near- and far-field earthquakes. Therefore, according to the result of conducted study the following results are presented:

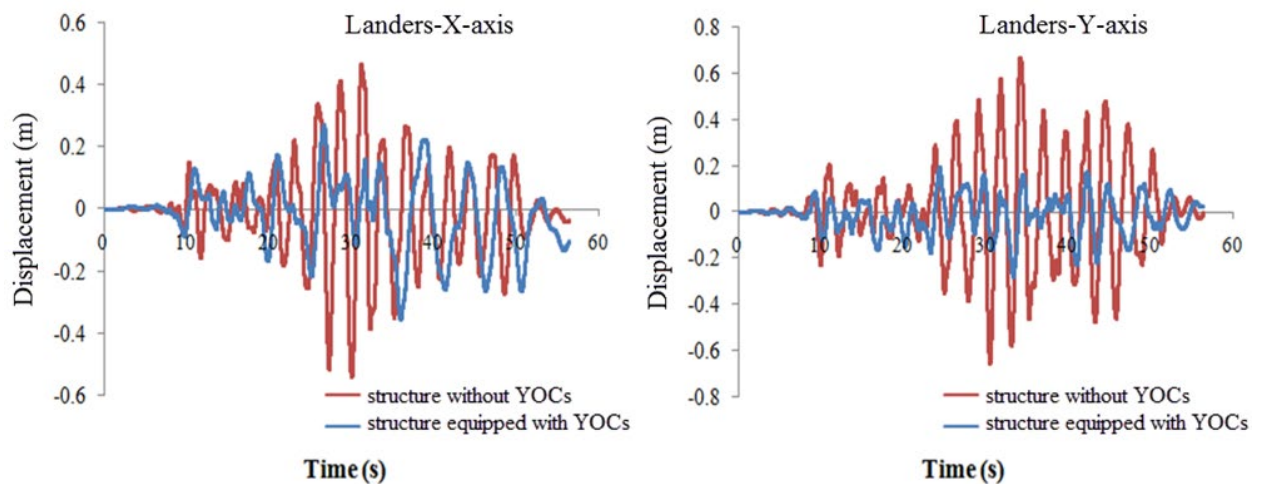


Figure 48. Roof displacement histories of the building along X- and Y- axes subjected to Landers earthquake.

- The Non-linear time history analyses performed using the Sap2000 software show that inelastic deformations are concentrated only in the YOCs, and the main structural components were essentially elastic while the structure experienced severe earthquakes. The reason for this is no plastic hinges formed in structural members, and there was no yielding or buckling in the braces.
- Test results show that YOCs are very effective in reducing excessive vibration of the structure due to seismic excitations. The structure equipped with YOC achieves a reduction of the peak floor acceleration in whole stories under near- and far- field earthquakes.
- The analysis findings of the structure containing connection equipped with YOC indicate that although it doesn't keep maximum displacement of stories extent for most of the earthquakes used, it reduces the base reaction to a considerable extent.
- According to the numerical studies carried out in this paper, it was concluded that the amounts of story drift ratios in the structure equipped with YOCs are different under various earthquakes, sometimes are increased or decreased. But the results show that Finally, this study represents a first attempt to describe the cyclic behavior of the proposed YOC numerically. The results of analyzing real structures with such a numerical model can be used to assess design a prototype system for full-scale experimental work. Further studies are necessary to extend experimentally, this scenario for reaching the final goal.

References

1. Franco, J.M., Cahís, X., Gracia, L., López, F. Experimental testing of a new anti-seismic dissipater energy device based on the plasticity of metals. *Engineering Structures*. 2010. Vol. 32(9). Pp. 2672–2682.
2. Mistakidis, E. Numerical study of low-yield point steel shear walls used for seismic applications. *Engineering computations*. 2010. Vol. 27(2). Pp. 257–279.
3. Benavent-Climent, A. A brace-type seismic damper based on yielding the walls of hollow structural sections. *Engineering Structures*. 2010. Vol. 32(4). Pp. 1113–1122.
4. Ward, K.M., Fleischman, R.B., Federico, G. A cast modular bracing system for steel special concentrically braced frames. *Engineering Structures*. 2012. Vol. 45. Pp. 104–116.
5. Gray, M.G., Christopoulos, C., Packer, J.A. Cast steel yielding brace system for concentrically braced frames: concept development and experimental validations. *Journal of Structural Engineering*. 2013. Vol. 140(4). 04013095.
6. Beheshti-Aval, S.B., Mahbanouei, H., Zareian, F. A hybrid friction-yielding damper to equip concentrically braced steel frames. *International Journal of Steel Structures*. 2013. Vol. 13(4). Pp. 577–587.
7. Li, H.N., Li, G. Experimental study of structure with «dual function» metallic dampers. *Engineering Structures*. 2007. Vol. 29(8). Pp. 1917–1928.
8. Nejati, F., Hosseini, M., Mahmoudzadeh, A. Design of repairable regular steel buildings with square plan based on seesaw motion of building structure and using DADAS dampers. *International Journal of Structural Integrity*. 2017. Vol. 8(3). Pp. 326–340.
9. Hsu, H.L., Halim, H. Brace performance with steel curved dampers and amplified deformation mechanisms. *Engineering Structures*. 2018. Vol. 175. Pp. 628–644.
10. Baiguera, M., Vasdravellis, G., Karavasilis, T. L. Dual seismic-resistant steel frame with high post-yield stiffness energy-dissipative braces for residual drift reduction. *Journal of Constructional Steel Research*. 2016. Vol. 122. Pp. 198–212.
11. Taiyari, F., Mazzolani, F.M., Bagheri, S. A proposal for energy dissipative braces with U-shaped steel strips. *Journal of Constructional Steel Research*. 2019. Vol. 154. Pp. 110–122.
12. Jarrah, M., Khezzzadeh, H., Mofid, M., Jafari, K. Experimental and numerical evaluation of piston metallic damper (PMD). *Journal of Constructional Steel Research*. 2019. Vol. 154. Pp. 99–109.
13. SAP2000, C. Integrated software for structural analysis and design. Analysis reference manual. Computers and Structures Inc. 2017.
14. ASTM. Standard specification for low and intermediate tensile strength carbon steel plates. ASTM A283/A283M-13, West Conshohocken, PA. 2013.

15. ATC24, Guidelines for Cyclic Seismic Testing of Components of Steel Structures. Applied technology council. 1992.
16. FEMA 356. Pre-standard and Commentary for the Seismic Rehabilitation of Buildings. Washington, DC. ASCE Standards Committee on Seismic Rehabilitation. 2000.
17. Abbasnia, R., Vetr, M.G.H., Ahmadi, R., Kafi, M.A. Experimental and analytical investigation on the steel ring ductility. Sharif J. Sci. Technol. 2008. Vol. 52. Pp. 41–48. (Persian)
18. ABAQUS Ver. 6.12, User's Manual, RI, USA. 2012.
19. BHRC. Iranian code of practice for seismic resistant design of buildings: standard No. 2800 (4th. Edition). [Building and Housing Research Center]. 2017. Tehran. 211 p. (Persian)
20. ASCE/SEI Standard 41-13. Seismic Evaluation and of Retrofit of Existing Buildings. Structural Engineering Institute, American society of civil engineers. 2014.
21. PEER Ground Motion Database, Pacific Earthquake Engineering Research Center [Online]. URL: <http://ngawest2.berkeley.edu/>

Contacts

Faezeh Nejati, civilifa_nj@yahoo.com

Milad Zhian, miladjyane@gmail.com

Fatemeh Safar Mashaie, honik_ir@yahoo.com

Seyyed Ahmad Edalatpanah, saedalatpanah@gmail.com

© Nejati, F., Zhian, M., Safar Mashaie, F., Edalatpanah, S.A. 2020



DOI: 10.18720/MCE.94.5

Evolving crack influence on the strength of frozen sand soils

T.A. Gavrilov*, **G.N. Kolesnikov**

Petrozavodsk State University, Petrozavodsk, Russia

* E-mail: gtimmo@mail.ru

Keywords: mechanical properties, elastic moduli, tensile strength, cracks, bending tests, experimental investigations, mathematical modeling

Abstract. The object of the study in this work is the relationship between the elastic modulus, tensile stresses and deformations of frozen sandy soil with evolving cracks using the example of three-point bending. The goal is to develop a methodology for determining the modulus of elasticity and tensile stresses in frozen sandy soil under force indirectly. The choice of the object and the purpose of the study is motivated by the relevance of the soil strength problems during seasonal freezing. To achieve the goal, methods of mathematical modeling of mechanical systems with changing characteristics during the deformation, also the testing methods of samples on the SHIMADZU AGS-X test machine were used. A mathematical model has been developed, the realism of which is ensured by taking into account the evolution of a crack and using the effective geometric characteristics known from fracture mechanics. It has been substantiated that the destruction of the material occurs on the descending branch of the «load - displacement» diagram. The simulation results are consistent with the data known in the scientific literature. The condition for the model application is the existence of an extremum point on the curve «load - displacement». Prospects for the development of the topic are associated with the adaptation of the proposed approach to the analysis of the of frozen soil state, taking into account its rheological properties.

1. Introduction

The object of study in this work is the relationship between the elastic modulus, tensile stresses and deformations of frozen sandy soil with evolving cracks. The choice of the research object is motivated by the relevance of the problem of soil strength during seasonal freezing and the need in continuing the research focused on solving these problems. To develop the topic of the work, we pay attention to the following facts.

Large volumes of sandy soils, which include both sand and gravel mixtures, are used in the construction of roads, buildings and other engineering structures. The strength of the soil under power and temperature influences should be sufficient to ensure the reliability of these objects. Tensile stresses are known to appear in the soil mass during seasonal freezing. These stresses can cause frost cracking in the upper layer of the highway, if the soil strength is insufficient [1, 2]. In this case, tensile stresses are proportional to the elastic modulus; therefore, simple methods for determining its values are necessary. In addition, the modulus of elasticity characterizes the rigidity and strength of frozen soil [3]. Obviously, it is necessary to know the strength and elastic modulus of frozen soil while designing, building, monitoring and forecasting the condition of roads and other construction objects [4–6].

The analysis of the scientific literature showed that intensive studies of the state of frozen soils are currently being conducted taking into account various factors. Studies are usually experimental, and the publication of their contributes to the better understanding of the frozen soils behavior under influences of various kinds. Tests of the frozen soils samples described in scientific works show that the relationship between load and displacement (for example, between force and vertical displacement of the point of its application in three-point bending) is usually non-linear. Nonlinearity is explained by the influence of plastic deformations.

In [7, p. 31], it was shown that plastic deformations and fractures happened when the nucleation of microcracks predominated. It follows that the appearance and evolution of cracks can be considered as the primary cause of the frozen soil destruction. The key issue in this case is the ratio between the damage and the displacement. Then the above nonlinearity of the relationship between load and displacement can be explained by the crack evolution.

Gavrilov, T.A., Kolesnikov, G.N. Evolving crack influence on the strength of frozen sand soils. Magazine of Civil Engineering. 2020. 94(2). Pp. 54–64. DOI: 10.18720/MCE.94.5



This work is licensed under a [CC BY-NC 4.0](https://creativecommons.org/licenses/by-nc/4.0/)

An additional argument in favor of this conclusion can be one of the results of [8], in which a model of the mechanical condition of soil has been proposed on the base of an analysis of tests under uniaxial compression using a logistic equation in this four parameter model, from the results of uniaxial compression tests it becomes possible to determine the elastic modulus of intact material. In addition, the bifurcation phenomenon of cracks in these tests has been explained. In this case, the use of the results of mechanical testing of rocks in the study of the frozen sandy soil strength seem appropriate, since frozen sandy soil can be considered as a kind of composite inhomogeneous material consisting of mineral particles, ice as a binder, unfrozen water inclusions, pores with air and microcracks.

With increasing mechanical stress, the bearing capacity of the soil gradually decreases due to the evolution of microcracks to meso- and macro-damage to the material. Excessive crack evolution significantly reduces the strength and rigidity of frozen ground. However, despite the obvious need, the problem of frozen soils with cracks modeling in order to determine the elastic modulus and evaluate tensile stresses still does not have a sufficiently complete solution [2, 8].

Tensile stresses are known to play the main role in the evolution of cracks. However, uniaxial compression tests dominate in the experimental literature on frozen soils due to the technical difficulties of both specimen preparation and direct measurement of tensile stresses. Therefore, along with direct methods, indirect methods to determining tensile stresses during tests are used, for example, acoustic technologies, three- and four-point bending [7]. In this work three-point bending tests for the indirect determination of the elastic modulus and tensile stresses in a section with an evolving crack were used.

Tests for three-point bending of a frozen soil beam were used by the authors of [7, 9] to determine the stress intensity factor in the neighborhood of the crack tip. According to the Griffiths – Irwin criterion, crack propagation will begin if the stress intensity factor at the crack tip reaches a certain critical value [10]. The influence of evolving cracks on the stress – strain state of sandstone and other brittle rocks during uniaxial compression was studied in [8] using the logistic equation of a three-point bending test. The three-point bending of samples consisting of sand and ice was studied in [11]. The test results showed that such a material is brittle, its strength increases with the decreasing temperature. A model based on a failure arising from the propagation of defects in an ice matrix is presented. Despite the good agreement between the model and experimental results, it was noted that the further work is needed to refine the model.

A modern understanding of the problems of modeling the mechanical state of frozen soils is shown in [1, 2, 12–16, etc.].

The review showed that in literature there is no solution to the problem of determining the elastic modulus of frozen sandy soil and tensile stresses in the cross section of a beam with an evolving crack according to the results of tests for three-point bending.

Objective: to develop a methodology for determining the modulus of elasticity and tensile stresses in frozen sandy soil with an evolving crack under a force.

2. Material and Methods

Object of study: a beam of rectangular cross section with a width of 55 mm, a height of 39 mm; the span of 280 mm (Figure 1, 2).

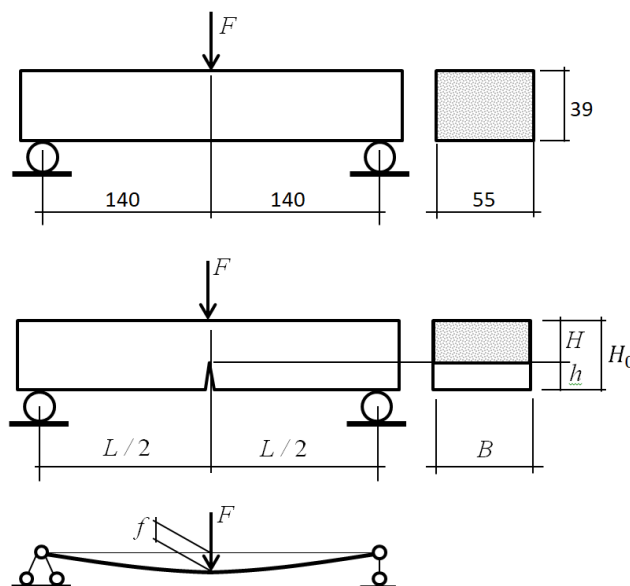


Figure 1. Beam diagrams before and after cracking (dimensions in mm).

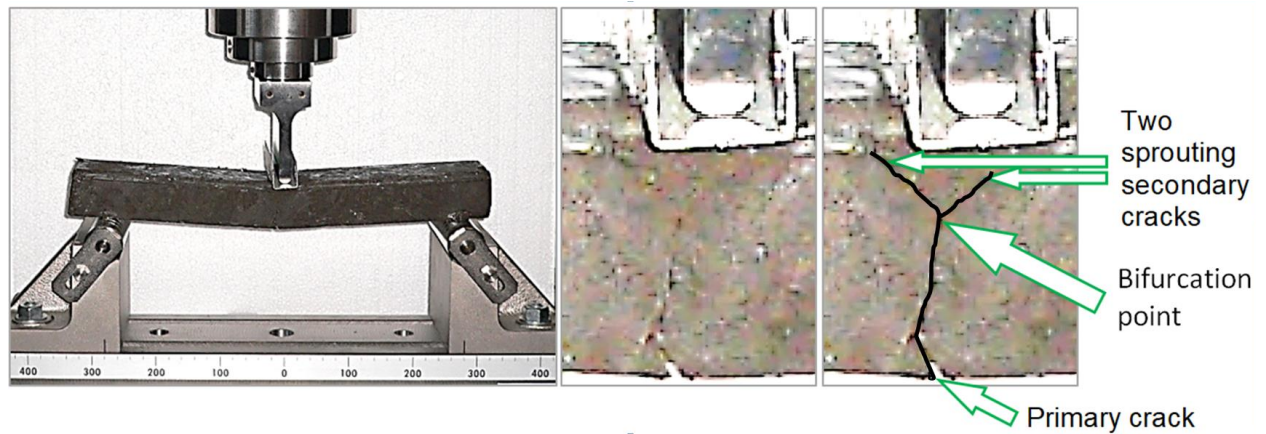


Figure 2. A beam and its central part with an evolving crack.

Samples preparation for testing was carried out by the analogy with [9].

However, there are some particular features. Samples were made from a mixture of sandy soil (with particle sizes not exceeding 2 mm) and gravel (with particle sizes from 2 to 10 mm). This mixture belongs to the first group of fortified sand and gravel mixtures according to Russian State Standard GOST 23735-2014. In the case under discussion, the sand-gravel mixture serves as the material of the upper layer of the dirt road. To predict the bearing capacity of such a road in winter, it is necessary to determine the strength of the above mixture when it freezes.

The particle size distribution of the mix was determined by the sieve method and is characterized by the presence of the soil particles remainder on sieves with openings with a diameter of 10, 7, 5, 3, 2 mm and on the pallet for particles of the size less than 2 mm, respectively, 10.0, 7.5, 5.2, 21.0, 30.1 and 26.2 % (by mass).

The particle size distribution for the sand-gravel mixture is shown in Figure 2.1.

Particle size distribution and the properties of the of soil mixture components affect their strength and stiffness [31]. However, we consider only one soil mixture, but with different water contents. The practical value of the humidity indicator is explained by the fact that freezing water significantly changes the strength of the soil. For example, the Figure (2.2) shows the curves “Displacement f – Force F ” for beams from Figure 2, consisting of the frozen soil mixture mentioned above (Figure 2.1), but different in the water content in the material of the beams.

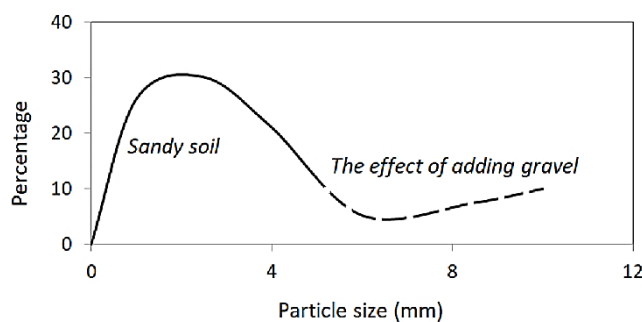


Figure 2.1. The particle size distribution for sand-gravel mixture.

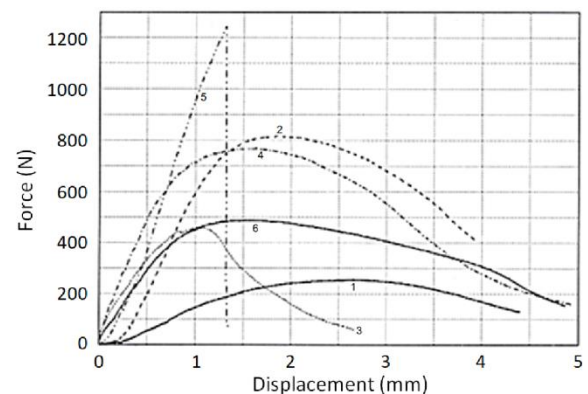


Figure 2.2. Curves «Force F – Displacement f » of the beams according to Figure 2 with different water content in the material of the beams/

Beam 5 (Figure 2.2) contained a large amount of water, which explains the analogy of the dependence “displacement f – force F ” for this beam with the data known on the dependence of the strength on the displacement for the beams consisting of ice [32]. Beam 5 is excluded from the further consideration, since the analysis of the strength of ice beams is beyond the scope of our work.

The water content in the material of each sample was measured using a SHIMADZU MOC-120H moisture analyzer at the temperature of 105 °C in the drying chamber of the analyzer. The decrease in moisture content in the sample during drying was automatically controlled with an accuracy of 0.01 % (by weight) every 30 seconds. The water content (relative humidity) in the material of beams 1, 2, 3, 4 and 6 was equal, respectively, to 7.88, 10.89, 8.75, 12.53 and 14.19 %.

At the moisture value indicated above, the tensile stresses of each of the beams in the section with a crack were calculated (Figures 1 and 2): $\sigma = M / W$, where $M = F_{\max} L / 4$, $W = BH_0^2 / 6$. The calculation results are shown in Figure 2.3. Thus, five series of beams were processed. To determine the number of samples in a series, you can use the method of analogies. Indeed, from a mechanical point of view, ice in frozen ground functions as a cement analogue in concrete [33, 34]. This means that frozen ground can be considered as an analogue of lightweight concrete, for example, cellular concrete. Therefore, to determine a sufficient number of samples for frozen soil testing the recommendations of Russian State Standard GOST 10180-2012 (paragraph 4.1.3 can be used). According to these recommendations the number of samples made from cellular concrete is taken to be 3 in each series. Additional assessments of the of the research results reliability were obtained using the determination coefficient R^2 (Figure 2.3), as well as the elements of the indirect measurements theory (Figures 4, 5).

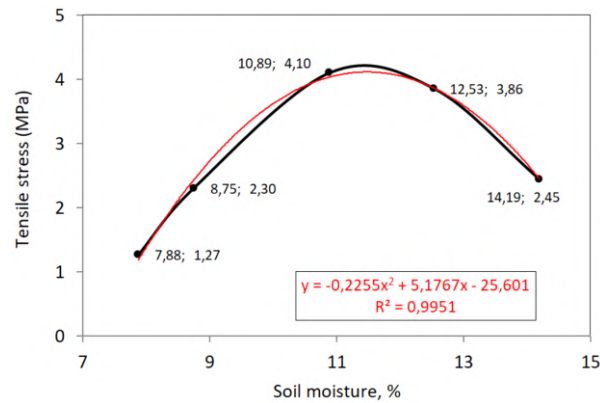


Figure 2.3. Tensile stresses in the beam according to Figure 2 for $F = F_{\max}$.

The data obtained show (Figure 2.3) that the dependence of tensile stresses on humidity in the range from 7.88 to 14.19 % can be described by a polynomial of the second degree with a determination coefficient of almost 1. This means that there is a functional dependence of stresses on the water content in soil. The reliability of the data presented in Figure 2.3 is also confirmed by their consistency to the results known from the scientific literature [33, p. 152–158].

Three-point bending tests were carried out on a SHIMADZU AGS-X testing machine, for which the relative measurement error is not more than 1.0 %. The download speed was chosen equal to 5 mm / min. The temperature of the material on the fracture surface of the samples (minus 4.6 °C) was measured in a non-contact manner using a pyrometer immediately after the test.

Tests have shown that in the process of fracture during three-point bending, a primary crack forms, the length and width of which increase with the load increasing and this is natural. In addition, the signs of bifurcation of the primary fracture and the formation of secondary fractures can be seen (Figure 2).

Note that the bifurcation of a crack during uniaxial compression of sandstone and other brittle materials was predicted in [8, p. 1016] using the logistic equation in a mathematical model of the evolution of the stress-strain state of a material.

In our case (Figures 1 and 2), it is important to pay attention to the fact that with the increasing crack length h , the effective cross-section height H decreases: $0 \leq h \leq H_0$; $H = H_0 - h$.

According to the test results, the diagram “load F – the vertical displacement of the point of force F ” application is obtained. The mathematical processing of the test results is discussed in the following section.

3. Results and Discussion

3.1. Mathematical Processing of the Test Results

Let B and H_0 be, respectively, the width and the height of the cross section of the beam, f is the vertical displacement of the point of force F application, h is the length of the crack (Figure 1). As noted above, with increasing crack length h , the effective cross-sectional height $H = H_0 - h$ decreases. Accordingly, if f changes by some Δf , then the change in effective height is ΔH . With small changes, the dependence of ΔH on Δf can be written as a linear relation with a constant proportionality coefficient K_1 :

$$\Delta H = \frac{\Delta f}{H_0} K_1 H. \quad (1)$$

Let us divide both sides of equality (1) by H_0 and move on to the dimensionless parameters θ and $\Delta\theta$:

$$\theta = \frac{H}{H_0}, \quad \Delta\theta = \frac{\Delta H}{H_0}. \quad (2)$$

The parameter θ can be considered as a geometric characteristic of the effective area. The values of θ vary from 0 to 1, with 0 corresponding to a completely damaged material, and 1 to a material without damage (without cracks).

Equality (1) with $\Delta\theta \rightarrow 0$ transforms to the form:

$$\frac{d\theta}{\theta} = \frac{df}{H_0} K_1. \quad (3)$$

Integrating both sides of the equality (3), we determine the integration constant from the condition: if $f = 0$, then $H = H_0$, i.e. $\theta = 1$. We get:

$$H = H_0 e^{\frac{f}{H_0} K_1}. \quad (4)$$

Using (4), we define I – the effective moment of inertia of the cross section with an evolving crack and W – the effective moment of resistance of the same section:

$$I = \frac{BH^3}{12}, \quad (5)$$

$$W = \frac{BH^2}{6}. \quad (6)$$

For the considered example (Figure 1), we get: $I = 2.719 \cdot 10^{-7} \exp(76.92fK_1)$, $W = 0.1394 \cdot 10^{-4} \exp(51.28fK_1)$.

The experiments showed that the ratio “load F – displacement f ” can be represented with sufficient accuracy in the form:

$$F = \frac{48EI f^3}{L^3}. \quad (7)$$

Taking into account equalities (4) and (5), we note that in relation (7) are f , I , F are the variables. In order to obtain explicitly the dependences $F(f)$ and $\sigma(f)$, where σ is the tensile stress in the cross section with a crack, it is necessary to determine the coefficient K_1 (1) indicated above and the elastic modulus E . We will find the values of K_1 and E using the test results. The dependence $F(f)$ obtained in the tests is nonlinear, $F_{extr} = 769$ N and $f_{extr_F} = 1.574$ mm (curve 4 in Figure 2.2). The test results are shown in Figure 3 with markers.

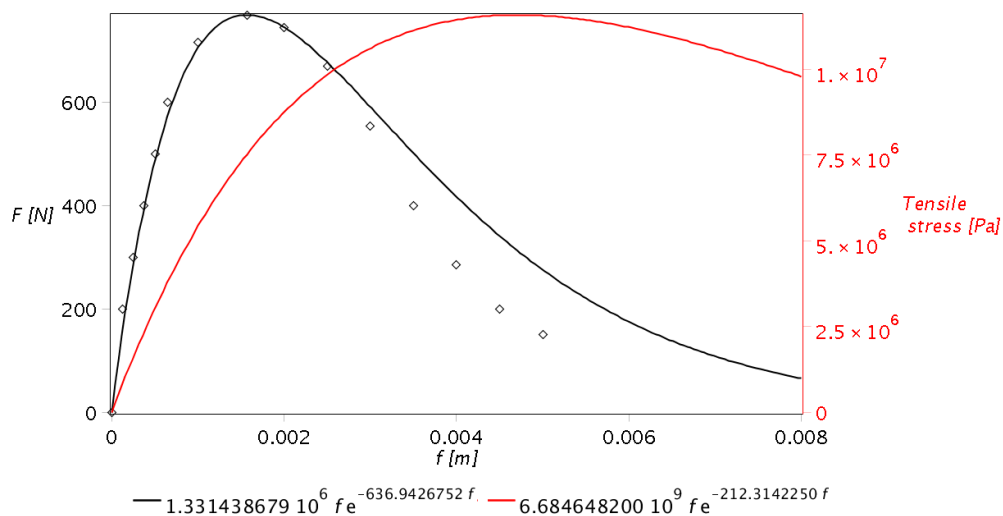


Figure 3. The results of tests (markers) and simulations (red and black lines).

Taking into account the relation (7) and the experimental value f_{extr} , we find coefficient K_1 (1) indicated above from the condition:

$$\frac{dF}{df} = 0. \quad (8)$$

For the example considered (Figure 1) after the transformations we get: $dF / df = E(0.5944 \cdot 10^{-3} + 0.4573 \cdot 10^{-1} f K_1) \exp(76.92 f K_1)$, $K_1 = -8.280$.

Then, again taking into account (7), and using the calculated coefficient K_1 and the experimental values f_{extr} and F_{extr} , we determine the elastic modulus E from the equation $F = F_{extr}$. For the example considered (Figure 1) we find $E = 2240$ MPa after the transformations. Note that this value was obtained at the above temperature (minus 4.6 °C) and is consistent with the data published. For example, in [1] it was shown that the elastic modulus of the upper part of the roadway in winter increases and can reach 10000 MPa.

Using the calculated values of K_1 , E and taking into account relation (7), after the transformations, we find the dependence $F(f)$ explicitly. For the example under consideration, the curve $F(f)$ is presented in Figure 3.

The information obtained is sufficient to determine the maximum tensile stresses σ in the section with a crack. Using the bending moment $M = FL/4$ and the effective moment of resistance (6), we write:

$$\sigma = \frac{FL}{4W}. \quad (9)$$

After the transformations and taking into account (6), (7), (4) and (1), we obtain the dependence $\sigma(f)$ in an explicit form. For the example considered, the curve $\sigma(f)$ is shown in Figure 3. In the example considered, $\sigma_{extr} = 11.58$ MPa, the corresponding displacement is $f_{extr_\sigma} = 4.71$ mm.

Thus, the technique of mathematical processing of the tests results for three-point bending is developed. However, all initial data and calculation results were assumed to be deterministic. In the next section, we will discuss the influence of random deviations of the input data on the simulation results.

3.2. The Random Factors Influence on the Simulation Results

Comparison of the experimental results (markers in Figure 3) and the analytical description of the load – displacement dependence (solid line in the same figure) show that the simulation results do not contradict the experimental data.

Nevertheless, there are many factors (distance between supports, transverse dimensions of the sample, temperature, ice and mineral particles in the soil, particle size distribution, etc.), the quantitative characteristics of which include small random deviations from average values. For engineering practice, it is important to analyze the effect of random deviations on simulation results.

In the case under consideration, the analysis of the influence of random factors is simplified due to the fact that we have obtained analytical expressions of the force F and stress σ in the form of functions f (Figure 3). Assuming that the deflection f is determined with a relative error of not more than 5 %, we use the well-known method for estimating the accuracy of indirect measurements [18], according to which the error in determining the force F is calculated by the formula:

$$\Delta F = \pm \left| \frac{dF}{df} \right| 0.05 f. \quad (10)$$

The derivative dF/df is also used in equation (8).

Taking into account (10), we can calculate the relative error $\varepsilon_F = |\Delta F/f|$.

For illustration, the calculation results of ΔF and ε_F are presented in graphical form in Figure 4, 5, respectively. The markers in Figure 4 show the results of the experiment on Figure 3.

Intensive destruction of the sample (Figure 2) was observed at $f \approx 0.0031 \pm 0.00016$ m = 3.1 ± 0.16 mm. It should be noted that at $f > 0.0031$ m, the difference between the experiment and the simulation increases (Figure 4). This feature indicates the presence of factors that are not taken into account in the simulation. However, it is important for engineering practice to prevent fracture. Hence, in the range $0 \leq f \leq 3.1$ mm, the state of the material is of most interest for practice. It is at this interval that the agreement between the experiment and the simulation is quite high (Figure 5).

So, if $f > 3.1 \pm 0.16$ mm, then the experiment can be terminated. However, we are publishing a full load displacement diagram for possible use in further research.

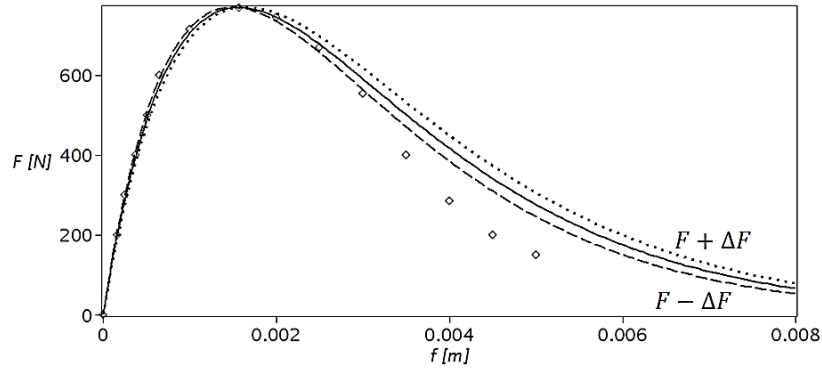


Figure 4. To the analysis of the random factors influence.

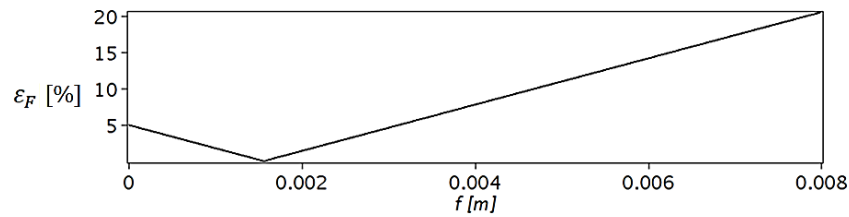


Figure 5. Relative error variation ε_F depending on deflection f .

Similarly, assuming that the deflection f is determined with a relative error of no more than 5 %, we analyze the accuracy of the tensile stress σ calculating. In this case, the error is calculated by the formula

$$\Delta\sigma = \pm \left| \frac{d\sigma}{df} \right| 0.05f. \quad (11)$$

Taking into account (11), we can calculate the relative error $\varepsilon_\sigma = |\Delta\sigma / \sigma|$.

The calculation results of $\Delta\sigma$ and ε_σ are presented in graphical form in Figures 6 and 7, respectively.

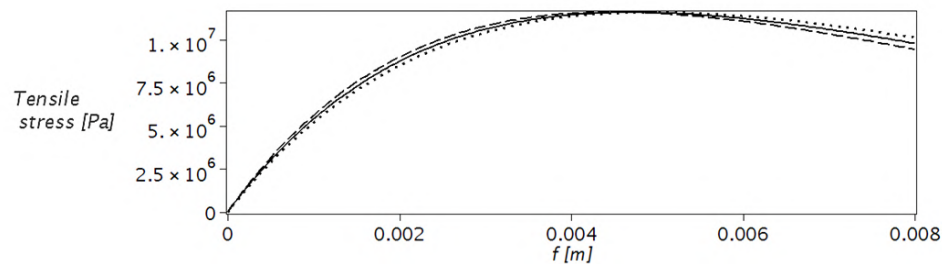


Figure 6. To the analysis of the random factors influence.

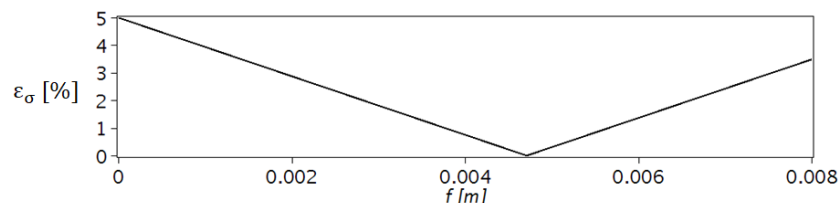


Figure 7. Relative error variation ε_σ depending on deflection f .

We conclude that the influence of random factors on the tensile stress σ in the section with a crack is small (Figure 6) and does not exceed 5 % (Figure 7).

In the example above $F_{extr} = 769$ N, $f_{extr_F} = 1.574$ mm; tensile stress in the section with a crack is 7.52 MPa, if $F = F_{extr}$; $\sigma_{extr} = 11.58$ MPa, $f_{extr_σ} = 4.71$ mm, $F_{extr_σ} = 312$ N.

Using relation (4), we calculate H and the crack length $h = H_0 - H$ (Figure 1) if $f = f_{extr_\sigma}$. We get: $H_{extr_\sigma} \approx 14$ mm, $h_{extr_\sigma} \approx 25$ mm. Then $h_{extr_\sigma}/H_{extr_\sigma} = 25 / 14 \approx 1.8$. Using Figure 2, you can determine the conditional distances from the bifurcation point to the lower edge of the beam, as well as from the bifurcation point to the upper edge of the beam. The ratio of these distances is approximately equal to 2.0. If we take into account that the calculated ratio is approximately equal to the ratio found in the experiment ($1.8 \approx 2$), then we can assume that the bifurcation of the crack is realized if $\sigma \approx \sigma_{extr}$. At the same time, some deviations are explained by the influence of material heterogeneity, small differences in the shape of the real sample from the ideal shape, and other random factors.

In the following section, we will consider the interpretation and comparison of the results of the methodology applied with the results got by other authors.

3.3. Comparison of the Obtained Results with the Results of Other Authors

The model developed is based on the experimental data and relations (1)–(9), describing the full history of the force acting on the beam, and can be assigned to the class of constitutive models that have appeared relatively recently, but are increasingly used in research and prediction of the mechanical condition of frozen soils [14, 17].

The technique developed does not require a large amount of input data and is characterized by the low cost of numerical implementation. From the point of view of practice, it is important to note that for the numerical implementation of the model developed, two test results (F_{extr} and f_{extr_F}) for three-point bending are necessary (Figure 2). In addition, a physically based hypothesis on the dependence of ΔH on Δf is needed. In the case considered, such a hypothesis is presented in the form of equality (1). However, this is not the only option. For example, in [8], a damage variable was used, which varies from 0 to 1, with 0 corresponding to the undamaged (intact) and 1 – completely damaged states of the material under uniaxial compression.

In our case, the geometric characteristics of the effective area (1) were introduced; the form of the equations of the sample state also differs from the relations known from the scientific literature. As a result, a methodology was developed for modeling the state of fairly wide class materials, of state which was confirmed by the practice of applying the technique. For example, using the results of tests for three-point bending of specimen B11 with a notch according to [7, p. 26], as the initial data we will perform their processing according to the methodology discussed above. We will obtain the data presented in Figure 8 by solid lines. Experimental data known from the work [7, p. 26] are shown in Figure 8 by markers.

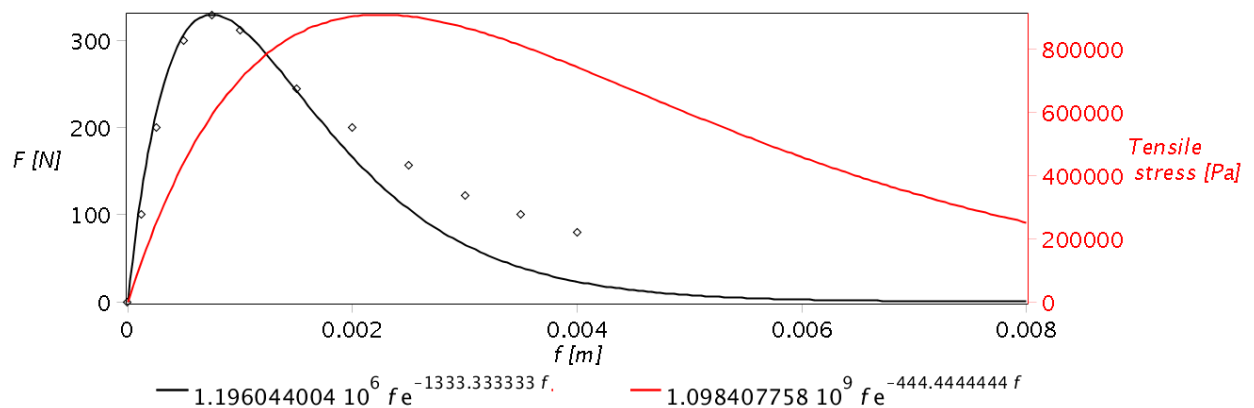


Figure 8. Test results by [7, p. 26] (markers) and our simulations (lines).

For large movements, the predicted values of the load F according to Figure 4 (a beam without a notch) are less than real, and according to Figure 8 (a beam with a notch by [7]) are more. This difference can be explained by the effect of the notch. It is important to note that in the cases considered there are two general patterns, namely: the consistency of the experimental data with the results of mathematical modeling; the increase of random factors influence of the deflection increases after passing the points of extrema (Figures 4 and 8). Thus, the adequacy of the developed model (1-9) is confirmed by the results of the processing the test results, both copyright (Figures 4 and 6), and well-known from the scientific literature (Figure 8).

The influence increase of random factors with an increase in the deflection after passing through the points of extrema (Figures. 4 and 8) can be explained by a decrease in the effective cross-sectional area of the beam due to the cracks evolution. Indeed, crack growth (Figure 2) is accompanied by local fracture and a decrease in the number of frozen soil particles that transmit internal forces from one part of the beam to another.

Formally, according to the statistics, this means a decrease in sample size and, as a consequence, an increase in measurement error. Experimental confirmation can be found in article [19], the authors of which

have tested frozen, thawed and thawing loams using the method of ball stamps of various diameters (0.022; 0.1; 0.3 and 1.0 m). Tests were conducted with controlled precipitation. The rheological properties of the soil have also been taken into account [20].

It was found that the larger the diameter of the stamp is, the higher is the accuracy of the measurements. Obviously, the larger the contact area of the stamp with the soil is, the greater is the number of soil particles in the contact area. Formally, according to statistics, this is equivalent to the sample size increase and the random factors influence on the test results decrease.

In our case, tests at three points bending were carried out with the controlled movement of the loading device (Figure 1). As it was noted above with an increase in the deflection cracks evolve. And it leads to the decrease in the contact amount and, accordingly, and to the increase in the experimental error. This is due to an increase in the random factors influence with an increase in the deflection after passing through the points of extrema (Figures 4 and 8).

The analysis of the results of applying the methodology developed (Figure 3) shows sufficient adequacy of the model in the ascending and in a section of the descending branch of the diagram "load F – displacement f ". With increasing displacement f , the mismatch increases, but is not critical. The search for the causes of this discrepancy may constitute the subject of further experimental and theoretical studies on the topic of the work.

The model developed is nonlinear, and nonlinearity is explained by the evolution of the crack and, accordingly, the change in the effective geometric characteristics (4), (5), (6) of the cross section with the crack. The data obtained are sufficient to conclude that in the full diagram (Figure 3), the deflection f_{extr_F} corresponding to the extremum of the force F_{extr} is less than the deflection $f_{extr_σ}$, which corresponds to the extremum of the tensile stress $σ_{extr}$. From the physical point of view, this means that the destruction of the material occurs on the descending branch of the diagram $F(f)$, i.e. when the force is $F < F_{extr}$, but $σ = σ_{extr}$. Generally speaking, destruction can occur with $σ ≤ σ_{extr}$ and the corresponding displacement $f ≤ f_{extr_σ}$.

As an additional argument confirming the adequacy of the model developed, we refer to the aforementioned work [8], which theoretically substantiates the appearance of a bifurcation of a crack during uniaxial compression of sandstone and other brittle materials.

Limitations on the scope of the model are determined by the properties of soils. From a formal point of view, a necessary condition for applying the model developed is the existence of an extremum on the curve $F(f)$. The class of such materials and the corresponding diagrams obtained in bending tests was studied in [7].

Estimating the results of the work from a practical point of view, it should be noted that using a small amount of initial data, the developed technique allows us to obtain estimates of the elastic modulus of frozen soil and the highest tensile stresses in the section with a crack. The need to obtain such estimates is repeatedly stated in the literature [20, 21]. The analysis showed that the most pressing issues relate to the improving the technology of building roads [1, 3, 4, 23], including logging roads [24], to sufficient (but not excessive) protection of engineering structures from freezing, to designing and forecasting the state of foundations in permafrost regions [25, 26] taking into account temperature deformations [2, 27–29].

Prospects for the development of the present work topic relate to the refinement of the geometric characteristics of the effective area (2) for adapting the approach used in the engineering analysis of soils under the influence of "freeze – thaw" cycles and time factor [1, 30].

4. Conclusions

1. A nonlinear model has been developed for the complete process of deformation of a frozen soil beam with an evolving crack at three-point bending. Nonlinearity is explained by the evolution of the crack and, accordingly, the change in the effective geometric characteristics of a cross section with a crack. For the numerical implementation of the model, it is sufficient to use two parameters: the extremum of the force in the tests for three-point bending before fracture and the value of the vertical displacement of the force application point corresponding to the extremum.

2. The model developed was used for mathematical processing of the of tests results for three-point bending. It was found that the magnitude of the deflection corresponding to the extremum of the force is less than the deflection, which corresponds to the extremum of the tensile stress in the section with a crack. Thus, it is substantiated that the destruction of the material occurs in the descending branch of the «load – displacement» diagram.

3. Using the model proposed a methodology for determining the elastic modulus and the highest tensile stresses has been developed. Analytical dependences of the tensile stress force and extremum in a section with an evolving crack on the deflection value have been obtained. The developed model enables calculating the length of an evolving crack in the entire process of deformation of a beam from frozen soil.

4. The adequacy of the model developed and the reliability of the results of its application are confirmed by consistency with the results of three-point bending on the SHIMADZU AGS-X machine, which provides measurement of force and displacement with a relative error of no more than 1.0 %. The simulation results obtained are also consistent with the experimental and theoretical data known in the literature.

5. Restrictions on the scope of the method are determined by the properties of soils. From a formal point of view, a necessary condition for applying the model is the existence of an extremum on the «load – displacement» curve. Prospects for the study relate to the adaptation of the approach used to the analysis of the mechanical condition of soils under the influence of «freezing – thawing» cycles and time factor.

5. Acknowledgments

The authors are grateful to the editors and anonymous reviewers for careful reading the article and their comments.

References

1. Teltayev, B.B., Liu, J., Suppes, E.A. Distribution of temperature, moisture, stress and strain in the highway. *Magazine of Civil Engineering*. 2018. 83(7). Pp. 102–113. DOI: 10.18720/MCE.83.10.
2. Merzlyakov, V.P. Physical and mechanical conditions for primary frost crack formation. *Soil Mechanics and Foundation Engineering*. 2016. 53(4). Pp. 221–225. DOI: 10.1007/s11204-016-9389-1.
3. Rys, D., Judycki, J., Pszczola, M., Jaczewski, M., Mejlun, L. Comparison of low-temperature cracks intensity on pavements with high modulus asphalt concrete and conventional asphalt concrete bases. *Construction and Building Materials*. 2017. 147. Pp. 478–487. DOI: 10.1016/j.conbuildmat.2017.04.179.
4. Uglova, E.V., Tiraturyan, A.N., Lyapin, A.A. Integrated approach to studying characteristics of dynamic deformation on flexible pavement surface using nondestructive testing. *PNRPU Mechanics Bulletin*. 2016. 2. Pp. 111–130. DOI: 10.15593/perm.mech/2016.2.08.
5. Duvillard, P.A., Raveland, L., Marcer, M., Schoeneich, P. Recent evolution of damage to infrastructure on permafrost in the French Alps. *Regional Environmental Change*. 2019. 19. Pp. 1281–1293. DOI: 10.1007/s10113-019-01465-z.
6. Chao, G., Lu, Z. Frost heaving of foundation pit for seasonal permafrost areas. *Magazine of Civil Engineering*. 2019. 86(2). Pp. 61–71. DOI: 10.18720/MCE.86.6.
7. Yamamoto, Y., Springman, S.M. Three- and four-point bending tests on artificial frozen soil samples at temperatures close to 0 °C. *Cold Regions Science and Technology*. 2017. 134. Pp. 20–32. DOI: 10.1016/j.coldregions.2016.11.003.
8. Liu, D., He, M., Cai, M. A damage model for modeling the complete stress–strain relations of brittle rocks under uniaxial compression. *International Journal of Damage Mechanics*. 2018. 27(7). Pp. 1000–1019. DOI: 10.1177/1056789517720804.
9. Aksenov, V.I., Gevorkyan, S.G., Doroshin, V.V. Dependence of Strength and Physical Properties of Frozen Sands on Moisture Content. *Soil Mechanics and Foundation Engineering*. 2018. 54(6). Pp. 420–424.
10. Li, S., Wang, J. The stress intensity factors of multiple inclined cracks in a composite laminate subjected to in-plane loading. *Physical Mesomechanics*. 2019. 22. Pp. 35–48. DOI: 10.24411/1683-805X-2019-12003.
11. Nixon, W.A., Weber, L.J. Flexural strength of sand-reinforced ice. *Journal of Cold Regions Engineering*. 1991. 5(1). Pp. 14–27. DOI: 10.1061/(ASCE)0887-381X(1991)5:1(14).
12. Zhang, D., Liu, E., Liu, X., Zhang, G., Yin, X., Song, B. Investigation on the Nonlinear Strength Properties and Damage Statistical Constitutive Model for Frozen Sandy Soils. *Advances in Materials Science and Engineering*. 2018. Article ID 4620101. Pp. 1–15. DOI: 10.1155/2018/4620101.
13. Wang, P., Liu, E.L., Song, B.T., Liu, X.Y., Zhang, G., Zhang, D. Binary medium creep constitutive model for frozen soils based on homogenization theory. *Cold Regions Science and Technology*. 2019. 162. Pp. 35–42. DOI: 10.1016/j.coldregions.2019.03.019.
14. Liu, X., Liu, E., Yu, Q. A new double hardening constitutive model for frozen mixed soils. *European Journal of Environmental and Civil Engineering*. 2019. Pp. 1–21. DOI: 10.1080/19648189.2019.1610072.
15. Energy Consumption Analysis of Frozen Sandy Soil and an Improved Double Yield Surface Elastoplastic Model considering the Particle Breakage. *Advances in Civil Engineering*. 2019. Article ID 9716748. Pp. 1–13. DOI: 10.1155/2019/9716748.
16. Huang, X., Li, D., Ming, F., Fang, J. An experimental study on the relationship between acoustic parameters and mechanical properties of frozen silty clay. *Sciences in Cold and Arid Regions*. 2013. 5(5). Pp. 596–602.
17. Lai, Y., Liao, M., Hu, K. A constitutive model of frozen saline sandy soil based on energy dissipation theory. *International Journal of Plasticity*. 2016. 78. Pp. 84–113. DOI: 10.1016/j.ijplas.2015.10.008.
18. Szpika, K., Laspas, T., Archenti, A. Measurement and analysis of machine tool errors under quasi-static and loaded conditions. 2018. *Precision Engineering*. 51. Pp. 59-67. DOI: 10.1016/j.precisioneng.2017.07.011.
19. Korolev M.V., Kutsevich O.I. Development of a method for determining the mechanical characteristics of soils with a ball stamp. In the collection: Ensuring the quality of construction in Moscow on the basis of modern achievements of science and technology. Proceedings of the First Joint Scientific-Practical Conference of GBU «CEIIS» and IPRIM RAS. 2019. Pp. 166-175. [Razvitiye sposoba opredeleniya mekhanicheskikh kharakteristik gruntov sharovym shtampom. V sbornike: obespecheniye kachestva stroitelstva v g. Moskve na osnove sovremennykh dostizheniy nauki i tekhniki. Sbornik trudov Pervoy sovместnoy nauchno-prakticheskoy konferentsii GBU «TsEiIS» i IPRIM RAN]. 2019. Pp. 166-175. (rus)
20. Korolev M. V., Vlasov A. N., Kutsevich O. I., Korolev P. M. Multifunctional mobile complex for Express determination of soil mechanical properties. In the collection: Ensuring the quality of construction in Moscow on the basis of modern achievements of science and technology. Proceedings of the First Joint Scientific-Practical Conference of GBU «CEIIS» and IPRIM RAS. 2019. Pp. 46-63. [Razvitiye sposoba opredeleniya mekhanicheskikh kharakteristik gruntov sharovym shtampom. V sbornike: obespecheniye kachestva stroitelstva v g. Moskve na osnove sovremennykh dostizheniy nauki i tekhniki. Sbornik trudov Pervoy sovместnoy nauchno-prakticheskoy konferentsii GBU «TsEiIS» i IPRIM RAN]. 2019. Pp. 46-63. (rus)
21. Ming, F., Li, D., Zhang, M., Zhang, Y. A novel method for estimating the elastic modulus of frozen soil. *Cold Regions Science and Technology*. 2017. 141. Pp. 1–7. DOI: 10.1016/j.coldregions.2017.05.005.
22. Azmatch, T.F., Segoo, D.C., Arenson, L.U., Biggar, K.W. Tensile strength and stress–strain behavior of Devon silt under frozen fringe conditions. *Cold Regions Science and Technology*. 2011. 68. Pp. 85–90. DOI: 10.1016/j.coldregions.2011.05.002.

23. Kolesnikov, G.N., Gavrilov, T.A. Simulation of the conditions for a low-temperature crack appearance in the asphalt concrete layer of a road. Tomsk State University Journal of Mathematics and Mechanics. 2018. 56. Pp. 57–66. DOI: 10.17223/19988621/56/5. (rus)
24. Gavrilov, T., Khoroshilov, K., Kolesnikov, G. Seasonal freezing of a logging dirt road: modeling of conditions of transverse cracks emergence. Resources and Technology. 2018. 15(3). Pp. 29–42. (rus)
25. Vvedenskij, V.R., Gendler, S.G., Titova, T.S. Environmental impact of the tunnel construction. Magazine of Civil Engineering. 2018. 79(3). Pp. 140–149. DOI: 10.18720/MCE.79.15.
26. Ivanov, K.S. Granulated foam-glass ceramics for ground protection against freezing. Magazine of Civil Engineering. 2018. 79 (3). Pp. 95–102. DOI: 10.18720/MCE.79.10.
27. Wang, W., Qi, J., Yu, F., Liu, F. A novel modeling of settlement of foundations in permafrost regions. Geomechanics and Engineering. 2016. 10(2). Pp. 225–245. DOI: 10.12989/gae.2016.10.2.225.
28. Volokhov, S.S., Nikitin, I.N., Lavrov, D.S. Temperature deformations of frozen soils caused by rapid changes in temperature. Moscow University Geology Bulletin. 2017. 72(3). Pp. 224–229. DOI: 10.3103/S0145875217030103.
29. Kirukhin, G.N. Temperature modes of asphalt concrete pavement of roads. Roads and Bridges. 2013. 2(30). Pp. 309–328. (rus)
30. Dai, S., Santamarina, J.C. Stiffness Evolution in Frozen Sands Subjected to Stress Changes. Journal of Geotechnical and Geoenvironmental Engineering. 2017. 143(9). – Pp. 04017042.
31. Fredlund, M.D., Wilson, G.W., Fredlund, D.G. Use of the grain-size distribution for estimation of the soil-water characteristic curve. Canadian Geotechnical Journal. 2002. 39(5). – Pp. 1103-1117.
32. Ehlers, S., Kujala, P. Optimization-based material parameter identification for the numerical simulation of sea ice in four-point bending. Proceedings of the Institution of Mechanical Engineers, Part M: Journal of Engineering for the Maritime Environment. 2014. 228(1). – Pp. 70-80.
33. Tsyтович, N.A. Mekhanika merzlyh gruntov [Frozen soil mechanics]. Moscow, 1973.– 448 p. (rus)
34. Yang, Y., Gao, F., Cheng, H., Lai, Y., Zhang, X. Researches on the constitutive models of artificial frozen silt in underground engineering. Advances in Materials Science and Engineering. 2014. Article ID 902164.– Pp. 1-8. DOI: 10.1155/2014/902164.

Contacts

Timmo Gavrilov, gtimmo@mail.ru

Gennady Kolesnikov, kolesnikovgn@yandex.ru



DOI: 10.18720/MCE.94.6

Intake rate through openings in the side wall of the duct

D.V. Maklakov^a, V.N. Posohin^b, R.G. Safiullin^b, J.R. Kareeva^{*b}

^a Kazan (Volga region) Federal University, Kazan, Russia

^b Kazan State University of Architecture and Engineering, Kazan, Russia

* E-mail: jkareeva2503@gmail.com

Keywords: intake ducts, openings in the side wall, intake rate, ideal fluid, conformal mappings, numerical calculation

Abstract. Subject. In technological and general ventilation ducts with a given uniformity of intake is often needed to be designed. The calculation of pressure losses in such ducts is complicated by the lack of reliable information about the characteristics of the flows at the inlet to the intake openings and slots. Intensity of air intake through slot openings located on one and two opposite walls of the duct in a series of sequentially placed slots, which determines the presence of a transit air stream passing by the hole is calculated. The slots are perpendicular to the generatrix panel and can be opposite or offset relative to each other. The presence of a stagnant zone formed when the flow is cut off from a sharp edge at the inlet is taken into account. Methods. The search for a solution is carried out in the framework of ideal fluid jets theory using the Kirchhoff scheme and Chaplygin method of singularities, as well as by the numerical method using Flow3d software package, where the system of equations of plane turbulent motion was ended with “standard” k-e model. Results. The flow rates of the air entering through the slots were found, depending on their width and value of the transit flow. Dependencies for the attached flow with and without flow separation are obtained. The shape of the free streamline separating the jet and vortex zones, the compression coefficients of the jet are determined. Current flow lines are constructed for different values of the geometric parameters of the duct and the hole. Conclusion. Analytical and numerical calculations showed that the kinematics of currents and values of the attached flow rate are very similar, but the size and shape of the stagnant zone are significantly different. A numerical solution gives more physics of stagnant zone formation. It was found that flow separation reduces the associated flow rate. It was also found that the intensity of absorption is minimal with the opposite order of cracks.

1. Introduction

The intake of air through slots or a series of local openings of various shapes (round, square, slotted) in the side wall when exposed to intense transit flow is a typical task for many technical devices. For example, it is used when calculating cooling of the turbine blades surface [1], during the operation of ejectors [2, 3]. In technological applications of ventilation, there is often a need to design ducts with a given uniformity (nonuniformity) of intake along the length. Failure to comply with the specified intake conditions can lead to ineffective local intake from sources of harmful emissions, a violation of regulations for the operation of technological equipment, etc. [3–10]. Uniform intake ducts (USD) are also used in public buildings to remove air from the upper zone by general ventilation.

Depending on the current task, uniform intake along the entire length can be achieved by selecting the optimal hole sizes and distances between them. With sufficient length, such air ducts are more technologically advanced and economical in comparison with air ducts having variable parameters. The main characteristic of the energy-efficient choice of geometry and location of the openings in the USD is the local resistance coefficient (LRC) of its main perturbing elements. The analytical determination of USD flow parameters, which are important for calculating the LRC (associated flow rate, intake rate, stream compression ratio, flow stream lines, shape and size of stagnant zones), is very difficult, because when entering through openings and slots, air loses energy in the opening itself, and when passing through the duct near such a hole. Therefore, the LRC values are determined, as a rule, experimentally. A large amount of LRC data is contained in the well-known Reference book on hydraulic resistance by I.E. Idelchik [11], which has already been published in four editions in 1960, 1975, 1992 and 2005. But this fundamental work is far from exhausting the whole variety of

Maklakov, D.V., Posohin, V.N., Safiullin, R.G., Kareeva, J.R. Intake rate through openings in the side wall of the duct. Magazine of Civil Engineering. 2020. 94(2). Pp. 65–80. DOI: 10.18720/MCE.94.6



This work is licensed under a CC BY-NC 4.0

constructive situations encountered in practice. In these handbooks there is no data on separation zones, compression ratios of flow at the entrance and passage through the side openings of the air-blast.

Significant simplifications introduced in the USD analysis in the well-known works on this topic [13] do not make it possible to consider this problem as a solved one, and theoretical and experimental studies of transit ducts with constant parameters of channel and slot or channel and side openings are relevant. Therefore, now there still appear works devoted to the study of USD currents, for example. In these works, the authors use numerical experiment using computational fluid dynamics methods. Modern software systems, such as Fluent [13], Flow3d [14], which implement computational fluid dynamics methods, allow one to study such flows quite accurately and in detail. However, the accuracy and adequacy of results obtained by such methods should be monitored by comparison with already known and reliable methods.

The paper considers methods for calculating flows during intake through a series of slit-like openings, which can be located on one or two opposite walls of the duct. The purpose of the calculation is to determine the intensity of absorption through the holes for different geometric situations, as well as the flow parameters necessary to calculate the CLR of the flow in the turbine fouling (connected flow rate, absorption rate, stream compression ratio, flow stream lines, shape and size of stagnant zones). The analysis is carried out within the framework of the ideal fluid flow model and numerically taking into account viscosity C using Flow3d software package.

2. Methods

2.1. Hole on one side of the intake duct wall

A flow diagram is given in Figure 1a where l – long CA slot in the wall of the intake duct with height h (Figure 1a). Transit airflow from overlying openings moves with velocity v_∞ , accordingly, specific transit flow is $q_0 = v_\infty h$. It is necessary to determine the intensity of air intake Δq_0 through the gap (adjoined flow rate) and construct the currents flow lines.

2.1.1. Ideal fluid, unseparated flow

First, we consider the unseparated flow model (Figure 1, a), which does not take into account the fact of formation of a weakly-vortex (stagnant) zone when stream flows around a sharp edge A. We will find the solution using the conformal mapping method [15, 16].

As a parametric region, we take the upper half-plane $t = \xi + i\eta$ with the location of points indicated in Figure 1, a, b. The flow region in the plane of complex potential $w = \phi + i\psi$ is shown in Figure 1, c.

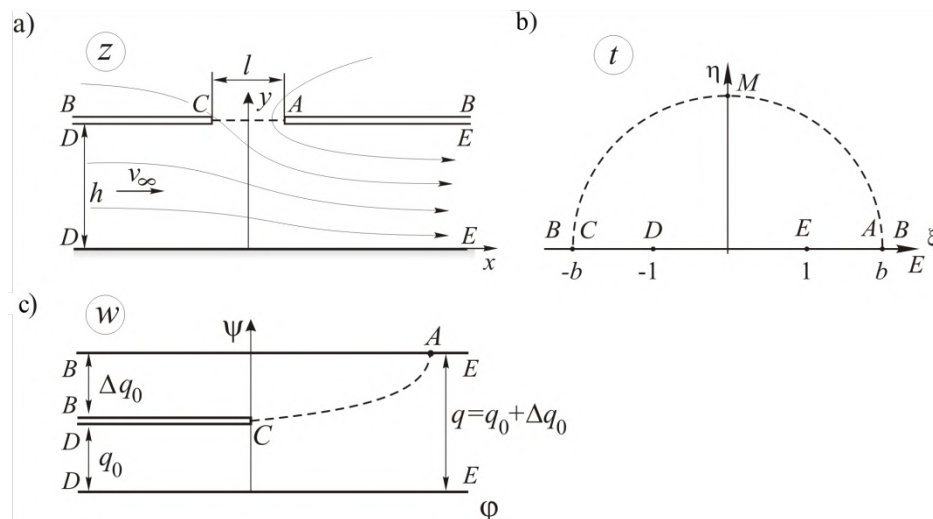


Figure 1. Flow areas for unseparated flow model: a is physical plane $z = x + iy$; b is parametric plane $t = \xi + i\eta$; c is plane of complex potential $w = \phi + i\psi$

The matching between the flow areas in the z and t planes is established using the Christoffel-Schwartz formula [15]

$$\frac{dz}{dt} = c \frac{t^2 - b^2}{t^2 - 1},$$

where c and b are the mapping parameters.

After integration the following expression is obtained:

$$z = c \left[t + \frac{1-b^2}{2} \ln \frac{t-1}{t+1} - \frac{1-b^2}{2} \pi i \right]. \quad (1)$$

At the point D ($t = -1$), the function dz/dt has a first order pole. By determining the residue of function at this point, we obtain

$$h = c\pi \frac{b^2 - 1}{2}, \quad (2)$$

and find the final form of the mapping formula

$$z = \frac{h}{\pi} \left[\frac{2t}{b^2 - 1} + \ln \frac{t+1}{t-1} \right] + iH. \quad (3)$$

At points A and C we have

$$z_A = z(b) = c \left(b + \frac{1-b^2}{2} \ln \frac{b-1}{b+1} - \frac{1-b^2}{2} \pi i \right);$$

$$z_C = z(-b) = c \left(-b + \frac{1-b^2}{2} \ln \frac{b+1}{b-1} - \frac{1-b^2}{2} \pi i \right).$$

Consequently,

$$z_A - z_C = l = 2c \left(b + \frac{b^2 - 1}{2} \ln \frac{b+1}{b-1} \right)$$

and further

$$c = \frac{l}{2} \left(b + \frac{b^2 - 1}{2} \ln \frac{b+1}{b-1} \right)^{-1}. \quad (4)$$

From equations (2), (4) we obtain the formula for determining the parameter $b > 1$

$$\frac{l}{h} = \frac{2}{\pi} \left(\frac{2b}{b^2 - 1} + \ln \frac{b+1}{b-1} \right). \quad (5)$$

Further we find the equation of the AC line in the parametric plane $t = \xi + i\eta$. It is a consequence of the expression

$$\operatorname{Im} \left[\frac{2t}{b^2 - 1} + \ln \frac{t+1}{t-1} \right] = 0.$$

Having completed the necessary transformations, we obtain

$$\xi = \pm \sqrt{2\eta \operatorname{ctg} \frac{2\eta}{b^2 - 1} + 1 - \eta^2}, \quad 0 \leq \eta < \eta_M, \quad (6)$$

where $\eta_M > 0$ is determined from the equation $2\eta_M \operatorname{ctg} \frac{2\eta_M}{b^2 - 1} + 1 - \eta_M^2 = 0$.

Note that for large values of b , from formula (6) it follows that the line BE in the parametric plane is determined by equation (at $b \rightarrow \infty$) $\xi = \pm \sqrt{b^2 - \eta^2}$, that is, this line is almost a circle of radius b .

On the segment AC

$$\bar{y} = \frac{y}{h} = 1, \quad \bar{x} = \frac{x}{h} = \pm \frac{1}{\pi} \left[\frac{2\xi}{b^2 - 1} + \ln \frac{\sqrt{(\xi^2 + \eta^2 - 1)^2 + 4\eta^2}}{(\xi - 1)^2 + \eta^2} \right], \quad |\xi| > b, \quad 0 \leq \eta < \eta_M. \quad (7)$$

In the plane t , we have sources at points D ($t = -1$); B ($t = \infty$) and drain at E ($t = 1$). The complex potential of such a flow will be

$$w = \frac{q_0}{\pi} \ln(t+1) - \frac{q_0 + \Delta q_0}{\pi} \ln(t-1) = \frac{q_0}{\pi} \left[\ln(t+1) - (1 + C_q) \ln(t-1) \right], \quad (8)$$

where $C_q = \Delta q_0 / q_0$ is the dimensionless adjoined flow.

The complex adjoined velocity is

$$v_x - iv_y = \frac{dw}{dt} \cdot \frac{dt}{dz} = \frac{q_0}{\pi} \cdot \frac{(t-1) - (1+C_q)(t+1)}{t^2 - b^2}. \quad (9)$$

By defining residues of function dw/dt at points D and B , we find the dimensionless adjoined flow

$$C_q = \frac{2}{b-1}. \quad (10)$$

By separating the real and imaginary parts of equalities (8), (9), we find the equations for the flow function

$$\psi = \frac{q_0}{\pi} \left[\operatorname{arcCos} \frac{\xi+1}{\sqrt{(\xi+1)^2 + \eta^2}} - (1+C_q) \operatorname{arcCos} \frac{\xi-1}{\sqrt{(\xi-1)^2 + \eta^2}} \right], \quad (11)$$

and for the flow velocity components:

$$v_x = \frac{q_0}{\pi c} \cdot \frac{\left[\xi - 1 - (1+C_q)(\xi+1) \right] \cdot (\xi^2 - \eta^2 - b^2) + 2\xi\eta^2 C_q}{(\xi^2 - \eta^2 - b^2)^2 + 4\xi^2\eta^2}, \quad (12)$$

$$v_y = \frac{q_0}{\pi c} \cdot \frac{2\xi\eta \left[1 - \xi + (1+C_q)(1+\xi) \right] - C_q\eta(\xi^2 - \eta^2 - b^2)}{(\xi^2 - \eta^2 - b^2)^2 + 4\xi^2\eta^2}, \quad (13)$$

where $\xi \geq 0$, $\eta \geq 0$.

We let us consider the problem of an ideal fluid flow, taking into account the separated flow (the diagram is shown in Figure 2 a). At point A , the flow breaks away from the wall, forming a stagnant (weakly vortex) zone. The velocity at the free AE boundary is v_0 . At point C , the leakage rate is finite. As before, it is necessary to determine the adjoined flow rate and construct the flow stream lines. We will find the general solution to the problem by the method of singular points of S.A. Chaplygin [15]. As a parametric region, we choose the upper right quadrant with the corresponding points shown in Figures 2, a, b.

We construct the function dw/dt , which is a the complex conjugate velocity of the imaginary flow in the parametric plane. We take into account that the fluid flows from the infinitely distant points B , D and is absorbed at the infinitely distant point E , that is, the streamlines start at points B , D and close at point E . There exist a separation point C , where the general streamline is perpendicular to the axis ξ .

We define the features of the function dw/dt . At points A and C , the right angles are flowed around, so $t_A = 0$, $t_C = c$ are zeros of the first order. Points E lie at infinity; therefore, they do not participate in the construction of the function dw/dt . At points B ($t_B = b$) and D ($t_D = 1$) we have the poles of the first order.

We analytically continue dw/dt on the entire complex plane. On the real axis ξ the condition $\operatorname{Im} \frac{dw}{dt} = 0$ is satisfied. According to the principle of symmetry, we analytically continue dw/dt through this axis to the lower right quadrant, with no additional features. On the imaginary axis η the condition $\operatorname{Re} \frac{dw}{dt} = 0$ is satisfied that allows one to analytically continue dw/dt on the whole complex plane. Moreover, at the point C ($t_C = -c$) we get zero, and at the points B ($t_B = -b$) and D ($t_D = -1$) we obtain the first order poles.

As a result of these continuations, the function dw/dt is built in the form

$$\frac{dw}{dt} = \phi_0 \frac{t(t^2 - c^2)}{(t^2 - 1)(t^2 - b^2)} = \phi_0 f(t). \tag{14}$$

On ADE $\text{Im} \frac{dw}{dt} = 0$ and therefore, is a real number.

The picture of the flow lines of an imaginary flow in the parametric plane, constructed using the *StreamPlot* option of the *Mathematica* software [14], is shown in Figure 3.

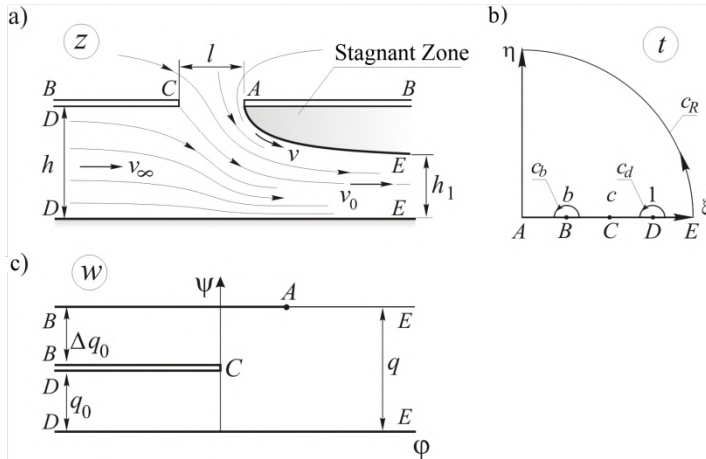


Figure 2. Flow areas for separated flow model:
a is physical plane $z = x + iy$; b is parametric plane $t = \xi + i\eta$; c is plane of complex potential $w = \phi + i\psi$.

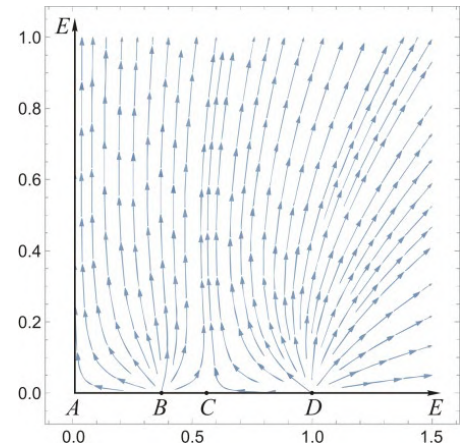


Figure 3. Imaginary flow.

We construct a function $\frac{dw}{v_0 dz} = \frac{v_x}{v_0} - i \frac{v_y}{v_0}$. This function has a unique zero at the point $t = b$, which, after

analytic continuation through the imaginary axis, turns into a pole at the point $t = -b$, since $\left| \frac{dw}{v_0 dz} \right| = 1$ on the

imaginary axis. Given that with $t \rightarrow \infty \frac{dw}{v_0 dz} = 1$, we obtain

$$\frac{dw}{v_0 dz} = \frac{t - b}{t + b}.$$

Next, we find the derivative of the mapping function $z = z(t)$

$$q = v_0 h_1 \frac{dz}{dt} = \frac{dz}{dw} \cdot \frac{dw}{dt} = \frac{\phi_0}{v_0} \frac{t(t^2 - c^2)}{(t^2 - 1)(t^2 - b^2)} \cdot \frac{t - b}{t + b} = \frac{\phi_0}{v_0} F(t). \tag{15}$$

The expressions (14), (15), in principle, allow constructing streamlines in the parametric and physical planes.

We proceed to determine the flow rate of air sucked through the gap. The flow rate at point D is $q_0 = v_\infty h$, and at point E it is $q = v_0 h_1$, so flow through the gap is $\Delta q_0 = q - q_0$.

Function dw/dt is analytical in the upper right quadrant, excluding points B, C, E . Points B, C on the parametric plane are marked by semicircles of infinitely small radius; we surround the remote point E with a quarter of a circle of infinitely large radius (Figure 2, b). When switching from DC to DE in a semicircle C_d $\text{Im } w$ experiences a jump q_0 (Figure 2, c).

Using the residue theorem, we find

$$iq_0 = \oint_{C_d} \frac{dw}{c_d dt} dt = \pi i \text{res}_{t=1} [\phi_0 f(t)] = \pi i \phi_0 \frac{1 - c^2}{2(1 - b^2)},$$

whence it follows that the transit flow intensity is

$$q_0 = \pi\phi_0 \frac{1-c^2}{2(1-b^2)}. \quad (16)$$

When moving from BC to BA in a semicircle C_b $Im w$ experiences a jump Δq_0 , hence

$$i\Delta q_0 = \oint_{C_b} \frac{dw}{dt} dt = \pi i \operatorname{res}_{t=b} [\phi_0 f(t)] = \pi i \phi_0 \frac{b^2 - c^2}{2(b^2 - 1)},$$

and the intensity of flow entering the gap is

$$\Delta q_0 = \pi\phi_0 \frac{b^2 - c^2}{2(b^2 - 1)}, \quad (17)$$

when switching from DE to AE in a quarter circle C_R $Im w$ experiencing a jump q and

$$iq = \oint_{C_R} \frac{dw}{dt} dt = \frac{\pi}{2} i \operatorname{res}_{t=\infty} [\phi_0 f(t)] = \phi_0 i \frac{\pi}{2},$$

which means the intensity of the total flow

$$q = \frac{\pi\phi_0}{2}. \quad (18)$$

From formulas (16)÷(18) we find the dimensionless associated flow

$$C_q = \frac{\Delta q_0}{q_0} = \frac{q}{q_0} - 1 = \frac{1-b^2}{1-c^2} - 1. \quad (19)$$

Now we determine the sizes h and h_1 . When switching from DC to DE by semicircles c_d $Im z$ experiences a jump h . From here

$$ih = \oint_{c_d} \frac{dz}{dt} dt = \frac{\phi_0}{v_0} \pi i \operatorname{res}_{t=1} F(t) = \frac{\phi_0}{v_0} \pi i \frac{1-c^2}{2(1-b^2)},$$

$$h = \frac{\phi_0}{v_0} \pi \frac{1-c^2}{2(1-b^2)}, \quad (20)$$

when switching from DE to AE in a quarter circle c_R $Im z$ experiences a jump h_1 and it means that

$$ih_1 = \oint_{c_R} \frac{dz}{dt} dt = \frac{\phi_0}{v_0} \frac{\pi i}{2} \operatorname{res}_{t=\infty} F(t) = \frac{\phi_0}{v_0} \frac{\pi i}{2},$$

$$h_1 = \frac{\phi_0}{v_0} \frac{\pi}{2}. \quad (21)$$

Combining expressions (20), (21) we find the compression ratio of the flow

$$K = \frac{h_1}{h} = \frac{(1-b)^2}{1-c^2}. \quad (22)$$

It remains to determine the mapping parameters b , c and the coefficient ϕ_0 . Since point B in the physical plane at infinity to the left and to the right of the gap is at the same level, then

$$\operatorname{Im} \oint_{t=b} \frac{dz}{dt} dt = 0 \Rightarrow \operatorname{res}_{t=b} F(t) = 0. \quad (23)$$

On the other hand

$$\operatorname{res}_{t=b} F(t) = \frac{d}{dt} \left[\frac{t(t^2 - c^2)}{t^2 - 1} \right]_{t=b} = 0.$$

We take the logarithmic derivative

$$\left. \frac{d}{dt} \ln \frac{t(t^2 - c^2)}{t^2 - 1} \right|_{t=b} = \left[\frac{1}{t} + \frac{2t}{t^2 - c^2} - \frac{2t}{t^2 - 1} \right]_{t=b} = 0$$

From the previous equalities it follows

$$\frac{1}{b} + \frac{2b}{b^2 - c^2} - \frac{2b}{b^2 - 1} = 0$$

and

$$c = b \sqrt{\frac{3 - b^2}{1 + b^2}}. \tag{24}$$

From the graph of function (24) (Figure 4) it can be seen that for $0 < b < 1$, the following is always true: $b < c < 1$.

The function $F(t) = \frac{t(t^2 - c^2)}{(t^2 - 1)(t^2 - b^2)}$, entering the mapping formula (15), will be decomposed to a sum of partial fractions

$$F(t) = \frac{M}{t-1} + \frac{N}{t+1} + \frac{P}{(t-b)^2} + \frac{K}{t-b}.$$

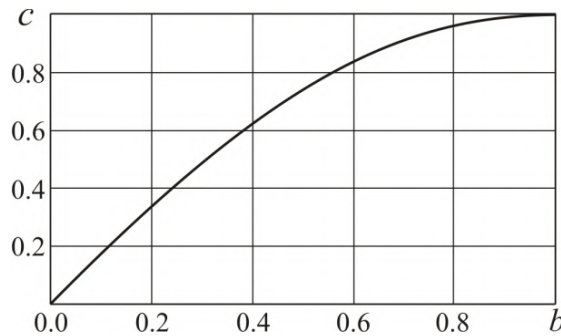


Figure 4. Plot of function $c = c(b)$.

In view of (23) the coefficient $K = 0$, for other coefficients we get

$$\left. \begin{aligned} M &= \oint_{t=1} \frac{dz}{dt} dt = \operatorname{res}_{t=1} F(t) = \frac{1 - c^2}{2(1 - b)^2} \\ B &= \oint_{t=-1} \frac{dz}{dt} dt = \operatorname{res}_{t=-1} F(t) = \frac{1 - c^2}{2(1 + b)^2} \\ C &= \oint_{t=b} \frac{dz}{dt} dt = \frac{b(b^2 - c^2)}{b^2 - 1} \end{aligned} \right\} \tag{25}$$

We find the primitive for function $F(t)$

$$G(t) = \int F(t) dt = M \ln(t-1) + N \ln(t+1) - \frac{P}{t-b}. \tag{26}$$

For the parametric plane the slot of the width l corresponds to a segment AC

$$l = \frac{\phi_0}{v_0} \operatorname{Re} [G(0) - G(c)].$$

Using the expression (20), we obtain

$$\frac{l}{h} = \frac{2(1-b)^2}{\pi(1-c^2)} \operatorname{Re} [G(0) - G(c)]. \quad (27)$$

So, to find b and c , which meet the criteria $0 < b < c < 1$, one should solve a system of equations (24)–(27). By combining them, we get

$$\frac{(1-b)^2}{(1+b)^2} \cdot \frac{4b^2c + (b-c) \left[(1+b^2) \ln(1-c) + (1-b^2) \ln(1+c) \right]}{\pi(c-b)(1-c^2)} = \frac{l}{h}. \quad (28)$$

The equation (28) is solved using the *Find_Root* of the *Mathematica* software, and the parameter c is defined using the formula (24).

Let $v_0 = 1$, $h = 1$. We introduce notations:

$$M_1 = M\phi_0, \quad N_1 = N\phi_0, \quad -P_1 = P\phi_0.$$

Taking into account (20), (25), (28) we obtain

$$M_1 = \frac{1}{\pi}, \quad N_1 = \frac{(b-1)^2}{\pi(b+1)^2}, \quad P_1 = \frac{4b^2}{\pi(b+1)^2}.$$

As point A has coordinates $(1/2, 0)$, we have a conformal mapping of the parametric plane onto the physical plane in the form

$$z(t) = \frac{1}{\pi} \ln(t-1) + \frac{(b-1)^2}{\pi(b+1)^2} \ln(t+1) - \frac{4b^2}{\pi(b+1)^2} - i + \frac{1}{2}. \quad (29)$$

We proceed to the construction of streamlines. This is easier to perform in the parametric plane, and then, using the conformal mapping (29), to transfer them to the physical plane. The imaginary flow in the parametric plane has velocities

$$v_\xi = v_\xi(\xi, \eta) = \phi_0 \operatorname{Re} [f(\xi + i\eta)],$$

$$v_\eta = v_\eta(\xi, \eta) = -\phi_0 \operatorname{Im} [f(\xi + i\eta)].$$

Since the imaginary flow is steady, the streamlines coincide with the particle trajectories. Therefore, the differential equations of streamlines will be

$$\xi'(\tau) = v_\xi[\xi(\tau), \eta(\tau)], \quad \eta'(\tau) = v_\eta[\xi(\tau), \eta(\tau)], \quad (30)$$

where τ is the time of particles motion in the parametric plane.

We construct N streamlines of the transit flow. Initial conditions must be added to the system of differential equations (30). On the semicircle C_d of a small radius ε_1 , we arrange N points. The initial conditions are formulated as

$$\xi(0) = \varepsilon_1 \cos \frac{\pi j}{N+1} + 1, \quad \eta(0) = \varepsilon_1 \sin \frac{\pi j}{N+1}, \quad j = \overline{1 \dots N}, \quad (31)$$

Using *NDSolve* program of the *Mathematica* software the Cauchy problem (30), (31) was solved on the interval $\tau \in [0, \tau_{\max}]$. As a result, we obtain the coordinates of streamlines in the parametric plane

$$\xi = \xi(\tau), \eta = \eta(\tau), \tau \in [0, \tau_{\max}].$$

The values τ_{\max} were determined from a numerical experiment.

The problem described above for a viscous fluid was solved numerically by Flow3d software package. The system of equations for plane turbulent motion of a viscous fluid was closed using the "standard" $k-\varepsilon$ model (k is the kinetic energy of turbulence, ε is the dissipation rate k). For flow zones in the immediate vicinity of the duct walls, standard wall functions were used.

At the boundaries of the computational domain, the following boundary conditions were adopted (see Figure 1, a):

- On DD, the condition for uniform distribution and constancy of velocity \vec{v}_∞ in the positive direction of the x axis corresponding to a given specific intensity q_0 ;
- On EE, the condition for a smooth continuation of the flow through the boundary (normal derivatives at the boundary for all quantities are equal to zero);
- At the permeable boundaries of the area of air leakage to the gap, the excessive static pressure $\Delta P = 0$;
- On the boundaries BC, AB, DE , solid impermeable walls on which the condition of adhesion (non-slip) is fulfilled $\vec{v}_\tau = 0$.

The temperature at all boundaries is equal to air temperature of 293K.

The total number of grid cells in the channel is 80 thousand, along the length of the slotted hole it is at least 20, as it is recommended in [14]. The channel length to the slot hole was taken equal to $3h$ in order to exclude the influence of boundary conditions in the DD section on the flow near the slot hole. The length of the channel after the slot hole was taken to be at least $10h$ to smooth the flow deformation due to adjoining of the flow through the slot and separation of flow from the sharp edge, which affects the accuracy of determining the total flow rate $q = q_0 + \Delta q_0$.

2.2. Bilateral arrangement of slotted openings in the duct

An element of the intake panel with a two-sided arrangement of slotted openings is shown in Figure 5 a. Transit flow from upstream openings has velocity v_∞ . Here it is also necessary to determine the flow rates of air entering through the slots and to build the flow stream lines.

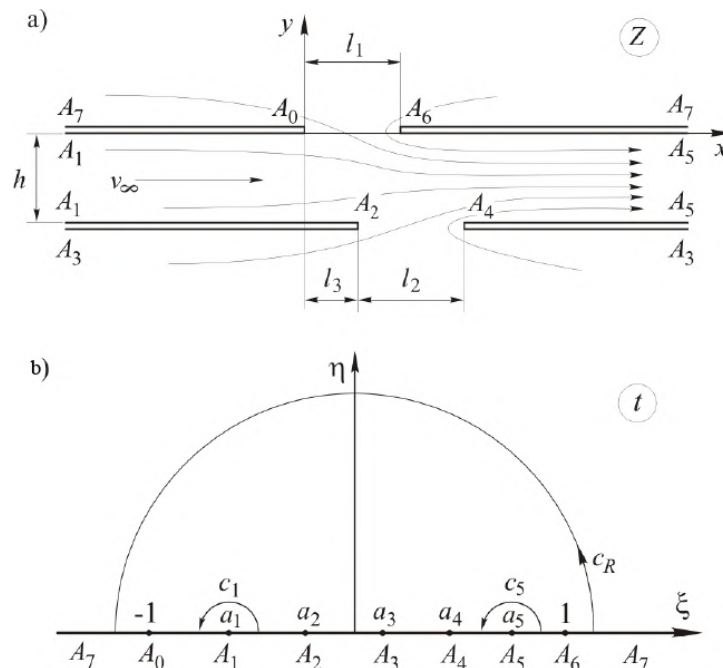


Figure 5. Flow areas: a) physical plane $z = x + iy$; b) parametric plane $t = \xi + i\eta$.

Ideal fluid, unseparated flow. We find the solution using the theory of potential flows of ideal fluid by the method of conformal mappings. We do not take into account the presence of vortex zones in the places of

boundaries fractures (points A_4, A_6). We assume that at points A_0 and A_2 the Kutta-Joukowski condition of the limited velocity [20] is satisfied.

We will construct the flow in the parametric region, which in our case will be the upper half-plane with the correspondence of points shown in Figure 7a, b. The relationship between the flow regions in the z and t planes is established using the Christoffel – Schwartz formula

$$z = A \int_{-1}^t F(u) du; \quad F(t) = \frac{(t^2 - 1)(t - a_2)(t - a_4)}{(t - a_1)(t - a_3)^2(t - a_5)}, \quad (32)$$

where u is the integration variable.

The mapping parameters a_1, a_2, a_3, a_4, a_5 and coefficient A must be defined. We expand the function $F(t)$ at the sum of simple rational fractions

$$F(t) = \frac{\alpha}{t - a_1} + \frac{\alpha_1}{t - a_5} + \frac{\beta}{(t - a_3)^2} + \frac{\beta_1}{t - a_3} + 1,$$

where coefficients $\alpha, \alpha_1, \beta, \beta_1$ are real. The coefficient A is also real and positive, since for A_6A_7 we have $dx/d\xi > 0$.

In order to obtain the same duct width at points A_1 and A_5 , the following conditions must be met

$$\operatorname{Im} \int_{C_1} \frac{dz}{dt} = ih \quad \text{and} \quad \operatorname{Im} \int_{C_5} \frac{dz}{dt} = -ih,$$

where C_1 and C_5 are semicircles of infinitely small radius, surrounding points A_1 and A_5 in the parametric plane t (see Figure 7, b).

Using the residue theorem, we obtain

$$\begin{aligned} \operatorname{Im} \int_{C_1} \frac{A\alpha dt}{t - a_1} = ih &\rightarrow A\alpha\pi i = ih \rightarrow A\alpha = \frac{h}{\pi}; \\ \operatorname{Im} \int_{C_5} \frac{A\alpha_1 dt}{t - a_5} = -ih &\rightarrow A\alpha_1\pi i = -ih \rightarrow A\alpha_1 = -\frac{h}{\pi}.. \end{aligned}$$

It follows that

$$A = \frac{h}{\alpha\pi} = -\frac{h}{\alpha_1\pi}; \quad (33)$$

$$\alpha_1 + \alpha = 0. \quad (34)$$

In order to have the straight lines A_7A_0, A_6A_7 at the same level in the physical plane, we additionally use the condition

$$\operatorname{Im} \int_{C_R} \frac{dz}{dt} = 0 \rightarrow \operatorname{Im} \int_{C_R} F(t) dt = 0, \quad (35)$$

or otherwise

$$\operatorname{Im} \left[\int_{C_R} \frac{\alpha dt}{t - a_1} + \int_{C_R} \frac{\alpha_1 dt}{t - a_5} + \int_{C_R} \frac{\beta_1 dt}{t - a_3} + \int_{C_R} \frac{\beta dt}{(t - a_3)^2} + \int_{C_R} dt \right] = 0,$$

where C_R is the semicircle of an infinitely large radius surrounding the point A_7 in the parametric plane (see Figure 5, b).

According to the residue theorem $\int_{C_R} \frac{\beta dt}{(t - a_3)^2} = 0$, and besides, $\operatorname{Im} \int_{C_R} dt = 0$, which means $\pi i\alpha + \pi i\alpha_1 + \pi i\beta_1 = 0$. Taking into account expression (34), $\beta_1 = 0$, and the function $F(t)$ takes the form

$$F(t) = \frac{\alpha}{t-a_1} - \frac{\alpha}{t-a_5} + \frac{\beta}{(t-a_3)^2} + 1.$$

Having determined the residues of function $F(t)$ at points A_1, A_5 and the limit of function value $F(t)(t-a_3)^2$ at $t \rightarrow a_3$, we express the coefficients α, α_1, β through mapping parameters a_1, a_2, a_3, a_4, a_5

$$\alpha = \frac{(a_1^2 - 1)(a_1 - a_2)(a_1 - a_4)}{(a_1 - a_3)^2(a_1 - a_5)}; \quad \alpha_1 = \frac{(a_5^2 - 1)(a_5 - a_2)(a_5 - a_4)}{(a_5 - a_3)^2(a_5 - a_1)};$$

$$\beta = \frac{(a_3^2 - 1)(a_3 - a_2)(a_3 - a_4)}{(a_3 - a_1)(a_3 - a_5)}.$$

Using condition (3) from the first two expressions we find

$$\frac{(a_1^2 - 1)(a_1 - a_2)(a_1 - a_4)}{(a_1 - a_3)^2} - \frac{(a_5^2 - 1)(a_5 - a_2)(a_5 - a_4)}{(a_5 - a_3)^2} = 0. \quad (36)$$

Now consider the condition $\text{Im} \int_{C_R} F(t) dt = 0 \rightarrow \text{res}_{t=\infty} F(t) = 0$. By determining the residue of the function $F(t)$ at infinity, we get

$$-a_1 + a_2 - 2a_3 + a_4 - a_5 = 0. \quad (37)$$

If the mapping parameters satisfy conditions (36), (37), then

$$f(t) = \int F(t) dt = \alpha \ln(t - a_1) - \alpha \ln(t - a_5) - \frac{\beta}{t - a_3} + t.$$

The well-known geometric characteristics of the flow region make it possible to write down three more equalities

$$l_1 = \text{Re}[f(1) - f(-1)] \cdot A; \quad l_2 = \text{Re}[f(a_4) - f(a_2)] \cdot A; \quad l_3 = \text{Re}[f(a_2) - f(-1)] \cdot A.$$

Given that $A = h/\alpha\pi$, and introducing new notations $l_1/h = \bar{l}_1, l_2/h = \bar{l}_2, l_3/h = \bar{l}_3$ we get three equations that are missing to determine the five mapping parameters $a_j, j=1,2,\dots,5$

$$\text{Re}[f(1) - f(-1)] - \bar{l}_1 \alpha \pi = 0; \quad (38)$$

$$\text{Re}[f(a_4) - f(a_2)] - \bar{l}_2 \alpha \pi = 0; \quad (39)$$

$$\text{Re}[f(a_2) - f(-1)] - \bar{l}_3 \alpha \pi = 0. \quad (40)$$

Now it is necessary to solve a system of five nonlinear equations (35), (36), (38)-(40) with respect to five mapping parameters. The main difficulty in solving this system by the Newton method is the ordering of parameters:

$$-1 < a_1 < a_2 < a_3 < a_4 < a_5 < 1$$

The point is that the method iterations regularly violate this ordering. To preserve it, we use the technique proposed in [18] (see also [19]). We introduce new variables

$$b_i = \ln \frac{a_i - a_{i-1}}{a_{i+1} - a_i}, \quad i = 1, 5, \quad a_0 = -1, \quad a_6 = 1. \quad (41)$$

We turn the last equalities to variables a_i , for this we solve the following system of linear equations with a tridiagonal matrix

$$a_i - a_{i-1} - e^{b_i} (a_{i+1} - a_i) = 0, \quad \text{where } i = 1, 5.$$

Solving this system of equations in the *Mathematica* package, we obtain

$$a_i = G_i(b_1, b_2, \dots, b_5), \quad i = \overline{1, 5}. \quad (42)$$

where functions G_i are built explicitly.

Now, taking into account equalities (42), we transform the system of equations (35), (36), (38)–(40), solving which we find the mapping parameters. Note that variables b_i are unordered, but any set of them gives an ordered set of variables a_i . When applying the Newton method to the transformed system, the zero values of variables b_i were simply chosen as the zeroth approximation, and the iteration process was always converged.

Thus, we have an opportunity to construct a function

$$f(t) = \int F(t)dt = \alpha \ln(t - a_1) - \alpha \ln(t - a_5) - \frac{\beta}{t - a_3} + t$$

and conformal mapping

$$z(t) = A[f(t) - f(-1)] \quad (43)$$

Now we calculate the adjoined flow rate through the slotted openings in the walls of duct. In the parametric plane, we have sources at points $A_1 (t = a_1)$, $A_3 (t = a_3)$, $A_7 (t = \infty)$ and stock at point $A_5 (t = a_5)$. The complex potential $w = \phi + i\psi$ of such a flow will be equal to

$$w = \frac{q}{\pi} \ln(t - a_1) - \frac{(q + q_1 + q_2)}{\pi} \ln(t - a_5) + \frac{q_2}{\pi} \ln(t - a_3), \quad (44)$$

where ϕ , ψ are potential and function of flow, q_1 and q_2 are flow rates through the corresponding slotted openings, $q = v_\infty h$ is the transit flow rate. We find the derivative

$$\frac{dw}{dt} = \frac{q}{\pi(t - a_1)} - \frac{q_1 + q_2 + q}{\pi(t - a_5)} + \frac{q_2}{\pi(t - a_3)}.$$

At points A_0, A_2 velocities are limited and therefore $dw/dt, dw/dt = 0$. We solve the system of equations

$$\begin{cases} \frac{dw}{dt}(t = -1) = \frac{q}{\pi(-1 - a_1)} - \frac{q_1 + q_2 + q}{\pi(-1 - a_5)} + \frac{q_2}{\pi(-1 - a_3)} = 0; \\ \frac{dw}{dt}(t = a_2) = \frac{q}{\pi(a_2 - a_1)} - \frac{q_1 + q_2 + q}{\pi(a_2 - a_5)} + \frac{q_2}{\pi(a_2 - a_3)} = 0 \end{cases}$$

with respect to q_1 and q_2 . As a result, we obtain

$$q_1 = \frac{q(a_3 - a_1)(a_5 - a_1)}{(1 + a_1)(a_2 - a_1)}, \quad q_2 = \frac{q(a_3 + 1)(a_3 - a_2)(a_1 - a_5)}{(1 + a_1)(a_2 - a_1)(a_3 - a_5)}.$$

Now we can calculate the adjoined flow rate, which we present in the dimensionless form

$$C_q = \frac{q_1 + q_2}{q} = \frac{(a_3 - a_1)(a_5 - a_1)}{(1 + a_1)(a_2 - a_1)} + \frac{(a_3 + 1)(a_3 - a_2)(a_1 - a_5)}{(1 + a_1)(a_2 - a_1)(a_3 - a_5)}. \quad (45)$$

The problem for a viscous fluid was also solved numerically in the Flow3d software package. The boundary conditions were formulated in the same way as in Problem 1. The calculation results are presented below.

3. Results and Discussion

3.1. Hole on one side of the intake duct wall

During the calculations, we also determined the dimensionless adjoined flow rate C_q and the jet contraction coefficient K . Figure 6 shows graphs of the corresponding dependences (19) and (22). Recall that the parameters b and c at given values l/h are determined by formulas (24), (28). The dashed line shows the graph C_q for the flow, where the flow separation at point A is not taken into account.

Comparison of graphs shows that separation of flow reduces the adjoined flow. We also see that the jet contraction coefficient tends to 0.5 with an increase in the length of the gap, that is, the flow in the channel becomes close to the flow in the Bord nozzle [17].

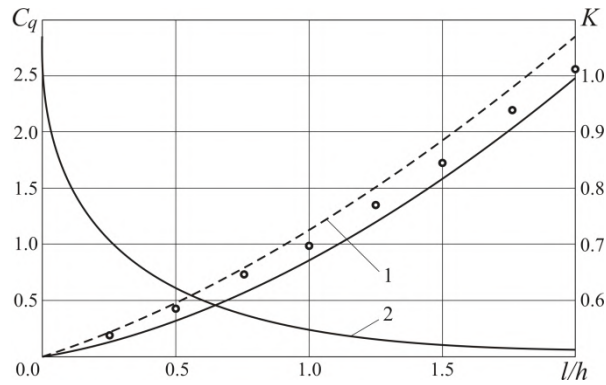


Figure 6. Function graphs: 1 – adjoined flow taking into account flow separation (solid line), without taking into account flow separation (dashed line), 2 – jet contraction coefficient, (C_q values obtained numerically in the *Flow3d* program are shown by circles).

Using the mapping formula (29), the streamlines' coordinates in the physical plane are determined. Similarly, the intake flow streamlines are constructed, but a semicircle of small radius C_b is constructed around point B ($t = b$). Figure 5a shows the streamlines constructed in the described way for various values of l/h .

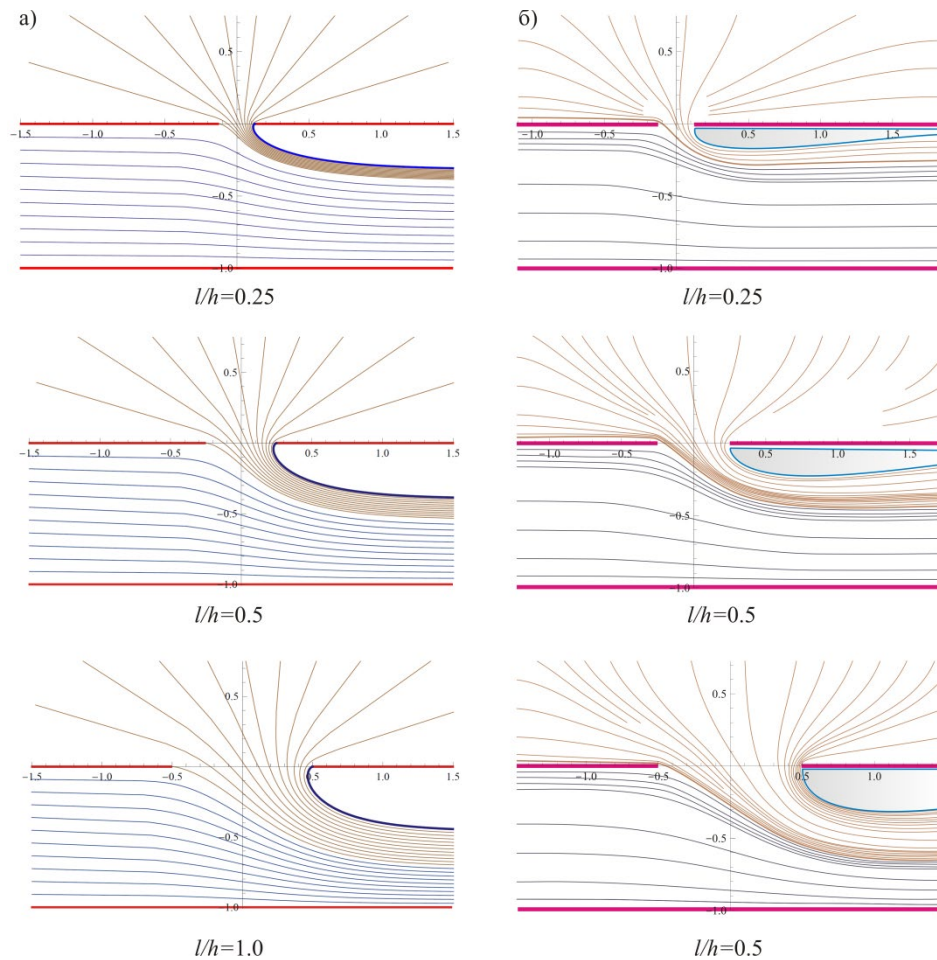


Figure 7. Flow lines near the hole in one wall of the duct: a – analytical solution in NDSolve program of Mathematica software, b – numerical solution in the *Flow3d* program

3.2. Double-sided intake panel element

Figure 8 presents a graph of dependence of C_q on the device geometry. Minimum of C_q is achieved for opposed openings. As the gap between the slots increases, the adjoined flow tends to a constant value.

The intake rate is minimal with the opposite arrangement of openings, with an increase in the spacing it increases. Starting from a distance $\bar{l}_3 = 2$, it reaches its maximum value and then remains constant. That is, it can be argued that at $\bar{l}_3 > 2$ the mutual influence of the openings disappears.

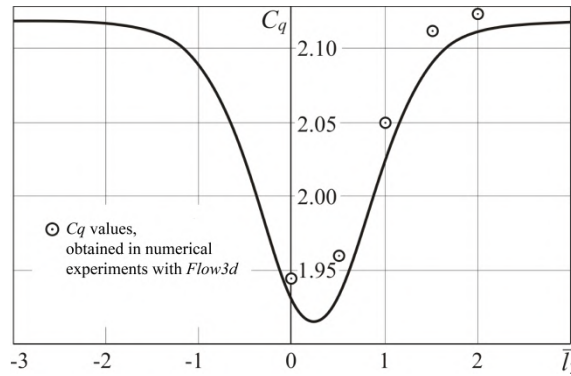


Figure 8. The graph of dependence of the adjoined flow from the spacing between openings $\bar{l}_1 = 1, \bar{l}_2 = 0.5$.

Knowing the complex potential (44) and the conformal mapping formula (43), we can further construct the flow streamlines in the physical domain. Figure 9a shows the flow map for different locations and sizes of slot openings.

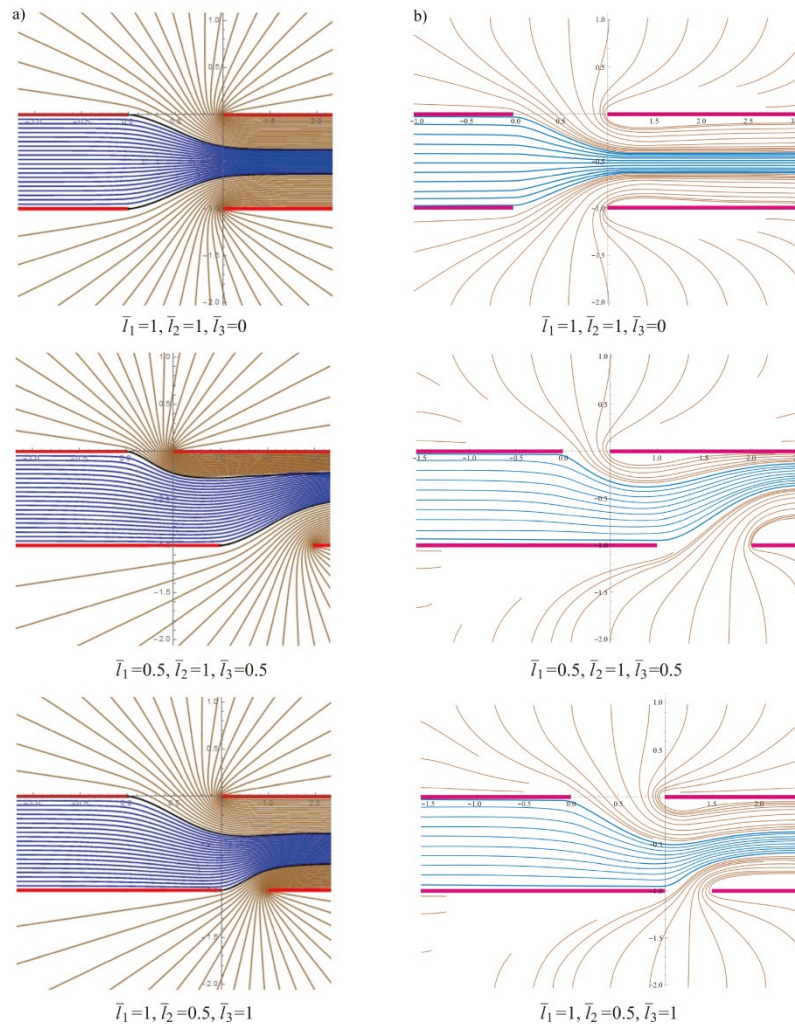


Figure 9. Flow streamlines in openings on opposite walls of the duct: a – analytical solution in the NDSolve program of Mathematica package, b – numerical solution in the Flow3d program.

The intake rate is minimal with the opposite arrangement of holes, with an increase in the spacing it increases. Starting from a distance $\bar{l}_3 = 2$, it reaches its maximum value and then remains constant. I.e. it

can be argued that with $\bar{l}_3 > 2$ the mutual influence of the cracks disappears. Considering the complex potential (44) and the conformal mapping formula (43), we can further construct the flow streamlines in the physical domain. In Figure 9a a flow pattern for different locations and sizes of slit openings is shown. Pictures of flows constructed by Flow3d software package are shown in Figure 9, b.

The results of calculating the attached flow are shown by dots in Figure 8. We can state the accordance between analytical and numerical calculations

The numerical method allows to obtain more physics of the flow and, in particular, determines the geometry of the stagnant zone formed when the flow is cut off from sharp edges. Within the framework of the used analytical model, the shape of the stagnant zone is not determined.

The problem was also solved numerically in the *Flow3d* software package. The boundary conditions were formulated in the same way as in Problem 1. The flow maps constructed using the *Flow3d* software package are shown in Figure 9, b. The results of calculating the adjoined flow are shown by dots in Figure 8. We can state a good agreement between analytical and numerical calculations.

The numerical method allows one to obtain a more physical picture of the flow and, in particular, it determines the geometry of the stagnant zone formed when the flow is cut off from sharp edges. Within the framework of the used analytical model, the shape of the stagnant zone is not determined.

4. Conclusions

In the work, the velocity field created by the action of the slotted hole on the duct wall, as well as at the intake panel with a two-sided arrangement of slotted holes, is analytically and numerically calculated. In the framework of the inseparable and detached models of potential ideal fluid flows, equations for the flow streamlines are obtained. The flow patterns are compared with the results of numerical calculations performed for a viscous fluid. The intensity of absorption is determined depending on the width of the slit and the flow rate.

Important results have been obtained that can be used in the design of air duct systems:

- the flow rates of air entering through the slots in the walls of the duct are determined, depending on their width, relative position and transit flow value;
- current flow lines are constructed;
- it was found that the intake intensity is minimal with the opposite arrangement of slots;
- The shape and size of the stagnant zones are determined numerically.

It should be noted that the qualitative patterns of the flows obtained by analytical and numerical methods are slightly different, since the flow model underlying the analytical calculation does not imply that the boundaries of the stagnant zone are closed on the duct wall. The values of the attached flow, determined analytically and numerically, practically coincide.

The results of the experimental determination of the flow characteristics and the intensity of absorption through the openings for the considered geometric situations are being prepared for publication. In particular, Figure 10 shows photographs of the boundaries of the separation zones at the middle suction inlet in a rectangular duct at $l/h = 0.32$. The experiments were run by Ph.D. Ziganshin A.M. in the laboratory of Kazan State University of Architecture and Engineerin (KSUAE).

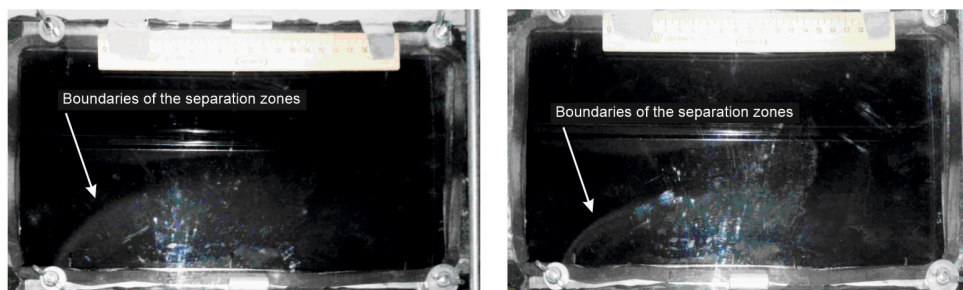


Figure 10. Boundaries of the separation zones at the middle intake hole in a rectangular duct at $l/h = 0.32$ at different velocity of the transit flow.

References

1. Altuntas, O., Sogut, M.Z., Yalcin, E., Karakoc, T.H. Assessment of thermodynamic and environmental performances in subcooling process for different refrigerants. *International Journal of Exergy*. 2017. 24 (2-4). Pp. 216–234. DOI: 10.1504/IJEX.2017.087655.
2. Singh, L., Singh, S.N., Sinha, S.S. Effect of standoff distance and area ratio on the performance of circular exhaust ejector using computational fluid dynamics. *Proceedings of the Institution of Mechanical Engineers, Part G: Journal of Aerospace Engineering*. 2018. 232 (15). Pp. 2821–2832. DOI: 10.1177/0954410017717287.

3. Singh, L., Singh, S.N., Sinha, S.S. Effect of Slot-Guidance and Slot-Area on Air Entrainment in a Conical Ejector Diffuser for Infrared Suppression. *Journal of Applied Fluid Mechanics*. 2019. 12(4). Pp. 1303–1318. DOI: 10.29252/jafm.12.04.29593.
4. ASHRAE. 2017 ASHRAE handbook : fundamentals. ASHRAE handbook : fundamentals2017.
5. Goodfellow, H.D., Tähti, E. PREFACE. *Industrial Ventilation Design Guidebook2001*. San Diego, CA: Academic Press. 1555 p.
6. Logachev, I.N., Logachev, K.I., Averkova, O.A., Azarov, V.N., Uvarov, V.A. Methods of Reducing the Power Requirements of Ventilation Systems. Part 4. Theoretical Prerequisites for the Creation of Dust Localizing Devices with Swirling Air Flows1. *Refractories and Industrial Ceramics*. 2014. 55(4). Pp. 365–370. DOI: 10.1007/s11148-014-9728-6.
7. American Conference of Governmental Industrial Hygienists. *Industrial ventilation : a manual of recommended practice for operation and maintenance2007*.
8. Burgess, W.A., Ellenbecker, M.J., Treitman, R.D. *Ventilation for Control of the Work Environment: Second Edition*. 2004. Wiley-Interscience. 443 pp.
9. Cao, Z., Wang, Y., Duan, M., Zhu, H. Study of the vortex principle for improving the efficiency of an exhaust ventilation system. *Energy and Buildings*. 2017. 142. Pp. 39–48. DOI: 10.1016/j.enbuild.2017.03.007.
10. Yang, Y., Wang, Y., Song, B., Fan, J., Cao, Y. Stability and accuracy of numerical investigation of droplet motion under local ventilation airflow. *Building and Environment*. 2018. 1470. Pp. 32–42. DOI: 10.1016/j.buildenv.2018.05.023.
11. Koshkarev, S., Azarov, V., Azarov, D. The Decreasing Dust Emissions of Aspiration Schemes Applying a Fluidized Granular Particulate Material bed Separator at the Building Construction Factories. *Procedia Engineering*. 2016. 165. Pp. 1070–1079.
12. *Handbook of Hydraulic Resistance*, 3rd Edn. By I.E. Idelchik. Begell House, *Journal of Fluid Mechanics*. 1994. 790 pp.
13. ANSYS. ANSYS FLUENT User's Guide 2013.
14. FLOW-3D® User's Manual, Version 9.3, Flow Science, Inc., (2008).
15. Cordes, G.M.I. Gurevich, The Theory of Jets in an Ideal Fluid. (International Series of Monographs in Pure and Applied Mathematics, Volume 93) VIII + 412 S. m. 262 Abb. Oxford/London/Edinburgh/New York/Toronto/Paris/Braunschweig 1966. Preis geb. £ 5 net. Pergamon . ZAMM – Zeitschrift für Angewandte Mathematik und Mechanik. 1967. DOI:10.1002/zamm.19670470418.
16. Santalo, L.A. Book Reviews: – 1. Conformal Mapping: Methods and Applications: R. Schinzinger and P.A.A. Laura Elsevier Amsterdam, Oxford, New York, Tokyo 1991. 581 p.
17. Logachev, I.N., Logachev, K.I., Averkova, O.A., Azarov, V.N., Uvarov, V.A. Methods of Reducing the Power Requirements of Ventilation Systems. Part 4. Theoretical Prerequisites for the Creation of Dust Localizing Devices with Swirling Air Flows1. *Refractories and Industrial Ceramics*. 2014. 55. Pp. 365–370. DOI: 10.1007/s11148-014-9728-6.
18. Elcrat, A.R., Trefethen, L.N. Classical free-streamline flow over a polygonal obstacle. *Journal of Computational and Applied Mathematics*. 1986. 14(1-2). Pp. 251–265. DOI: 10.1016/0377-0427(86)90142-1.
19. Maklakov, D.V., Valitov, R.R., Posokhin, V.N., Safiullin, R.G. Calculation of intensity of air absorption through the openings in the side wall of air line. message 2. *Journal «Izvestiya vuzov. Investitsiyi. Stroyitelstvo. Nedvizhimost»*. 2018. 8(1). Pp. 160–167. DOI: 10.21285/2227-2917-2018-1-160-167.
20. John D. Anderson *Fundamentals of Aerodynamics: Fifth edition*. 2011. 1106 p.

Contacts:

Dmitry Maklakov, dmaklak@kpfu.ru

Vladimir Posohin, posohin@mail.ru

Rinat Safiullin, safiullin_rinat@mail.ru

Julia Kareeva, jkareeva2503@gmail.com



DOI: 10.18720/MCE.94.7

Evaluation of the basalt fiber reinforced pumice lightweight concrete

S.N. Karaburc, S.A. Yildizel, G.C. Calis*

Karamanoglu Mehmetbey University, Karaman, Turkey

* E-mail: gokhancalis@kmu.edu.tr

Keywords: lightweight concrete, ground calcium carbonate, basalt fiber, cement

Abstract. This paper aimed to investigate the mechanical and durability properties of basalt fiber reinforced pumice lightweight concrete (BPLC) containing nano ground calcium carbonate (GCC). GCC was utilized as ordinary Portland cement replacement material at the percentages of 5 %, 10 %, 15 %, 20 % and 25 %, and basalt fibers with the 6 mm length were added in two contents of 0.5 % and 1 % by volume. The experimental results showed that GCC added mixes had lower mechanical strength results at the early ages; however, comparable strengths with the reference mixes at later ages. The addition of GCC addition also resulted in decreased water absorption, sorptivity and increased magnesium sulphate resistance compared to the reference lightweight concrete. Basalt fiber utilization enhanced the mechanical properties of the BPLC, but fiber inclusion lessened the fresh concrete properties. With respect to the enhanced material properties and less cement usage with produced BPLCs, it can be suitable for the green concrete block production industry.

1. Introduction

Lightweight concrete has been widely used in several parts of the construction industry such as masonry concrete block and wall panel productions due to its low density and thermal conductivity, and high strength to density ratio [1]. However, some disadvantageous properties have been also reported such as brittleness, lower mechanical strength and crack forming at early ages [2]. The application of lightweight concrete reduces the structural loads and the cost of the structural elements production. For this reason, it is widely preferred for the structures constructed in seismic zones [3, 4]. Portland cement containing lightweight concrete are traditionally produced with lightweight aggregates such as diatomite, perlite, pumice (from natural sources), and recycled clay bricks (recycled sources) in many researches [5–7]. Construction industry requires new developments due to increased needs, therefore fiber additions [8, 9], nano additives [10] have become significant solution to these increased needs.

The reinforcing fiber inclusion to the lightweight concrete mixes has been reported in many experimental studies. Fiber is used in order to enhance the fresh and hardened state behaviour of the concrete. Many types of the lightweight concrete have been developed to investigate the behavior differences that can be attributed to the fiber types (steel, carbon, etc.) and their lengths [11, 12].

Due to the environmental reasons, the demand for the cement replacement material to formulate environment friendly and economical concrete is rapidly growing. Therefore, many researches have been focused on cement replacement materials and alternative binding materials [13, 14]. Utilizing cement replacement materials such as GCC may enhance the strength and the cohesiveness of the concrete mixes or mortars. Nano GCC is widely used for filling the structural gaps in the microstructures and providing bleeding and shrinkage mechanism control [15].

The tensile strength property of the concrete mixes can be significantly improved with the inclusion of fibers. The cost of the fibers can be reduced by adding cheaper synthetic fibers compared to the metal fibers [16]. Basalt fibers are one of the environments friendly and high-performance fibers, and it has been widely utilized in many researches [17, 18]. These types of fibers can improve the flexural strength and toughness properties of the cement based composite materials [19]. Basalt fiber is also preferred due to its positive impact on corrosion resistance, high tensile strength [20]

Karaburc, S.N., Yildizel, S.A., Calis, G.C. Evaluation of the basalt fiber reinforced pumice lightweight concrete. Magazine of Civil Engineering. 2020. 94(2). Pp. 81–92. DOI: 10.18720/MCE.94.7



This work is licensed under a [CC BY-NC 4.0](https://creativecommons.org/licenses/by-nc/4.0/)

As it is widely known compressive and flexural strength of concrete is vitally important. Furthermore, sorptivity, dry bulk density, water absorption, setting times and sump test results are also included. In terms of containing two materials namely fiber and grand calcium, this study is unique.

It is reported by many researcher that fiber addition, especially steel, carbon and polypropylene fibers inclusion to the lightweight concrete mixes improved the material properties such as modulus of elasticity, abrasion resistance, freeze-thaw resistance, drying shrinkage and porosity [21, 22]. Among all fiber types, carbon fiber are commonly utilized due to its superior contribution to the composite materials such as high strength, good stability and good bonding behavior with the cement; however, its high cost limits the application of carbon fiber reinforced concrete [23]. Basalt fiber is also used as an eco-friendly and high-performance fiber in the research of fiber reinforced concrete materials. Basalt fibers can enhance the both compressive and flexural strengths, and toughness together with the fracture energy in the cement matrix composite applications [24]. Basalt fibers are also have a better binding performance with the cement due to its similar chemical properties with cement, and it is cheaper compared to the other widely used fibers in civil engineering researches [25]. Basalt fibers have many times greater tensile strength than steel fibers, and it has been widely used as small pieces during the mix design of concrete composites in civil engineering applications [26]. Steel and polypropylene fibers addition to the lightweight concrete mixes has been widely researched, and different results reported due to the variety of the examined parameters. In most cases, positive influences [27–29] have been reported for the strength improvement of the cementitious composites. However, very limited literature exists for the basalt fibers on the lightweight concrete composite production. The researches into basalt fiber added conventional concrete were generally focused on the mechanical properties of the composites. Those research results indicate that basalt fibers addition up to 0.5 % by volume was beneficial, and optimum fiber dosage can vary significantly according to the types of the concretes [17, 30, 31]. Primary benefit of basalt fiber addition can be evaluated as a shift from a brittle failure behavior to more ductile one for conventional concrete mixes under compressive loads [31]. And literature suggest that basalt fiber addition can significantly increase the tensile strength of concrete [32]. Basalt fiber inclusion has also been shown to increase toughness of the concrete; however, it is difficult to assess the relative benefits since different test methods were applied [33].

Portland cement is one of the fundamental components of the mortar, grout and concrete production. Approximately, 5.78 GJ of thermal and 138 kWh of electricity energies are consumed intensively during the production of one ton of Portland cement [34]. Cement production is also responsible for the release of significant amount of CO₂ emissions. It was estimated by International Energy Agency (IEA) that CO₂ emissions during the cement production could be reduced by 18 % compared to the current levels by 2050 [35]. There are many ways to reduce the carbon footprint of the cement production such as carbon capture and storage, improving thermal and electric efficiency, clinker substitution and reducing usage of cement amount in construction industry. By product materials such as silica fume, fly ash and slags are daily used in the production of concrete as cement replacement materials [36]. In addition, many researches have been conducted focusing on the potential usage of minerals as cement supplementary materials [37–40]. GCC have typical particle size comparable to Portland cement. Nano GCC is generally utilized as mineral filler in concrete mixes [41]. Increased early strengths were obtained in many studies by replacing cement with the nano GCC, however, high dosage GCC inclusion as cement supplementary material in concrete can be resulted in reduced strength [15, 42]. The reactivity of the nano GCC depends on its surface area, and smaller particles provide more surface area for the reaction with the C₃A [43]. GCC has small grinding energy consumption compared to the other supplementary materials due to its low hardness [44].

Available experimental results from the literature review revealed that the use of basalt fiber in pumice lightweight concrete containing nano GCC cannot be considered as sufficient. Reported research results reflect many dissimilarities due to variety of examined parameters. This study aims to discover mechanical and durability properties of basalt fiber reinforced pumice lightweight concrete containing nano ground calcium carbonate. Compressive and flexural strength tests were carried out within the scope of the study. This study also aims to enrich available experimental data in the literature on the pumice lightweight concrete production in order to reach a better understanding of its behavior.

2. Methods

2.1. Materials and Mixture Design

The materials used in this study are Fine Aggregates (FA), Pumice Aggregates (PA), Basalt Fibers (BF), commercially available nano GCC (Betocarb® F) and CEM I 42.5 R Cement. Particle size distribution of and physical properties of the blended aggregates are given in Figure 1 and Table 1, respectively.

BFs with the length of 6 mm were used in the experimental study. The technical properties of the BF are summarized in Table 2. Polycarboxylic based hyper plasticizer was utilized in all mixtures at the amount of 1.25 % of cement by weight.

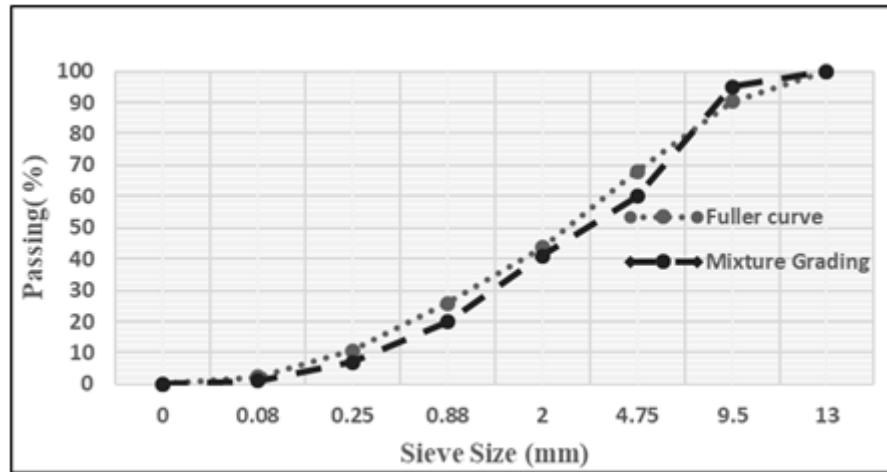


Figure 1. Particle size distribution of mixture and Fuller curve.

Table 1. Physical properties of the aggregates.

Aggregates	Particle size (mm)	Particle density (g/cm ³)	Los Angeles abrasion loss (%)
Fine aggregate(FA)	0–4	1.071	–
Pumice Aggregate(PA)	2–12	0.395	70.9

Table 2. Physical and chemical properties of the BF.

Technical property	
Elasticity module, MPa	90
Tensile strength, MPa	4832
Melting point, C°	1452
Application temperature, C°	–220/+980
Chemical composition	
Chemical composition	Percentages (%)
SiO ₂	51.2–58.9
Al ₂ O ₃	14.5–18.2
Fe ₂ O ₃	5.7–9.6
MgO	3.0–5.4
FeO + Fe ₂ O ₃	9.2–14.0
TiO ₂	0.8–2.25
Na ₂ O + K ₂ O	0.8–2.25
Others	0.08–0.14

Material properties of cement and Betocarb® F are presented in Table 3. It can be clearly seen from the chemical composition of the materials (Table 2 and 3) that BF and cement have similar very similar chemical properties, and this similarity can be resulted in good bonding mechanism among these materials [25].

Table 3. Material properties of cement, PA and Betocarb® F.

Chemical composition (%) & Physical property	Cement	PA	Betocarb® F
Fe ₂ O ₃	3.52	1.5	3.19
CaO	60.21	0.2	11.77
SiO ₂	20.19	75.84	61.14
MgO	2.32	0.4	2.43
SO ₃	2.61	0.5	–
Al ₂ O ₃	4.32	12.54	7.42
Free CaO, %	1.7	–	–
Loss on ignition	2.85	5.63	4.6
Specific gravity	3.12	1.05	–
Specific surface (cm ² /g)	3,618	–	>30,000
Blue value	–	–	<3
d50 %	–	–	3

Table 4 summarizes the mix design and material proportions. Mixtures were prepared with a pan mixer and its capacity is 60 L. The mixer rate was kept constant as 250 r/min in order to prevent the BF breakings. 16 lightweight concrete mixes were designed within the scope of this study. The blends were coded in line with the nano GCC addition and BF contents. "R" defines reference mix with no GCC inclusion and any BF content. Other mixes were coded as "PCx-y", where "x" represents the changed ratio (%) of nano GCC by cement by weight, and "y" defines the BF inclusions (%) by volume of the concrete.

Table 4. Mixture proportions of lightweight concrete specimens (kg/m³).

Mixture code	Cement (kg)	GCC (kg)	FA (kg)	PA (kg)	Water (kg)	BF (V_f , %)	Superplasticizer (kg)
R	170	0	775	416	78	0	2.55
PC5	161.5	8.5	775	416	78	0	2.55
PC5-0.5	161.5	8.5	775	416	78	0.5	2.55
PC5-1	161.5	8.5	775	416	78	1	2.55
PC10	153	17	775	416	78	0	2.55
PC10-0.5	153	17	775	416	78	0.5	2.55
PC10-1	153	17	775	416	78	1	2.55
PC15	144.5	25.5	775	416	78	0	2.55
PC15-0.5	144.5	25.5	775	416	78	0.5	2.55
PC15-1	144.5	25.5	775	416	78	1	2.55
PC20	136	34	775	416	78	0	2.55
PC20-0.5	136	34	775	416	78	0.5	2.55
PC20-1	136	34	775	416	78	1	2.55
PC25	127.5	42.5	775	416	78	0	2.55
PC25-0.5	127.5	42.5	775	416	78	0.5	2.55
PC25-1	127.5	42.5	775	416	78	1	2.55

2.2. Sample preparation and testing

The effect of BF addition and replacing cement with nano GCC was investigated by physical, mechanical and durability laboratory tests. Spread diameters of the blends were evaluated by slump test. Slump test were repeated three times with 20 min (first test time includes mixing duration) intervals in order to determine slump losses. Setting times of the specimens were determined according to the requirements of BS EN 196-3 [45]. Physical test includes the measurements of sorptivity, bulk dry density and water absorption. And mechanical test were flexural strength test and compression tests. All physical, durability and mechanical tests were conducted at 7, 28, 90 and 180 days.

Bulk density and water absorption of the specimens were recorded according to the requirements of ASTM C 642 [46]. The disc specimens ($\varnothing 100/50$) were prepared and initially oven dried at 105 °C and cooled in room temperature and their weight were recorded (W_1). Following this process, the specimens were boiled for 5 hours in a container and left in the container for a natural cooling process. Then boiled surface dried mass of the specimens were recorded (W_2). Mass of the specimens after the boiling and immersion processes were recorded as W_3 . Bulk dry density (B_{dd} , kg/m³) and water absorption (W_a , %) of the concrete mixes were determined by Equations (1) and (2), respectively:

$$B_{dd} = W_1 / (W_2 - W_3); \quad (1)$$

$$W_a = [(W_2 - W_1) / W_1] \times 100. \quad (2)$$

Sorptivity test was recorded according to the ASTM C 1585 [47]. Disc specimens ($\varnothing 100/50$) were isolated with paraffin material as per the requirements of the standard. The mass of the specimen was measured at 7, 28, 90 and 180 days.

Compressive strength test was conducted on $\varnothing 150/300$ mm cylindrical specimens according to the ASTM C 469 standard [48]. Flexural strength tests were performed on 100×100×500 mm specimens as per the requirements of EN 14651 [49]. Prismatic specimens were notched before the test procedure according to the EN 14651 standard at their mid-span width.

Lightweight concrete blocks are widely used in the animal shelters; therefore, it is of great importance to evaluate the acid effect on concrete blocks. Magnesium sulfate attack effect on concrete specimens was evaluated with compressive strength change. Two groups of specimens were prepared during the test. One group was kept curing in water, and the second group was exposed to magnesium sulfate concentration of 10 % in a separate container. Magnesium sulfate concentration was renewed every 20 days till the end of the test time (180 days). Compressive strength changes of the two groups were recorded at 7, 28, 90 and 180 days.

3. Results and Discussion

3.1. Fresh concrete properties

Slump and setting time test results are presented in Figure 4 and 5, respectively. Effects of nano GCC addition on slump tests are shown in Figure 4. Nano GCC inclusion up to 20 % by weight increased the spread diameter of the mixes. This can be attributed to the irregular shape of nano GCC particles (Figure 2). These results also show that nano GCC replacement by more than 20 % of the cement weight had very adverse effects on concrete workability, and this effect should be taken into consideration well when aiming to utilize such mixes for long term slump preservation behaviors. In addition, the negative impact of the presence of PA on the workability should not be neglected, since it has a porous microstructure (Figure 3).

Increasing the BF reduces the slump flow diameter of the produced concrete mixes as seen in Figure 4. BF utilization in concrete mixes generally result in slump decreases [50]. This situation can be explained as the extra cement paste and mixing water consumption of BFs and increase in the friction of coefficient between cement and BF during the mixing process. Slump test results were obtained in parallel with the previously conducted studies [30, 51]. Figure 4 also shows that all mixture kept their plasticity and cohesive behavior at 60 min.

BF and nano GCC addition negatively affected the setting times of the concrete mixes as shown in Figure 5. The results indicated a slower hydration process compared to the reference paste. In other words, slow hydration process means of releasing less heat during hydration reactions [52]. Therefore, BF and nano GCC added blends at specific ratios can be beneficial in mass concrete construction.

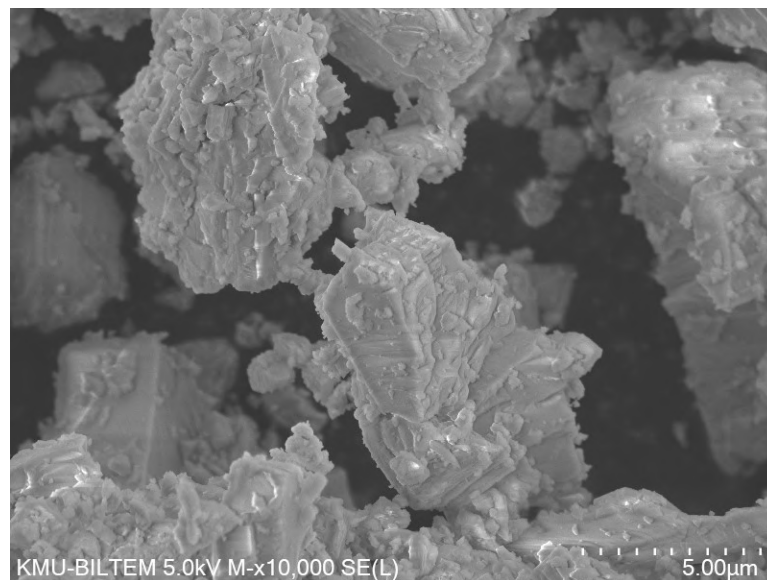


Figure 2. SEM images of GCC particles.

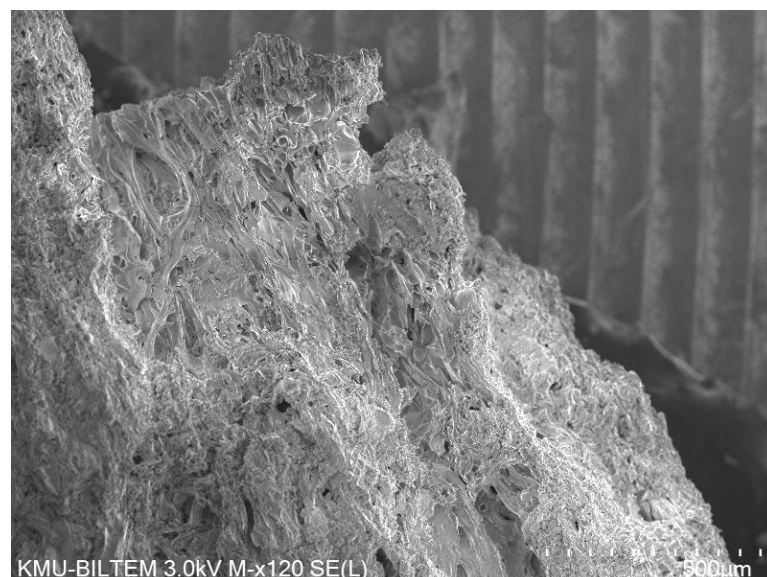


Figure 3. SEM images of PA particles.

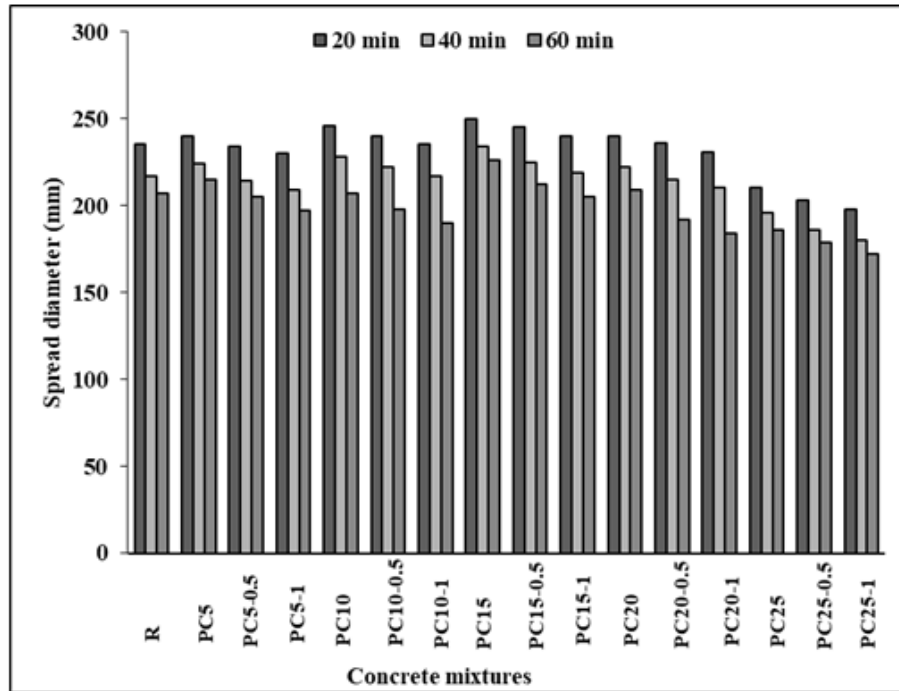


Figure 4. Slump test results.

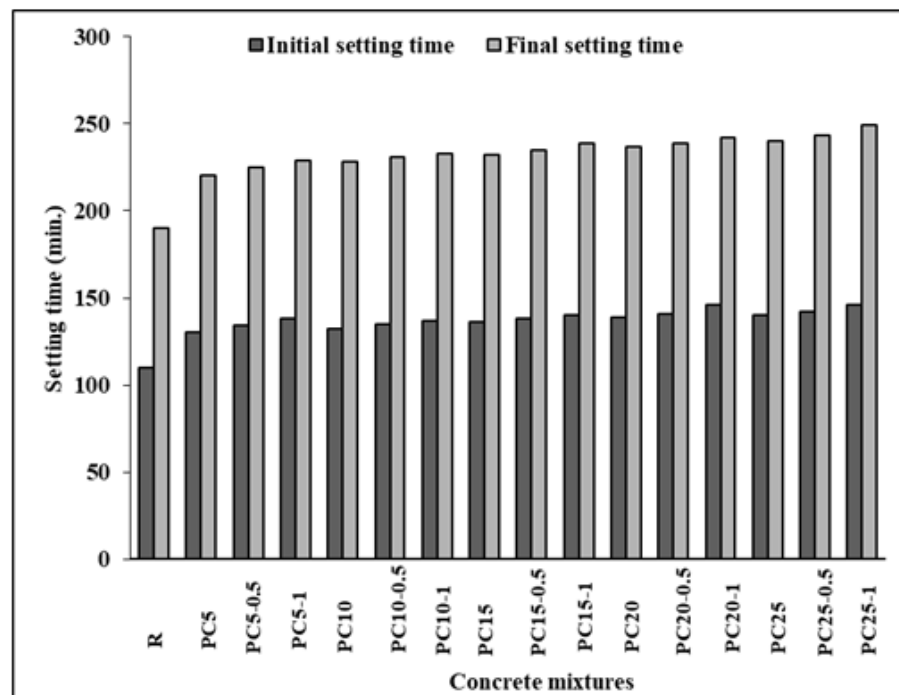


Figure 5. Setting times of the concrete mixes.

3.2. Physical properties

Water absorption and bulk dry density of the concrete mixes at 7, 28, 90 and 180 days are presented in Figure 6 and 7, respectively. Figure 6 show that water absorption rate of the all pumice concrete mixes are gradually reduced at later ages. Water absorption rates of the specimens vary between 20.54 % and 22.24 % at 7 days. PC10-1 had the minimum value. Nano GCC and BF addition both lowered the water absorption ratio at 7 days. This can be attributed to filling of void volumes by BF and GCC particles. Water absorption rates of the mixtures continued to decrease at 180 days, where PC10-1 had the lowest value as 12.28 %. It can also be noted that BF inclusion increased the water absorption rate compared to the mixtures having same nano GCC content.

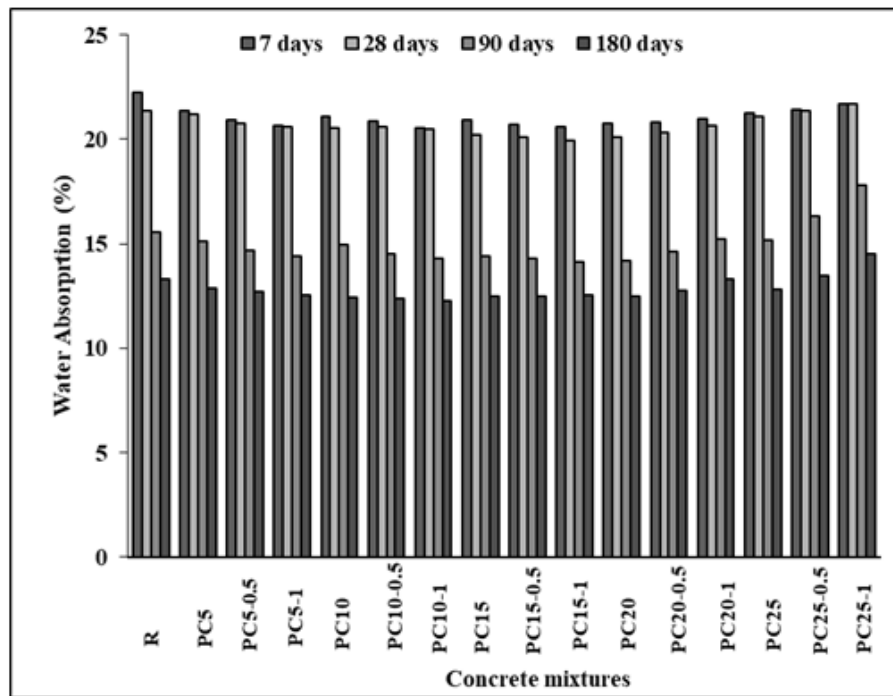


Figure 6. Water absorption test results.

Dry bulk density test results of the concrete mixes are given in Figure 7. Density values are increased with the curing time and, highest dry bulk density values were obtained at 180 days. Nano GCC addition increased the dry bulk densities compared to the reference mix. BF reinforced mixes indicated slightly lower values than the only GCC added mixes on every experimental set up.

Sorptivity test results of the concretes are given in Figure 8, where it can be noted that sorptivity values decreased with the increasing curing time. Lowest value obtained at 180 days, and BF and GCC addition both decreased the sorptivity of mixes compared to the reference mix.

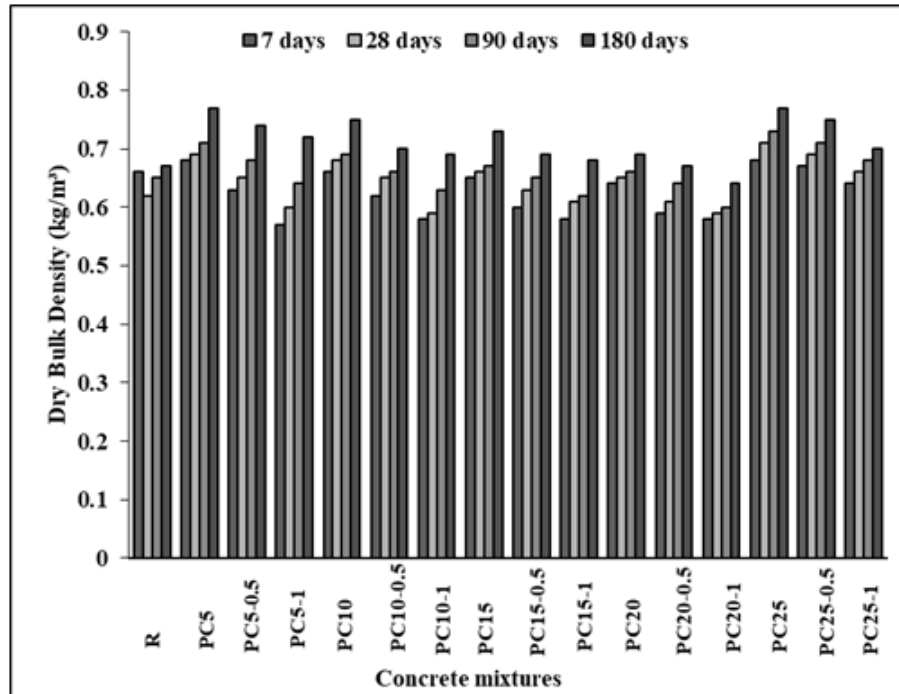


Figure 7. Dry bulk density test results.

In most cases, denser microstructure and lower absorption test results were obtained during the physical property tests. It can be expected positive contributions to the concrete durability according to the test results. The improvement in physical properties of the BPLC can be clarified by filling of voids by nano GCC and BFs. Nano GCC acted as inert mineral filler as stated in previously concluded researches [53, 54].

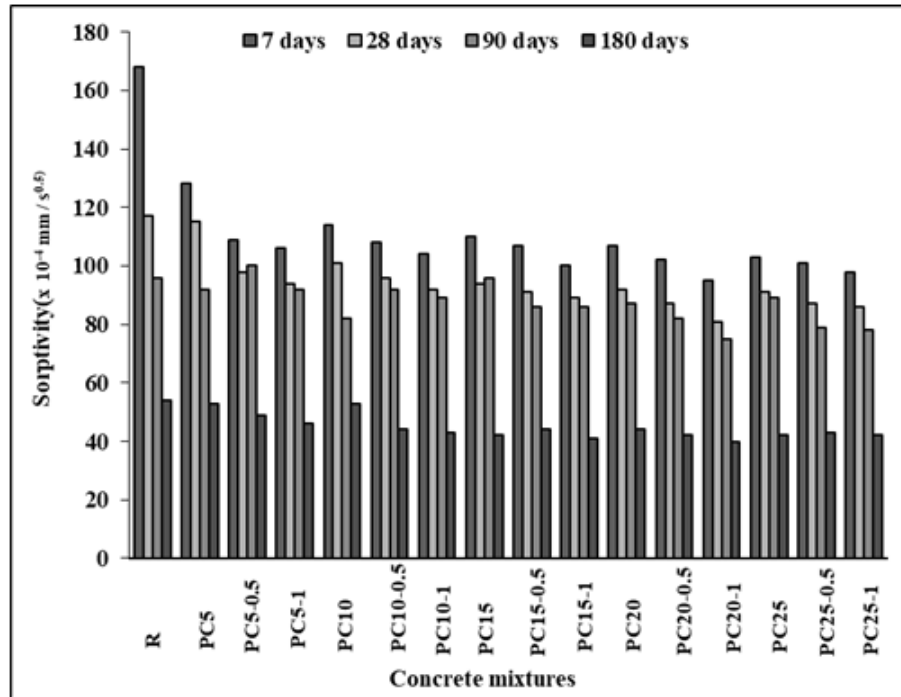


Figure 8. Sorptivity of concretes.

3.3. Mechanical properties

The average compressive strength test results are presented in Figure 9, where nano GCC addition up to 10 % and BF inclusion increased the test results compared to the reference mix. GCC addition was contributed to early strength development of the specimens. The compressive strength values of the mixes containing more than 10 % replaced cement, reduced at all ages. This can be attributed to high GCC content and the dilution effect. Adding certain amount of GCC could be reacted with aluminate phases in the cement, and this reaction can produce more ettringite which as a larger volume than other hydration products. As a result, denser concrete microstructure can be formed, and this situation leads to better strength properties.

BF reinforced specimens indicated better compressive strength performances compared to the other specimens. Especially, it was also found that BF addition of 1 % of volume showed the best compressive strength test results. Many researches highlighted that basalt finer usage up to 0.5 % by volume provides better results [55]; however, test results according to the used fiber content notably varied in terms of produced concrete types [18].

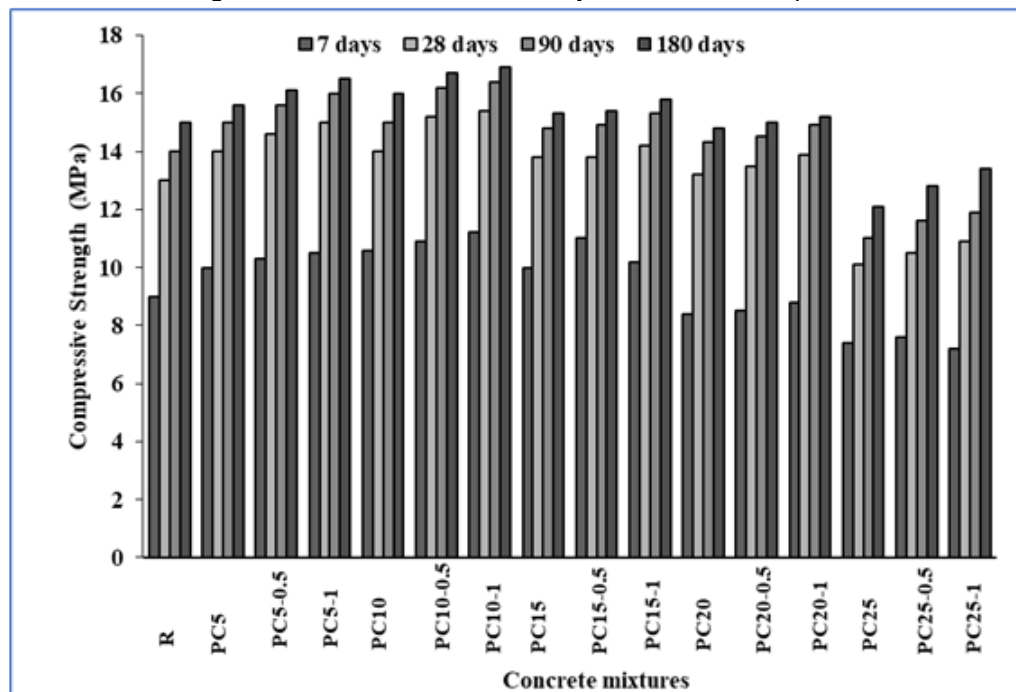


Figure 9. Compressive test results.

Figure 10 presents the flexural test results of the lightweight concretes. Flexural strength values increased with the increase in BF content of the concrete specimens. Mixes containing more than 10 % of replaced cement content showed lower performance than other mixes. In addition, a gradual increase with the curing time was also observed. Specimen PC10-1 showed the best flexural performance compared to the other specimens.

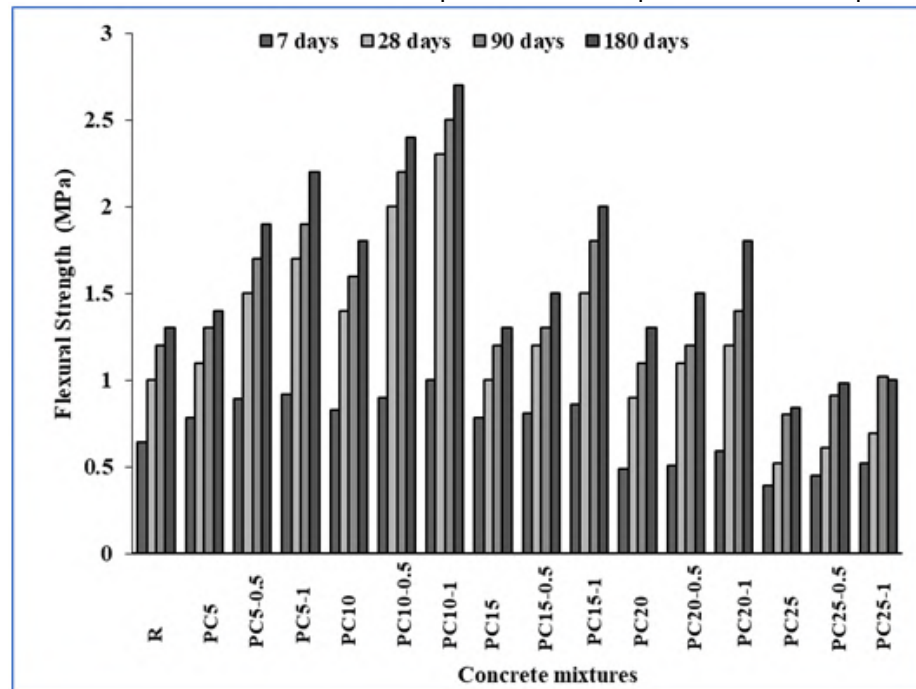


Figure 10. Flexural test results.

3.4. Magnesium sulfate resistance

Sulfate resistance of concrete has great importance in the concrete production focused literature studies [56]. It was also noted that magnesium sulfate attack can be resulted in the transformation of C-S-H gel to a non-cementitious M-S-H gel (Equation (3)) [57].



In this research, concrete behavior against magnesium sulfate was determined by compressive strength changes of mixes at 7, 28, 90 and 180 days. Magnesium sulfate effect increased with the exposure time as seen in Figure 11. The most deleterious sulfate effect was observed on the reference mix at both ages. Contrary, GCC and BF addition to mixes (except PC25, PC25-0.5 and PC25-1 specimens) improved the behavior of concretes against sulfate solution. PC10-1 and PC5-1 specimens showed the lowest compressive strength losses compared to the other mixes as 25.24 % and 25.98 % at 180 days, respectively. This value was obtained as 37 % for the reference specimens.

The overall magnesium sulfate resistance test results indicated that the replacement of cement with certain amount of nano GCC (up to 10 %) had very significant effect on the concrete in terms of durability properties. BFs addition up to 1 % of volume also contributed to enhance the sulphate attack resistance by filling up voids in the concrete structure. More impermeable and low carbon footed BPLC specimens were produced within the scope of this study.

4. Conclusion

In this paper, the influences of utilizing nano GCC as cement supplementary materials on the BF reinforced lightweight concrete mixes were examined. The main conclusion of this research can be drawn as follows:

1. Nano GCC replacement with cement up to 20 % increased the slump value of the concretes with no BF content. BF reinforced concrete mixes spread diameter values decreased with the increasing BF content. BF and nano GCC content contributed concrete mixes to preserve their plasticity and cohesive behavior up to 60 min, in some cases. However, both GCC and BF inclusion increased the setting times of the mixes.
2. Utilizing GCC as cement supplementary materials and BF reinforcement resulted in lower absorption rates and sorptivity with the increasing time compared to the reference mixes.
3. The addition of BF up to 1 % of concrete volume and GCC inclusion up to 10 %, as expected, increased the both early and late age strength properties of concrete. Especially, early strength properties were enhanced with the addition certain amount of nano GCC.

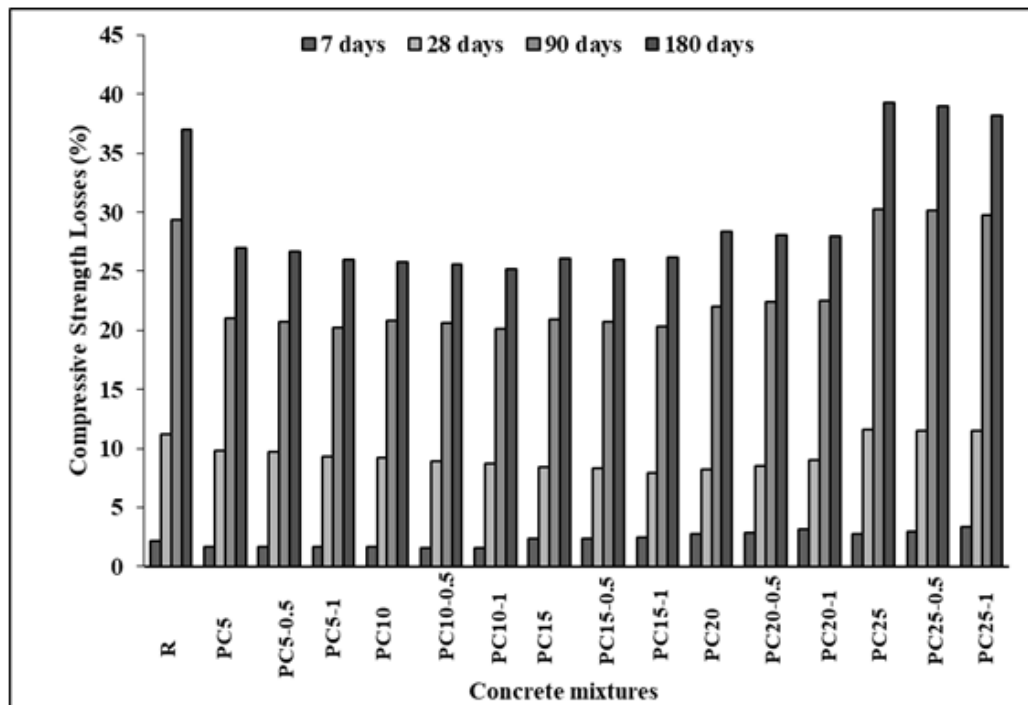


Figure 11. Magnesium sulfate attack effects on compressive strength of concretes.

4. Magnesium sulfate resistance of concretes improved with prepared mixes. PC10-1 and PC5-1 specimens showed the best performance against sulfate attack.

5. In this study, BF and GCC additions to blends in certain amounts improved the durability, fresh state and mechanical properties of the concretes. Produced BPLC mixture design can be considered for lightweight concrete block industry, since pumice is abundant in Turkey.

5. Acknowledgement

The author would like to acknowledge to staff of KMU-BILTEM for their helps and supports.

References

1. Zaetang, Y., Wongsa, A., Sata, V., Chindaprasirt, P. Use of lightweight aggregates in pervious concrete. *Construction and Building Materials*. 2013. DOI: 10.1016/j.conbuildmat.2013.07.077.
2. Hamad, A.J. Materials, Production, Properties and Application of Aerated Lightweight Concrete: Review. *International Journal of Materials Science and Engineering*. 2014. DOI: 10.12720/ijmse.2.2.152-157.
3. Kockal, N.U., Ozturan, T. Durability of lightweight concretes with lightweight fly ash aggregates. *Construction and Building Materials*. 2011. DOI: 10.1016/j.conbuildmat.2010.09.022.
4. Posi, P., Teerachanwit, C., Tanutong, C., Limkamoltip, S., Lertnimoolchai, S., Sata, V., Chindaprasirt, P. Lightweight geopolymer concrete containing aggregate from recycle lightweight block. *Materials and Design*. 2013. DOI: 10.1016/j.matdes.2013.06.001.
5. Aliabdo, A.A., Abd-Elmoaty, A.E.M., Hassan, H.H. Utilization of crushed clay brick in concrete industry. *Alexandria Engineering Journal*. 2014. DOI: 10.1016/j.aej.2013.12.003.
6. The Pennsylvania State University. *The Effect of Aggregate Properties on Concrete*. 2014.
7. Kramar, D., Bindiganavile, V. Impact response of lightweight mortars containing expanded perlite. *Cement and Concrete Composites*. 2013. DOI: 10.1016/j.cemconcomp.2012.10.004.
8. Barabanshchikov, Y., Gutskalov, I. Strength and Deformability of Fiber Reinforced Cement Paste on the Basis of Basalt Fiber. *Advances in Civil Engineering*. 2016. 2016. DOI: 10.1155/2016/6562526.
9. Nizina, T.A., Balykov, A.S., Volodin, V. V., Korovkin, D.I. Fiber fine-grained concretes with polyfunctional modifying additives. *Magazine of Civil Engineering*. 2017. 72(4). Pp. 73–83. DOI: 10.18720/MCE.72.9.
10. Nizina, T.A., Ponomarev, A.N., Balykov, A.S., Pankin, N.A. Fine-grained fibre concretes modified by complexed nanoadditives. *International Journal of Nanotechnology*. 2017. 14(7–8). Pp. 665–679. DOI: 10.1504/IJNT.2017.083441.
11. Alhassan, M., Al-Rousan, R., Ababneh, A. Flexural behavior of lightweight concrete beams encompassing various dosages of macro synthetic fibers and steel ratios. *Case Studies in Construction Materials*. 2017. DOI: 10.1016/j.cscm.2017.09.004.
12. Nguyen-Minh, L., Rovňák, M., Tran-Quoc, T., Nguyen-Kim, K. Punching shear resistance of steel fiber reinforced concrete flat slabs. *Procedia Engineering*. 2011.
13. Juenger, M.C.G., Winnefeld, F., Provis, J.L., Ideker, J.H. *Advances in alternative cementitious binders*. 2011.
14. Show, K.-Y., Tay, J.-H., Lee, D.-J. *Cement Replacement Materials. Sustainable Sludge Management*. 2018.
15. Antoni, Chandra, L., Hardjito, D. The impact of using fly ash, silica fume and calcium carbonate on the workability and compressive strength of mortar. *Procedia Engineering* 2015.
16. Yew, M.K., Mahmud, H. Bin, Ang, B.C., Yew, M.C. Influence of different types of polypropylene fibre on the mechanical properties of high-strength oil palm shell lightweight concrete. *Construction and Building Materials*. 2015. DOI: 10.1016/j.conbuildmat.2015.04.024.
17. Jiang, C., Fan, K., Wu, F., Chen, D. Experimental study on the mechanical properties and microstructure of chopped basalt fibre

- reinforced concrete. *Materials and Design*. 2014. DOI: 10.1016/j.matdes.2014.01.056.
18. Branston, J., Das, S., Kenno, S.Y., Taylor, C. Mechanical behaviour of basalt fibre reinforced concrete. *Construction and Building Materials*. 2016. DOI: 10.1016/j.conbuildmat.2016.08.009.
 19. Asprone, D., Cadoni, E., Iucolano, F., Prota, A. Analysis of the strain-rate behavior of a basalt fiber reinforced natural hydraulic mortar. *Cement and Concrete Composites*. 2014. DOI: 10.1016/j.cemconcomp.2014.06.009.
 20. Šliseris, J., Gaile, L., Pakraštinš, L., Rocēns, K. Nonlinear numerical modelling of basalt rebar reinforced concrete structures. *Vide Tehnologija. Resursi – Environment, Technology, Resources*. 2017. 3. Pp. 304–309. DOI: 10.17770/etr2017vol3.2655.
 21. Shariq, M., Prasad, J., Abbas, H. Effect of GGBFS on age dependent static modulus of elasticity of concrete. *Construction and Building Materials*. 2012. DOI: 10.1016/j.conbuildmat.2012.12.035.
 22. Saha, A.K. Effect of class F fly ash on the durability properties of concrete. *Sustainable Environment Research*. 2018. DOI: 10.1016/j.serj.2017.09.001.
 23. Frazão, C., Barros, J., Toledo Filho, R., Ferreira, S., Gonçalves, D. Development of sandwich panels combining Sisal Fiber-Cement Composites and Fiber-Reinforced Lightweight Concrete. *Cement and Concrete Composites*. 2018. DOI: 10.1016/j.cemconcomp.2017.11.008.
 24. Ralegaonkar, R., Gavali, H., Aswath, P., Abolmaali, S. Application of chopped basalt fibers in reinforced mortar. 2018.
 25. Libre, N.A., Shekarchi, M., Mahoutian, M., Soroushian, P. Mechanical properties of hybrid fiber reinforced lightweight aggregate concrete made with natural pumice [Online]. *Construction and Building Materials*. 2011. 25(5). Pp. 2458–2464. DOI: 10.1016/j.conbuildmat.2010.11.058. URL: <http://dx.doi.org/10.1016/j.conbuildmat.2010.11.058>.
 26. Arslan, M.E. Effects of basalt and glass chopped fibers addition on fracture energy and mechanical properties of ordinary concrete: CMOD measurement. *Construction and Building Materials*. 2016. DOI: 10.1016/j.conbuildmat.2016.03.176.
 27. Grabois, T.M., Cordeiro, G.C., Toledo Filho, R.D. Fresh and hardened-state properties of self-compacting lightweight concrete reinforced with steel fibers. *Construction and Building Materials*. 2016. DOI: 10.1016/j.conbuildmat.2015.12.060.
 28. Kim, Y.-J., Hu, J., Lee, S.-J., You, B.-H. Mechanical Properties of Fiber Reinforced Lightweight Concrete Containing Surfactant. *Advances in Civil Engineering*. 2010. DOI: 10.1155/2010/549642.
 29. Balendran, R.V., Zhou, F.P., Nadeem, A., Leung, A.Y.T. Influence of steel fibres on strength and ductility of normal and lightweight high strength concrete. *Building and Environment*. 2002. DOI: 10.1016/S0360-1323(01)00109-3.
 30. Dias, D.P., Thaumaturgo, C. Fracture toughness of geopolymeric concretes reinforced with basalt fibers. *Cement and Concrete Composites*. 2005. DOI: 10.1016/j.cemconcomp.2004.02.044.
 31. Iyer, P., Kenno, S.Y., Das, S. Mechanical Properties of Fiber-Reinforced Concrete Made with Basalt Filament Fibers. *Journal of Materials in Civil Engineering*. 2015. DOI: 10.1061/(asce)mt.1943-5533.0001272.
 32. Lipatov, Y. V., Gutnikov, S.I., Manylov, M.S., Zhukovskaya, E.S., Lazoryak, B.I. High alkali-resistant basalt fiber for reinforcing concrete. *Materials and Design*. 2015. DOI: 10.1016/j.matdes.2015.02.022.
 33. Elgabbas, F., Vincent, P., Ahmed, E.A., Benmokrane, B. Experimental testing of basalt-fiber-reinforced polymer bars in concrete beams. *Composites Part B: Engineering*. 2016. DOI: 10.1016/j.compositesb.2016.01.045.
 34. Stafford, F.N., Raupp-Pereira, F., Labrincha, J.A., Hotza, D. Life cycle assessment of the production of cement: A Brazilian case study. *Journal of Cleaner Production*. 2016. DOI: 10.1016/j.jclepro.2016.07.050.
 35. WBCSD. *Cement Technology Roadmap 2009: Carbon emissions reduction up to 2050*2009.
 36. Halicka, A., Ogrodnik, P., Zegardlo, B. Using ceramic sanitary ware waste as concrete aggregate. *Construction and Building Materials*. 2013. DOI: 10.1016/j.conbuildmat.2013.06.063.
 37. Taylor-Lange, S.C., Lamon, E.L., Riding, K.A., Juenger, M.C.G. Calcined kaolinite-bentonite clay blends as supplementary cementitious materials. *Applied Clay Science*. 2015. DOI: 10.1016/j.clay.2015.01.025.
 38. Lothenbach, B., Scrivener, K., Hooton, R.D. Cement and Concrete Research Supplementary cementitious materials. *Cement and Concrete Research*. 2011. DOI: 10.1016/j.cemconres.2010.12.001.
 39. Juenger, M.C.G., Siddique, R. Recent advances in understanding the role of supplementary cementitious materials in concrete. 2015.
 40. Chandra, S., Berntsson, L. *Supplementary Cementing Materials. Lightweight Aggregate Concrete*. 2008.
 41. Performance of Concrete Incorporating Limestone Dust as Partial Replacement for Sand. *ACI Journal Proceedings*. 2014. DOI: 10.14359/10344.
 42. Qian, X., Wang, J., Wang, L., Fang, Y. Enhancing the performance of metakaolin blended cement mortar through in-situ production of nano to sub-micro calcium carbonate particles. *Construction and Building Materials*. 2019. DOI: 10.1016/j.conbuildmat.2018.11.134.
 43. Matschei, T., Lothenbach, B., Glasser, F.P. The role of calcium carbonate in cement hydration. *Cement and Concrete Research*. 2007. DOI: 10.1016/j.cemconres.2006.10.013.
 44. Chen, Y., Yu, H., Yi, L., Liu, Y., Cao, L., Cao, K., Liu, Y., Zhao, W., Qi, T. Preparation of ground calcium carbonate-based TiO₂ pigment by a two-step coating method. *Powder Technology*. 2018. DOI: 10.1016/j.powtec.2017.11.040.
 45. BS EN 196-3. *Methods of testing cement — Part 3: determination of setting times and soundness*. British Standard. 2016. DOI: 10.1111/j.1748-720X.1990.tb01123.x.
 46. ASTM International. *ASTM C 642-06 Standard Test Method for Density, Absorption, and Voids in Hardened Concrete*. United States: American Society for Testing and Material. 2008. DOI: 10.1520/C0642-13.5.
 47. ASTM C 1585. *Standard Test Method for Measurement of Rate of Absorption of Water by Hydraulic-*. ASTM International. 2013. DOI: 10.1520/C1585-13.2.
 48. ASTM C469. *Standard Test Method for Static Modulus of Elasticity and Poisson's Ratio of Concrete*. 2015.
 49. EN 14651. *Test method for metallic fibred concrete — Measuring the flexural tensile strength (limit of proportionality (LOP), residual)*. British Standards Institute. 2005. DOI: 9780580610523.
 50. Kabay, N. Abrasion resistance and fracture energy of concretes with basalt fiber. *Construction and Building Materials*. 2014. DOI: 10.1016/j.conbuildmat.2013.09.040.
 51. Ma, J., Qiu, X., Cheng, L., Wang, Y. Experimental Research on the Fundamental Mechanical Properties of Presoaked Basalt Fiber Concrete. *Advances in FRP Composites in Civil Engineering*2012.
 52. Hossain, K.M.A. Blended cement using volcanic ash and pumice. *Cement and Concrete Research*. 2003. DOI: 10.1016/S0008-8846(03)00127-3.

53. Diamanti, M. V., Lollini, F., Pedferri, M.P., Bertolini, L. Mutual interactions between carbonation and titanium dioxide photoactivity in concrete. *Building and Environment*. 2013. DOI: 10.1016/j.buildenv.2013.01.023.
54. Jiang, Z., Li, W., Yuan, Z. Influence of mineral additives and environmental conditions on the self-healing capabilities of cementitious materials. *Cement and Concrete Composites*. 2015. DOI: 10.1016/j.cemconcomp.2014.11.014.
55. Fiore, V., Scalici, T., Di Bella, G., Valenza, A. A review on basalt fibre and its composites. *Composites Part B: Engineering*. 2015. DOI: 10.1016/j.compositesb.2014.12.034.
56. Aye, T., Oguchi, C.T. Resistance of plain and blended cement mortars exposed to severe sulfate attacks. *Construction and Building Materials*. 2011. DOI: 10.1016/j.conbuildmat.2010.11.106.
57. Lee, S.T., Moon, H.Y., Hooton, R.D., Kim, J.P. Effect of solution concentrations and replacement levels of metakaolin on the resistance of mortars exposed to magnesium sulfate solutions. *Cement and Concrete Research*. 2005. DOI: 10.1016/j.cemconres.2004.10.035.
58. Kabay, N., Tufekci, M.M., Kizilkanat, A.B., Oktay, D. Properties of concrete with pumice powder and fly ash as cement replacement materials. *Construction and Building Materials*. 2015. DOI: 10.1016/j.conbuildmat.2015.03.026.

Contacts:

Seyma Nur Karaburc, seymanurkaraburc@gmail.com

Sadik Alper Yildizel, sayildizel@kmu.edu.tr

Gokhan Calis, gokhancalis@kmu.edu.tr

© Karaburc, S.N., Yildizel, S.A., Calis, G.C., 2020



DOI: 10.18720/MCE.94.8

Behavior of strengthened concrete beams damaged by thermal shock

R. Al-Rousan*

Jordan University of Science and Technology, Irbid, Jordan

* E-mail: rzalrousan@just.edu.jo

Keywords: reinforced concrete, thermal shock, structural strength, shear, flexural strength, fiber reinforced polymer, nonlinear, finite element analysis

Abstract. In the last two decades, using of Carbon Fiber Reinforced Polymers (CFRP) in strengthening of deficient reinforced concrete structural elements has been increased due to their ease of installation, low invasiveness, high corrosion resistance, and high strength to weight ratio. Strengthening damage structures is a relatively new technique. The aims of this study is to investigate the effectiveness of using CFRP to regain shear capacity of shear-deficient reinforced concrete (RC) beams after being damaged by thermal shock. Firstly, a novel Nonlinear Finite Element Analysis (NLFEA) model is created and validated. Then, Ten RC beams (100×150×1400 mm) have been constructed and divided into two groups to scrutinize the effect of CFRP strip number and thermal shock impact. The performance of each beam was evaluated in terms of failure mode, CFRP strain, load-deflection behavior, ultimate deflection, ultimate load capacity, elastic stiffness, toughness, performance factor, and profitability Index of the CFRP Strips. Load carrying capacity and stiffness of RC beams decreased about 68 % and 71 %, respectively, as compared with reference undamaged beam. Strengthening the thermal damaged RC beams allowed recovering the original load carrying without achieving the original stiffness. Strengthened beams with fully CFRP plates regained the original load capacity with a corresponding stiffness from 79 % to 105 %, respectively. Finally, the enhancement percentage increased with the increase of bonded area or number of CFRP strips and these percentages sharply dropped for damaged beams.

1. Introduction

Flexural and shear are the main failure modes of RC beams. Shear failure of RC beams is classified as brittle and occurs unexpectedly without any warning while the flexural failure is ductile. Therefore, it is a necessity to make sure that the shear design of RC beams must be safe in order to develop their full flexural capacity. Unfortunately, many of existing RC beams suffering shear deficiencies due to construction faults, poor construction practices, mistakes in design calculations, changing in structure function, improper detailing of shear reinforcement and steel corrosion. Elevated temperatures cause severe damage for reinforced concrete (RC) structures, such as RC beams. RC beams have been reported to loss strength and stiffness with relatively large permanent deformations because of exposure to high temperatures [1]. These harmful effects could be attributed to the deterioration of mechanical characteristics of concrete and steel rebars and the redistribution of stresses within the beam due to the elevated temperatures [2–17]. Currently, the most commonly used technique to repair the heat-damaged RC beams is using carbon fiber reinforced polymer (CFRP) composites. These sheets are advanced materials that can be easily applied on the structures and characterized by outstanding mechanical and corrosion resistance characteristics. Various studies were performed to investigate the flexural behavior of RC beams wrapped with CFRP. The results showed that externally bonded carbon FRP (CFRP) sheets and laminates has the ability to enhance the flexural behavior of the beams and recover, to certain limit, the flexural strength of heat-damaged beams. Strengthening level or recovery depends on several factors such as degree of beam's damage, geometry and type of fiber sheet, CFRP layers number, and the resin's type and properties [18–33].

Reinforcing concrete structures are often subjected to cycles of heating–cooling such as in chimneys, concrete foundations for launching rockets carrying spaceships, concrete near to furnace, clinker silos and nuclear power plants, or those subjected to fire then extinguished using water. Temperature cycles are critical

Al-Rousan, R. Behavior of strengthened concrete beams damaged by thermal shock. Magazine of Civil Engineering, 2020. 94(2). Pp. 93–107. DOI: 10.18720/MCE.94.8



This work is licensed under a [CC BY-NC 4.0](https://creativecommons.org/licenses/by-nc/4.0/)

to the stability of concrete structures and require considerations upon design [34, 35]. As well stipulated, the mechanical properties of concrete are preserved for exposure temperatures below 300 °C, yet are decreased considerably as temperature exceeds 500 °C. Additional damage results from rapid cooling such as in the case of distinguishing of fire with cool water due to creation of temperature gradient between concrete core and its surface. This results in tensile stresses on the concrete surface that are high enough to crack concrete and this considered as another source of damage results from incompatible expansion and contraction of aggregate and surrounding cement paste. The magnitude of damage is influenced by many factors such as the size of concrete members, the type of cement and aggregate, the concrete moisture content and the predominant environmental factors, Those are represented in heating exposure time and rate, type of cooling, and maximum temperature attained [36].

The shear deficient Reinforced concrete (RC) beams may be externally strengthened with bonded fiber reinforced polymer (FRP) composites through bonding on their sides only, U jacketing, or complete wrapping. Debonding and FRP rupture are the main shear failure modes of strengthened beams with FRP [37–46]. Different types of materials and techniques were used in strengthening and retrofitting of existing concrete structures such as steel plates bolting, reinforced concrete jackets, pre-stressed external tendons, and most recently FRP composite which has been used on a large scale in different countries. FRP composites have many advantages over conventional methods represented in ease of application, high strength-to-weight ratio, excellent mechanical strength, and good resistance to corrosion, especially that most structures are damaged due to dynamic loads, corrosion of steel, and freeze-thaw cycles [46, 47].

In the construction industry, there is growing attention of using effective external strengthening techniques such as bonding of CFRP composites onto the external deficient faces of the structural members due to their ease of installation, low invasiveness, high corrosion resistance, and high strength to weight ratio. As a result, the center of consideration of the majority of previously published studies was either only on the impact of fibers on the structural behavior of reinforced concrete elements or using CFRP composite as external strengthening for flexural or shear. The intent was to arrive at the vital CFRP strengthening technique that provides an effective increase in the shear strength while maintaining ductile failure mode. Therefore, essential issues to produce effective, economical, and successful CFRP strengthening were needed. Also, exposure of such beams to thermal shock due to any of the reasons described earlier would aggravate the weakness of the high shear zone that unless otherwise strengthened would cause imminent shear failure. External strengthening with CFRP composites have established itself as an efficient method for strengthening of deficient beams in regaining shear strength, especially when concrete is thermally damaged, has not been well established. The scientific problem considered in the study is indeed one of the problems in the modern theory of deficient reinforced concrete shear beams. A lack of literature regarding behavior of shear deficient beams damaged by thermal shock necessitated conducting the present investigation.

2. Methods

Nonlinear finite element analysis (NLFEA) is an effective and important tool in the analysis of complex structures. The main benefits that NLFEA include: 1) substantial savings in the cost, time, and effort compared with the fabrication and experimental testing of structure elements; 2) allows to change any parameter of interest to evaluate its influence on the structure, such as the concrete compressive strength; 3) allows to see the stress, strain, and displacement values at any location and at any load level. Twenty-six full-scale models strengthened using CFRP are developed to carry out different investigated parameters.

2.1. Experimental Work Review

The validation process of the finite element model is based on the experimental work performed by Haddad and Al-Rousan [48]. Four high strength reinforced concrete (RC) beams (100×150×1400 mm) were designed without shear reinforcement in the shear region. Stirrups were placed only within the constant moment region to allow easier positioning of flexural reinforcement and to provide improved confinement of concrete within the constant moment region, as shown in Figure 1. Steel reinforcement: Grade 60 deformed steel bars of 16 mm diameter were used in the tension zone of the reinforced concrete (RC) beams, a steel bars of 12 mm diameter used as top steel reinforcement, and 8 mm diameter bars were used for stirrups. Unidirectional plates and sheets at a thickness of 1.4 and 0.17 mm and a width of 50 and 500 mm, respectively, were used in repairing of thermally damage RC beams. The tensile strength, modulus of elasticity, and strain at failure for CFRP plate and sheet are (3900 MPa, 2700 MPa), (230000 MPa, 165000 MPa), and (1.5 % and 1.4 %), respectively. RC beam specimens were subjected to heat at 500 °C for about two hours using the electrical furnace before immersion inside the water. Figure 1 shows the configuration of different repair techniques. The RC beams were tested under four-point loading, as shown in Figure 1. The span between the supports was 1300 mm and the distance between two point loads was 300 mm. Table 1 shows the Failure load, maximum CFRP strain, and modes of failure from the tested [48] and NLFEA.

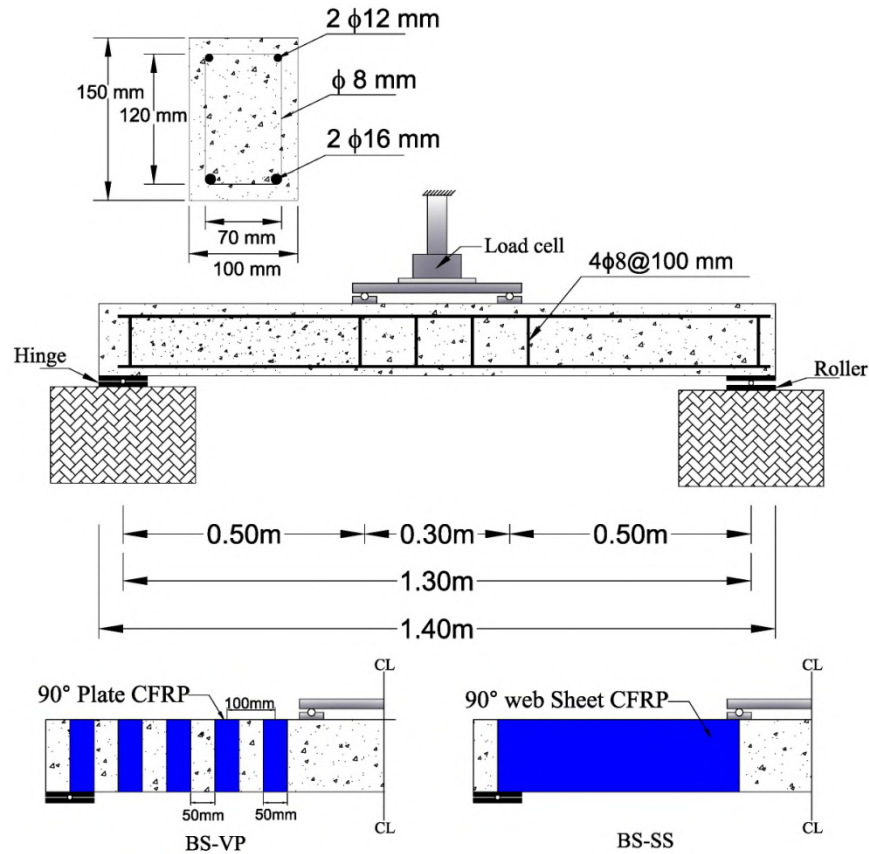


Figure 1. Setup and reinforcement details of the beams [48].

Table 1. Failure load, maximum CFRP strain, and modes of failure.

Specimens	Test/NLFEA	Ultimate Load (kN)	δ_u (mm)	Maximum CFRP strain (ϵ_{max})	Failure Mode
BC	Experimental	35.2	5.94	N.A	DS
	NLFEA	35.6	4.72	N.A	DS
BC-TD	Experimental	11.3	4.13	N.A	DS
	NLFEA	11.3	4.48	N.A	DS
BS-VP	Experimental	31.7	6.09	13270	DS
	NLFEA	32.1	6.23	13274	DS+LDP
BS-SS	Experimental	35.9	5.81	11700	DS
	NLFEA	37.3	6.84	14540	DS+LDP

Note: DS: diagonal shear; LDP Local debonding.

2.2. Description of Non-linear Finite Element Analysis (NLFEA)

Concrete is non-homogenous and brittle material and has different behavior in tension and compression. SOLID 65 element is capable to predict the nonlinear behavior of concrete materials by using a smeared crack approach by ultimate uniaxial tensile and compressive strengths. The average compressive strength of the cylinders before and after being damaged by thermal shock were 53.5 and 9.8 MPa, respectively, and the average splitting tensile strength of the cylinders before and after being damaged by thermal shock were 2.9 and 0.7 MPa, respectively. Poisson's ratio of 0.2 and shear transfer coefficient (β_t) of 0.2 for β_t was used in this study. Figure 14(a) shows the stress-strain relationship for unconfined concrete which describes the post-peak stress-strain behavior.

The steel in simulated models was assumed to be an elastic-perfectly plastic material and the same in compression and tension. Poisson's ratio of 0.3 and the yield stress of undamaged and damaged beams were 420 MPa and $0.78f_y$ [49], respectively, as well as the elastic modulus were 200 GPa and $0.6E_s$ [49], respectively, were used for the steel reinforcement. Figure 2(b) shows the idealized stress-strain relationship. The steel plates were assumed to be linear elastic materials with a Poisson ratio and elastic modulus of 0.3 and 200 GPa, respectively. The CFRP sheet is assumed to be an orthotropic material 0.17 mm thick, tensile strength of 3900 MPa, elastic modulus of 230 GPa, and ultimate tensile strain of 0.0169 as shown in Figure 2(c).

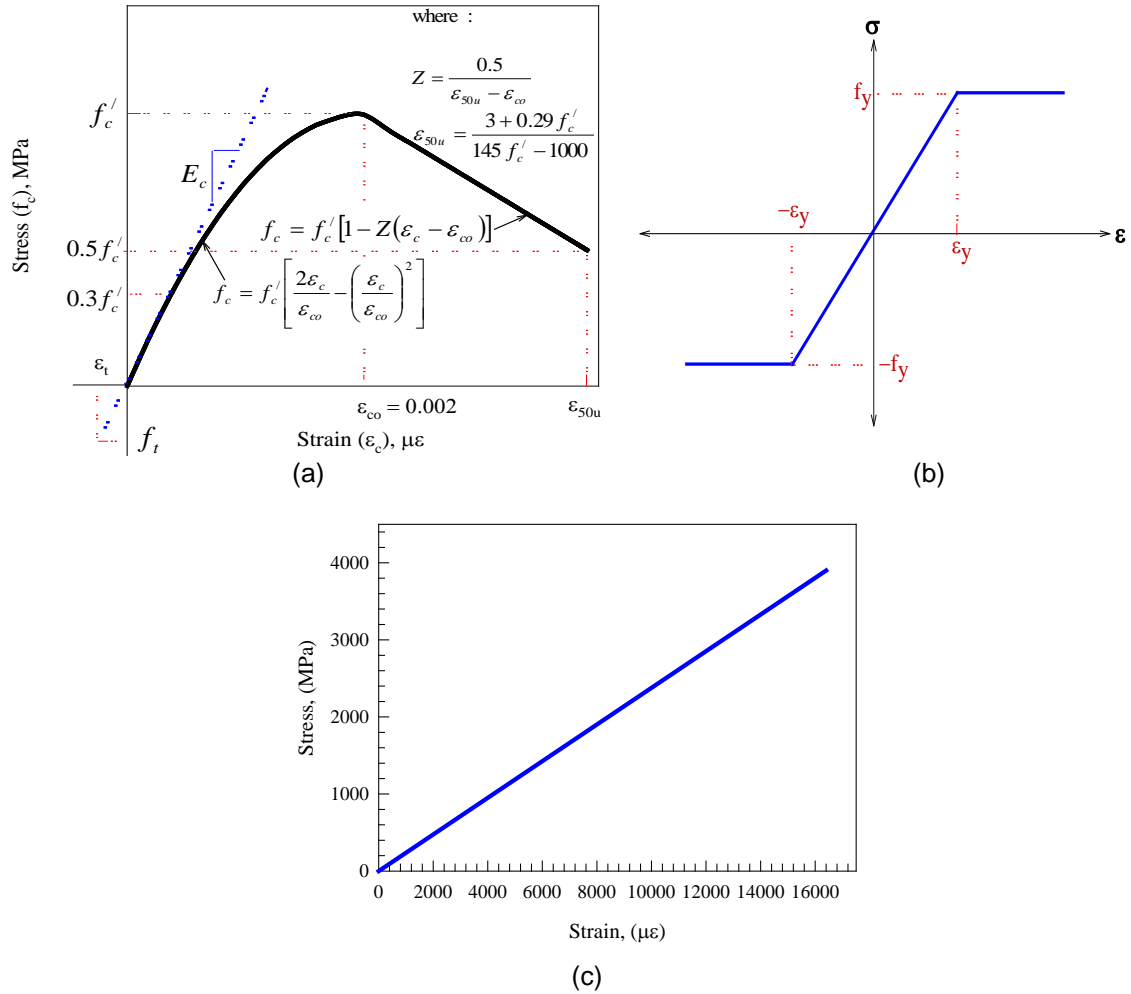


Figure 2. Stress-strain curves for: (a) unconfined concrete [48], (b) steel reinforcement [49], and CFRP composite.

The contact area between the concrete and CFRP composite was modeled by a CONTA174 element. In this study, the bond stress-slip model between CFRP plates and damaged concrete by thermal shock proposed by Haddad and Al-Rousan [50] was used as shown in Figure 3. Figure 4 shows a typical finite element meshing of all beams. The total load applied was divided into a series of load increments or load steps. Newton-Raphson equilibrium iterations provide convergence at the end of each load increment within tolerance limits equal to 0.001 with load increment of 0.35 kN.

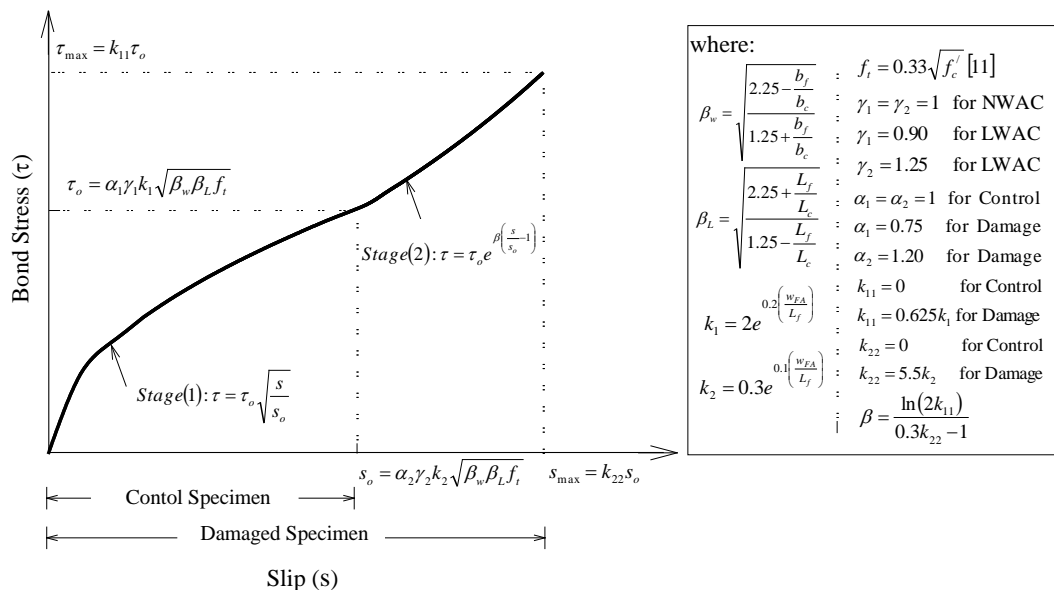


Figure 3. CFRP to concrete bond slip model [50].

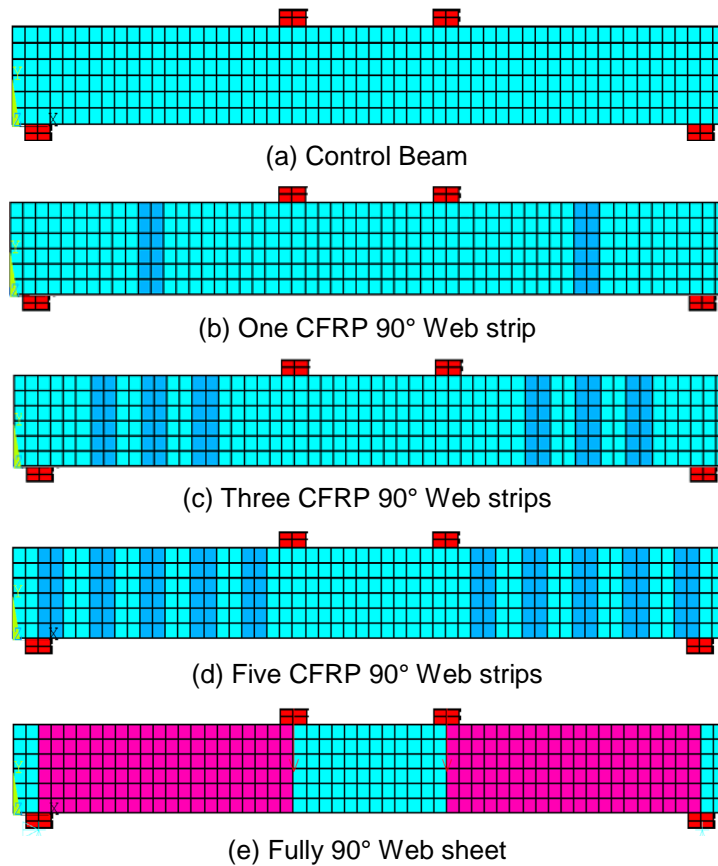


Figure 4. Typical finite element meshing of the beams.

2.3. Investigated Parameters

Figure 4 shows the configuration of different strengthening techniques, where unlike one un-damaged control beam (BC-UD) and one control damaged beam (BC-D), and the other eight beams were strengthened in shear using CFRP sheets as follows: BS1-UD and BS1-D (undamaged and damaged, respectively) were strengthened using one vertical strip (50 mm wide \times 0.17 mm thick) on both sides within the constant shear zone of 500 mm. BS3-UD and BS3-D (undamaged and damaged, respectively) were strengthened using three vertical strip (50 mm wide \times 0.17 mm thick), spaced at 100 mm center to center on both sides within the constant shear zone of 500 mm. BS5-UD and BS5-D (undamaged and damaged, respectively) were strengthened using five vertical strip (50 mm wide \times 0.17 mm thick) on both sides within the constant shear zone of 500 mm. BSS-UD and BSS-D (undamaged and damaged, respectively) were strengthened using sheet to the web sides only (500 mm wide \times 0.17 thick) on both sides within the constant shear zone of 500 mm. A full description of the finite element modeling groups is shown in Table 2.

Table 2. Investigated parameters.

Group Number	Beam number	Un-damaged/ Damaged	CFRP strengthening configuration
	BC-UD		Control beam without strengthening
1	BS1-UD	Un-damaged	One vertical strip (50 mm wide \times 0.17 mm thick) on both sides within the constant shear zone of 500 mm.
	BS3-UD		Three vertical strip (50 mm wide \times 0.17 mm thick), spaced at 100 mm center to center on both sides within the constant shear zone of 500 mm
	BS5-UD		Five vertical strip (50 mm wide \times 0.17 mm thick), spaced at 100 mm center to center on both sides within the constant shear zone of 500 mm
	BSS-UD		Fully sheet to the web sides only (500 mm wide \times 0.17 thick) on both sides within the constant shear zone of 500 mm
	BC-D		Control beam without strengthening
2	BS1-D	Damaged	One vertical strip (50 mm wide \times 0.17 mm thick) on both sides within the constant shear zone of 500 mm.
	BS3-D		Three vertical strip (50 mm wide \times 0.17 mm thick), spaced at 100 mm center to center on both sides within the constant shear zone of 500 mm
	BS5-D		Five vertical strip (50 mm wide \times 0.17 mm thick), spaced at 100 mm center to center on both sides within the constant shear zone of 500 mm
	BSS-D		Fully sheet to the web sides only (500 mm wide \times 0.17 thick) on both sides within the constant shear zone of 500 mm

Note: B: Beam, UD: un-damaged, D: Damaged, S1: one vertical sheet, S3: three vertical sheets, S5: five vertical sheets, SS: fully sheet.

2.4. Validation Process

Four beams were simulated to validate the NLFEA of the reinforced concrete beams. The results from the experimental and NLFEA were compared in terms of ultimate load, ultimate deflection, and the maximum strain induced in CFRP composites. The results obtained from the experimental tests are compared with the finite element analysis as shown in Figure 5. Inspection of Figure 5 reveals that the load-deflection curves from NLFEA had a good agreement with the experimental ones. Inspection of Figure 6 reflects that the NLFEA load-CFRP strain showed a little difference as compared with the experimental curves. Additionally, Table 1 reflected that the NLFEA can be considered as a mirror of experimental ones in terms of ultimate strength and corresponding deflection as well as mode of failure and crack patterns.

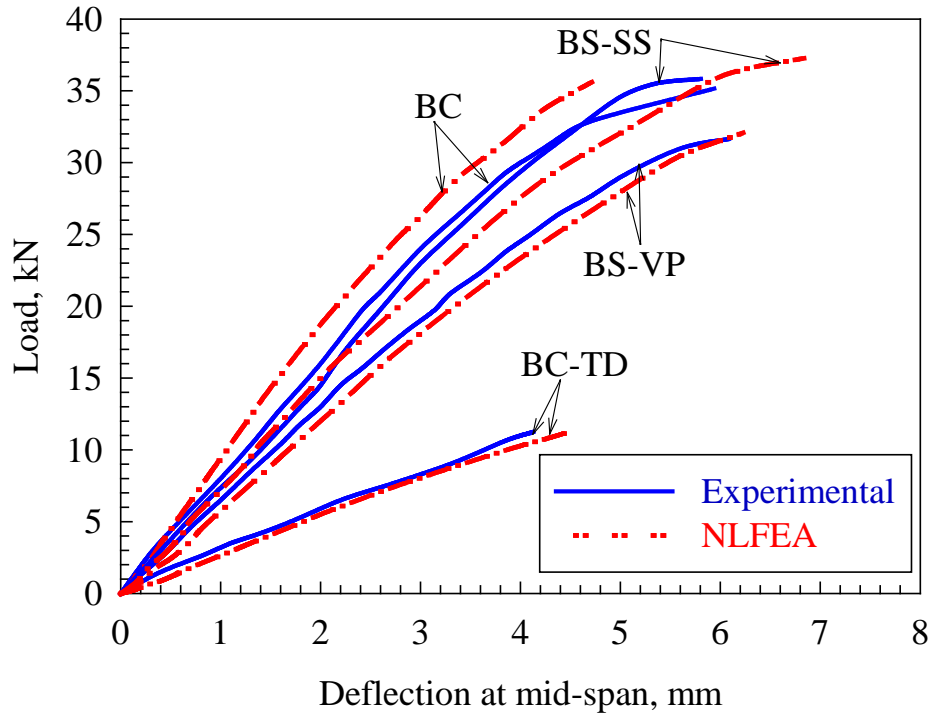


Figure 5. Experimental [48] and NLFEA load-deflection curves.

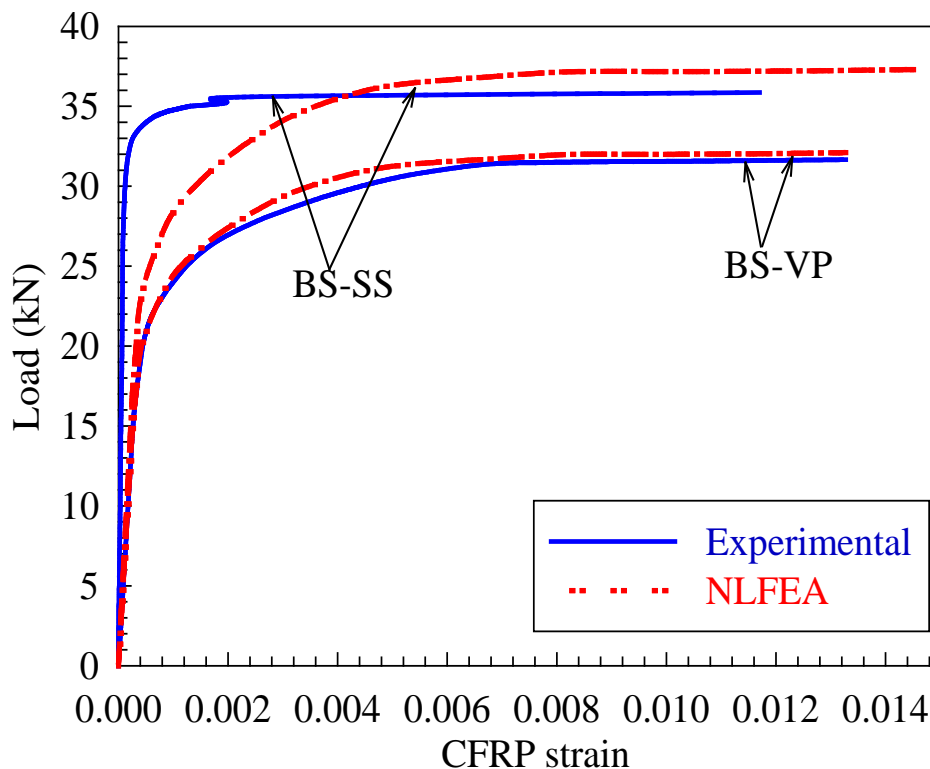


Figure 6. Experimental [48] and NLFEA CFRP strain curves.

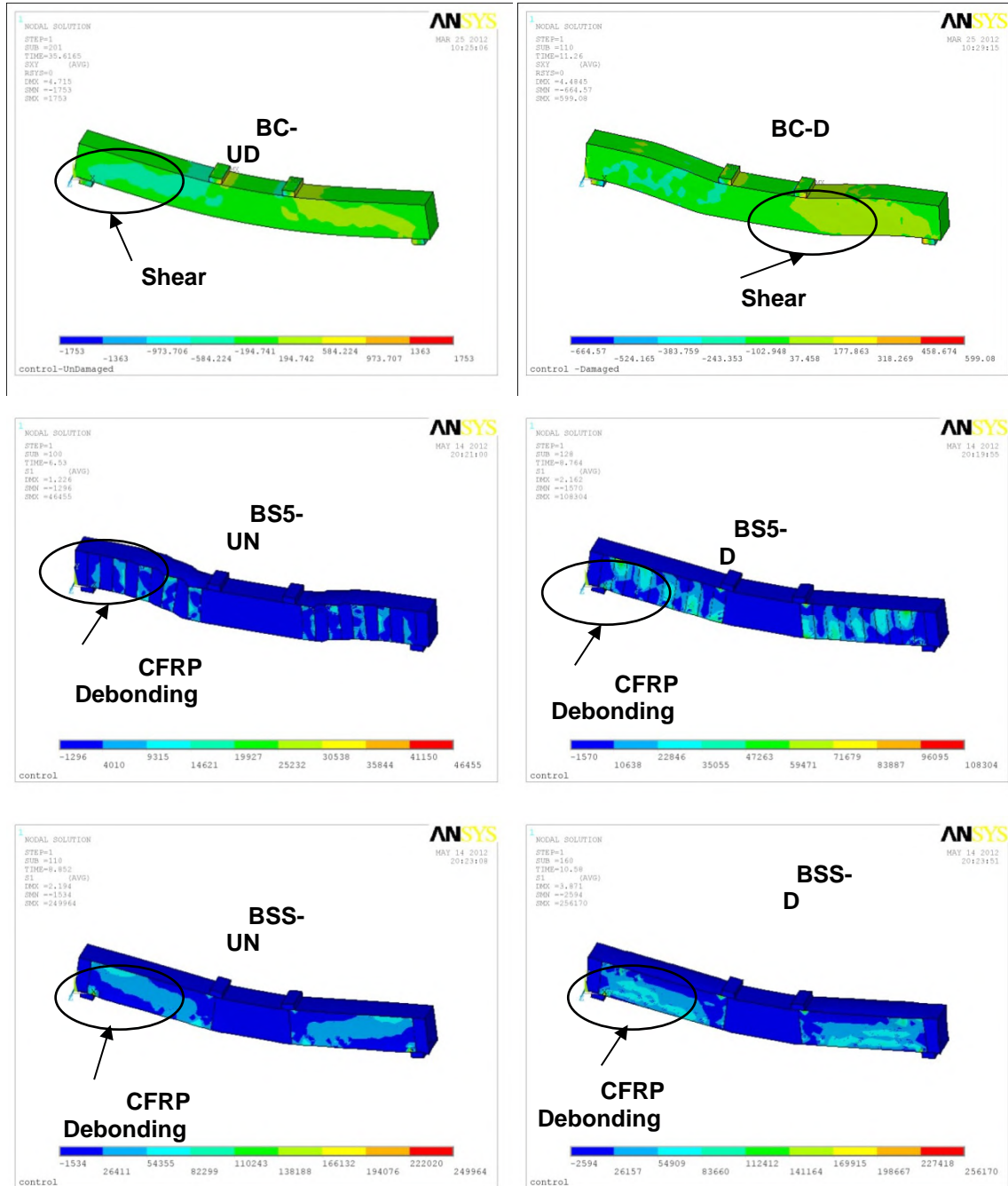


Figure 7. Typical NLFEA stress contours of undamaged, damaged, and strengthened beams.

3. Results and Discussion

3.1. Failure Mode

The trajectories of the stress obtained from the finite element analysis and modes of failure for control, damaged, and different strengthened RC beams are shown in Figure 7. A typical brittle shear failure was observed for control and damaged RC beams. The first flexural crack started within the constant moment region. As the load increased, cracks extended and additional flexural cracks developed throughout the beam length. An inclined shear crack was initiated close to the middle of the shear span. As the load increased, the shear crack propagated towards the loading and supporting points leading to a sudden brittle shear failure. Figure 7 shows the typical shear failure for control and damaged beams. Table 1 illustrated the cracking characteristics and modes of failure of different RC beams. The cracking patterns at failure for beams strengthened with vertical CFRP strips are shown in Figure 7. The strengthened beams showed less number cracks and large spacing as compared with control specimen. The flexural cracking load for beams strengthened with vertical and inclined CFRP plates were increased significantly to about 2 times that of control beams. The strengthened beams with fully sheet exhibited an initial flexural crack at the constant moment region. With further load increasing, the CFRP sheets rupture in the longitudinal direction of the fiber, after that the beam failed suddenly, no crack were visible on the shear span region due to the fully CFRP sheet. Also it can be noted that the use of fully CFRP plate was effective to delay the formation of the diagonal cracks and to arrest the propagation of the diagonal cracks than vertical CFRP ones.

Table 3. Results for all simulated models.

Group Number	Beam number	Ultimate deflection (mm)	Ultimate load (kN)	Elastic stiffness (kN/mm)	Toughness (kN.mm ²)	CFRP strain ($\mu\epsilon$)	SF	DF	PF
1	BC-UD	4.7	35.6	9.2	95	---	1.00	1.00	1.00
	BS1-UD	5.8	46.3	9.7	153	12870	1.23	1.30	1.60
	BS3-UD	6.5	52.4	9.8	193	13580	1.38	1.47	2.03
	BS5-UD	7.1	57.0	9.7	230	14360	1.51	1.60	2.42
	BSS-UD	7.9	62.3	9.6	277	15010	1.66	1.75	2.91
2	BC-D	4.5	11.3	2.6	27	---	0.95	0.32	0.30
	BS1-D	5.4	23.1	4.9	69	12270	1.15	0.65	0.74
	BS3-D	5.8	27.3	5.4	87	13050	1.23	0.77	0.94
	BS5-D	6.2	32.1	5.9	110	13630	1.32	0.90	1.19
	BSS-D	6.8	37.3	7.2	152	14540	1.45	1.05	1.52

Note: SF: strength factor, DF: Ductility factor, PF: Performance Factor = SFxDF, STF: Stiffness Factor, ϵ_{CFRP} is the strain in CFRP strips and ϵ_{fu} is the ultimate strain in CFRP strips of 16400 $\mu\epsilon$.

3.2. CFRP strain

Figure 8 shows the typical distribution of CFRP strain through the depth for all simulated beams. Inspection of Figure 8 reveals that the tensile stresses develop in the CFRP composites once the diagonal crack initiated in the concrete due to shear force. Furthermore, the maximum tensile stresses occurred close to the middle of the CFRP composite that intersect diagonal cracking near to the mid height of the beam cross section. Also, it is noticed that all simulated beams had CFRP strain below the maximum value of 16400 as shown in Table 3 and Table 4 as percentage of CFRP ultimate strain. Inspection of Table 4 reveals that the number of CFRP strips had a strong impact on the efficiency of CFRP strips for Group#1 (Un-Damaged) with a percentage with respect to ultimate strain of CFRP strips of 78 %, 83 %, 88 %, and 92 % for one, three, five, and fully strips, respectively. While, the percentage of Group#2(Damaged) with respect to ultimate strain of CFRP strips is 75 %, 80 %, 83 %, and 89 % for one, three, five, and fully stirrups, respectively, and this equivalent to 96 % of the Group 1 strains. In pre-cracking (diagonal shear crack) stage, CFRP strain development was equal to zero. After the creation of diagonal shear crack (the shear strength exceeds the concrete shear strength) within the shear span, the CFRP strain increased rapidly and continued to increase until the beam failure as shown in Figure 9. It can be observed that the strain in the CFRP developed at a low rate as the bond surface area decrease. Also the results indicated that the beams strengthened with fully CFRP sheet had highest impact on the CFRP strain.

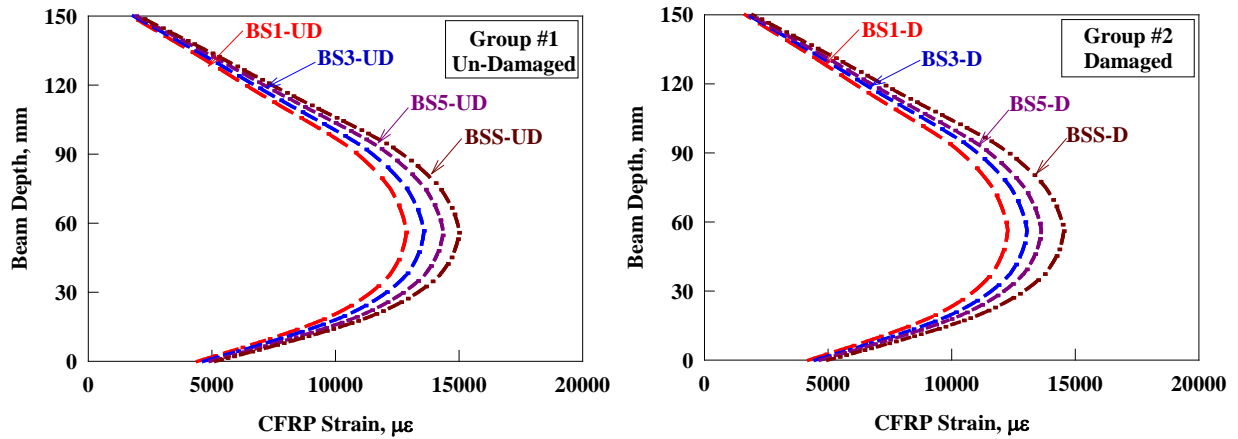


Figure 8. Typical CFRP strain versus beam depth.

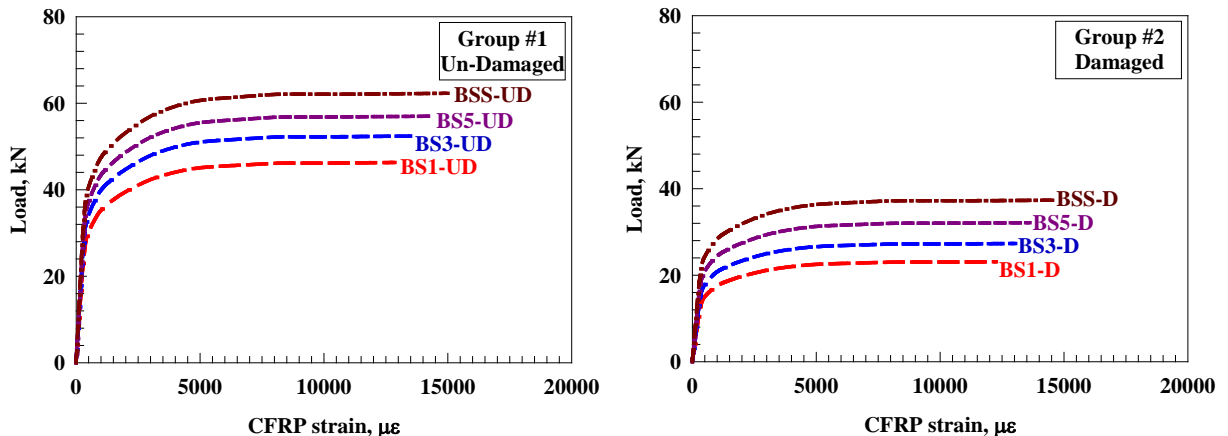


Figure 9. Typical load-CFRP strain curve.

Table 4. Percentage value of investigated parameters respect to control un-damaged beam.

Group Number	Beam	Ultimate deflection (%)	Ultimate load (%)	Performance factor (%)	Energy absorption (%)	Elastic stiffness (%)	\mathcal{E}_{CFRP}
1	BC-UD	0	0	0	0	0	–
	BS1-UD	23	30	60	6	60	$0.78\mathcal{E}_{\phi U}$
	BS3-UD	38	47	103	6	103	$0.83\mathcal{E}_{\phi U}$
	BS5-UD	51	60	142	6	142	$0.88\mathcal{E}_{\phi U}$
	BSS-UD	66	75	191	5	191	$0.92\mathcal{E}_{\phi U}$
2	BC-D	–5	–68	–70	–71	–72	–
	BS1-D	15	–35	–26	–47	–28	$0.75\mathcal{E}_{\phi U}$
	BS3-D	23	–23	–6	–42	–8	$0.80\mathcal{E}_{\phi U}$
	BS5-D	32	–10	19	–36	16	$0.83\mathcal{E}_{\phi U}$
	BSS-D	45	5	52	–22	60	$0.89\mathcal{E}_{\phi U}$

Note: \mathcal{E}_{fu} is the ultimate strain in CFRP strips of $16400 \mu\mathcal{E}$.

3.3. Load-deflection behavior

Table 3 shows the characteristics of the load-deflection curves for control, thermal shock damage, and strengthened beams. The characteristics include the ultimate load capacity and the corresponding deflection at the mid-span, toughness, and stiffness. The initial stiffness is defined as the slope of linear elastic portion of beam at load-deflection curve ($k = P/\delta$). The toughness is defined as the area underneath the load-deflection curve until ultimate load capacity. The curves of load versus mid-span deflection can be divided into three specific regions: a linear elastic region up to first flexural crack, transition region up to the development of diagonal shear crack, and a post cracking region up to ultimate beam capacity as shown in Figure 10. Inspection of Figure 10 reveals that the load-deflection curve was extensively affected by thermal shock in terms of ultimate load, ultimate deflection, toughness, and stiffness as shown before in Table 3. The average ultimate load for control undamaged and damaged beams were 35.6 and 11.3 kN, respectively, with a percentage of reduction of about 68 %, as well as a reduction of 5 % in the ultimate deflection. In addition, the average stiffness for control undamaged and damaged beams were 9.2 and 2.6 kN/mm, respectively, with a reduction of 72 %, while the percentage of reduction in toughness was about 71 %. This significant reduction in ultimate load of damage beams is due to the reduction in compressive strength. In addition, the larger CFRP bonded area showed better performance than those with small CFRP bonded area.

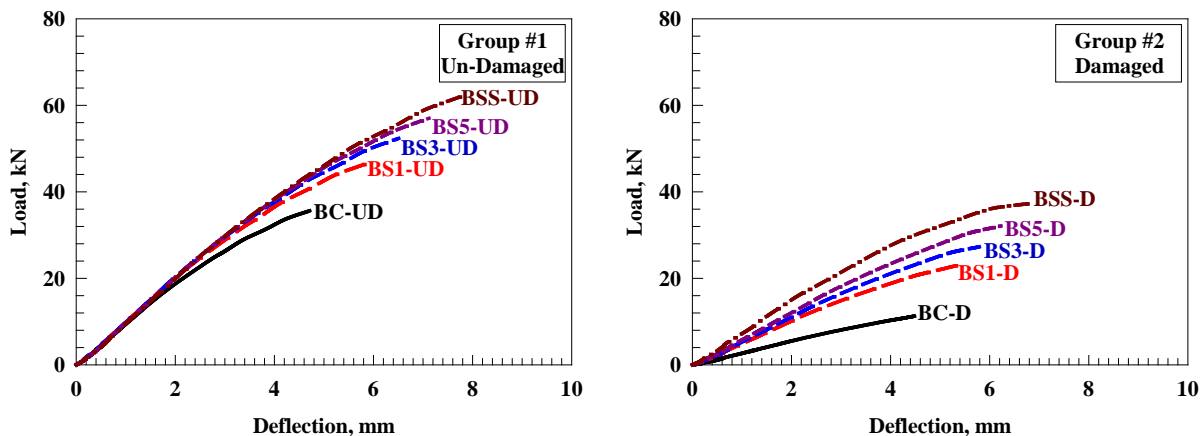


Figure 10. Typical load-deflection curve.

3.4. Ultimate load capacity and corresponding deflection

The assessment of beams for load capacity and corresponding deflection shows the excellent performance of RC members. For strengthened RC members, deflection and ultimate load capacity can be related to the serviceability and ultimate load limit states, respectively, as shown in Table 3. The load capacity and deflection percentages are defined as the ultimate load capacity and deflection, respectively, of CFRP strengthened beam divided by the ultimate deflection and load capacity of the un-strengthened beam (undamaged beam) as shown in Table 4. The deflection indicates how much the strengthened RC beams can sustain deformations without failure. The deflection percentage is defined as the ratio of the ultimate deflection of the strengthened beam to the ultimate deflection of the control beam (undamaged beam) as shown in Table 4. Strength ratio also predicts the increase of load that the model can sustain.

Figure 11 and 12 show the strength and ductility percentages with respect to un-damaged control beam, respectively, for all simulated models. Inspection of Figure 11 reveals that the strength percentage increased significantly with the increase of number of CFRP strips. The strength percentage (Figure 11) for Group #1 beams (Un-Damaged) is 30 %, 47 %, 60 %, and 75 % for beam strengthened with one, three, five and fully strips, respectively, with an significant average enhancement of 53 %. Also, the strength percentage (Figure 11) for Group #2 beams (Damaged) is -35 %, -23 %, -10 %, and 5 % for beam strengthened with one, three, five and fully strips, respectively,, with an significant average reduction of 16 % and this percentage is 0.25 times the percentage for Group#1 (Un-Damaged).

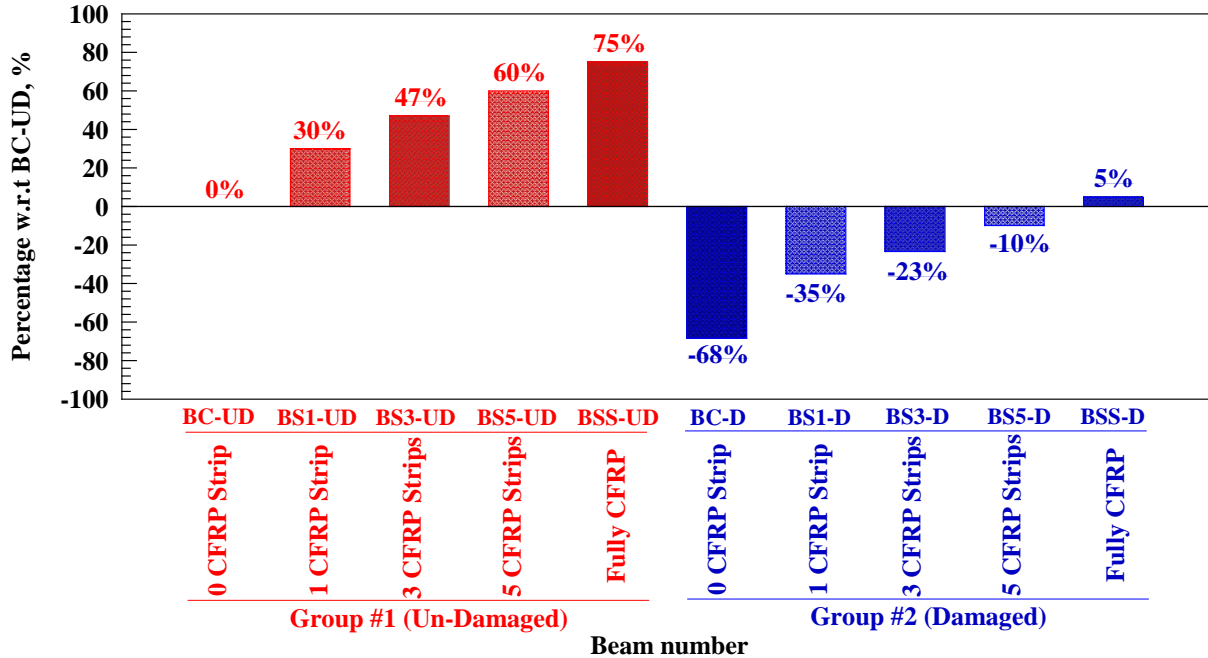


Figure 11. Ultimate load capacity percentage with respect to control undamaged beam

Figure 12 shows that the ductility percentage also significantly increased with the increase of number of CFRP strips. The ductility percentage (Figure 12) for Group #1 beams (Un-Damaged) is 23 %, 38 %, 51 %, and 66 % for beam strengthened with one, three, five and fully strips, respectively, with an significant average enhancement of 45 %. Also, the ductility percentage (Figure 12) for Group #2 beams (Damaged) is 15 %, 23 %, 32 %, and 45 % for beam strengthened with one, three, five and fully strips, respectively,, with an significant average enhancement of 29 % and this percentage is 0.64 times the percentage for Group#1 (Un-Damaged).

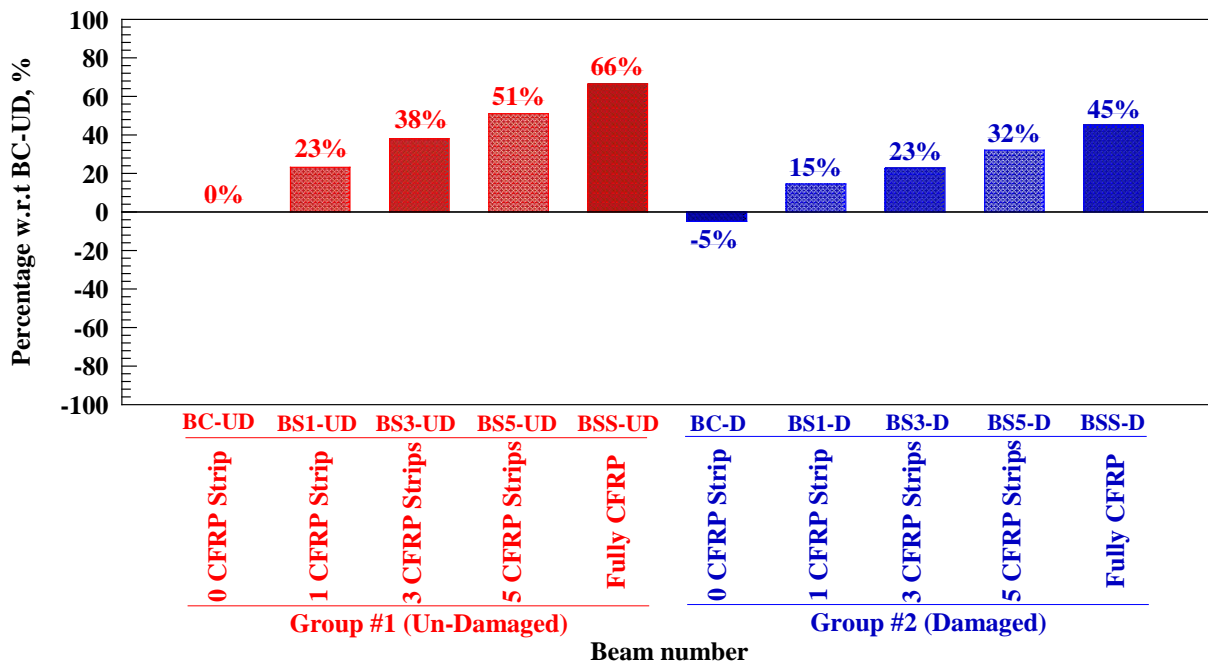


Figure 12. Ultimate deflection percentage with respect to control undamaged beam.

3.5. Elastic stiffness

The elastic stiffness determines the response of the crystal to an externally applied strain (or stress) and provides information about the bonding characteristics, mechanical and structural stability. The slope of the first stage of the load-deflection curve before initiation of the first main flexural crack is represented the elastic stiffness. For comparison, the elastic stiffness of each strengthened beam with CFRP sheets was normalized with respect to the control beam (Un-Damaged) without CFRP sheets as shown in Table 4.

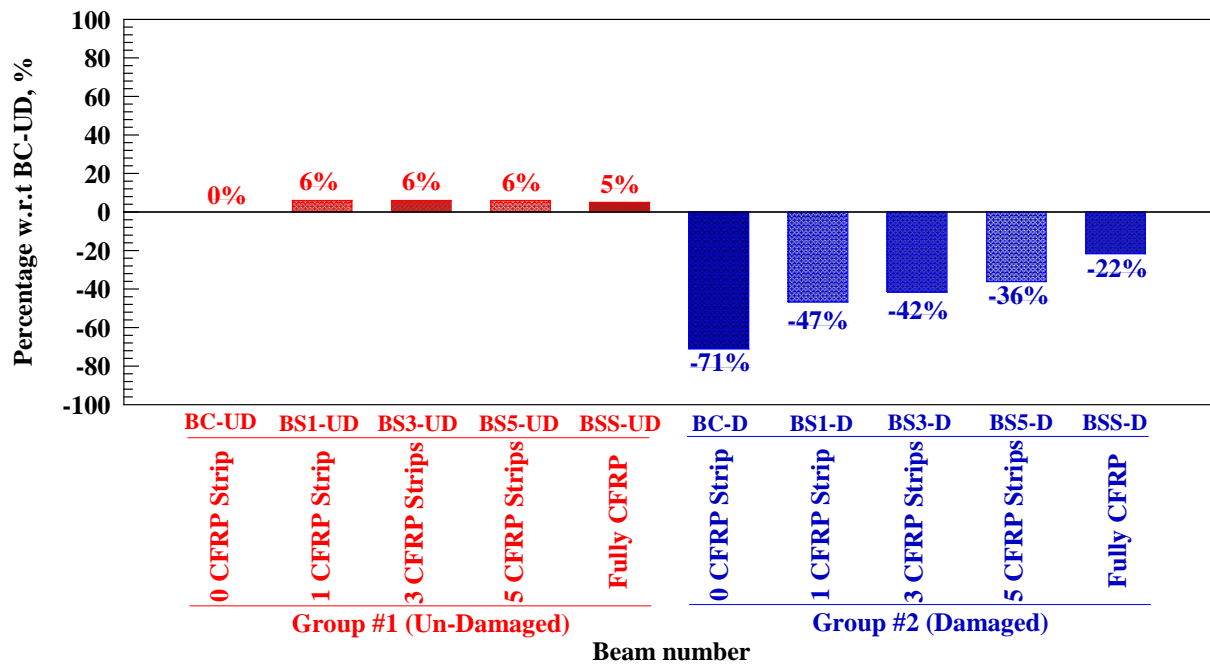


Figure 13. Stiffness percentage with respect to control undamaged beam.

Figure 13 shows the elastic stiffness percentages with respect to un-damaged control beam, respectively, for all simulated models. Inspection of Figure 13 reveals that the elastic stiffness percentage for un-damaged beams is the same for all strengthening techniques and equal to average value of 6 %. While, the elastic stiffness percentage for damaged beams is less than percentage of un-damaged beam and this value decreased with the increase of CFRP strips number. The elastic stiffness percentage (Figure 13) for Group #2 beams (Damaged) is -47 %, -42 %, -36 %, and -22 % for beam strengthened with one, three, five and fully strips, respectively, with an significant average reduction of 37 % and this percentage is eight times the percentage for Group#1 (Un-Damaged).

3.6. Toughness

In materials science and metallurgy, toughness is the ability of a material to absorb energy and plastically deform without fracturing. One definition of material toughness is the amount of energy per unit volume that a material can absorb before rupturing. Toughness is calculated as the entire area under the load-deflection curve. In addition, the toughness of each strengthened beam with CFRP sheets was normalized with respect to the control beams without CFRP sheets as shown in Table 4. Figure 14 shows that the toughness percentage also significantly increased with the increase of number of CFRP strips. The toughness percentage (Figure 14) for Group #1 beams (Un-Damaged) is 60 %, 103 %, 142 %, and 191 % for beam strengthened with one, three, five and fully strips, respectively, with an significant average enhancement of 124 %. Also, the toughness percentage (Figure 14) for Group #2 beams (Damaged) is -28 %, -8 %, 16 %, and 60 % for beam strengthened with one, three, five and fully strips, respectively, with an significant average enhancement of 10 % and this percentage is 0.08 times the percentage for Group#1 (Un-Damaged).

3.7. Evaluation of Performance of NLFEA Results

The effect of CFRP composite materials is evaluated by the strength factor (SF), deformability factor (DF), and performance factor (PF) for different strengthened RC beams normalized with respect to control beams (undamaged). Performance factor is a combination of the strength factor and the deformability factor to generate an overall structural performance as shown in Figure 15. Based on Figure 15 the DF, SF, and PF increased as the number of CFRP strips (bonded area of CFRP) increase. Finally, as the bonded area increase the beam reached the performance of control beams (undamaged) and protected the beams against brittle shear failure. The RC beams strengthened with fully CFRP sheet were much more effective in improving the performance of the strengthened beams than those beams strengthened with vertical strips. Thus, the beams strengthened with fully CFRP sheet is the most efficient technique than those strengthened with CFRP strips on the web.

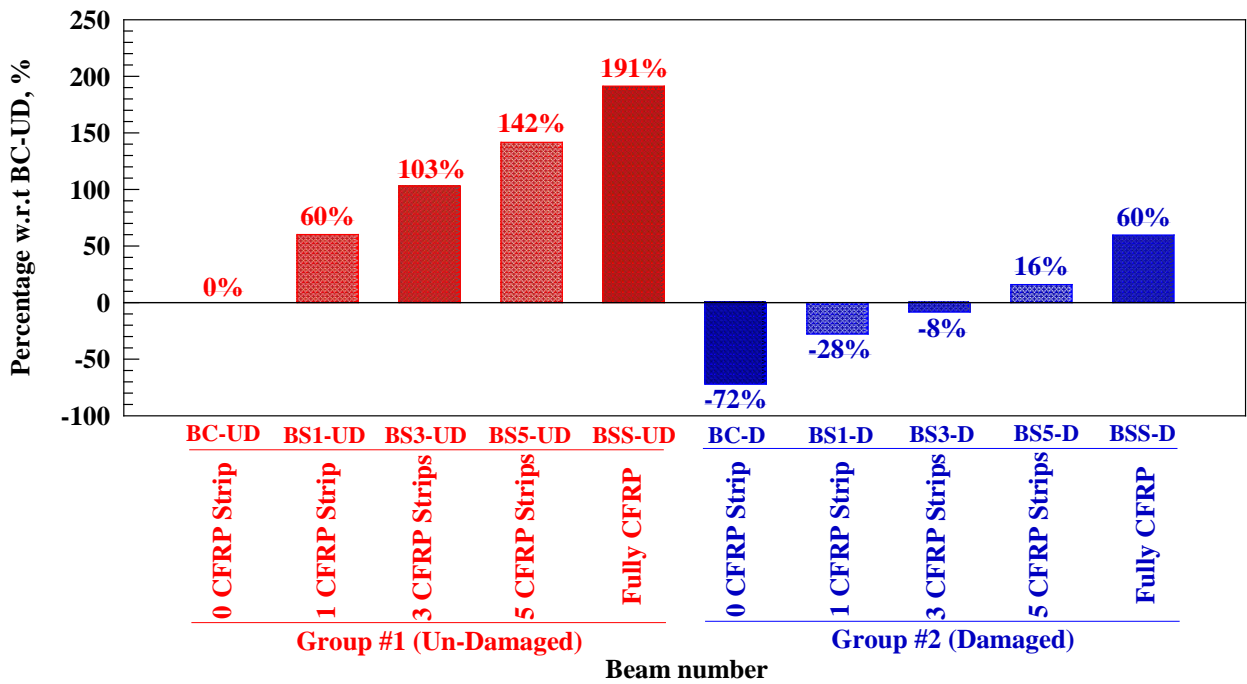


Figure 14. Toughness percentage with respect to control undamaged beam.

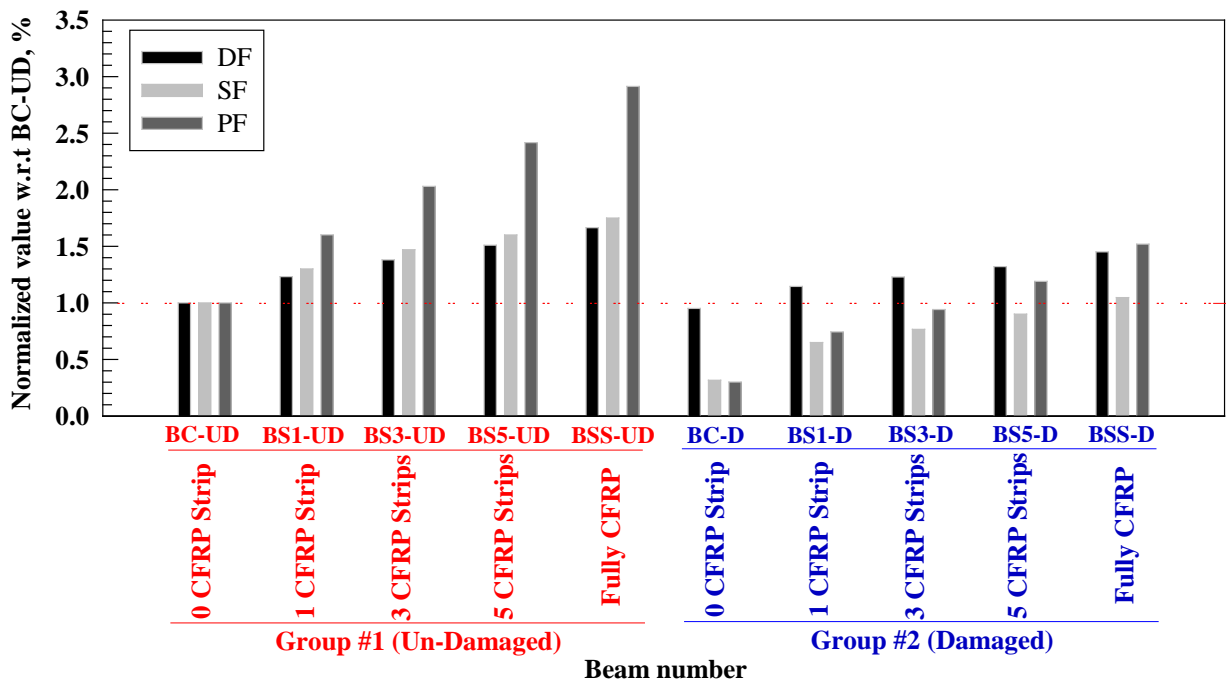


Figure 15. Normalized characteristic factor for different strengthened RC beams.

3.8. Profitability Index of the CFRP Strips Number

Table 5 shows the shear contribution of the concrete (V_c), shear contribution of the CFRP composites (V_f), and the final loads from the NLFEA for various RC beams strengthened using CFRP composites with different techniques. Table 5 indicated that the contribution of CFRP (V_f) to the shear capacity had increased as the CFRP bonded area increase or number of CFRP strips. To evaluate the efficiency of various CFRP composites strengthening techniques in terms of the amount of CFRP consumed, profitability indices were computed. The profitability index is defined as the ratio of CFRP contribution in shearing capacity to the total CFRP bonded area within the shear span of strengthened beams. Table 5 shows the profitability indices for the different strengthening techniques. Inspection of Table 5 reveals that the profitability index for undamaged beams were 3.57, 1.87, 1.43, and 0.99 MPa for 1, 2, 3, 4, and 9 CFRP strips (Fully), respectively. While, the profitability index for damaged beams were 3.93, 1.78, 1.39, and 0.96 MPa for 1, 2, 3, 4, and 9 CFRP strips (Fully), respectively, and these equivalent to 1.10, 0.95, 0.97, and 0.97, respectively, of the undamaged ones.

Table 5. Profitability index of CFRP strips.

Group Number	Beam number	V_c , kN	V_f , kN	V_u , kN	V_f/A_f , MPa
1	BC-UD	17.8	0.0	17.8	---
	BS1-UD	17.8	5.4	23.2	3.57
	BS3-UD	17.8	8.4	26.2	1.87
	BS5-UD	17.8	10.7	28.5	1.43
	BSS-UD	17.8	13.4	31.2	0.99
2	BC-D	5.7	0.0	5.7	---
	BS1-D	5.7	5.9	11.6	3.93
	BS3-D	5.7	8.0	13.7	1.78
	BS5-D	5.7	10.4	16.1	1.39
	BSS-D	5.7	13.0	18.7	0.96

Note: V_c is the shear contribution of the concrete, V_f is the shear contribution of the CFRP composites, A_f is the total CFRP bonded area within the shear span of strengthened beams

3.9. Comparison of NLFEA with other results

Comparison of NLFEA with Irshidat and Al-Saleh [51], the heat-damaged specimens repaired with FRP sheets based on neat epoxy (NE-500 and NE-600) experienced similar crack patterns of NLFEA. However, the presence of FRP sheet delayed the initiation of the flexural cracks in the area high moment zone. Specimen NE-500 was failed by sheet debonding followed by concrete crushing. The debonding started at the end of the specimen and extended to reach its center. Specimen NE-600 was failed by FRP sheet delaminating initiated at one end of the beam and extended toward the second end, followed by concrete crushing and splitting. Heating RC beams significantly affected their flexural behavior. Using externally bonded carbon fiber sheet/epoxy composite to repair the heat-damaged RC beams help them to partially recover their flexural capacity is almost the same performance as the NLFEA.

4. Conclusions

1. NLFEA can be considered as a mirror of experimental ones in terms of ultimate strength and corresponding deflection as well as mode of failure and crack patterns. Hence, its results can be extended to generate data for cases, not studied experimentally.

2. NLFEA helped tracking propagation of cracks especially in case of beams externally strengthened with CFRP sheets in which crack patterns cannot be seen experimentally. The cracking patterns at failure as obtained from the NLFEA compared well with those observed experimentally for control, thermally damaged, and strengthened beams.

3. Subjecting thermal shock has a notable and significant impact on the mechanical properties and structural behavior represented in reduced shear capacity, stiffness, and toughness at percentages of 70 %, 72 % and 71 %, respectively, and formed extensive cracking in their concrete.

4. The beams strengthened with fully CFRP sheets achieved the highest load capacity, deflection, elastic stiffness, and toughness followed, in sequence, by those strengthened using five CFRP strips, three CFRP strips, one CFRP strip.

References

- Kodur, A.V. The experimental behavior of FRP-strengthened RC beams subjected to design fire exposure. *Engineering Structures*. 2011. 33(1). Pp. 2201–2211. DOI: 10.1016/j.engstruct.2011.03.010.
- Kodur, V.K.R., Agrawal, A. An approach for evaluating residual capacity of reinforced concrete beams exposed to fire. *Engineering Structures*. 2016. 110(1). Pp. 293–306. DOI: 10.1016/j.engstruct.2015.11.047.
- Al-Ostaz, M. Irshidat, B. Tenkhoff, P.S. Ponnappalli. Deterioration of bond integrity between repair material and concrete due to thermal and mechanical incompatibilities. *Journal of Materials in Civil Engineering*. 2010. 22(2). Pp. 136–144. DOI: 10.1061/(ASCE)0899-1561(2010) 22:2(136).
- Nedviga, E., Beresneva, N., Gravit, M., Blagodatskaya, A. Fire Resistance of Prefabricated Monolithic Reinforced Concrete Slabs of «Marko» Technology. *Adv. Intell. Syst. Comput.* 2018. 692(1): Pp. 739–749. DOI: 10.1007/978-3-319-70987-1_78.
- Hezhev, T.A., Zhurtov, A.V., Tspinov, A.S., Klyuev, S.V. Fire resistant fibre reinforced vermiculite concrete with volcanic application. *Mag. Civ. Eng.* 2018. 80(1). Pp. 181–194. DOI:10.18720/MCE.80.16.
- Goremikins, V., Blesak, L., Novak, J., Wald, F. Experimental investigation on SFRC behaviour under elevated temperature. *J. Struct. Fire Eng.* 2017. 8(1). Pp. 287–299. DOI: 10.1108/JSE-05-2017-0034.
- Goremikins, V., Blesak, L., Novak, J., Wald, F. To testing of steel fibre reinforced concrete at elevated temperature. *Appl. Struct. Fire Eng.* 2017. DOI: 10.14311/asfe.2015.055.
- Blesak, L., Goremikins, V., Wald, F., Sajdlova, T. Constitutive model of steel fibre reinforced concrete subjected to high temperatures. *Acta Polytech.* 2016. 56(1). Pp. 417–424. DOI: 10.14311/AP.2016.56.0417.
- Goremikins, V., Blesak, L., Novak, J., Wald, F. Experimental method on investigation of fibre reinforced concrete at elevated temperatures. *Acta Polytech.* 2016. 56(1). Pp. 258–264. DOI: 10.14311/AP.2016.56.0258.

10. Selyaev, V.P., Nizina, T.A., Balykov, A.S., Nizin, D.R., Balbalin, A.V. Fractal analysis of deformation curves of fiber-reinforced fine-grained concretes under compression. *PNRPU Mech. Bull.* 2016. 1(1). Pp. 129–146. DOI: 10.15593/perm.mech/2016.1.09.
11. P. Bily, J. Fladr, A. Kohoutkova. Finite Element Modelling of a Prestressed Concrete Containment with a Steel Liner. *Proceedings of the Fifteenth International Conference on Civil, Structural and Environmental Engineering Computing.* Civil-Comp Press. 2015. DOI: 10.4203/ccp.108.1.
12. Bílý, P., Kohoutková, A. Sensitivity analysis of numerical model of prestressed concrete containment. *Nucl. Eng. Des.* 2015. 295(1). Pp. 204–214. DOI: 10.1016/j.nucengdes.2015.09.027.
13. Krishan, A., Rimshin, V., Erofeev, V., Kurbatov, V., Markov, S. The energy integrity resistance to the destruction of the long-term strength concrete. *Procedia Eng.* 2015. 117(1). Pp. 211–217. DOI: 10.1016/j.proeng.2015.08.143.
14. Korsun, V., Vatin, N., Franchi, A., Korsun, A., Crespi, P., Mashtaler, S. The strength and strain of high-strength concrete elements with confinement and steel fiber reinforcement including the conditions of the effect of elevated temperatures. *Procedia Eng.* 2015. 117(1). Pp. 970–979. DOI: 10.1016/j.proeng.2015.08.192.
15. Bily, P., Kohoutková, A. Numerical analysis of anchorage between steel liner and prestressed nuclear containment wall. *Proc. 10th fib Int. PhD Symp. Civ. Eng.* 2014. 529–534.
16. Korsun, V., Vatin, N., Korsun, A., Nemova, D. Physical-mechanical properties of the modified fine-grained concrete subjected to thermal effects up to 200°C. *Appl. Mech. Mater.* 2014. 633–634. Pp. 1013–1017. DOI: 10.4028/www.scientific.net/AMM.633-634.1013.
17. Korsun, V., Korsun, A., Volkov, A. Characteristics of mechanical and rheological properties of concrete under heating conditions up to 200°C. *MATEC Web Conf.* 2013. 6(1). Pp. 07002. DOI: 10.1051/mateconf/20130607002.
18. Petkova, T. Donchev, J. Wen. Experimental study of the performance of CFRP strengthened small scale beams after heating to high temperatures. *Construction and Building Materials.* 2014. 68(1): Pp. 55–61. DOI: 10.1016/j.conbuildmat.2014.06.014.
19. Ji, G., Li, G., Alaywan, W. A new fire resistant FRP for externally bonded concrete repair. *Construction and Building Materials.* 2013. 42(1). Pp. 87–96. DOI: 10.1016/j.conbuildmat.2013.01.008.
20. Trentin, J.R. Casas. Safety factors for CFRP strengthening in bending of reinforced concrete bridges. *Composite Structures.* 2015. 128(1). Pp. 188–198. DOI: 10.1016/j.compstruct.2015.03.048.
21. Ferrari, V.J., de Hanai, J.B., de Souza, R.A. Flexural strengthening of reinforcement concrete beams using high performance fiber reinforcement cement-based composite (HPFRCC) and carbon fiber reinforced polymers (CFRP). *Construction and Building Materials.* 2013. 48(1). Pp. 485–498. DOI: 10.1016/j.conbuildmat.2013.07.026.
22. Attari, N., Amziane, S., Chemrouk, M. Flexural strengthening of concrete beams using CFRP, GFRP and hybrid FRP sheets. *Construction and Building Materials.* 2012. 37(1). Pp. 746–757. DOI: 10.1016/j.conbuildmat.2012.07.052.
23. Kara, I.F., Ashour, A.F., Kóroglu, M.A. Flexural behavior of hybrid FRP/steel reinforced concrete beams. *Composite Structures.* 2015. 129(1). Pp. 111–121. DOI: 10.1016/j.compstruct.2015.03.073.
24. Alver, N., Tanarlan, H.M., Sülün, Ö.Y., Ercan, E., Karcılı, M., Selman, E., Ohno, K. Effect of CFRP-spacing on fracture mechanism of CFRP-strengthened reinforced concrete beam identified by AE-SiGMA. *Construction and Building Materials.* 2014. 67(1). Pp. 146–156. DOI: 10.1016/j.conbuildmat.2014.05.017.
25. Khan, ur R., Fareed, S. Behaviour of reinforced concrete beams strengthened by CFRP wraps with and without end anchorages. *Procedia Engineering.* 2014. 77(1). Pp. 123–130. DOI: 10.1016/j.proeng.2014.07.011.
26. Hawileh, R.A., Rasheed, H.A., Abdalla, J.A., Al-Tamimi, A.K. Behavior of reinforced concrete beams strengthened with externally bonded hybrid fiber reinforced polymer systems. *Mater. Des.* 2014. 53(1). Pp. 972–982. DOI: 10.1016/j.matdes.2013.07.087.
27. You, Y.-C., Choi, K.-S., Kim, J. An experimental investigation on flexural behavior of RC beams strengthened with prestressed CFRP strips using a durable anchorage system. *Composites Part B: Engineering.* 2012. 43(1). Pp. 3026–3036. DOI: 10.1016/j.compositesb.2012.05.030.
28. Al-Rousan Rajai and Abo-Msamh Isra'a. Bending and Torsion Behaviour of CFRP Strengthened RC Beams. *Magazine of Civil Engineering.* 2019. 92(8). Pp. 62–71. DOI: 10.18720/MCE.92.8
29. Kiyaneets, A.V. Concrete with recycled polyethylene terephthalate fiber. *Magazine of Civil Engineering.* 2018. 84(8). Pp. 109–118. doi: 10.18720/MCE.84.11.
30. Kolchunov, V.I., Dem'yanov, A.I. The modeling method of discrete cracks in reinforced concrete under the torsion with bending. *Magazine of Civil Engineering.* 2018. 81(5). Pp. 160–173. doi: 10.18720/MCE.81.16.
31. Travush, V.I., Konin, D.V., Krylov, A.S. Strength of reinforced concrete beams of high-performance concrete and fiber reinforced concrete. *Magazine of Civil Engineering.* 2018. No. 77(1). Pp. 90–100. doi: 10.18720/MCE.77.8.
32. Al-Rousan, R. Behavior of two-way slabs subjected to drop-weight. *Magazine of Civil Engineering.* 2019. 90(6). Pp. 62–71. DOI: 10.18720/MCE.90.6
33. Al-Rousan, R. The impact of cable spacing on the behavior of cable-stayed bridges. *Magazine of Civil Engineering.* 2019. 91(7). Pp. 49–59. DOI: 10.18720/MCE.91.5
34. Yu, V.K.R. Kodur. Fire behavior of concrete T-beams strengthened with nearsurface mounted FRP reinforcement. *Engineering Structures.* 2014. 80(1). Pp. 350–361. DOI: 10.1016/j.engstruct.2014.09.003.
35. Khan, M.S., Prasad, J., Abbas, H. Shear strength of RC beams subjected to cyclic thermal loading. *Construction and Building Materials.* 2010. 24(10). Pp. 1869–1877. DOI: 10.1016/j.conbuildmat.2010.04.016
36. Xiangwei, Liang, Chengqing, Wu, Yekai, Yang, Cheng, Wu, Zhongxian, Li. Coupled effect of temperature and impact loading on tensile strength of ultra-high performance fibre reinforced concrete. *Composite Structures.* 2019. 229(1). Pp. 111432. DOI: 10.1016/j.compstruct.2019.111432.
37. Bingol, A.F., Gul, R. Effect of elevated temperatures and cooling regimes on normal strength concrete. *Fire and Materials.* 2009.33(1). Pp. 79–88. DOI: 10.1002/fam.987
38. Lu, X.Z., Chen, J.F., Ye, L.P., Teng, J.G., Rotter, J.M. RC beams shear-strengthened with FRP: Stress distributions in the FRP reinforcement. *Construction and Building Materials.* 2009. 23(1). Pp. 1544–1554. DOI: 10.1016/j.conbuildmat.2008.09.019
39. Jiangfeng Dong, Qingyuan Wang, and Zhongwei Guan. Structural behaviour of RC beams with external flexural and flexural-shear strengthening by FRP sheets. *Composites Part B: Engineering.* 2013. 44(1). Pp. 604–612. DOI: 0.1016/j.compositesb.2012.02.018
40. Ahmed K. El-Sayed. Effect of longitudinal CFRP strengthening on the shear resistance of reinforced concrete beams. *Composites Part B: Engineering.* 2014. 55(1). Pp. 422–429. DOI: 10.1016/j.compositesb.2013.10.061

41. Carlo Pellegrino and Mira Vasic. Assessment of design procedures for the use of externally bonded FRP composites in shear strengthening of reinforced concrete beams. *Composites Part B: Engineering*. 2013. 45(1). Pp. 727–741. DOI: 10.1016/j.compositesb.2012.07.039
42. Davood Mostofinejad and Amirhomayoon Tabatabaei Kashani. Experimental study on effect of EBR and EBROG methods on debonding of FRP sheets used for shear strengthening of RC beams. *Composites Part B: Engineering*. 2013. 45(1). Pp. 1704–1713. DOI: 10.1016/j.compositesb.2012.09.081
43. Marco Corradi, Antonio Borri, Giulio Castori, and Romina Sisti. Shear strengthening of wall panels through jacketing with cement mortar reinforced by GFRP grids. *Composites Part B: Engineering*. 2014. 64(1). Pp. 33–42. DOI: 10.1016/j.compositesb.2014.03.022
44. Dias, S.J.E., Barros, J.A.O. NSM shear strengthening technique with CFRP laminates applied in high-strength concrete beams with or without pre-cracking. *Composites Part B: Engineering*. 2012. 43(2). Pp. 290–301. DOI: 10.1016/j.compositesb.2011.09.006
45. Massimiliano Bocciarelli, Serena Gambarelli, Nicola Nisticò, Marco Andrea Pisani, and Carlo Poggi. Shear failure of RC elements strengthened with steel profiles and CFRP wraps. *Composites Part B: Engineering*. 2014. 67(1). Pp. 9–21. DOI: 10.1016/j.compositesb.2014.06.009
46. Sheikh, S.A. Performance of concrete structures retrofitted with fiber reinforced polymers. *Engineering Structures*. 2002. 24(7). Pp. 869–879. DOI: 10.1016/S0141-0296(02)00025-1
47. Liu, F., Wu, B., Wei, D. Failure modes of reinforced concrete beams strengthened with carbon fiber sheet in fire. *Fire Safety Journal*. 2009. 44(7). Pp. 941–950. DOI: 10.1016/j.firesaf.2009.05.006
48. Rajai Z. Al-Rousan, Rami H. Haddad, Alaa O. Swesi. Repair of shear-deficient normal weight concrete beams damaged by thermal shock using advanced composite materials. *Composites Part B: Engineering*. 2015; 70(1). Pp. 20–34. DOI: 10.1016/j.compositesb.2014.10.032.
49. Zhang, Y.X., Bradford, M.A. Nonlinear analysis of moderately thick reinforced concrete slabs at elevated temperatures using a rectangular layered plate element with Timoshenko beam functions. *Engineering Structures*. 2007. 29(10). Pp. 2751–2761. DOI: 10.1016/j.engstruct.2007.01.016
50. Rami H. Haddad, Rajai Z. Al-Rousan. An anchorage system for CFRP strips bonded to thermally shocked concrete. *International Journal of Adhesion and Adhesives*. 2016. 71(1). Pp. 10–22. DOI: 10.1016/j.ijadhadh.2016.08.003
51. Mohammad, R. Irshidat, Mohammed H. Al-Saleh. Flexural strength recovery of heat-damaged RC beams using carbon nanotubes modified CFRP. *Construction and Building Materials*. 2017. 145(1). Pp. 474–482. DOI: 10.1016/j.conbuildmat.2017.04.047.

Contacts

Rajai Al-Rousan, rzalrousan@just.edu.jo

© Al-Rousan, R., 2020



DOI: 10.18720/MCE.94.9

Two-way patched RC slabs under concentrated loads

S.A. Kristiawan*, **A. Supriyadi**

^a Universitas Sebelas Maret, Surakarta, Indonesia,

* E-mail: s.a.kristiawan@ft.uns.ac.id

Keywords: patching, slab, spalling, ultimate load, unsaturated polyester resin mortar, yield line

Abstract. Damage that occurs in reinforced concrete elements can reduce the capacity and serviceability of these elements. One of the damages that may be encountered is spalling or delamination of concrete covers. Repairs to this type of damage can be carried out by patching methods. This research uses unsaturated polyester resin mortar (UPR-mortar) as a patch repair material to recover the damage of two-way slabs. Laboratory investigations were carried out to determine the effects of variations in patching location and loading on the ultimate capacity. The development of crack patterns as the load increases, the final yield lines formed at the time of collapse, and the magnitude of the ultimate load are the main data discussed in this research. In addition, load-deflection behavior, stiffness and toughness are also presented and discussed. Yield Line Theory (YLT) has been applied using virtual work principle with several assumptions and simplifications to estimate the ultimate load of the slabs. The experimental results show that UPR-mortar is able to recover the capacity and stiffness of the damaged slab, but it can not restore the toughness to the original level. The theoretical strength of the patched repair slabs estimated by simplified YLT shows that it is at least 90 % compared to experimental results.

1. Introduction

Reinforced concrete slab is widely used as floor elements in multi-story building structures. One type of slabs that is commonly found is rectangular slab which is supported on all four sides. This type of slab is known as a two-way slab. As part of structural system, reinforced concrete slab must be designed in such a way that they have sufficient capacity to be able to bear all the load combinations that the building will receive. The adequacy of the slab capacity in carrying the load can be expressed from the value of the safety factor. The structural concrete designers refer to Codes of Practice to ensure that the value of this safety factor is met [1, 2]. In reality, we must realize that the ultimate strength of slab may decrease along with the life of the building, and so it lowers the safety factor level over time. There are several factors that can reduce the value of this strength, for example, the degradation of concrete components that arise a result of high intensity of seismic load [3], fire exposure [4], reinforcement corrosion [5, 6], etc. In the case of reinforcement corrosion, the degradation of concrete components can be in the form of cracking, spalling and delamination of concrete covers [7–11]. In such situation, it is necessary to repair the damaged concrete components and corroded reinforcement so that the strength and serviceability of reinforced concrete slabs are restored. Several methods can be used to repair such damage including patching [12–14] and strengthening [15–24] with various materials and techniques. In term of patching, this method requires patch repair material which must meet several criteria including compatibility in mechanical properties, compatibility in dimensional properties, and compatibility in durability [13, 25–30]. One potential repair material that meets these criteria is unsaturated polyester resin mortar or UPR-mortar [31–34].

The ability of UPR-mortar in recovering the capacity of reinforced concrete slab patched with this material can be demonstrated by comparing the ultimate capacity of the patched repair RC slab with the normal RC slab. The ultimate capacity of reinforced concrete slab can be determined from the loading test results and estimated through theoretical calculations. In the loading test, ultimate capacity refers to when the slab is no longer able to bear an increase in load before it finally collapses [17, 34–37]. When the slab reaches the collapse phase, the crack lines show a certain pattern that can explain the mechanism of slab collapse. Crack lines that describe the collapse mechanism are also known as yield lines. Yield line pattern is an important parameter that is interesting to study because it becomes the basis in estimating the ultimate load of reinforced concrete slabs according to Yield Line Theory or YLT [38–42]

Kristiawan, S.A., Supriyadi, A. Two-way patched RC slabs under concentrated loads. Magazine of Civil Engineering. 2020. 94(2). Pp. 108–119. DOI: 10.18720/MCE.94.9



This work is licensed under a CC BY-NC 4.0

In principle, YLT assumes that reinforced concrete slabs have a uniform cross section and has a flexural collapse mode. Other important variables that influence the analysis according to this theory include the type of boundary conditions and the pattern of loading. In the case of reinforced concrete slabs that have been patched with UPR-mortar, the existence of patching zones makes the uniformity assumption unfulfilled. In the case of patched repair one-way slabs that carry a concentrated load in the center of the slabs, it has been shown that patching zones cause changes in yield line patterns and consequently ultimate load values also change [34].

Calculation of ultimate load according to YLT can be explained briefly as follows [43]. When the slab collapse mechanism occurs, the yield line is seen as the axis of rotation of the slab segments. The slab support line also acts as a rotation axis. The ultimate moment capacity (m_u) of reinforced concrete slabs per 1 m wide for a given reinforcement ratio can be calculated by Equation (1) as follows:

$$m_u = A_s \cdot f_y \cdot \left(d - 0.59 \cdot A_s \cdot \frac{f_y}{f_c} \right), \quad (1)$$

where A_s is the area of tensile reinforcement per meter width of the slab, f_y the yield stress of the steel reinforcement, f_c concrete compressive strength, d the distance between the center of the tensile reinforcement and the outer concrete compressive fiber. In certain cases, it is often necessary to determine the ultimate bending moment capacity along the yield line that has a direction not the same as the main axis of reinforcement of the slab. If the ultimate bending moments per unit width in the x and y directions respectively are m_{ux} dan m_{uy} , then the ultimate bending moment in any yield line (m_{un}) is obtained from Johansen's criteria (Figure 1), and is expressed in Equation (2) as follows:

$$m_{un} = m_{ux} \cos^2 \alpha + m_{uy} \sin^2 \alpha, \quad (2)$$

where the x and y axes are the reinforcement slabs, while α is the angle formed by the direction of the yield line with the y axis (see Figure 1).

The yield line pattern obtained from experimental investigations was used as validity for the assumption of location and yield line orientation that occurred on reinforced concrete slabs. Ultimate load P_u calculation was derived by the virtual work method [41]. Internal work done by the bending moment that occurs on the slab is $\sum m_{un} \cdot \theta_n \cdot L_o$ where θ_n is the relative rotation angle of the two slab segments to a yield line (Figure 2) and L_o is the length of the yield line. External work done by external forces in the form of concentrated load is $\sum P_u \cdot \Delta$, where P_u is the ultimate load, and Δ is slab deflection. The principle of virtual work states that external work is equal to internal work as expressed in Equation (3):

$$\sum m_{un} \cdot \theta_n \cdot l_o = \sum P_u \cdot \Delta. \quad (3)$$

The value of θ_n is explained by Figure 2 which is $\Delta / b1 + \Delta / b2$.

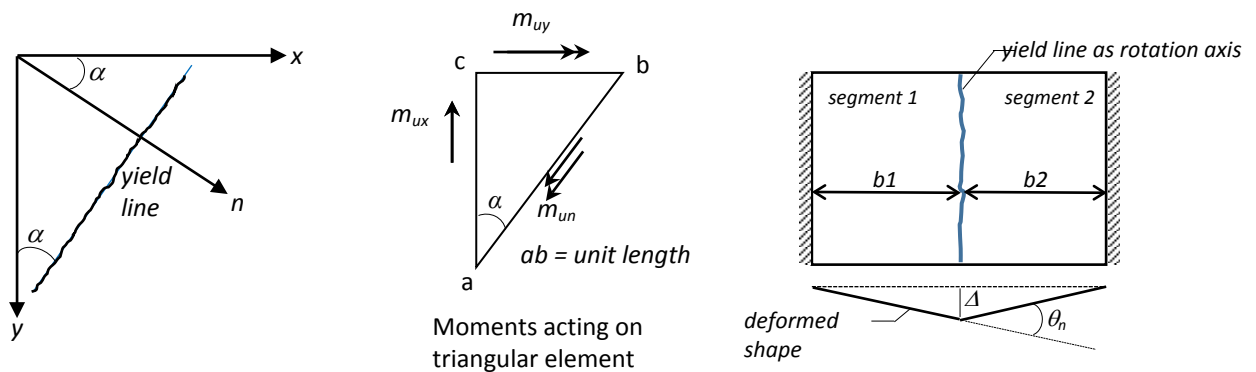


Figure 1. Yield line at general angle to orthogonal slab reinforcement.

Figure 2. Rotation of slab segments (θ_n) about each yield line.

Previous study suggests that UPR-mortar could be used to repair a damage on one-way slabs under concentrated load applied at the center of the slabs. Both experimental results and theoretical calculation using simplified YLT confirm the capability of UPR-mortar to restore the strength of the damaged slabs [34]. The results of the previous study encourage researchers to further investigate the application of UPR-mortar to restore more general cases of spalled reinforced concrete slabs. This research aims to determine the influence of patching zone locations on their associated yield line patterns and ultimate loads for the two-way

slab type. In addition to the patching zone variable, this research will also include an investigation on the effect of location/position of a concentrated load. Both experimental investigation and theoretical calculation of ultimate load using simplified YLT will be covered in this research.

2. Methods

In this research, 8 (eight) reinforced concrete slab specimens have been made with size (length×width×thickness) each of which is 1350×950×80 mm. In the short direction, the steel reinforcements are 7D10mm, while in the long direction they are 5D10mm (Figure 3). The first slab represents normal reinforced concrete slab without damage. The second slab represents reinforced concrete slab with spalling dimensions 300×200×30 mm and no patching. The spalling is simulated by cut out. The other six slabs represent spalling of reinforced concrete slabs but they have been patched with UPR-mortar with variations in patching locations. The types of slab specimens, identity, and parameter variations are summarized in Table 1 and 3.

Table 1. Types of reinforced concrete slab specimens.

Slab identity	Slab type, patching position, and concentrated load (P) position
N	Normal slab, without spalling (cut out), centric load
R0	Unrepaired slab, with spalling (cut out) but no patching, centric load
R1	Repaired slab, centric patching, centric load
R2	Repaired slab, eccentric patching, centric load
R3	Repaired slab, eccentric patching, centric load
R4	Repaired slab, eccentric patching, centric load
R5	Repaired slab, eccentric patching, eccentric load
R6	Repaired slab, eccentric patching, eccentric load

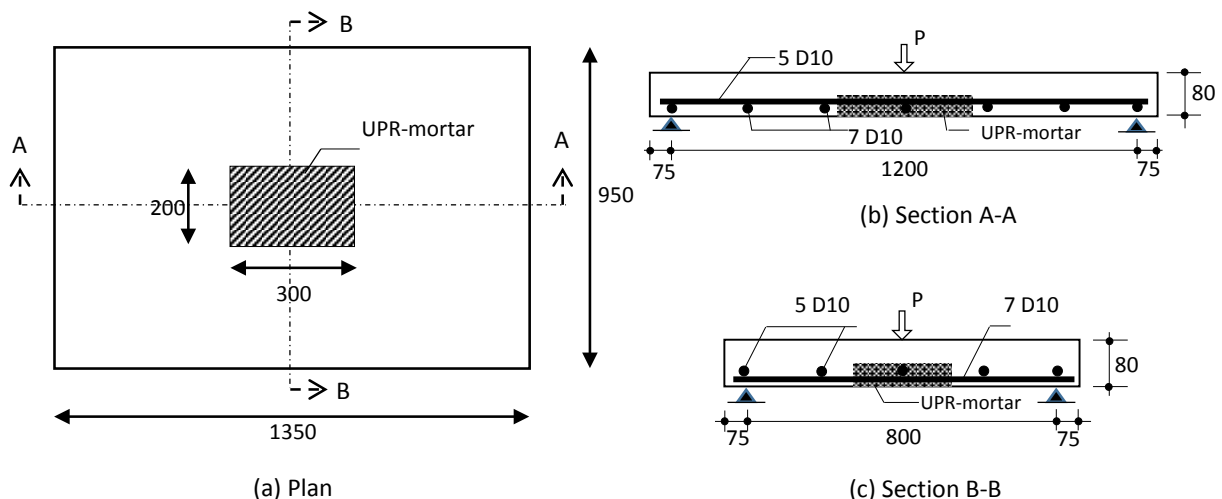


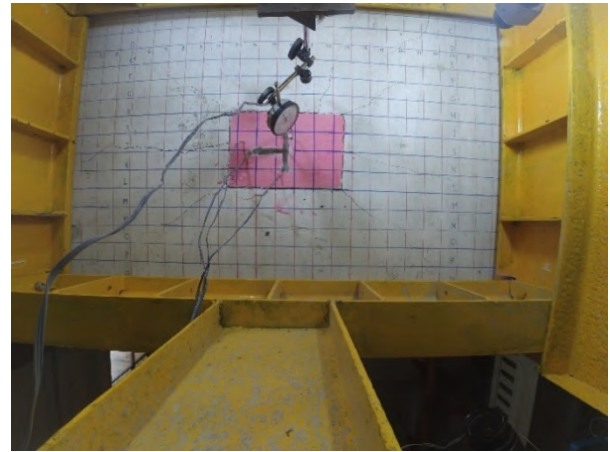
Figure 3. Slab size, reinforcement, patching position and load on plate specimen R1.

The slab size, reinforcement, patching position and load of one of specimen of reinforced concrete slabs (R1) are shown in Figure 3. The average compressive strength of concrete used to make reinforced concrete slabs was 29.47 MPa, while the tensile strength of reinforcing steel was 350.52 MPa. After the reinforced concrete slab has been casted, the curing process was done by wetting the specimen with water for 21 days and continued by storing the specimen in a laboratory environment for 3 months. After 3 months in a laboratory environment, reinforced concrete slabs were prepared for a load test. One day before the load test was carried out, the slabs (except slab N and R0) were patched first with a UPR mortar. UPR mortar was made with materials and composition: 950 kg of sand, 808 kg of cement, 143 kg of fly ash, 475 kg of UPR, and 14.25 kg of hardener per m³. This UPR mortar composition gave an average compressive strength of 75 MPa and a tensile strength (flexural) of 24.6 MPa when tested at 1 day of age.

All specimens of reinforced concrete slabs were laid on four sides with a simple-support type. The distance between the supports in the short and long spans were 800 mm and 1200 mm, respectively (Figure 3). External force in the form of concentrated load were applied according to their variations (Table 3). The load was applied to the slab at an increment of 0.5 kN. The maximum deflection that occurred under load was measured by a dial gauge. Observation of the crack pattern that occurred at the bottom of the slab was done from the initial load until the slab collapses. Figure 4 illustrates an example of testing on one of the slabs.



(a) Load applied on slab via hydraulic jack



(b) Measurement of deflection under the slab using dial gauge

Figure 4. Overview of loading and measurement of deflection on the slab.

3. Results and Discussion

3.1. Effects of Patching on the Development of Crack Pattern

Table 2 shows the development of crack patterns as load increases. At the initial phase before the first crack occurs, the distribution of the bending moment at the cross section of the slab follows the elastic theory. After a crack occurs, it causes a decrease in the stiffness of slab at the cracked section; consequently, it leads to a change in the moment distribution. At the tensile zone of the cracked section, a higher tensile stress is transferred to the steel reinforcements. Further increase of load causes the steel reinforcements at this cracked section reach their yielding stress. This crack forms the first yield line. Increasing load after the first yield line will produce more cracks to form a number of yield lines which divided the plane of the slab into several segments that incite the collapse mechanism. When the collapse mechanism has been formed, the slab reaches a phase of failure [38, 40].

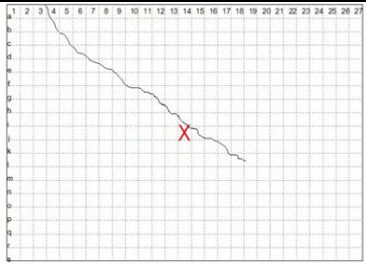
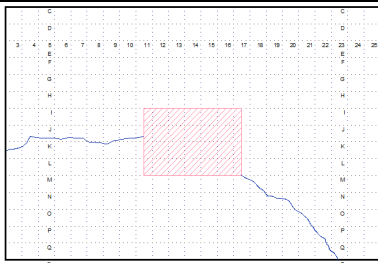
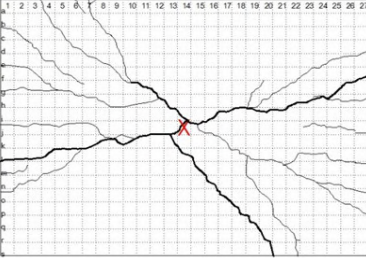
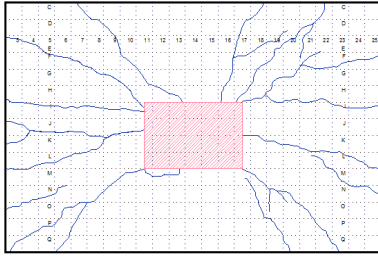
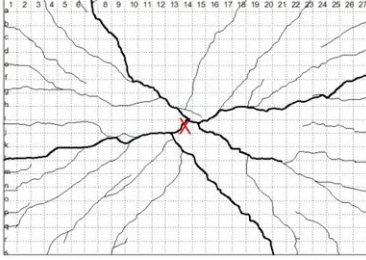
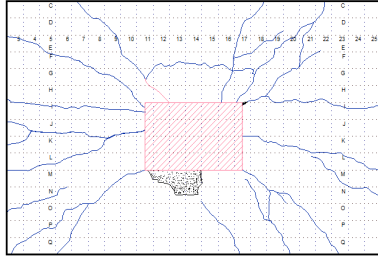
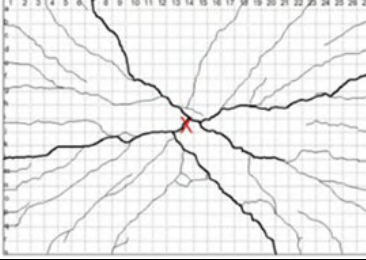
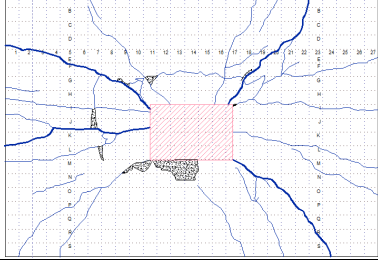
Table 2 also illustrates the comparison of the development of crack patterns that occur on one of the slabs that have been repaired with UPR-mortar (slab R1) compared to normal slab (slab N), starting from the first crack, yield, ultimate and failure phases. In the first crack phase, it is shown that patching causes the crack to occur not starting in the middle of the slab, but outside the patched area. Meanwhile, for normal slab, cracks are initiated from the center of the slab where maximum moments occurred. In subsequent phases (yield, ultimate, and failure), it is also shown that the crack line never crossed the patched area. In terms of crack intensities that occurred in slab N and slab R1, they show similarities. This indicates that patching with UPR-mortar produces slab which have the ability to redistribute bending moments well before collapse, as in the case of normal slab [34].

3.2. Effect of Patching and Load Position on Final Crack Pattern

The influence of patching area and concentrated load positions to the crack patterns are also examined in this research. Variations in the positions of the patching area include: centric position in the middle of the slab plane, eccentric on one axis, and eccentric on two axes. Variations of concentrated load positions are similar to patching area. The influence of patching area and load positions to the final crack patterns that describe the collapse mechanism of each slab and their corresponding ultimate load are presented in Table 3.

Generally, due to concentrated load, crack patterns in the collapse phase tend to form curves with radial lines forming circular fan patterns [34, 35]. This is different from the crack pattern in the slab with evenly distributed loads, which form triangular patterned segments between the yield lines [43]. Concentrated load position has a significant effect on crack patterns. The area under the concentrated load is a potential position for the initial crack. The development and propagation of the crack lines in the radial direction is started from the point under this concentrated load. When the concentrated load is placed at the center of the slabs or centric to the slab axes (N, R0, R1, R2 and R3), the crack lines is started in this point as well with the exception of R1. The present of patching on the center of the slab causes the crack lines occur outside the patching area. This is because the patching material (UPR-mortar) possess a higher tensile stress (about 24.6 MPa) compared to substrate concrete (about 3-7 MPa). Hence, the maximum bending moment at the center of the R1 does not initiate crack in this area. Meanwhile, when the concentrated load is shifted to be an eccentric to the axes (R4, R5, R6), it is seen that the starting point of the crack lines is also shifted following the load position. In all cases, the crack lines never cross the patched zone. This finding confirms the previous results [34].

Table 2. Development of crack patterns on normal slab and patched repair slab.

Phase	Normal slab (N)	Patched repair slab (R1)
First crack		
Yield		
Ultimate		
Failure		

✗ loading position

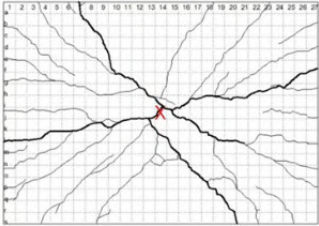
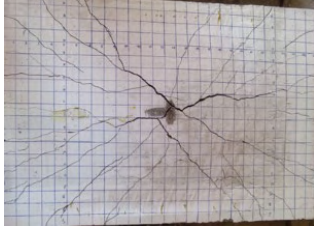
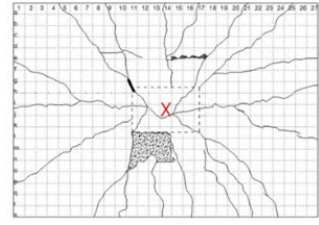
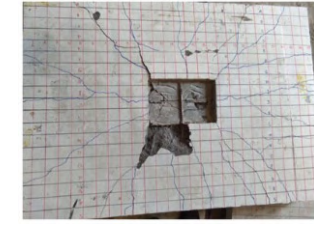
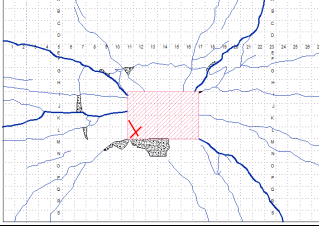
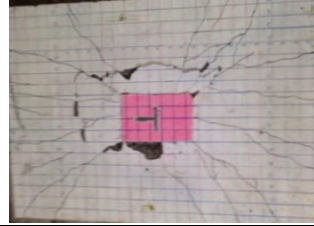
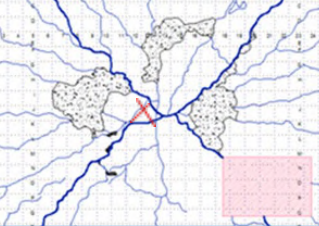
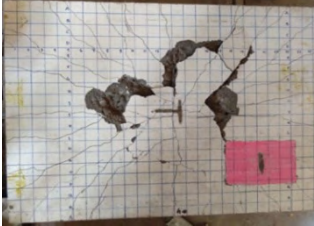
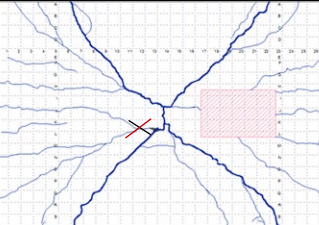
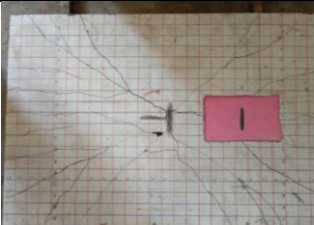
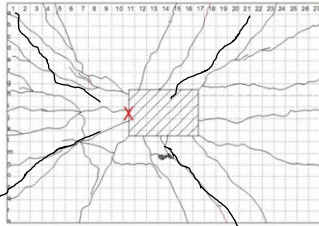
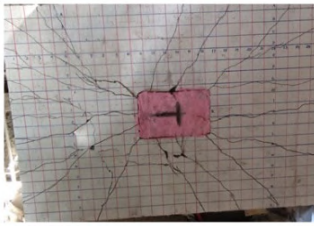
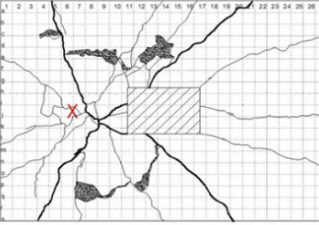
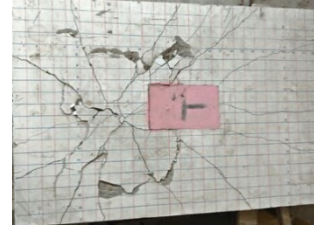
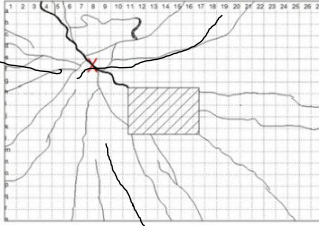
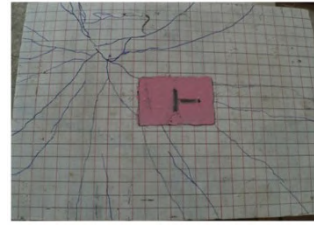
Table 3 also indicates the failure mode observed on slabs during the experimental investigation. Not all slabs exhibit flexural mode failure, but some slabs specimens show punching shear mode failure (slabs R0, R1 and R5). This punching shear is marked by the sinking of the steel plate which is used to transfer the concentrated load to the slab (Figure 5. (b)). Additional failure mode in the form of delamination is also noticed in slab R1 (Figure 5 (a)). Since this delamination is only occur in R1, it is of interest to investigate more detail on the bond between patching material and concrete substrate in this slab. It was noticed that when the patching material was applied to fill the cut out of the slab R1, the patching material did not entirely seal the cut out. There was a gap between the interface of cut out and patching material at one of the perimeters. This gap eventually triggered a “push off” when concentrated load was applied.

It is also interesting to note the effect of the supports. The slabs were laid on four supports without any restraints against upward displacement. Hence, when the concentrated load was imposed, it caused uplift at the corner of the supports. This uplift of the corner slab caused the yield lines direction to shift i.e. the yield lines did not form toward the corner point of the slabs as theoretically expected [38], instead they were diverted toward the side of the slabs. With this kind of yield line patterns, the slab's ultimate load will be lower than the pattern with yield lines toward the corner.

3.3. Ultimate load

The results of experimental investigations demonstrate how spalling on reinforced concrete slab (represented by cut out of slab R0) significantly causes a reduction in slab ultimate strength. From Table 3, it can be shown that the ultimate load (P_u) of R0 is 50.35 kN or 75.5 % to that of normal slab (N). The cut out reduces the thickness of the slab; consequently this thickness reduction leads to decrease in both the bending moment capacity [44] and punching shear capacity [45]. In the case of slab R0, reduction of punching shear capacity is more critical as shown by the emerged punching failure mode of this particular slab. Comparing the ultimate load of R0 and R1, R2, and R3, it is also confirmed that patching with UPR-mortar could restore the ultimate strength of the slabs to a level close to the original strength (N) with the exception of R1. The lower ultimate load of the R1 could be related to the failure mode of this slab as explained in the previous section.

Table 3. Final crack pattern of slabs and their ultimate load.

Type of slab	Sketch of final crack pattern	Bottom surface of slab after failure	Ultimate load and failure mode
Slab N			$P_{u,ex} = 66.68 \text{ kN}$ Flexural failure
Slab R0			$P_{u,ex} = 50.35 \text{ kN}$ Punching shear
Slab R1			$P_{u,ex} = 53.07 \text{ kN}$ Punching shear and delamination of patching material
Slab R2			$P_{u,ex} = 69.40 \text{ kN}$ Flexural failure
Slab R3			$P_{u,ex} = 63.05 \text{ kN}$ Flexural failure
Slab R4			$P_{u,ex} = 50.80 \text{ kN}$ Flexural failure
Slab R5			$P_{u,ex} = 57.61 \text{ kN}$ Punching shear
Slab R6			$P_{u,ex} = 60.78 \text{ kN}$ Flexural failure

✗ loading position

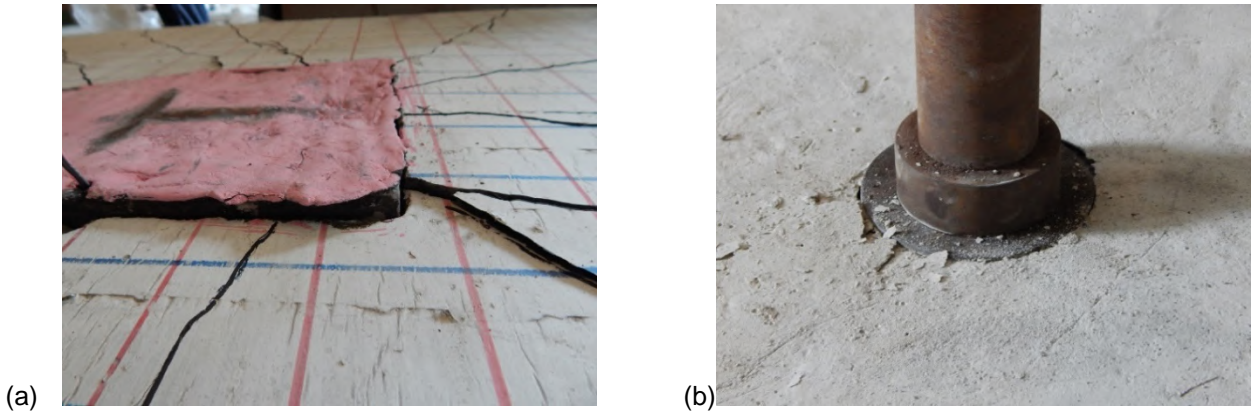
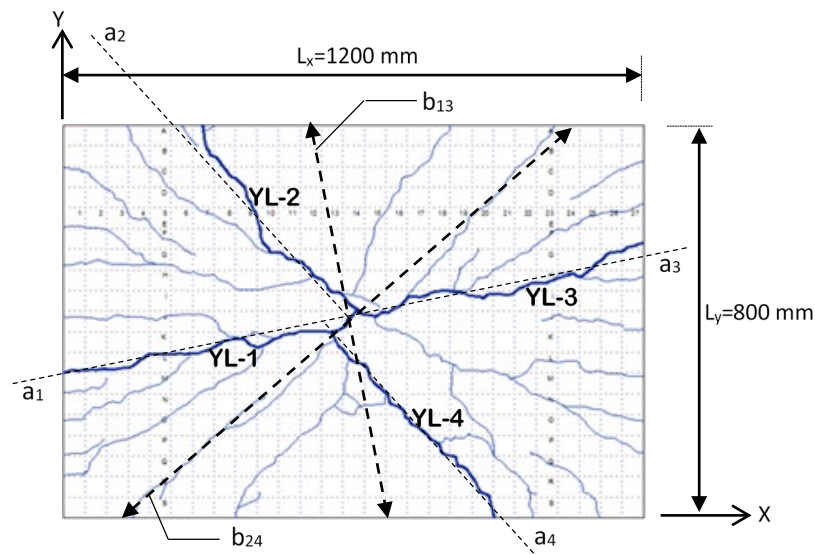


Figure 5. (a) Delamination of patching material UPR-mortar; (b) Punching shear in slabs.

The ultimate load of R4, R5, R6 represent the ultimate load of slab where the concentrated load is applied eccentric. It is unfortunate that we did not test a normal slab with an eccentric applied load to confirm the capability of the UPR-mortar in restoring the strength of the damaged slab. However, comparison of theoretical and experimental ultimate load can be used to indicate the strength recovery after patching with UPR-mortar as discussed in the following paragraphs.

Ultimate load of the slabs has been obtained from experimental investigations ($P_{u, ex}$). In this section, the value of $P_{u, ex}$ will be compared with a theoretical approach based on yield line theory (YLT). In using this theory, it is assumed that the cross section of the slab per unit width is the same. It is supposed that the presence of UPR-mortar will cause this assumption to be incorrect. However, in the context of simplification of ultimate load calculation, the assumption of uniformity is maintained. The influence of the patching is only taken into account in relation to the changes in the yield line patterns that occur between normal and patched slab. The yield line pattern will affect the estimated ultimate load as described in the next section. Thus, simplification in this theoretical approach was merely derived from the pattern of yield lines. Meanwhile, the various types of collapse (flexure, punching, delamination) and the phenomenon of corner levers are also ignored.



Notation:

YL-1, YL-2, YL-3, YL-4 = yield lines

a_1, a_2, a_3, a_4 = yield line slope direction (YL-1, YL-2, YL-3, YL-4)

b_{13} = length component to calculate the rotation angle θ_n on YL-1 and YL-3

b_{24} = length component to calculate the rotation angle θ_n on YL-2 and YL-4

Figure 6. Calculation of P_u on a normal plate with the virtual work method.

Figure 6 shows the yield line pattern on the normal slab (N) used to calculate P_u by the virtual work method. The calculated data used are as follows. Slab span in the long and short direction respectively are 1200 mm and 800 mm. The tensile strength of steel reinforcement is 350.5 MPa and the compressive strength of concrete is 29.47 MPa. Flexural reinforcements in the long direction are 5D10 mm ($A_s = 392.7$ mm²), while in the short direction are 7D10 mm ($A_s = 549.78$ mm²). With a slab thickness of 80 mm, the effective heights (d) in the long and short direction are 45 mm and 55 mm, respectively. By using Equation (1), the ultimate bending

moment capacity per 1 m width of the slab in the long direction (m_{ux}) and in the short direction (m_{uy}) are respectively 6,535,305 N.mm and 7,705,521 N.mm. The yield line of YL-1, YL-2, YL-3 and YL-4 are formed at an angle α to the y -axis successively at 80°, 42°, 80°, and 42°. By using Equation (2), an ultimate bending moment is obtained for each yield line (m_{un}) respectively of 7,670,235 N.mm, 7,059,252 N.mm, 7,670,235 N.mm and 7,059,252 N.mm. The length of each yield line (L_o) is respectively 0.609 m, 0.538 m, 0.609 m, and 0.538 m. With the length components of $b1$ and $b2$ for YL-1 (see Fig. 1), each is 406.2 mm and Δ (deflection of slab under loading) measured from experiments of 30.89 mm, a rotation angle (θ_n) is obtained for 0.1521 radians. In the same way, values (θ_n) for YL-2, YL-3 and YL-4 are respectively 0.1033 radians, 0.1521 radians and 0.1033 radians. Internal work (W_i) is calculated from the left-hand section of Equation (3) of 2,206,971 N.mm. Finally, with Equation (3), the ultimate load value (P_u) for normal slab is 71,446 N or 71,446 kN. The ratio of theoretical P_u values to experimental P_u ($R = P_u/P_{u, ex}$) is 1.07.

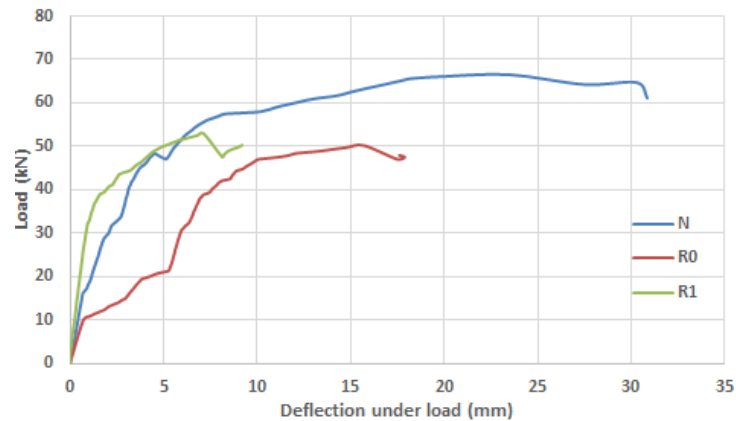
In the same way, the P_u is calculated for each slab according to its corresponding crack pattern and the results are presented in Table 4. The results of calculation by simplified YLT theory show that the ultimate strength is at least 90 % compared to the experimental result, except for slab R2. The possible reason of lower value of theoretical ultimate load of R2 compared to that of the experimental value could be traced from the crack's intensity. As shown in Table 3, the slab shows a greater intensity of cracks before failure. This intensity of cracks indicates that the R2 slab capable to redistribute the bending moment at high load level. Hence, the obtained experimental ultimate load is appreciably high (69.4 kN). Meanwhile, the simplified YLT does not consider the intensity of cracks for estimating the ultimate load.

Table 4. The estimated results of the ultimate load value (P_u) based on YLT.

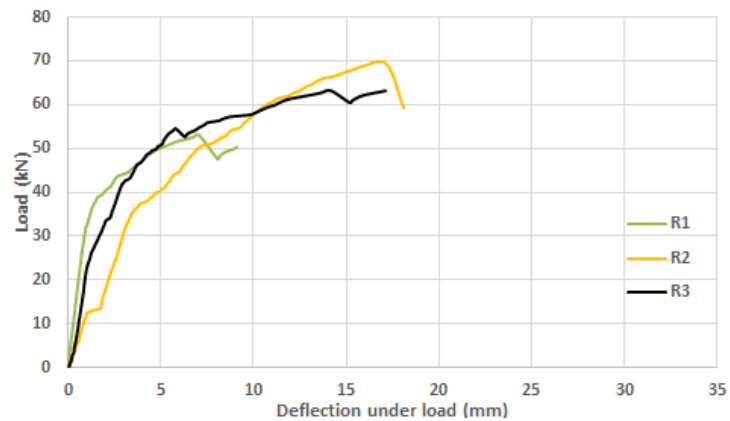
Slab	YL	α (°)	m_{un} (N.mm)	L_o (m)	Δ (mm)	$b1$ (mm)	$b2$ (mm)	θ_n (rad)	W_i (N.mm)	P_u (kN)	$P_{u,ex}$ (kN)	R
N	YL-1	80	7,670,235	0.609	30.89	406.2	406.2	0.1521	2,206,971	71.446	66.68	1.07
	YL-2	42	7,059,252	0.538		597.8	597.8	0.1033				
	YL-3	80	7,670,235	0.609		406.2	406.2	0.1521				
	YL-4	42	7,059,252	0.538		597.8	597.8	0.1033				
R1	YL-1	80	7,670,235	0.457	9.15	507.7	304.6	0.0481	522,181	57.069	53.07	1.08
	YL-2	70	7,568,632	0.479		532.1	319.3	0.0459				
	YL-3	40	7,018,810	0.392		466.7	777.9	0.0314				
	YL-4	35	6,920,294	0.523		523.0	871.7	0.0280				
R2	YL-1	43	7,079,598	0.547	18.12	546.9	586.5	0.0640	982,937	54.246	69.4	0.78
	YL-2	45	7,120,413	0.566		565.7	565.7	0.0641				
	YL-3	42	7,059,252	0.538		538.3	597.8	0.0640				
	YL-4	40	7,018,810	0.522		522.2	522.3	0.0638				
R3	YL-1	45	7,120,413	0.566	18.06	565.7	565.7	0.0639	1,028,757	56.963	63.05	0.90
	YL-2	45	7,120,413	0.566		565.7	565.7	0.0639				
	YL-3	45	7,120,413	0.566		565.7	565.7	0.0639				
	YL-4	45	7,120,413	0.566		565.7	565.7	0.0639				
R4	YL-1	40	7,018,810	0.522	14.27	622.3	622.3	0.0459	707,474	49.578	50.80	0.98
	YL-2	40	7,018,810	0.522		622.3	622.3	0.0459				
	YL-3	45	7,120,413	0.566		565.7	565.7	0.0505				
	YL-4	40	7,018,810	0.522		622.3	622.3	0.0459				
R5	YL-1	25	6,744,312	0.386	10.69	331.0	828.2	0.0452	566,929	53.034	57.61	0.92
	YL-2	25	6,744,312	0.497		331.0	1064.8	0.0423				
	YL-3	40	7,018,810	0.587		700.1	456.9	0.0387				
	YL-4	45	7,120,413	0.495		424.3	636.4	0.0420				
R6	YL-1	40	7,018,810	0.392	6.53	587.4	466.7	0.0251	383,376	58.710	60.78	0.97
	YL-2	70	7,568,632	0.585		212.8	638.5	0.0409				
	YL-3	30	6,827,859	0.346		600.0	1,000.0	0.0174				
	YL-4	70	7,568,632	0.319		212.8	877.1	0.0381				

3.4. Load-Deflection Behavior

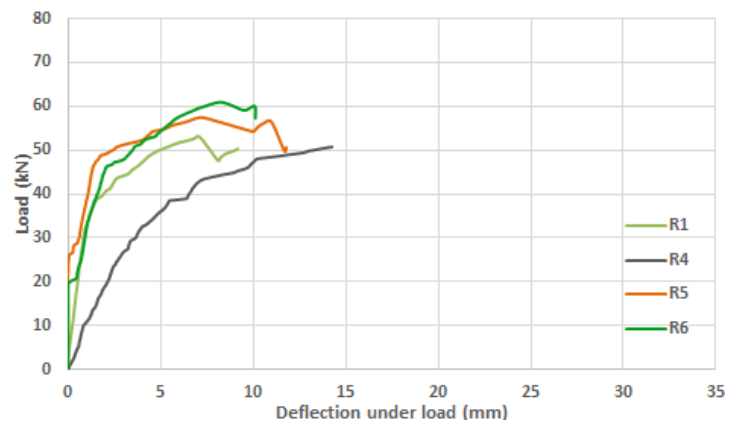
Global response of slabs under concentrated load could be characterised by the load-deflection behaviour. Figure 7 shows the load-deflection behaviours of the investigated slabs, which are presented into three groups. The first group (Figure 7 (a)) are slabs with centric imposed of concentrated load (N, R0, R1) but each slab represents respectively normal, cut out without being repaired, and patch repaired slab. This group (Figure 7 (b)) is intended to show the influence of spalling (cut out) and repair by UPR-mortar on the behaviour of slabs. The second group consists of R1, R2, R3 to identify the influence of patched area location on the global response of the slabs. Similar to the first group, the centric concentrated load is also applied. The last group (Figure 7 (c)) are slabs (R1, R4, R5, R6) having similar patched area and location, but the concentrated load is imposed at varying positions. Different to those of the first and second group where the maximum deflections are observed at the centre of the slabs, the maximum deflections of slabs in the third group occur eccentrically following the position of the imposed loads.



(a) Influence spalling (cut out) and patching



(b) Influence of patched area location



(c) Influence of concentrated load position

Figure 7. The load-deflection behaviour of the investigated slabs.

Generally, four phases of response can be identified: the first phase is a linear response with a high stiffness up to the initiation of cracks. The load causing the first crack (P_c) and its corresponding deflection (Δ_c) for each slab has been summarised in Table 5. The second phase indicates that the linear behaviour is

maintained but the stiffness of the slab is lower than that of the first phase. The lower stiffness is attributed to the propagation of cracks intensity as the imposed load increases. This phase is end when the reinforcement starts to yield. Table 5 shows the load (P_y) and its corresponding deflection (Δy) at the first yield of the reinforcement for each slab. After the first yield, the slab still capable to receive a higher load but a plastic response can be observed as indicated by large deformation. The peak load (P_u) marks the end of this phase. The value of peak load (P_u) and its corresponding deflection (Δu) for each slab can be seen in Table 5. After peak load, the slab still capable to show ductile behaviour before rupture, in which the slab deforms even though the imposed load is decreased. The maximum deformation (Δ_{max}) when the slab rupture is shown in Table 5.

Table 5. Load-deformation parameters of the slabs.

Slab ID	P_c (kN)	Δ_c (mm)	P_y (kN)	Δy (mm)	P_u (kN)	Δu (mm)	Δ_{max} (mm)
N	33.57	2.68	47.35	4.47	66.68	19.80	30.89
R0	9.98	0.71	21.21	3.86	50.35	15.70	17.88
R1	32.66	0.98	36.11	1.16	53.07	7.09	9.15
R2	13.61	0.60	36.29	3.58	69.40	17.20	18.12
R3	21.77	0.93	42.18	2.97	63.05	14.20	17.14
R4	23.59	2.47	35.87	3.64	50.80	14.27	15.55
R5	26.31	2.01	46.97	3.80	57.61	7.32	11.71
R6	17.24	0.61	43.72	2.49	60.78	8.38	10.14

There are other important parameters which can be deduced from the load-deflection behaviour i.e. stiffness, toughness, etc [15, 45, 46]. Stiffness indicates the deformation (deflection) resistance of the slab against the imposed load. The value may be determined by the slope of the load-deflection curve from the first initiation of cracks to the deflection equal to 3 mm. However, some of the investigated slabs show the reinforcement is already yielded at a deflection below 3 mm. Hence, for the current research the deflection at the first yield is used instead of the 3 mm limit to determine the stiffness. The characteristic of slab to absorb energy (toughness) can be recognised from the area under load-deflection curve. The value of stiffness and toughness are presented in Table 6.

Table 6. Stiffness and toughness of the slab,

Slab ID	Stiffness (kN/mm)	Toughness (kN.mm)
N	7.70	1774.19
R0	3.57	659.88
R1	19.17	403.59
R2	7.61	897.95
R3	10.00	887.10
R4	10.48	532.90
R5	11.55	607.48
R6	14.09	515.58

The influence of cut out and patching can be observed from Figure 7(a). It is obvious from the figure that spalling of slab (as simulated by cut out) causes reductions of the slab capacity, stiffness and toughness. Application of UPR-mortar to patch the cut out (R1) can be expected to recover the capacity, stiffness and toughness of the slab. However, the increase can only be observed at early phase up to a load of about 50 kN. After this load level, the repaired slab does not show large deformation due to the punching shear and delamination failure mode. It seems that delamination that occur in this slab (see Figure 5 (a)) terminates the response of the slab to receive higher load level. If there is no delamination, UPR-mortar could be effective to restore the deficient capacity and stiffness of spalling slab. This is confirmed by the higher capacity and stiffness of all other repaired slabs compared to those of the slab with cut out (R0). In term of toughness, it seems that UPR-mortar could not restore the toughness to the original toughness of normal slab (N).

The influence of patched area location can be observed from Figure 7 (b). The general trends of the load-deflection curves show similarity. However, there is evident that patched area location affects the characteristic values of strength, stiffness, and toughness of the slab (Table 6). Meanwhile, the influence of concentrated load position can be observed from Figure 7 (c). Except for R4, all other slabs show similar trend of the load-deflection curve. The different in the load-deflection curve of R4 from the other slabs could be associated with the fact that the concentrated load are applied right above the interface between the repair material and substrate concrete (Table 3). This load position will induce stress concentration at the interface leading to high deformation at this location. Hence, the stiffness, toughness and capacity of R4 are lower than others.

4. Conclusions

In this research, experimental investigations have been carried out to determine the cracks pattern and ultimate load of two-way reinforced concrete slabs patched with UPR-mortar under concentrated load, with variations of patching area and load positions. The main conclusions can be stated as follows:

- The development of cracks patterns in both normal slab and patched repair slabs show similarity where the crack is initiated at the tensile side of the slabs at a point under load position. It is interesting to note that the crack lines do not cross the patched area as a result of high flexural strength of the UPR-mortar (24.6 MPa).
- Final crack patterns (failure phase) in normal slab or patched repair slabs tend to form circular-fan pattern. The intensity of the crack lines in the two types of slabs show similarity. This indicates that the use of UPR-mortar as a patch repair material could redistribute the bending moment in similar way to that of normal slab.
- Not all slab specimens have a flexural failure mode, but some specimens show a punching shear mode (R0, R1, R5). Additional delamination of the repair material could occur if the patching process was not done properly (R1).
- The corner levers phenomenon (uplift in the slab corner region) due to the absence of restraint against upward displacement in the slab support affects the yield line patterns in which the yield lines tend to divert toward the side of the slab.
- The simplified YLT has been applied with the principle of virtual work to estimate the ultimate load of the slabs. The results of calculation by simplified YLT theory show that the ultimate strength is at least 90 % compared to the experimental result, except for slab R2.
- The load-deflection behavior of the slabs (either normal or repair) can be identified into four phases: linear response with high stiffness up to first cracks, linear response from the first cracks up to the first yield of reinforcement, plastic response from the first yield to the peak load, and further ductile response from the peak load to the rupture.
- UPR-mortar can recover the capacity and stiffness of the damage (cut out) slab but it cannot restore the toughness to the original value (normal slab).

5. Acknowledgement

The research was financially supported by Universitas Sebelas Maret, Indonesia through Fundamental Research Scheme (Contract No. 543/UN27.21/PP/2018).

References

1. ACI Committee 318. Building Code Requirements for Structural Concrete (ACI 318-14). 22(88)2014.
2. Rombach, G., Kohl, M. Shear design of RC bridge deck slabs according to eurocode 2. *Journal of Bridge Engineering*. 2013. 18(12). Pp. 1261–1269. DOI: 10.1061/(ASCE)BE.1943-5592.0000460.
3. Daniel N. Farhey, Moshe A. Adin, and D.Z.Y. REPAIRED RC FLAT-SLAB-COLUMN SUBASSEMBLAGES UNDER LATERAL LOADING. *Journal of Structural Engineering*. 1995. 121(11). Pp. 1710–1720.
4. Rybakov, V.A., Ananeva, I.A., Rodicheva, A.O., Ogidan, O.T. Stress-strain state of composite reinforced concrete slab elements under fire activity. *Magazine of Civil Engineering*. 2017. 74(6). Pp. 161–174. DOI: 10.18720/MCE.74.13.
5. Eyre, J.R., Nokhasteh, M.A. STRENGTH ASSESSMENT OF CORROSION DAMAGED REINFORCED CONCRETE SLABS AND BEAMS. *Proceedings of the Institution of Civil Engineers – Structures and Buildings*. 1992. 94(2). Pp. 197–203. DOI: 10.1680/istbu.1992.18788.
6. Lushnikova, V.Y., Tamrazyan, A.G. The effect of reinforcement corrosion on the adhesion between reinforcement and concrete. *Magazine of Civil Engineering*. 2018. 80(4). Pp. 128–137. DOI: 10.18720/MCE.80.12.
7. Kim, M.O., Bordelon, A., Lee, M.K., Oh, B.H. Cracking and failure of patch repairs in RC members subjected to bar corrosion. *Construction and Building Materials*. 2016. 107. Pp. 255–263. DOI: 10.1016/j.conbuildmat.2016.01.017.
8. Al-Harthy, A.S., Stewart, M.G., Mullard, J. Concrete cover cracking caused by steel reinforcement corrosion. *Magazine of Concrete Research*. 2011. 63(9). Pp. 655–667. DOI: 10.1680/macr.2011.63.9.655.
9. Mullard, J.A., Stewart, M.G. Corrosion-induced cover cracking: New test data and predictive models. *ACI Structural Journal*. 2011. 108(1). Pp. 71–79. DOI: 10.14359/51664204.
10. Chernin, L., Val, D. V. Prediction of corrosion-induced cover cracking in reinforced concrete structures. *Construction and Building Materials*. 2011. 25(4). Pp. 1854–1869. DOI: 10.1016/j.conbuildmat.2010.11.074.
11. Li, C.Q., Zheng, J.J., Lawanwisut, W., Melchers, R.E. Concrete Delamination Caused by Steel Reinforcement Corrosion. *Journal of Materials in Civil Engineering*. 2007. 19(7). Pp. 591–600. DOI: 10.1061/(ASCE)0899-1561(2007)19:7(591).
12. Chen, Y., Yu, J., Leung, C.K.Y. Use of high strength Strain-Hardening Cementitious Composites for flexural repair of concrete structures with significant steel corrosion. *Construction and Building Materials*. 2018. 167. Pp. 325–337. DOI: 10.1016/j.conbuildmat.2018.02.009.
13. Kim, H., Han, D., Kim, K., Romero, P. Performance assessment of repair material for deteriorated concrete slabs using chemically bonded cement. *Construction and Building Materials*. 2020. 237. Pp. 117468. DOI: 10.1016/j.conbuildmat.2019.117468.
14. Assaad, J.J. Development and use of polymer-modified cement for adhesive and repair applications. *Construction and Building Materials*. 2018. 163. Pp. 139–148. DOI: 10.1016/j.conbuildmat.2017.12.103.

15. Al-Rousan, R., Issa, M., Shabila, H. Performance of reinforced concrete slabs strengthened with different types and configurations of CFRP. *Composites Part B: Engineering*. 2012. 43(2). Pp. 510–521. DOI: 10.1016/j.compositesb.2011.08.050.
16. Pelà, L., Aprile, A., Benedetti, A. Experimental study of retrofit solutions for damaged concrete bridge slabs. *Composites Part B: Engineering*. 2012. 43(5). Pp. 2471–2479. DOI: 10.1016/j.compositesb.2011.08.038.
17. Yin, H., Teo, W., Shirai, K. Experimental investigation on the behaviour of reinforced concrete slabs strengthened with ultra-high performance concrete. *Construction and Building Materials*. 2017. 155. Pp. 463–474. DOI: 10.1016/j.conbuildmat.2017.08.077.
18. Schladitz, F., Frenzel, M., Ehlig, D., Curbach, M. Bending load capacity of reinforced concrete slabs strengthened with textile reinforced concrete. *Engineering Structures*. 2012. 40. Pp. 317–326. DOI: 10.1016/j.engstruct.2012.02.029.
19. Loreto, G., Leardini, L., Arboleda, D., Nanni, A. Performance of RC slab-type elements strengthened with fabric-reinforced cementitious-matrix composites. *Journal of Composites for Construction*. 2014. 18(3). DOI: 10.1061/(ASCE)CC.1943-5614.0000415.
20. Fernandes, H., Lúcio, V., Ramos, A. Strengthening of RC slabs with reinforced concrete overlay on the tensile face. *Engineering Structures*. 2017. 132. Pp. 540–550. DOI: 10.1016/j.engstruct.2016.10.011.
21. Zhu, Y., Zhang, Y., Hussein, H.H., Chen, G. Flexural strengthening of reinforced concrete beams or slabs using ultra- high performance concrete (UHPC): A state of the art review. *Engineering Structures*. 2020. 205(November 2019). Pp. 110035. DOI: 10.1016/j.engstruct.2019.110035.
22. Bonaldo, E., de Barros, J.A., Lourenço, P.B. Efficient Strengthening Technique to Increase the Flexural Resistance of Existing RC Slabs. *Journal of Composites for Construction*. 2008. 12(2). Pp. 149–159. DOI: 10.1061/(ASCE)1090-0268(2008)12:2(149).
23. Radik, M.J., Erdogmus, E., Schafer, T. Strengthening Two-Way Reinforced Concrete Floor Slabs Using Polypropylene Fiber Reinforcement. *Journal of Materials in Civil Engineering*. 2011. 23(5). Pp. 562–571. DOI: 10.1061/(ASCE)MT.1943-5533.0000206.
24. Koutas, L.N., Bournas, D.A. Flexural Strengthening of Two-Way RC Slabs with Textile-Reinforced Mortar: Experimental Investigation and Design Equations. *Journal of Composites for Construction*. 2017. 21(1). Pp. 04016065. DOI: 10.1061/(ASCE)CC.1943-5614.0000713.
25. Chen, D.H., Won, M. Field performance with state-of-the-art patching repair material. *Construction and Building Materials*. 2015. 93. Pp. 393–403. DOI: 10.1016/j.conbuildmat.2015.06.002.
26. Ali, M.S., Leyne, E., Saifuzzaman, M., Mirza, M.S. An experimental study of electrochemical incompatibility between repaired patch concrete and existing old concrete. *Construction and Building Materials*. 2018. 174. Pp. 159–172. DOI: 10.1016/j.conbuildmat.2018.04.059.
27. Abo Sabah, S.H., Hassan, M.H., Muhamad Bunnori, N., Megat Johari, M.A. Bond strength of the interface between normal concrete substrate and GUSMRC repair material overlay. *Construction and Building Materials*. 2019. 216. Pp. 261–271. DOI: 10.1016/j.conbuildmat.2019.04.270.
28. Kristiawan, S.A. Evaluation of Models for Estimating Shrinkage Stress in Patch Repair System. *International Journal of Concrete Structures and Materials*. 2012. 6(4). DOI: 10.1007/s40069-012-0023-y.
29. Yazdi, M.A., Dejager, E., Debraekeleer, M., Gruyaert, E., Van Tittelboom, K., De Belie, N. Bond strength between concrete and repair mortar and its relation with concrete removal techniques and substrate composition. *Construction and Building Materials*. 2020. 230. Pp. 116900. DOI: 10.1016/j.conbuildmat.2019.116900.
30. Nunes, V.A., Borges, P.H.R., Zanotti, C. Mechanical compatibility and adhesion between alkali-activated repair mortars and Portland cement concrete substrate. *Construction and Building Materials*. 2019. 215. Pp. 569–581. DOI: 10.1016/j.conbuildmat.2019.04.189.
31. Stefanus, K., Agus, S., Ageng, B.P., Siti, R. Mechanical properties of unsaturated polyester resin (UPR) – Mortar and its potential application to restore the strength and serviceability Of patched reinforced concrete slab. *Key Engineering Materials*. 2017. 737 KEM. Pp. 560–566. DOI: 10.4028/www.scientific.net/KEM.737.560.
32. Kristiawan, S.A., Fitrianto, R.S. Comparison of shrinkage related properties of various patch repair materials. *IOP Conference Series: Materials Science and Engineering*. 2017. 176. Pp. 012017. DOI: 10.1088/1757-899X/176/1/012017.
33. Adi Kristiawan, S., Bektı Prakoso, A. Flexural Behaviour of Patch-Repair Material Made from Unsaturated Polyester Resin (UPR)-Mortar. *Materials Science Forum*. 2016. 857. Pp. 426–430. DOI: 10.4028/www.scientific.net/MSF.857.426.
34. Kristiawan, S., Supriyadi, A., Pradana, D.R., Azhim, M.R.N. Flexural behaviour of one-way patched reinforced concrete (RC) slab under concentrated load. *Asian Journal of Civil Engineering*. 2018. 19(2). DOI: 10.1007/s42107-018-0014-7.
35. Zheng, Y., Zhou, L., Xia, L., Luo, Y., Taylor, S.E. Investigation of the behaviour of SCC bridge deck slabs reinforced with BFRP bars under concentrated loads. *Engineering Structures*. 2018. 171(April). Pp. 500–515. DOI: 10.1016/j.engstruct.2018.05.105.
36. Zheng, Y., Yu, G., Pan, Y. Investigation of ultimate strengths of concrete bridge deck slabs reinforced with GFRP bars. *Construction and Building Materials*. 2012. 28(1). Pp. 482–492. DOI: 10.1016/j.conbuildmat.2011.09.002.
37. Fang, H., Xu, X., Liu, W., Qi, Y., Bai, Y., Zhang, B., Hui, D. Flexural behavior of composite concrete slabs reinforced by FRP grid facesheets. *Composites Part B: Engineering*. 2016. 92. Pp. 46–62. DOI: 10.1016/j.compositesb.2016.02.029.
38. Alasam, M.A.A. Yield Line Method Applied to Slabs with Different Supports. (December). University of Khartoum, 2006.
39. Quintas, V. Two main methods for yield line analysis of slabs. *Journal of Engineering Mechanics*. 2003. 129(2). Pp. 223–231. DOI: 10.1061/(ASCE)0733-9399(2003)129:2(223).
40. Burgess, I. Yield-line plasticity and tensile membrane action in lightly-reinforced rectangular concrete slabs. *Engineering Structures*. 2017. 138. Pp. 195–214. DOI: 10.1016/j.engstruct.2017.01.072.
41. Bauer, D., Redwood, R.G. Numerical yield line analysis. *Computers and Structures*. 1987. 26(4). Pp. 587–596. DOI: 10.1016/0045-7949(87)90007-1.
42. Salehian, H., Barros, J.A.O. Prediction of the load carrying capacity of elevated steel fibre reinforced concrete slabs [Online]. *Composite Structures*. 2017. 170. Pp. 169–191. DOI: 10.1016/j.compstruct.2017.03.002. URL: <http://dx.doi.org/10.1016/j.compstruct.2017.03.002>.
43. Park, R.; Gamble, W.L. *Reinforced Concrete Slabs*. Second Edi. John Wiley & Sons, Inc. New York, 2000.
44. Buka-Vaivade, K., Sliseris, J., Serdjus, D., Pakrastins, L., Vatin, N.I. Rational use of HPSFRC in multi-storey building. *Magazine of Civil Engineering*. 2018. 84(8). Pp. 3–14. DOI: 10.18720/MCE.84.1.
45. Al-Rousan, R. Behavior of two-way slabs subjected to drop-weight. *Magazine of Civil Engineering*. 2019. 90(6). Pp. 62–71. DOI: 10.18720/MCE.90.6.
46. Ehsani, R., Sharbatdar, M.K., Kheyroddin, A. Ductility and moment redistribution capacity of two-span RC beams. *Magazine of Civil Engineering*. 2019. 90(6). Pp. 104–118. DOI: 10.18720/MCE.90.10.

Contacts:

Stefanus Kristiawan, s.a.kristiawan@ft.uns.ac.id

Agus Supriyadi, agussupriyadi@staff.uns.ac.id



DOI: 10.18720/MCE.94.10

Heat recovery efficiency of local decentralized ventilation devices

J. Zemitis*, **R. Bogdanovics**

Riga Technical University, Riga, Latvia,

** E-mail: jurgis.zemitis@rtu.lv*

Keywords: decentralized ventilation, heat recovery, efficiency, pressure difference

Abstract. Decentralized, room-based ventilation systems have become increasingly popular in the Baltic countries. Such systems are easy to install and, according to technical information, ensure high heat energy recovery potential for new and renovated buildings. The specified heat recovery efficiency is used for building energy simulations and to calculate the necessary heating energy that is needed to warm up the supply air. However, this value is stated at non-existent pressure difference between indoor of the building and the outside. In real-case situations, there is always some pressure difference due to wind and stack effect. In this study, a ventilation device is tested in a laboratory environment at different simulated outside air temperatures and pressure differences. The simulations are conducted in a climatic chamber where the air temperature and pressure differences can be set. The temperature is adjusted using a cooling device but the pressure difference with an exterior fan device. Different combinations of simulated outside air temperatures and pressure differences were tested. The results suggest that the heat recovery efficiency is highly dependent on the pressure difference and it rapidly decreases with the rise in pressure difference. If the pressure difference is in the range of 10–20 Pa, the heat recovery efficiency will be only between 20 and 50 %, while the stated value in the technical data sheet is 85 %. Even at a pressure difference of 0 Pa, the average heat recovery efficiency is 73 %, and only for the first few seconds of the supply cycle, the efficiency reaches 85 %. This can influence the calculated building energy efficiency class, as well as lead to undersized heating system elements.

1. Introduction

Nowadays almost all newly built buildings are equipped with some sort of mechanical ventilation system, whether it would be hybrid type, full supply/exhaust system or local, personalized ventilation system [1–3]. Such systems can also be applied to historical buildings [4]. This is done to increase indoor air quality (IAQ) and, at the same time, to maximally reduce the heat losses that occur through the natural ventilation system. For a moderate climate, as in Europe, combined infiltration and ventilation is responsible for approximately 50 % of the total heat losses in well-insulated buildings [5]. Similar results are presented for buildings located in Russia, stating that for multi-apartment buildings, heat losses due to ventilation, including infiltration, exceed transmission losses and account for about 60 % of total heat losses [6]. To reduce this, mechanical ventilation with heat recovery is used. Such systems can also help to significantly save primary energy, at the same time ensuring good indoor air quality while the airtightness of new and renovated buildings is increasing [7–9]. Several different heat recovery types can be applied to ventilation systems [10], but especially in cases of nearly zero-energy buildings (nZEB), it is vitally important to take into consideration that the exhaust temperature after heat exchanger for fully mechanical supply/exhaust ventilation systems must be limited to 0° to +5 °C, depending on the heat recovery type, as for such buildings more often the aim is to have as high heat recovery efficiency as possible [9]. A study analysing indoor relative humidity in apartments with a room-based ventilation system with a rotary heat exchanger indicated that it is suitable for single-room ventilation of dry rooms, such as living rooms and bedrooms, while excessive moisture from kitchens and bathrooms provided a mould risk [11]. Other publications indicate that a specific type of decentralized ventilation system with two heat exchangers, which are hydronically connected in parallel, is an appropriate solution for use in hot and humid climates because more cooling and dehumidification capacity is available [12]. Other studies have focused on developing modern ventilation solutions that are integrated into the façade and work on convective heat flow without the use of a mechanical ventilator [13].

Zemitis, J., Bogdanovics, R. Heat recovery efficiency of local decentralized ventilation devices. Magazine of Civil Engineering. 2020. 94(2). Pp. 120–128. DOI: 10.18720/MCE.94.10



This work is licensed under a CC BY-NC 4.0

The IAQ and adequate ventilation are linked to human wellbeing, health and even performance [14]. Studies on how to evaluate the performance and effectiveness of different ventilation system types have been performed for more than 20 years [15]. In some cases local recirculation diffusers, which in comparison to central recirculation ventilation systems eliminate such disadvantages as – increased power consumption for moving the ventilation air; increased size of the air ducts; recirculation of hazardous substances to the supply air with air transfer, can be applied to reduce the consumed heating energy [16]. These savings can be simulated and various scenarios analysed to find the best solution [17, 18]. However, it can often be hard to find the necessary funding and space to install full-size centralized ventilation systems with large ducts and AHU. Therefore, to save space and to reduce the amount of ductwork in buildings, quite often a room-based decentralized ventilation system is installed. It is especially desirable in case of renovations, as they require almost no indoor works and, according to existing studies, can provide good IAQ and thermal comfort [19]. There are various designs and types of such systems. These can be either as a small AHU with a rotary heat exchanger, which, according to studies, can have thermal recovery efficiency up to 85 % [20] or like a single fan that changes directions and leads air through the regenerative heat exchanger. At the same time, some research has indicated that the actual performance of ventilation systems on-site is often lower than expected [21]. Also, noise can be a negative factor, when operating room-based ventilation devices, as the ventilator and the user are in the same room. Additionally, in most cases, there are no sound dampening devices installed. Although, according to the manufacturer data, the sound pressure level of such devices is relatively low – from around 30 dB to 43 dB at 1m distance, in real case scenarios this can cause a nuisance. This can be linked by changes in the sound profile when the ventilator stops after each cycle and starts again in a reversed direction.

Although decentralized room-based ventilation systems with alternating airflow and storage type heat exchanger can provide good opportunities for heat energy savings and low energy consumption, their actual performance can be strongly influenced by external parameters like wind and stack effect, therefore noticeably lowering the actual heat recovery efficiency and overall building energy class [22]. The rated heat recovery energy efficiency is the only value stated in the datasheets of such units, but it is measured under specific conditions according to the standard EN 13141–8:2014 [23], which describes the measuring procedure for the alternating units. The standard does not require to perform measurements at various pressure differences between indoors and outside but only states that indoor temperature must be +20 °C and outside temp. +7 °C. This rated heat recovery energy efficiency is often the only information available for the individuals or software performing energy calculations it can be misleading as usually it is taken as a constant value. Therefore it can influence the heat loss calculation results that take into consideration the infiltration rate and supply air temperature [24].

In some cases, the negative or positive pressure is required by the local regulations to prevent pollution coming from the outside or to prevent exfiltration of moist indoor air into the structures [25]. Even if it is not designed specifically, the pressure difference between indoors and outdoors on average is approximately 7 Pa for naturally ventilated buildings, but this can vary widely, depending on the specific building form, location, orientation of openings and temperature difference [26]. Existing measurements in apartments with room-based air handling units with regenerative ceramic heat exchangers have shown insufficient results because they fail to guarantee a continuous air change in apartments and do not comply with energy efficiency requirements [25]. Such shortcomings are noticed also for heat recovery ventilators, as the measurements indicate that the heat exchange efficiency is not constant and changes depending on the actual operating conditions [27]. Another study suggests that external short circuits, internal air leakages, and heat flows through the casing can also reduce the performance of single-room ventilation units [28].

In previous studies, the changes in ventilation air volume that gets supplied/exhaust from building through decentralized ventilation devices at various pressure differences have been analysed. The results suggest that at a differential pressure of 10 Pa, the deviations in fresh air amount can vary between 30 to 100 % from the nominal flow of 30 m³/h flow. This means that the supply rates were higher and the extract rates were lower than the nominal flow rates, and on cold winter days, this could lead to drought and also to decreased heat recovery efficiency [29]. In the same study, it was mentioned that the specific heat recovery efficiency is lower than stated in the datasheets, but as the measurements were field-based, the exact values may be inaccurate and case dependent. Therefore, in this study, a specific ventilation device is tested in a laboratory environment at different simulated outside air temperatures and pressure differences to find out how heat recovery efficiency changes.

2. Methods

The study was conducted in a closed and controlled environment of a climatic chamber, simulating the variable outside air conditions. The climatic chamber has dimensions of 3 by 4 meters and a ceiling height of 2.3 m, thus the total volume of the chamber is 27.6 m³. The climatic chamber was tightly sealed, therefore making it almost perfectly airtight. In one of the chamber walls, the local decentralized ventilation system device was installed (see Figure 1 and 2). It supplied air to an open room, in such a way simulating indoor conditions. The conditions in this room were not specifically maintained but were stable by themselves as the

air, supplied from the climatic chamber, did not have an influence on the average temperature, according to the measurements. The technical parameters of the test ventilation device were as follows: max airflow 25 m³/h, electrical power consumption 13 W, specified heat recovery efficiency up to 85 %. The device operated in two 70 seconds long, varying cycles, switching between supply and exhaust.



Figure 1. The experimental setup – air intake from the simulated cold outside conditions through integrated wind protection frame (on the left); air supply side in the warm room (in the middle); ventilator, which generates the simulated overpressure in the climatic chamber (on the right).



Figure 2. The cooling device, which ensured simulated outdoor air temperature in the climatic chamber.

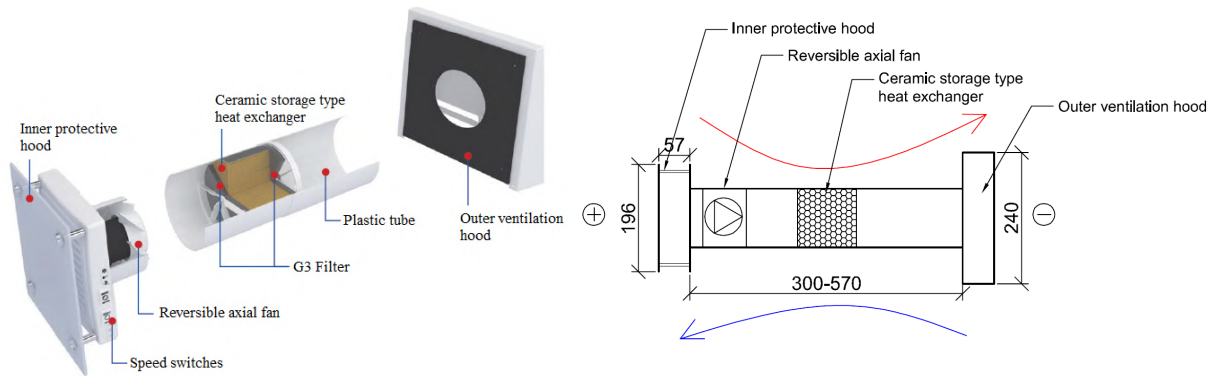


Figure 3. The ventilation device used in experiments – the construction of the device (on the left) and the section of equipment (on the right).

The inside of the chamber represents outside air conditions, as during the experiment the temperature of the chamber was controlled, and measurements were performed at a temperature range from +7 °C down to –5 °C. The relative humidity during the experiment in the climatic chamber varied between 30 to 60 %, while in the external premise it was constantly around 40 %. However, this should not affect the energy efficiency of the heat recovery unit as it is not an enthalpy type heat recovery unit and it only recovers sensible heat from exhaust air. Additionally, the inside air pressure of the chamber was controlled through the help of a Retrotech ventilator, which constantly adjusts the rotation speed to keep the specified pressure difference between the inside of the chamber and external premise. The ambient and climatic chamber temperatures were logged through the Extech SD800 logger with an accuracy of 0.8 °C. The temperature just in the front and back of the ventilation device was measured and logged with 1 second interval with Testo 435 device equipped with thermal velocity probe with temperature measuring range –20 to +70 °C ±0.3 °C and velocity measuring range of 0 to 20 m/s ±(0.03 m/s + 4 % of mv) and waterproof immersion probe, which has temperature measuring

range $-60\text{ }^{\circ}\text{C}$ to $+400\text{ }^{\circ}\text{C}$ and accuracy class 2. The measurements of temperature were performed in front of the ventilation device, located in the climatic chamber, herewith regarded as inlet temperature (θ_{12}), after the device as supply temperature (θ_{22}), the temperature in the climatic chamber is regarded as outside temperature (θ_{21}) and temperature in the open room as indoor temperature (θ_{11}). See the full experimental setup in Figure 4.

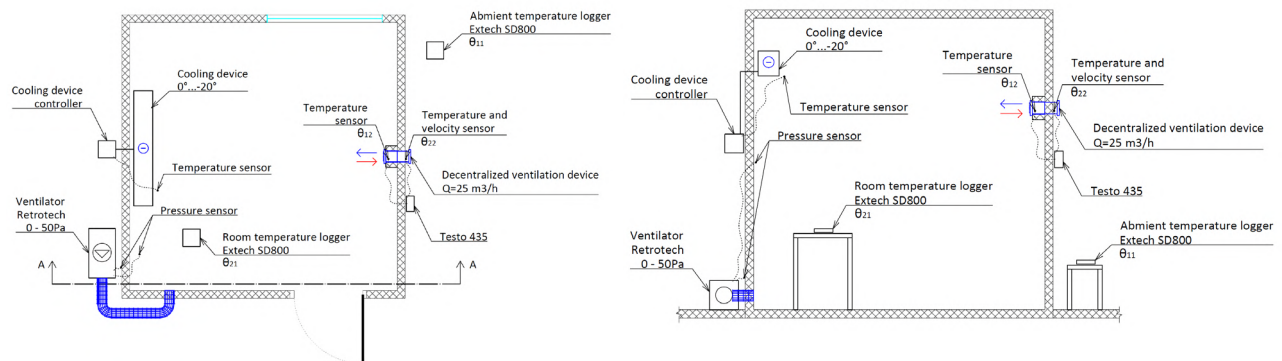


Figure 4. The plan of the experimental setup (on the left) and the section view A-A (on the right).

During the experiment, several sets of measurements were performed. For each set the temperature in the climatic chamber was regulated to be at $+5$, 0 or $-5\text{ }^{\circ}\text{C}$ while the air pressure difference between climatic chamber and external premise was changed to be 0 , 5 , 10 , 15 , 20 , 30 , 40 or 50 Pa , respectively, therefore representing a wide range of external simulated air velocities. Each of the measurements was run for at least 7 min , thus ensuring 3 full cycles of supply/exhaust. For a single measurement with set parameters of $+2\text{ }^{\circ}\text{C}$ in the climatic chamber and 0 Pa pressure difference, the experiment was run for 2 hours.

The heat recovery efficiency was calculated in accordance with the equation presented in the standard EN 13141-8:2014 [23]. It was calculated for each measuring time point (every second) and afterward, the average value for the supply working regime time (around 70 seconds) was determined according to the following equation:

$$\varphi = \frac{1}{t_{\text{cycle}}} \left[\int_t \left(\frac{\theta_{22} - \theta_{21}}{\theta_{11} - \theta_{21}} \right) dt \right] \cdot 100 [\%], \quad (1)$$

where t_{cycle} is time of an operating cycle (s);

θ_{22} is supply temperature ($^{\circ}\text{C}$);

θ_{21} is outside temperature ($^{\circ}\text{C}$);

θ_{11} is indoor temperature ($^{\circ}\text{C}$).

In addition, the electric running power of specific ventilation device at various pressure differences ranging from 0 Pa to 113 Pa was measured with Energy Check 3000, which has a measuring range from 0 to 3000 W and accuracy of $\pm 1\%$.

3. Results and Discussions

In Figure 5, the results of the middle part of a long-term experiment are presented. The graph represents the data obtained from the 33rd minute to 42nd minute, as during this period it can be considered that the system is stabilized, and the results represent the actual system working regime. The outside and inside temperatures were stable, around $+2\text{ }^{\circ}\text{C}$ and $+19.4\text{ }^{\circ}\text{C}$, respectively. At the same time, the supply temperature decreased from max $16.6\text{ }^{\circ}\text{C}$ to $11.7\text{ }^{\circ}\text{C}$ in each supply cycle. This represents the stage when the ventilation device is working in the supply regime, after which the ventilator changes the spinning direction and exhaust stage starts. In this stage, the temperature on the room side of the device increases and the heat recovery unit regenerates, as the warm room air gets sucked out. The graph also shows that the supply temperature during the supply working regime decreased linearly, at the same time the temperature on the cool side of the ventilation device decreased rapidly and almost instantly reached the simulated outside air temperature. On the other hand, during the exhaust phase, the temperature on the room side of the ventilation device increased logarithmically while the temperature after the device raised linearly.

During the experiment, it was found out that the actual length of the cycle was not exactly 70 seconds but a little bit shorter, around 68.5 seconds. Although this is not of high importance for end-users, it must be considered when calculating heat recovery energy efficiency, as for each second it is necessary to manually

state if the device is in supply or exhaust operating mode, or the results would be compromised. The calculated average temperature efficiency for supply was 72 %, which is lower than the one stated in the technical datasheet. On the other hand, approximately for the first 6 seconds of each supply cycle, the efficiency actually reached exactly 85 %, which is the value mentioned in the technical datasheet. Therefore, it can be concluded that, although it is technically correct to state such value, it does not represent the actual situation and can cause under-sizing of heating systems and inaccuracy in calculated building energy efficiency certificate.

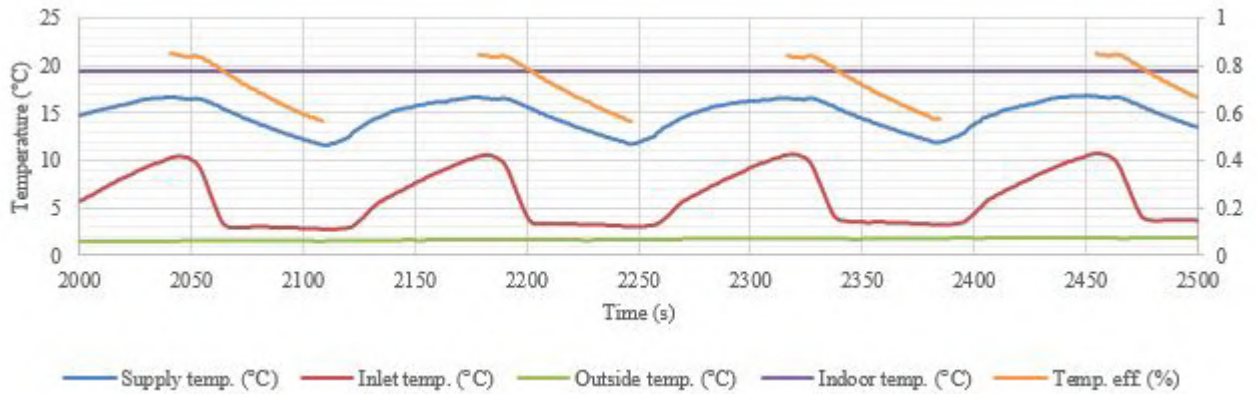


Figure 5. Variations in supply/exhaust temp. at +2 °C and $\Delta 0$ Pa.

Figure 6 to Figure 8 shows the results of short-term measurements at simulated outside air temperature of +0 °C and various pressure differences. As can be seen from the results, the pressure difference has a high impact on the supply temperature after the ventilation device. By increasing the pressure in the climatic chamber, which simulates the variable wind conditions of real case scenarios, the supply air temperature and, in retrospect, the heat recovery efficiency rapidly decreases. The graphs show that the maximal supply temperature after the ventilation device falls from +16 °C to +3 °C, depending on the air pressure difference, if the room temperature is +17.6 °C and outside air temp. +0 °C.

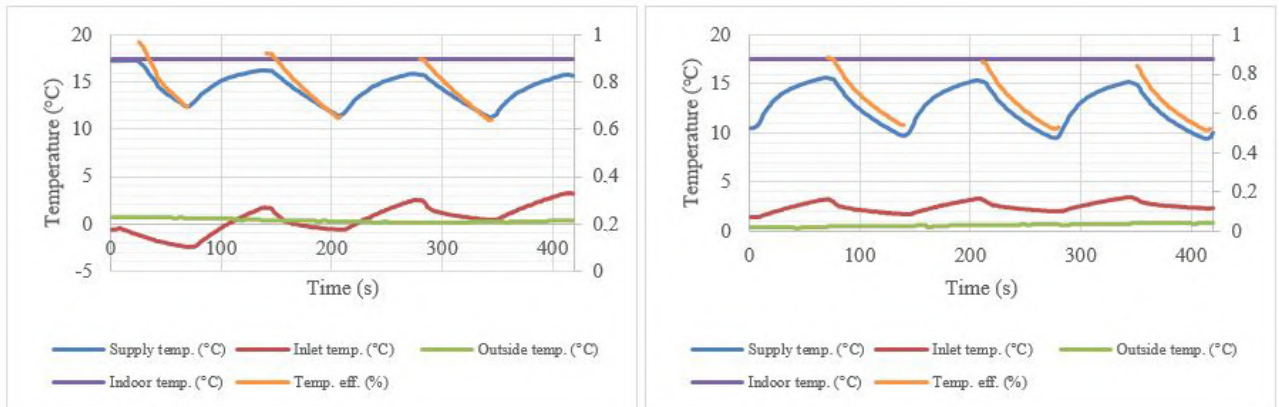


Figure 6. Short term measurements of supply/exhaust temp. variations at +0 °C outside air temp. and $\Delta 0$ Pa (left side) or $\Delta 5$ Pa (right side).

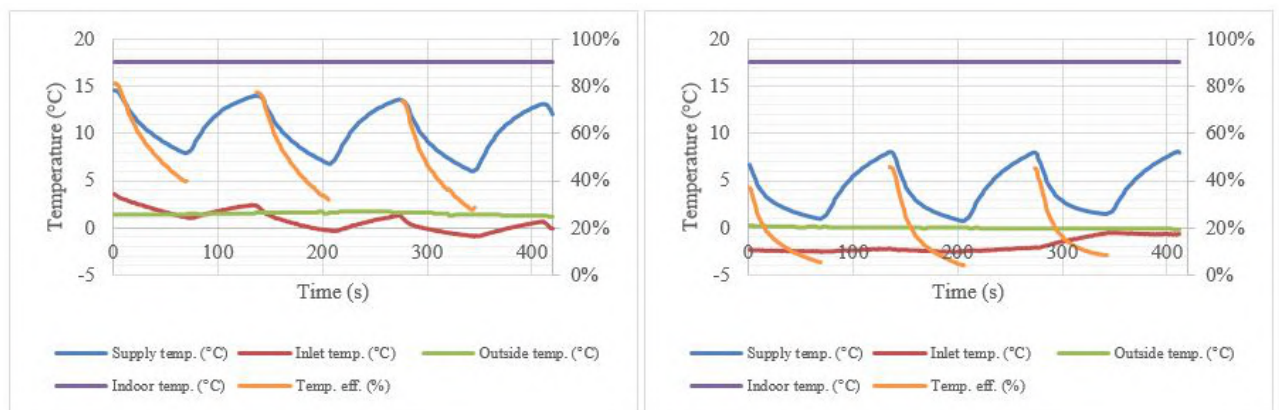


Figure 7. Short term measurements of supply/exhaust temp. variations at +0 °C outside air temp. and $\Delta 10$ Pa (left side) or $\Delta 20$ Pa (right side).

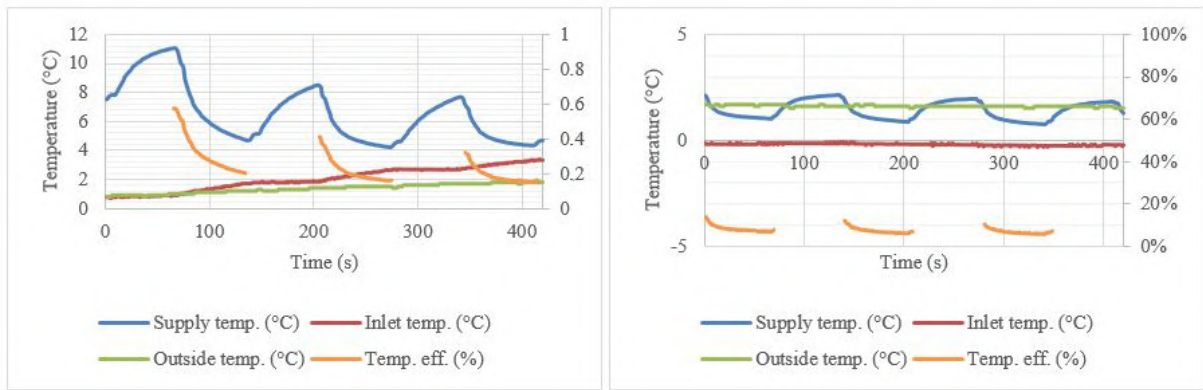
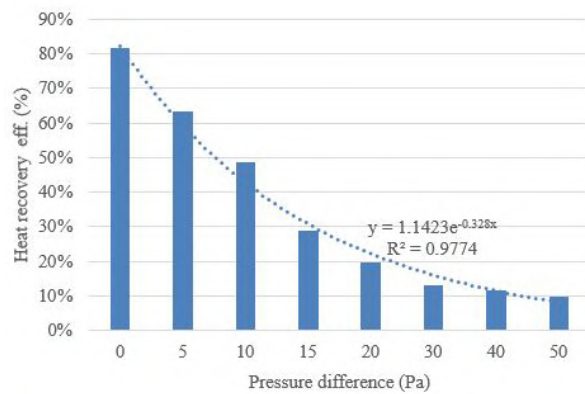


Figure 8. Short term measurements of supply/exhaust temp. variations at +0 °C outside air temp. and Δ30 Pa (left side) or Δ150 Pa (right side).

To obtain a more general overview of the results on how the pressure difference influences the heat recovery efficiency, they are combined in a single table/figure (see Table 1). As it shows, the average heat recovery efficiency decreases with the increase of pressure difference, independently of outside air temperature. The decrease follows an exponential trendline with high precision ($R^2 = 0.98$). At Δ50 Pa the heat recovery efficiency is only 10 %. Although this is according to the Russian building code SP 50.13330.2012, which states that the minimum efficiency of recuperator should be at least 10 %, this is a very low value and causes high energy consumption for air heating.

Table 1. Average heat recovery efficiency at various outside air temperatures and pressure difference combinations

Pressure difference; ΔPa	Outside temperature; °C			Average heat recovery eff. ; %
	+7	+2	-2	
0	86 %	78 %	81%	82 %
5	63 %	66 %	61%	63 %
10	45 %	50 %	51%	49 %
15	23 %	30 %	33%	29 %
20	26 %	16 %	17%	20 %
30	7 %	20 %	13%	13 %
40	14 %	9 %	N/A	12 %
50	12 %	8 %	N/A	10 %



The results on how the pressure difference influences the air velocity on the supply side of the ventilation device are shown in Figure 9. The results show that with increased pressure difference the air velocity after ventilation device exponentially increases. This means that an increased amount of air is passing through the ventilation device as the size of the device does not change. This corresponds to the data representing the fall of heat energy recovery efficiency as the device is not capable to heat up all the air passing through. The results show that for the specific ventilation device, an average air velocity almost doubles if the pressure difference rises from 0 to 10 Pa. However, this does not necessarily mean that the double amount of air volume is passing through. To make such a conclusion, more specific measurements should be performed, but it can still serve as a general indicator of change in magnitude.

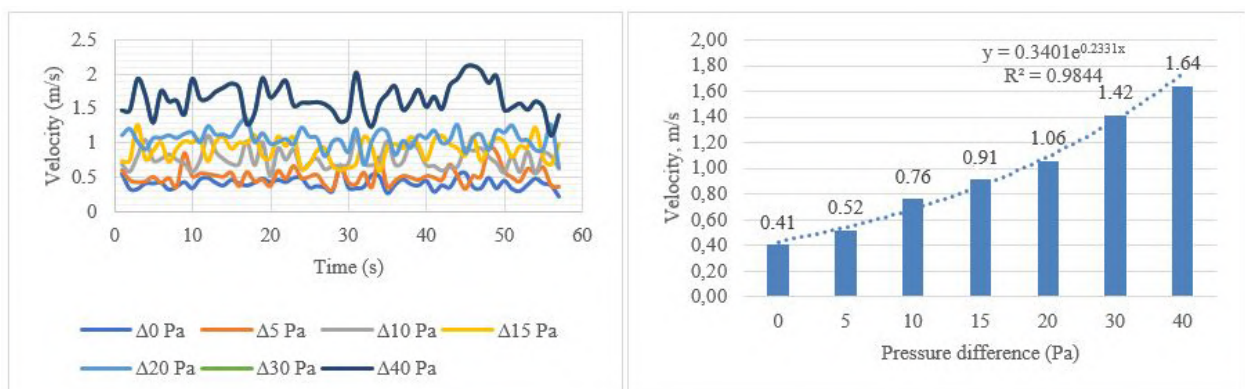


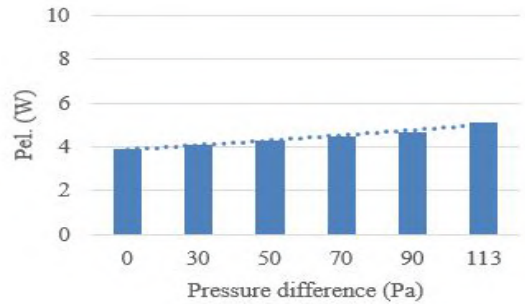
Figure 9. Velocity profiles (left side) and an average velocity depending on the pressure difference (right side).

The obtained results back up data from studies carried out previously from different studies. For example, the study [29] stated that at 10 Pa pressure difference the air volumes can vary from 50 % up to 100 % in comparison to no pressure difference. Similar data were obtained in our study, as can be seen from Figure 9, the average velocity at $\Delta 10$ Pa was 0.76 m/s compared to 0.41 m/s at $\Delta 0$ Pa. This would correspond to an increase in the volume flow of 85 %. Also, the obtained data are very similar to recent research [30]. The research shows that the heat recovery efficiency noticeably decreases with the rise of pressure difference and is only 25 % at $\Delta 20$ Pa, while at $\Delta 5$ Pa it can reach 70 %. These data are in close correspondence to the ones obtained in our study, see (see Table 1). Also, according to existing studies [31] such devices produce high noise levels and therefore are often operated at lower speed levels or switched off by occupants. This causes an increase in the difference between supply and exhaust airflow volumes and to the point that at $\Delta 8$ Pa the supply airflow is 2 times higher than the exhaust airflow. Therefore, the heat recovery efficiency is reduced.

Table 2 shows how the electric power of a specific ventilation device changed depending on the pressure difference. As the results show, the initial power is lower than specified by the manufacturer – 3.9 W compared to 6 W. As it was expected, the electric power increased when additional pressure was introduced, but it reached only 5.1 W even at 113 Pa pressure difference between the climatic chamber and the open room. This means that the actual electric consumption for running such a device will be lower if calculated theoretically according to the technical datasheet.

Table 2. Electric power of specific ventilation device at various pressure differences.

Pressure difference; Δ Pa	0	30	50	70	90	113
Electric power; W	3.9	4.1	4.3	4.5	4.7	5.1



4. Conclusions

In this study, the heat recovery efficiency of a decentralized ventilation device was measured and analysed for various pressure differences between the inlet and supply-side at a controlled environment of the climatic chamber. The results suggest that for a specific decentralized supply/exhaust ventilation device with an integrated heat recovery unit the average heat recovery efficiency for the supply cycle at 0 Pa pressure difference was 73 %. For the first few seconds of the supply cycle, the efficiency reached 85 %, which was the number specified in the datasheet, but afterward, it decreased and at the end of the cycle was only 57 %.

Data analysis suggests that the heat recovery efficiency was strictly related to the air pressure difference between the inlet and supply side of the ventilation device. The average temperature efficiency at $\Delta 5$ Pa was 63 % while at $\Delta 10$ Pa it fell to 49 % and at $\Delta 15$ Pa was only 29 %. The efficiency kept falling with a further increase in pressure and followed the equation of $y = 1.1415e - 0.328x$. This means that for actual buildings in real case scenarios, where the pressure difference is constantly higher than 0 Pa, the energy consumption for building heating will be higher than calculated if the specified heat recovery efficiency will be taken into account. The actual pressure difference will vary depending on specific building size, shape and location but, according to other studies, for the most part of the year is in the range of 10–20 Pa, thus meaning that the heat recovery efficiency will be between 20 and 50 %. This can influence the calculated building energy efficiency class, as well as lead to undersized heating system elements and, if the room temperature will drop due to the above, the occupants will try to seal off the ventilation devices, therefore, compromising the indoor air quality.

The measurements suggest that the air velocity also was affected by the increased pressure difference although the device was equipped with a special protection plate. The results suggest that the supply air velocity on the inside of the device increased more than two times (from 0.41 to 1.06 m/s) if the pressure difference increased from 0 Pa to 20 Pa. This can also lead to a decrease in thermal comfort for occupants if the supply air is too cold, causing a sensation of draught and therefore leading to blocking or shutting off the ventilation devices.

The study suggests that the electrical power of the device was very low (3.9 to 5.1 W) even if the pressure difference raised from 0 to 113 Pa. This was lower than specified in the technical datasheet.

For future experiments, it would be necessary to study the heat recovery efficiency for similar types of devices but from different manufacturers and with various sizes. It could be expected that larger size units

could have better results at higher pressure differences, as they have a larger heat recovery unit. Also, ventilation devices with an enthalpy type heat recovery unit should be tested to see if they can achieve higher efficiency and how they would perform in real case scenarios. Additionally, the thermal comfort rating ensured by such ventilation types should be tested to see how the relatively cold air during the windy outside conditions relates to it. Another thing to test could be how the changes in cycle working lengths would affect both the heat recovery efficiency as well as IAQ. At the moment most of the manufacturers have chosen 70 seconds to be the length of each cycle but maybe by making it a bit longer, the efficiency could be increased as the results showed that the temperature on the outside of the device did not reach room temperature during the exhaust phase. This could indicate that the heat recovery unit has still not been fully regenerated.

5. Acknowledgements

This work has been supported by the European Regional Development Fund within the Activity 1.1.1.2 "Post-doctoral Research Aid" of the Specific Aid Objective 1.1.1 "To increase the research and innovative capacity of scientific institutions of Latvia and the ability to attract external financing, investing in human resources and infrastructure" of the Operational Programme "Growth and Employment" (No. 1.1.1.2/VIAA/1/16/033).

References

1. Kim, M.K., Baldini, L. Energy analysis of a decentralized ventilation system compared with centralized ventilation systems in European climates: Based on review of analyses. *Energy and Buildings*. 2016. (111). Pp. 424–433. DOI: 10.1016/j.enbuild.2015.11.044.
2. Naumov, A.L., Tabunshchikov, I.A., Kapko, D.V., Brodach, M.M. Research of the microclimate formed by the local DCV. *Energy and Buildings*. 2015. 90. DOI: 10.1016/j.enbuild.2015.01.006
3. Murgul, V., Vuksanovic, D., Vatin, N., Pukhkal, V. Decentralized ventilation systems with exhaust air heat recovery in the case of residential buildings. *Applied Mechanics and Materials*. 2014.
4. Murgul, V., Vuksanovic, D., Vatin, N., Pukhkal, V. The use of decentralized ventilation systems with heat recovery in the historical buildings of St. Petersburg. *Applied Mechanics and Materials*. 2014.
5. Laverge, J., Janssens, A. Heat recovery ventilation operation traded off against natural and simple exhaust ventilation in Europe by primary energy factor, carbon dioxide emission, household consumer price and exergy. *Energy and Buildings*. 2012. 50. Pp. 315–323. DOI: 10.1016/j.enbuild.2012.04.005.
6. Korniyenko, S. Complex analysis of energy efficiency in operated high-rise residential building: Case study. *E3S Web of Conferences*. 2018. 33. Pp. 2005. DOI: 10.1051/e3sconf/20183302005.
7. Doodoo, A., Gustavsson, L., Sathre, R. Primary energy implications of ventilation heat recovery in residential buildings [Online]. *Energy and Buildings*. 2011. No. 7(43). Pp. 1566–1572. URL: <https://doi.org/10.1016/j.enbuild.2011.02.019>.
8. Silva, M.F., Maas, S., Souza, H.A. de, Gomes, A.P. Post-occupancy evaluation of residential buildings in Luxembourg with centralized and decentralized ventilation systems, focusing on indoor air quality (IAQ). Assessment by questionnaires and physical measurements. 2017. 148.
9. Vinha, J., Manelius, E., Korpi, M., Salminen, K., Kurnitski, J., Kiviste, M., Laukkanen, A. Airtightness of residential buildings in Finland. *Building and Environment*. 2015. 93. Pp. 128–140. URL: <https://doi.org/10.1016/j.buildenv.2015.06.011>.
10. Alonso, M.J., Liu, P., Mathisen, H.M., Ge, G., Simonson, C. Review of heat/energy recovery exchangers for use in ZEBs in cold climate countries [Online]. *Building and Environment*. 2015. 84. Pp. 228–237. URL: <https://doi.org/10.1016/j.buildenv.2014.11.014>.
11. Smith, K.M., Svendsen, S. The effect of a rotary heat exchanger in room-based ventilation on indoor humidity in existing apartments in temperate climates. 2016. 116.
12. Kim, M.K., Baldini, L., Leibundgut, H. Advanced Decentralized Ventilation Systems for Cooling and Dehumidification with Compact Heat Exchanger. 11th REHVA World Congress CLIMA 2013. Prague, Czech Republic, 2013.
13. Petrichenko, M., Nemova, D.V., Kotov, E.V., Tarasova, D., Sergeev, V.V. Ventilated facade integrated with the HVAC system for cold climate. *Magazine of Civil Engineering*. 2018. 77. Pp. 47–58. DOI: 10.18720/MCE.77.5.
14. Toyinbo, O., Shaughnessy, R., Turunen, M., Putus, T., Metsämuuronen, J., Kurnitski, J., Haverinen-Shaughnessy U. Building characteristics, indoor environmental quality, and mathematics achievement in Finnish elementary schools. *Building and Environment*. 2016. 104. Pp. 114–121. DOI: 10.1016/j.buildenv.2016.04.030.
15. Dorer, V., Breer, D. Residential mechanical ventilation systems: performance criteria and evaluations [Online]. *Energy and Buildings*. 1998. No. 3(27). Pp. 247–255. URL: [https://doi.org/10.1016/S0378-7788\(97\)00049-2](https://doi.org/10.1016/S0378-7788(97)00049-2).
16. Naumov, A.L., Kapko, D.V., Brodach, M.M. Ventilation systems with local recirculation diffusers. 2014. 85.
17. Gorshkov, A., Vatin, N., Rymkevich, P.P., Kydrevich, O.O. Payback period of investments in energy saving. *Magazine of Civil Engineering*. 2018. 78. Pp. 65–75. DOI: 10.18720/MCE.78.5.
18. Harmati, N., Jakšić, Ž., Vatin, N. Energy consumption modelling via heat balance method for energy performance of a building. *Procedia Engineering*. 2015. No. 1(117). Pp. 791–799.
19. Manz, H., Huber, H., Schälín, A., Weber, A., Ferrazzini, M., Studer, M. Performance of single room ventilation units with recuperative or regenerative heat recovery. 2000. No. 1(31).
20. Smith, K.M., Svendsen, S. Development of a plastic rotary heat exchanger for room-based ventilation in existing apartments. 2015. 107.
21. Roulet, C.A., Heidt, F.D., Foradini, F., Pibiri, M.C. Real heat recovery with air handling units. 2001. No. 5(33).
22. Zemitis, J., Borodinecs, A., Geikins, A., Kalamees, T., Kuusk, K. Ventilation System Design in Three European Geo Cluster. *Energy Procedia*. 2016. 96. Pp. 285–293. DOI: 10.1016/j.egypro.2016.09.151.

23. EN 13141-8:2014. Ventilation for buildings. Performance testing of components/products for residential ventilation. Performance testing of un-ducted mechanical supply and exhaust ventilation units (including heat recovery) for mechanical ventilation systems intended for a2014.
24. Bilous, I.Y., Deshko, V., Sukhodub, I. Building inside air temperature parametric study. 2017. 68.
25. Mikola, A., Kalamees, T., Kõiv, T.A. Performance of ventilation in Estonian apartment buildings. 2017. 132.
26. Leivo, V., Kiviste, M., Aaltonen, A., Turunen, M., Haverinen-Shaughnessy, U. Air pressure difference between indoor and outdoor or staircase in multi-family buildings with exhaust ventilation system in Finland. 2015. 78.
27. Choi, Y. hee, Song, D., Seo, D., Kim, J. Analysis of the variable heat exchange efficiency of heat recovery ventilators and the associated heating energy demand. Energy and Buildings. 2018. 172. Pp. 152–158. DOI: 10.1016/j.enbuild.2018.04.066.
28. Manz, H., Huber, H., Helfenfinger, D. Impact of air leakages and short circuits in ventilation units with heat recovery on ventilation efficiency and energy requirements for heating. 2001. No. 2(33).
29. Merzkirch, A., Maas, S., Scholzen, F., Waldmann, D. Field tests of centralized and decentralized ventilation units in residential buildings – Specific fan power, heat recovery efficiency, shortcuts and volume flow unbalances. 2016. 116.
30. Mikola, A., Simson, R., Kurnitski, J. The Impact of Air Pressure Conditions on the Performance of Single Room Ventilation Units in Multi-Story Buildings. Energies. 2019. 12. Pp. 2633. DOI: 10.3390/en12132633.
31. Mikola, A., Kõiv, T., Kalamees, T. Quality of ventilation systems in residential buildings: status and perspectives in Estonia. International Workshop Securing the quality of ventilation systems in residential buildings: status and perspectives. Brussels. 2013. Pp. 1–10.

Contacts

Jurgis Zemitis, jurgis.zemitis@rtu.lv

Raimonds Bogdanovics, Raimonds.Bogdanovics@rtu.lv

© Zemitis, J., Bogdanovics, R., 2020



DOI: 10.18720/MCE.94.11

Finite element modeling of cold-formed steel deck in bending

V.V. Degtyarev*

New Millennium Building Systems, LLC, Columbia, SC, USA

* E-mail: vitaliy.degtyarev@newmill.com

Keywords: cold-formed steel deck, flexural behavior, buckling, bending strength, finite element method, numerical methods, ANSYS

Abstract. Finite element simulations of structural members are a good alternative to physical testing for studying strength and structural response of the members when finite element models have been properly calibrated and validated. Published information on finite element modeling of cold-formed steel deck in bending is scarce. This paper presents the development of finite element models of corrugated steel deck in bending using a general-purpose software, ANSYS. Effects of the following parameters on elastic buckling and ultimate moments of models, as well as on their load-deflection curves, were studied: shell element types, mesh density, corner radius, number of deck corrugations, presence of transverse ties, initial geometric imperfection distribution and magnitude, deck boundary conditions, loading type, and stress-strain diagrams. Optimal parameters of the models were determined. Moment capacities, flexural stiffness, and load-deflection curves predicted by the models with the optimal parameters correlated well with test results available in literature, especially when the deck material behavior was described by nonlinear stress-strain diagrams. The developed FE models can be used for studying flexural strength and behavior of solid steel deck with various geometry under various loading types, which can be useful in development of new efficient profiles and in improving the current deck design methods. The models can also be used as a basis for the development of FE models of steel deck with openings and acoustical perforations, as well as built-up deck profiles, design methods for which are currently underdeveloped.

1. Introduction

Corrugated cold-formed steel (CFS) deck, which is available in many different shapes and depths, has been widely used in construction throughout the world. Figure 1 shows two representatives of the deck manufactured and used in Europe. Structural design of corrugated steel deck in different countries is governed by national standards [1–4]. Some countries also have manuals [5, 6], which offer additional guidance on the design and construction with steel decks. Despite the wide use of corrugated steel decks, some items, such as design of perforated steel deck [7, 8], deck with openings [5, 9], deck under concentrated loads [1, 6, 10, 11], and built-up deck sections, are not covered at all or covered with significant limitations in the design standards and manuals. Questions about the accuracy of flexural strength prediction of some deck profiles by the direct strength method adopted in [1] have been recently raised [12, 13]. There is an obvious need for additional research of strength and structural behavior of certain types of corrugated steel deck and steel deck under certain types of loads.

Physical testing has been traditionally considered as the most reliable way of obtaining information about the performance of structural members and systems. Physical testing, however, requires significant resources, which makes its use problematic for extensive studies, which involve wide ranges of design parameters. Finite element (FE) method, on the other hand, is an efficient alternative to physical testing when FE models have been properly validated and calibrated against available test data [14]. It allows for performing extensive parametric studies using limited resources. FE simulations can also give detailed information about elastic buckling loads of the deck and stress/strain distributions in deck profiles, obtaining of which from physical testing can be difficult.

Many researchers have successfully used FE method for simulations of CFS structural members under various loading types resulting in different failure modes [15–29]. FE models of CFS structural members were created using shell elements in different commercially available FE programs. It has been shown that the FE

Degtyarev, V.V., Finite element modeling of cold-formed steel deck in bending. Magazine of Civil Engineering. 2020. 94(2). Pp. 129–144. DOI: 10.18720/MCE.94.11



This work is licensed under a CC BY-NC 4.0

method can capture specifics of structural behavior of CFS structural members. It should be noted, however, that the majority of FE models of CFS structural members have been developed for C- and Z-shaped sections. There is a limited number of published papers on FE modeling of CFS deck in bending [10, 11, 30]. The available papers dealt with some specific applications, such as steel deck under concentrated loads and perforated deck, and do not discuss general FE modeling of CFS steel deck in bending.

The objectives of this paper are to develop FE models of corrugated CFS deck in bending, validate them using available test data, and study the effects of different parameters of the models on their elastic buckling moments, moment capacity, and structural response. The FE models were developed in a commercial general-purpose software, ANSYS [31] and validated against physical test data published in [32]. Effects of the following FE model parameters on their elastic buckling, ultimate strength, and structural response were studied: shell element type, mesh density, corner radius, number of deck corrugations, presence of transverse ties, initial geometric imperfection (IGI) distribution and magnitude, deck boundary conditions, loading type, and the material model of steel. Optimal parameters of the FE models for simulating steel deck strength and behavior in bending were determined from the study. The developed FE models can be used for studying flexural strength and behavior of solid steel deck with various geometry and loading types. The models can also be used as a basis for development of FE models of steel deck with acoustical perforations and openings, as well as built-up deck profiles.

2. Methods

FE models of CFS deck profiles shown in Figure 1 were developed in a commercial general-purpose software, ANSYS [31], using structural shell elements. The profiles were physically tested at the Karlsruhe Institute of Technology (KIT) for the research project titled "Guidelines and Recommendations for Integrating Specific Profiled Steel Sheets in the Eurocodes (GRISPE)" [32]. In the project, deck types JI_73-195-780 and JI_56-225-900 shown in Figure 1 with the nominal steel thickness of 0.75 and 1.00 mm were tested in bending in accordance with EN 1993-1-3:2006 [4]. The deck was produced by Joris Ide from galvanized steel grade S320GD according to EN 10346:2009 [33] with the nominal yield strength of 320 MPa. Results of 14 physical tests of solid deck in bending published in [32] were used for development and validation of FE deck models described in this paper.

Single deck sheets shown in Figure 1 installed in single 3300-mm long spans were tested in six-point bending simulating a uniformly distributed load. The deck was supported at top flanges with timber blocks to prevent web crippling. Timber blocks were also used to transfer loads to the deck bottom flanges. Transverse ties were provided at the load locations and near supports to prevent deck sheets from spreading. The failure loads and load-deflection curves were obtained from the tests for every tested specimen and presented in [32]. The mechanical properties of the steel used for fabrication of the tested deck specimens were determined from tensile tests of steel coupons. The base steel thickness, excluding zinc coating, was also determined.

In the FE models, the actual base steel thickness and mechanical properties of the deck reported in [32] were used. The study consisted of seven stages. In each stage, effects of one or several of the following parameters on the elastic buckling moments, moment capacity, and structural response of steel deck models were evaluated: shell element type, mesh density, corner radius, number of deck corrugations, presence of transverse ties, IGI distribution and magnitude, deck boundary conditions, loading type and stress-strain diagrams of steel. The following sections describe FE models used in each stage and discuss obtained results.

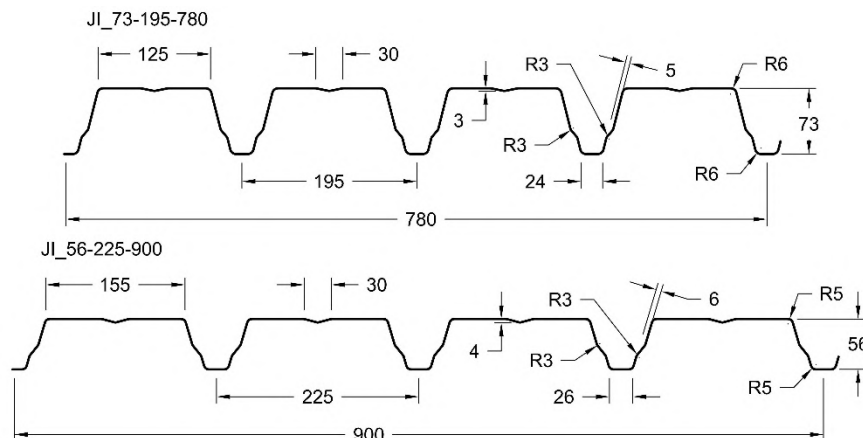


Figure 1. Dimensions [mm] of the deck profiles used for the development of FE models.

3. Results and Discussion

3.1. Effects of element type, mesh density, and initial geometric imperfection magnitude

In this stage, the effects of mesh density and element type on elastic buckling and ultimate moments were studied on the 73-mm deep deck with the nominal steel thickness of 0.75 mm and on the 56-mm deep deck with the nominal steel thickness of 1.00 mm. The selected deck profiles represented the lower and upper bounds of the deck heights and thicknesses considered in the study. Effects of IGI magnitude on the deck moment capacity were also evaluated.

Four-node and eight-node structural shell elements, SHELL181 and SHELL281, respectively, with five integration points were used for modeling the deck. Both element types have six degrees of freedom at each node. They are well suited for large-strain nonlinear applications and are capable of accounting for shell thickness change in nonlinear analyses. SHELL181 is a linear shell element. SHELL281 is a quadratic shell element. Quadratic shell elements generally allow for the use of coarser meshes, give greater flexibility in FE model meshing, and result in improved convergence of the solution when compared with linear shell elements [14]. The use of quadratic elements, however, results in considerably longer computation times.

Multilinear isotropic hardening models (MISO) with von Mises plasticity were used to define the material behavior of steel deck. The deck stress-strain curves were described by the nonlinear models proposed in [34] (Figure 2). The key input parameters of the models were determined using the yield stress and tensile strength of the steel obtained from coupon tests in [32]. An elastic modulus of 2.03×10^5 MPa and a Poisson's ratio of 0.3 were used. The engineering stresses and strains were converted into the true stresses and strains using the following well-known relationships from Appendix C.6 of EN 1993-1-5:2006 [35]: $f_{true} = f_{eng}(1 + \epsilon_{eng})$, where f_{true} and f_{eng} are true and engineering stresses, respectively, and $\epsilon_{true} = \ln(\epsilon_{eng} + 1)$, where ϵ_{true} and ϵ_{eng} are true and engineering strains, respectively.

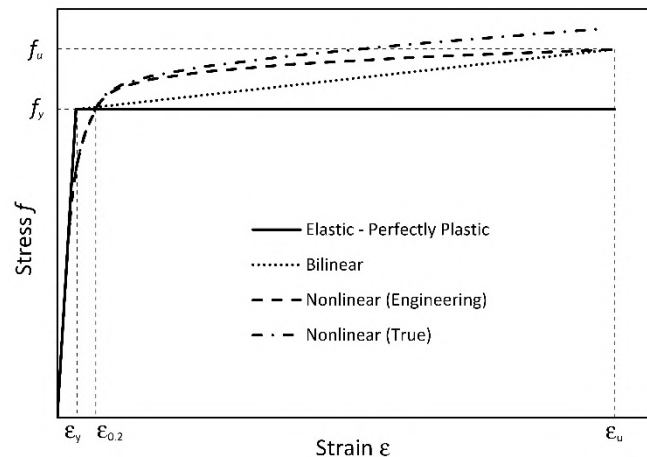


Figure 2. Steel stress-strain diagrams.

The deck models were meshed with quadrilateral elements. To determine an optimal mesh density, eight different mesh sizes shown in Table 1 and Figure 3 were considered. Corner radii of $6+t/2$ and $5+t/2$ mm (where t is the measured base steel thickness) were included for the models of the 73- and 56-mm deep decks, respectively, at the intersections of the deck top and bottom flanges with the deck webs. The web and top flange longitudinal stiffeners were modeled with sharp corners due to the small actual inside corner radii and large angles between the elements.

Table 1. Parameters of FE meshes considered in convergence study.

Mesh density designation	Maximum element size (mm) in the direction		Total number of elements	
	Perpendicular to deck length	Parallel to deck length	73-mm deck	56-mm deck
D1	15	40	6992	6624
D2	15	20	13528	14240
D3	10	40	9200	8096
D4	10	20	17800	17088
D5	10	10	35400	33984
D6	5	20	27056	27056
D7	5	10	53808	53808
D8	5	5	106704	106704

Figure 4 shows boundary conditions of deck models supported at top flanges and loaded through bottom flanges, which are referred to as TFS-BFL (top-flange-supported-bottom-flange-loaded) models hereafter. The symmetry in boundary and loading conditions allowed to model one-half of the deck span with the ANSYS symmetry degree-of-freedom constraints applied to the FE model nodes at the deck mid-span. At the deck support, vertical translations of nodes at the deck top flanges were restrained. To prevent rigid body motion, lateral displacement of one node at the edge of the deck bottom flange was restrained. The loads were modeled by forces applied to the deck bottom flanges. The forces applied at the deck longitudinal edges were two times smaller than the forces applied to the internal bottom flanges due to the smaller tributary widths of the edge bottom flanges. The nodes of each bottom flange at the load locations were coupled independently from the adjacent bottom flanges. The transverse ties used in the tests were modeled by coupling lateral displacements of the nodes at the deck panel edges at the load locations and near the deck supports.

Each model was analyzed in two steps: 1) elastic buckling analysis was performed to obtain elastic buckling modes and moments; 2) non-linear static analysis was performed with the IGI distribution based on the first elastic buckling mode obtained from the elastic buckling analysis. The first elastic buckling mode of both studied deck profiles was distortional buckling of the deck top flange characterized by vertical deformations of the top flange longitudinal stiffener (Figure 5a). The deck models also demonstrated local buckling of the top flange between the web and the longitudinal stiffener as one of the higher buckling modes (Figure 5b). Three different IGI magnitudes of $0.15t$, $0.64t$, and $b_{tf}/150$, where b_{tf} is the deck top flange width, recommended in [36, 37, 23] were used in the models to study the effect of the IGI magnitude on the moment capacity. The absolute IGI magnitude values based on the measured deck dimensions were 0.10, 0.45, and 0.83 mm for the 73-mm deep deck with the nominal thickness of 0.75 mm and 0.14, 0.59, and 1.03 mm for the 56-mm deep deck with the nominal thickness of 1.00 mm. Large-deflection effects were included into the FE models to account for the geometric nonlinearity.

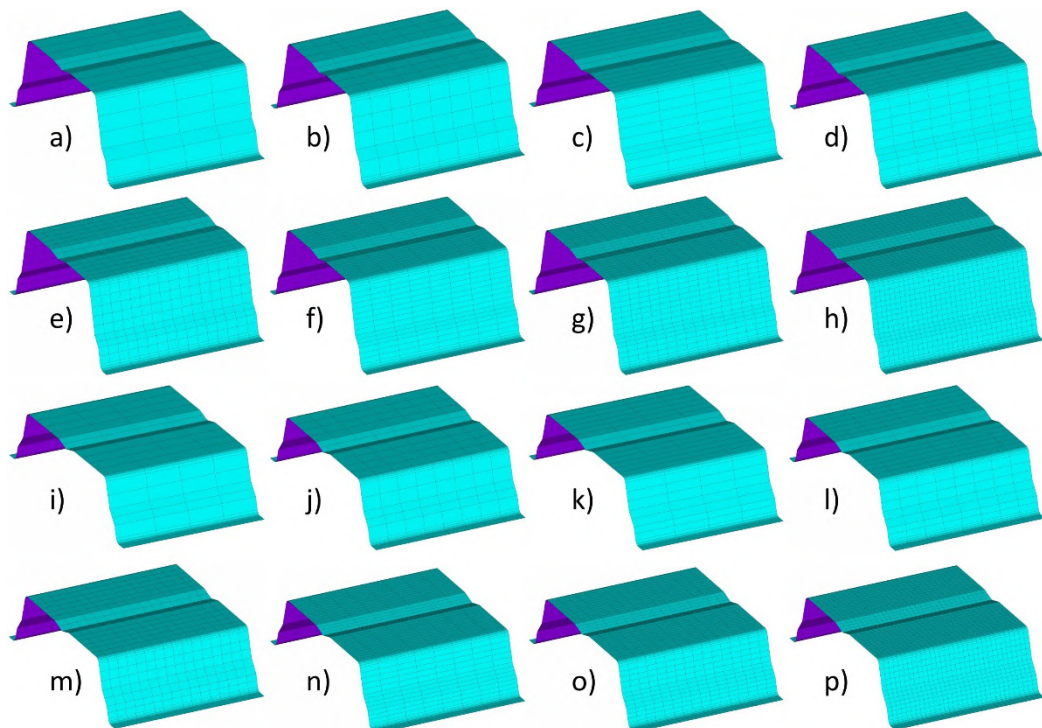


Figure 3. Mesh densities used in convergence study (one 160 mm long deck flute is shown for clarity): a) to h) 73-mm deep deck with mesh densities D1 to D8, respectively; i) to p) 56-mm deep deck with mesh densities D1 to D8, respectively.

Figure 6 shows the effects of the mesh density on the elastic buckling moments of the studied profiles. The distortional elastic buckling moments, M_{crd} , were practically independent of the mesh density for all studied models. On the other hand, the local elastic buckling moments, M_{crl} , were sensitive to the element sizes for the coarser meshes. For the coarser meshes, the numbers of top flange elements between the deck web and the stiffener were 3 and 4 for the 73- and 56-mm deep profiles, respectively (see Figure 3). These limited numbers of elements were insufficient for an accurate capturing of the local elastic buckling moments, especially for the linear 4-node elements. The local elastic buckling moments of the 73-mm deck models with the 4- and 8-node elements converged for the mesh densities D7 and D5, respectively. The local elastic buckling moments of the 56-mm deck models with the 4- and 8-node elements converged for the mesh densities D5 and D4, respectively. For these meshes, the number of top flange elements between the deck web and the stiffener were 9 and 5 for the 73-mm deck models with the 4- and 8-node elements, respectively, and 6 for the 56-mm deck models with both element types.

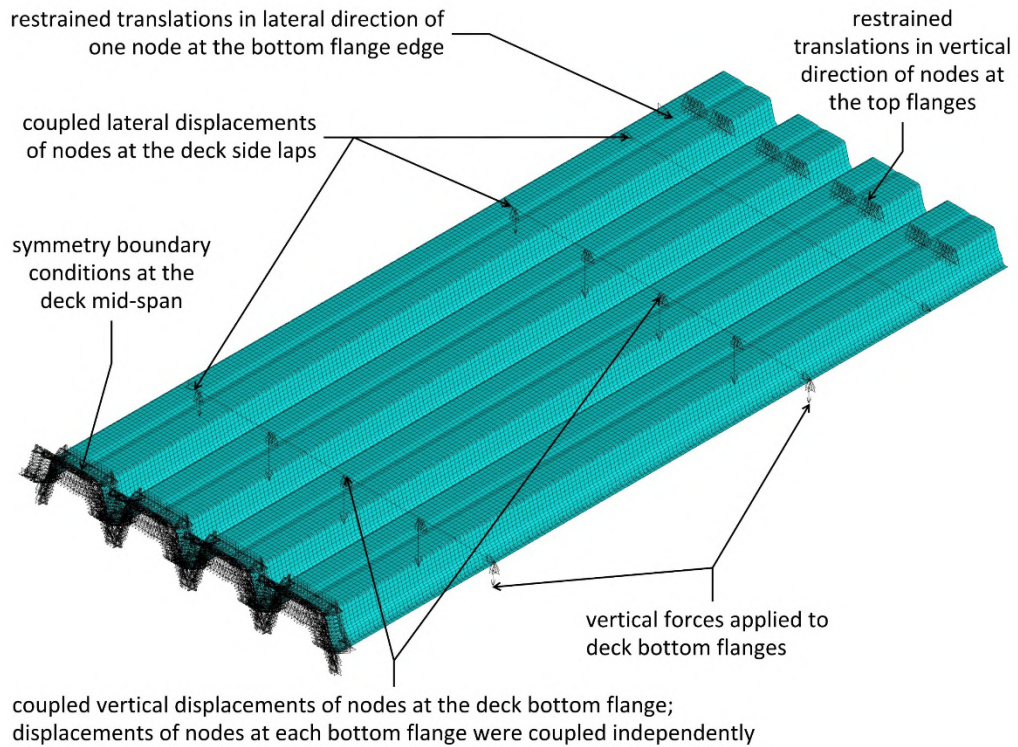


Figure 4. Boundary conditions of deck models supported at top flanges and loaded through bottom flanges (TFS-BFL models).

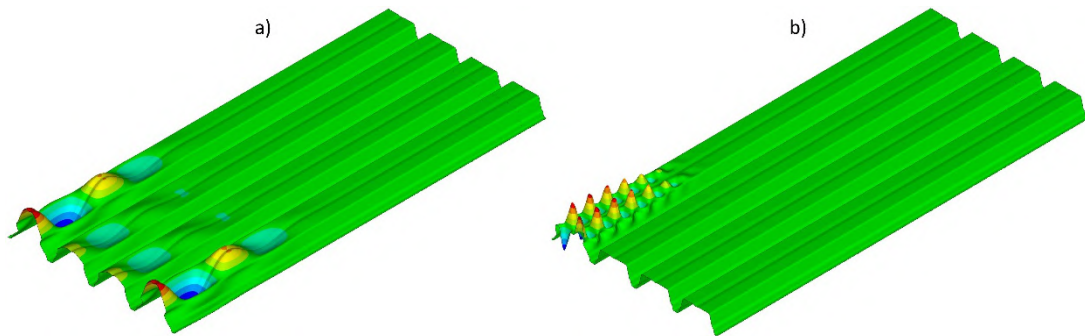


Figure 5. Buckling modes of studied deck profiles: a) distortional elastic buckling of deck top flange; b) local elastic buckling of deck top flange.

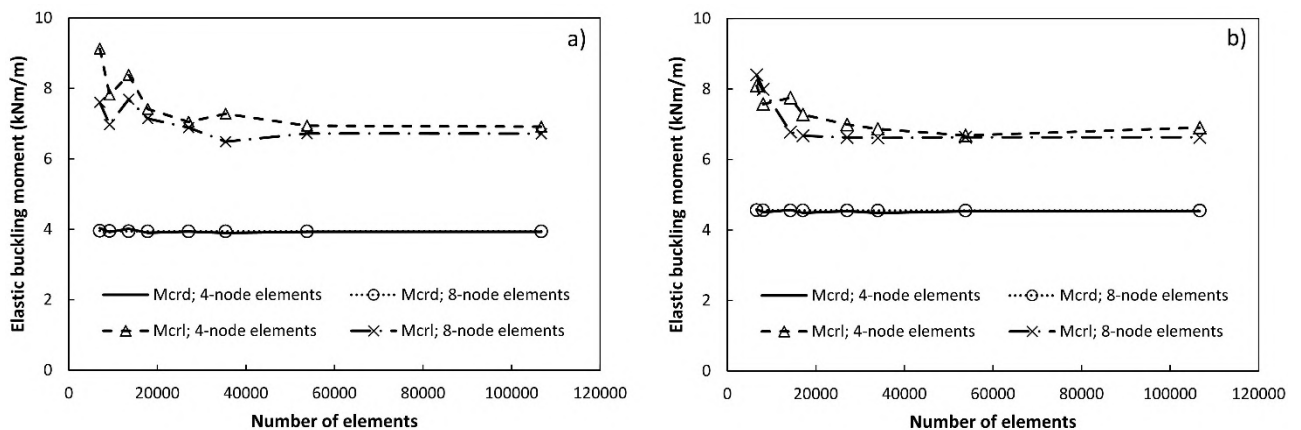


Figure 6. Effects of FE discretization on elastic buckling moments of a) 73- and b) 56-mm deep deck.

Figure 7 shows effects of the mesh density and the IGI magnitudes on the moment capacities of the studied profiles and average CPU time per iteration for models with different mesh densities and shell element types. The moment capacities of the 73- and 56-mm deep decks with both element types converged for the mesh densities D6 and D2, respectively. The considered IGI magnitudes had very small effects on the moment capacities. CPU time per iteration increased nearly linearly with an increase in the number of elements. The

computation time was 2–4 times (3 times on average) longer for the 8-node elements when compared with the 4-node elements.

Based on the convergence study presented herein, mesh densities D7 and D5 were selected for further studies for the deck models with the 4- and 8-node elements, respectively. The IGI magnitude of $b_{tf}/150$ was selected for the further studies.

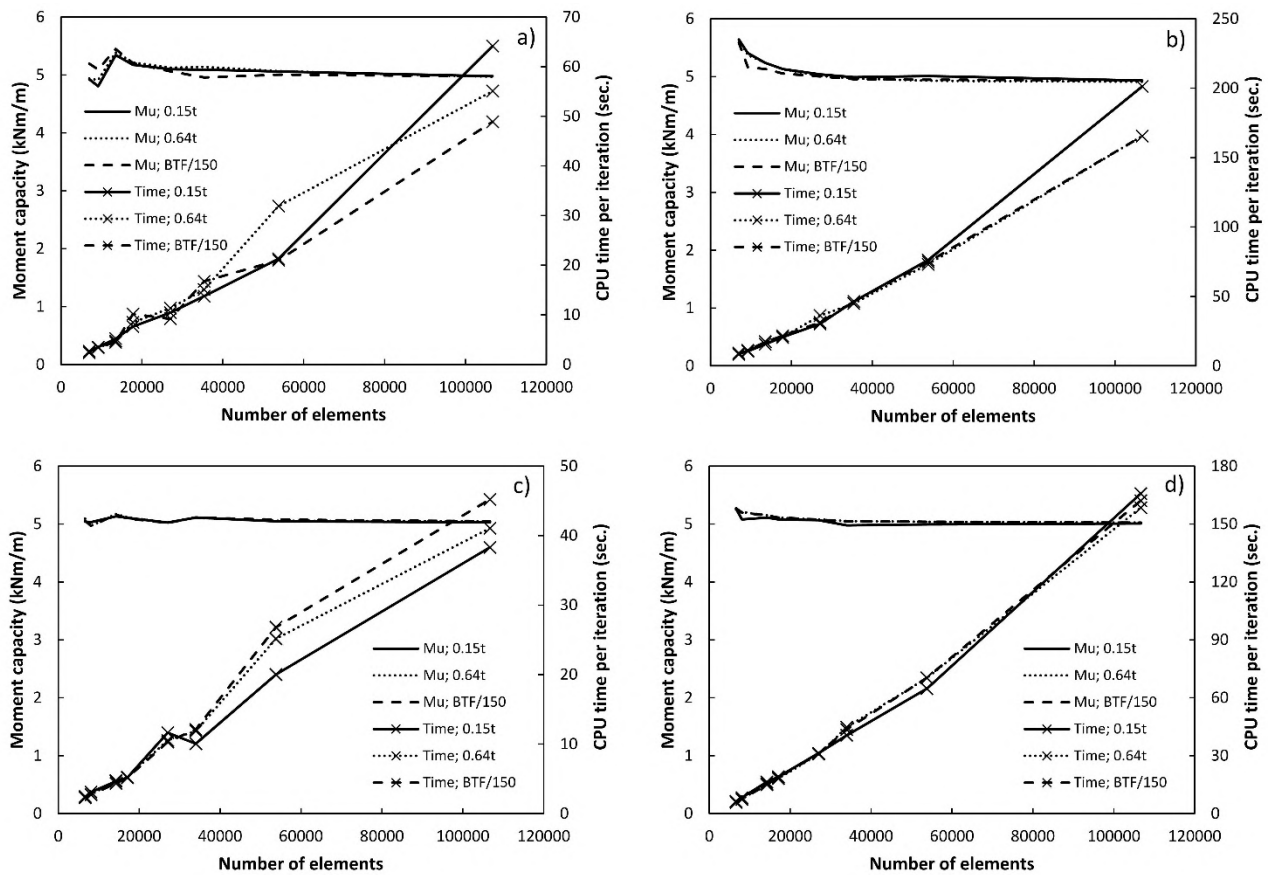


Figure 7. Effects of FE discretization on moment capacity and computation time of a) and b) 73-mm deep deck models with 4- and 8-node elements, respectively; c) and d) 56-mm deep deck models with 4- and 8-node elements, respectively.

3.2. Effects of corner radius

The effects of corner radius on the elastic buckling and ultimate moments of steel deck were studied on the profiles with the same geometry as those described in Section 3.1. Deck models with sharp corners, as well as models with the corner radii of $6+t/2$ and $12+t/2$ mm for the 73-mm deep deck and $5+t/2$ and $10+t/2$ mm for the 56-mm deep deck, were considered.

The deck was modeled with the same shell element types and material properties as those described in Section 3.1. The mesh densities D7 and D5 were used for the 4- and 8-node elements, respectively, based on the convergence study results. Boundary conditions and the analysis methods were as previously described. The IGI distributions were based on the distortional elastic buckling of the deck top flange and the IGI magnitude of $b_{tf}/150$.

Figure 8 shows effects of the corner radius on the elastic buckling and ultimate moments of the studied models. The corner radius in the considered ranges practically did not affect the distortional elastic buckling moment, M_{crd} , for all studied models. The local elastic buckling moments, M_{crl} , increased when the corner radius increased, which can be explained by the reduction in the flat width of the deck top flanges with the increase of the corner radius. Moment capacity, M_u , of the models reduced by 5 and 7 % for the 73- and 56-mm deck, respectively, when the corner radii increased from zero to the maximum studied values. These results show that the deck corner radius has relatively small effects on the moment capacity and the distortional elastic buckling moment. Therefore, FE deck models with sharp corners and actual corner radii can be used for studying deck strength and distortional elastic buckling moment. Deck models with sharp corners can also be used for studying the local elastic buckling moments, because they result in conservative estimates. The

corner radius should be included in FE models, however, if more accurate and realistic predictions of local elastic buckling moments are desired.

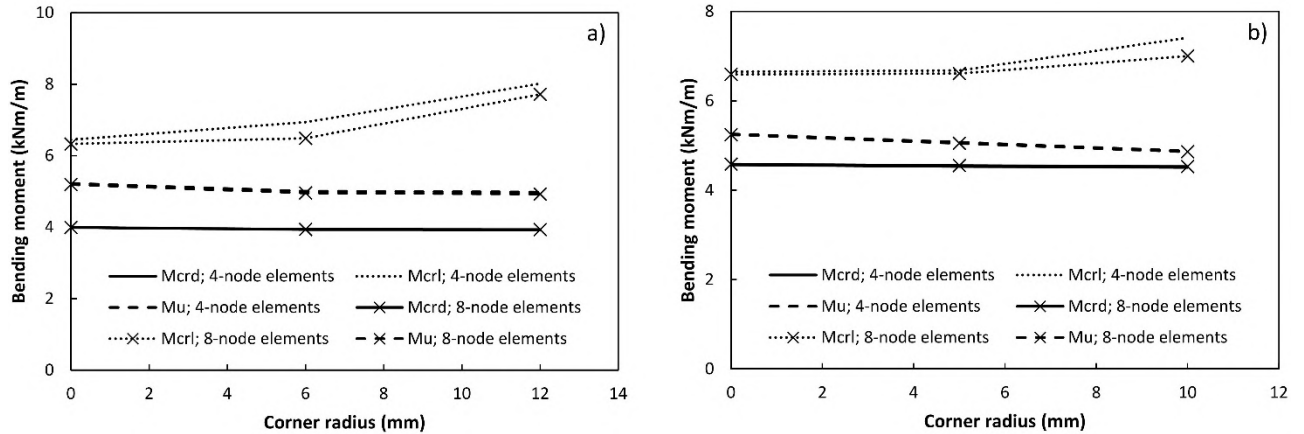


Figure 8. Effects of corner radius on elastic buckling and ultimate moments of a) 73-mm deep deck and b) 56-mm deep deck.

3.3. Effects of number of deck corrugations (hats)

A corrugated steel deck panel has a repetitive shape of the cross-section, which raises a question if modelling of only one corrugation (hat) or one-half corrugation, instead of the entire panel width, would give accurate results. To answer this question, the deck profiles analyzed in the previous stages were modeled with one-half corrugation and one corrugation. Figure 9 shows boundary conditions of the reduced-size models. To account for the panel continuity in the transverse direction, the symmetry boundary conditions were applied along the longitudinal edges of the one-half-hat and one-hat deck models. The corner radii of the models were $6+t/2$ mm for the 73-mm deep deck and $5+t/2$ mm for the 56-mm deep deck. All other parameters of the models were as those described in Section 3.2.

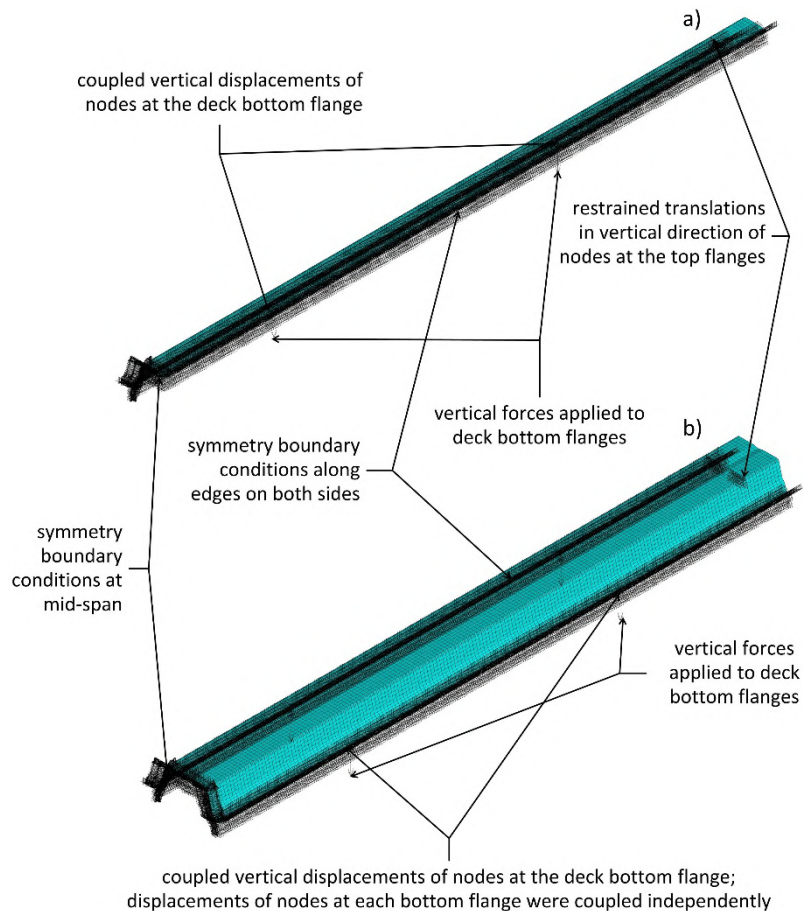


Figure 9. Boundary conditions of reduced-size deck models: a) one-half-hat model; b) one-hat model.

Figure 10 shows ratios of the elastic buckling and ultimate moments per unit width obtained for the one-half-hat and one-hat deck models to the moments obtained for the full-width, four-hat, models. Based on the presented results, it can be concluded that the reduced-size models provide elastic buckling moments and moment capacities identical to those predicted by the full-width models. The one-hat models were slightly more accurate than the one-half-hat models, especially in predicting the local elastic buckling load of the profile with more slender top flanges. The analyses were 6–8 times faster for the one-half-hat models and 3–5 times faster for the one-hat models when compared with the full-width models.

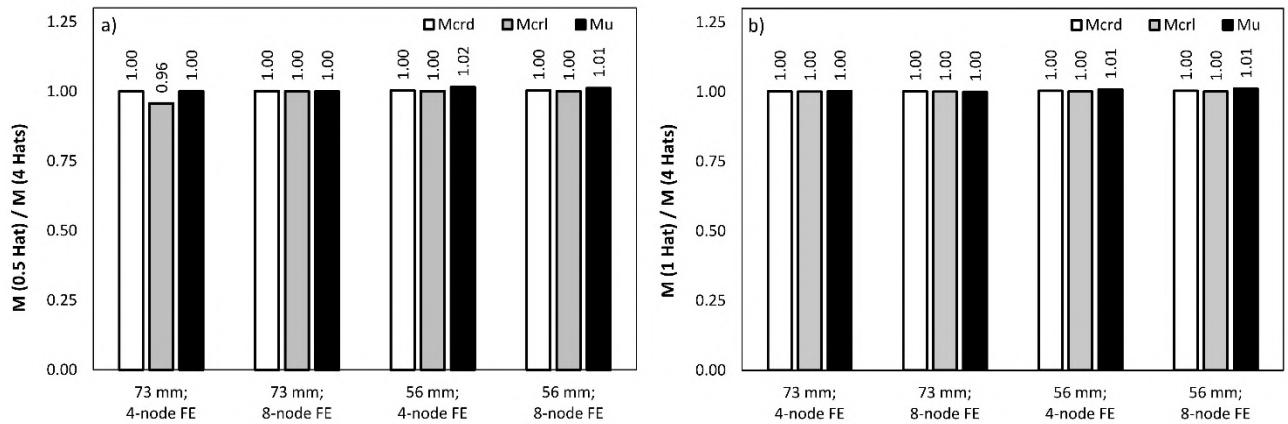


Figure 10. Ratios of elastic buckling and ultimate moments for one-half-hat models and b) one-hat models to moments for four-hat models.

3.4. Effects of initial geometric imperfection distribution

The first elastic buckling mode of cold-formed steel members is commonly used to model distribution of IGIs [14]. As was mentioned previously, the first elastic buckling mode of the studied profiles was distortional buckling of the deck top flanges shown in Figure 5a. The IGI distribution can also be modeled based on the local elastic buckling mode, which was one of the higher elastic buckling modes, shown in Figure 5b. To see if modeling of the IGI distribution based on the distortional and local buckling modes makes any differences in the predicted moment capacities, the full-width, four-hat, deck panels were modeled with the imperfection distributions based on the both buckling modes. The $0.15t$, $0.64t$, and $b_{tf}/150$ IGI magnitudes were used for both IGI distributions. All other parameters of the models were as those described in Section 3.3.

Figure 11 shows the ratios of ultimate moments for the models with the IGI distributions based on the local elastic buckling modes (LBM) to ultimate moments for the models with the IGI distributions based on the distortional elastic buckling modes (DBM). The ratios were in the ranges between 0.99 and 1.03, 0.96 and 0.99, and 0.98 and 1.00 for the IGI magnitudes of $0.15t$, $0.64t$, and $b_{tf}/150$, respectively. These results show that either local or distortional elastic buckling modes can be used for modeling the IGI distributions in steel deck profiles.

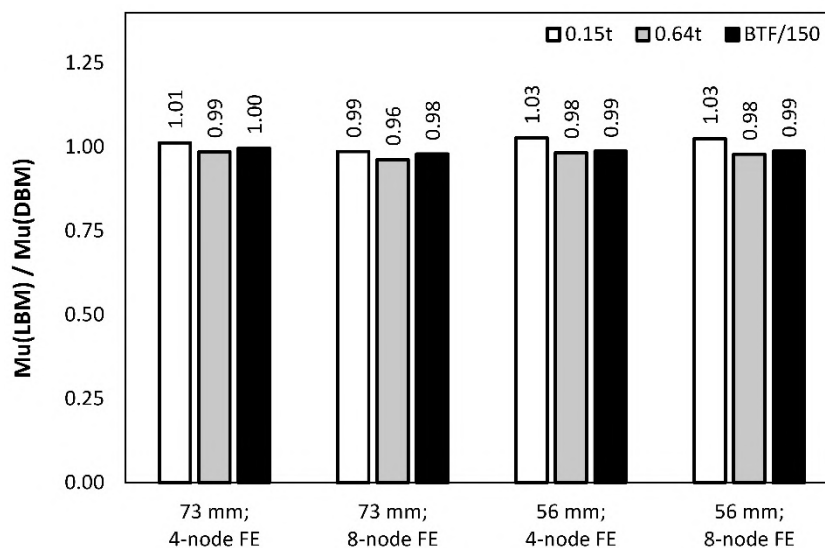


Figure 11. Ratios of ultimate moments for models with initial geometric imperfection distribution based on local elastic buckling mode to ultimate moments for models with initial geometric imperfection distribution based on distortional elastic buckling mode.

3.5. Effects of deck support conditions, loading application, and transverse ties

In the physical testing described in [32], the steel deck was supported at top flanges and loaded through bottom flanges to avoid the influence of local web deformations (web crippling) on the behavior and strength of the deck in bending. Transverse ties were used in the testing to prevent deck panel spreading. Steel deck can also be tested with support reactions transferred through deck bottom flanges and loads applied to deck top flanges [13]. The transverse ties may not be used in the testing.

To evaluate the effects of the boundary conditions and the transverse ties, the deck tested in [32] was modeled with the support conditions and loading application as in the tests (top-flange-supported-bottom-flange-loaded (TFS-BFL)) with and without ties, as well as with the support reactions transferred through the deck bottom flanges and loads applied to the deck top flanges (bottom-flange-supported-top-flange-loaded (BFS-TFL)) with and without ties. Figures 4 and 12 show boundary conditions for the TFS-BFL and BFS-TFL models, respectively. The IGI distributions were based on the distortional elastic buckling mode. The IGI magnitude was taken as $b_{tf}/150$. All other model parameters were as those described in Section 3.4.

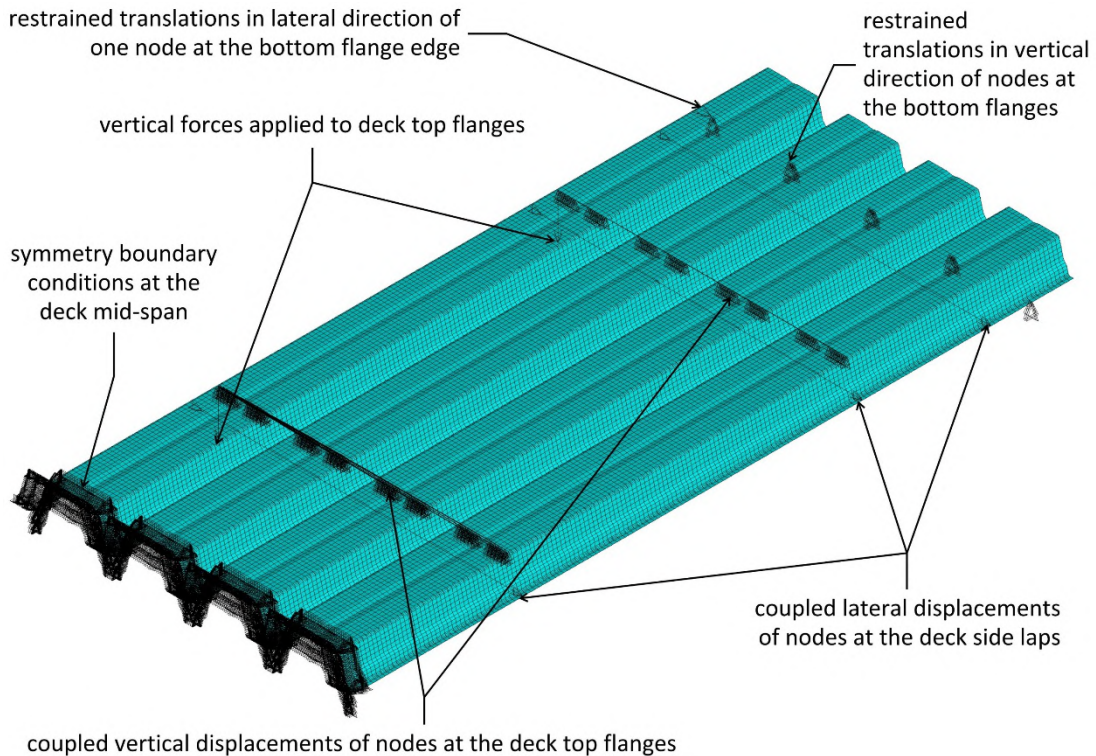


Figure 12. Boundary conditions of deck models supported at bottom flanges and loaded through top flanges (BFS-TFL models).

Figure 13 shows the effects of the studied boundary conditions on the elastic buckling and ultimate moments. Figures 13a and 13b show the ratios of moments for the BFS-TFL models to the moments for the TFS-BFL models without and with ties, respectively. When no transverse ties were provided, the distortional elastic buckling moments, M_{crd} , for the BFS-TFL models were 2–6 % greater than those for the TFS-BFL models. The local elastic buckling moments, M_{crl} , and ultimate moments, M_u , for the BFS-TFL models were 0–10 % and 3–7 %, respectively, smaller than those for the TFS-BFL models. When transverse ties were provided, the M_{crd} , M_{crl} , and M_u values for the BFS-TFL models were 1 % smaller or 1–5 % greater, 1–6 % smaller or 1–4 % greater, and 1 % smaller or 0–1 % greater, respectively, than those for the TFS-BFL models. These results show that the moment capacity of steel deck models without transverse ties is more sensitive to the change in the boundary conditions than the moment capacity of steel deck models with transverse ties. In the presence of the transverse ties, the differences in the moment capacities of the deck with the different boundary conditions considered in this study were very small. The elastic buckling moments of deck models with ties were also less sensitive to the change in the boundary conditions when compared with the models without ties.

Figure 13c shows the ratios of moments for the TFS-BFL models without ties to moments for the TFS-BFL models with ties. The M_{crd} values reduced by 3–4 %, while the M_{crl} values either reduced by 2–4 % or increased by 3 %, when the transverse ties were removed from the TFS-BFL models. The transverse ties removal resulted in an increase of the M_u values by 1 % for the 73-mm deep by 0.75-mm thick profile, whereas the 56-mm deep by 1.00-mm thick profile demonstrated a 7 % reduction in the moment capacities.

Figure 13d shows ratios of moments for the BFS-TFL models without ties to moments for the BFS-TFL models with ties. For the BFS-TFL models, the M_{crd} , M_{crl} , and M_u values reduced by 2, 0–6, and 5–10 %, respectively, when the transverse ties were eliminated.

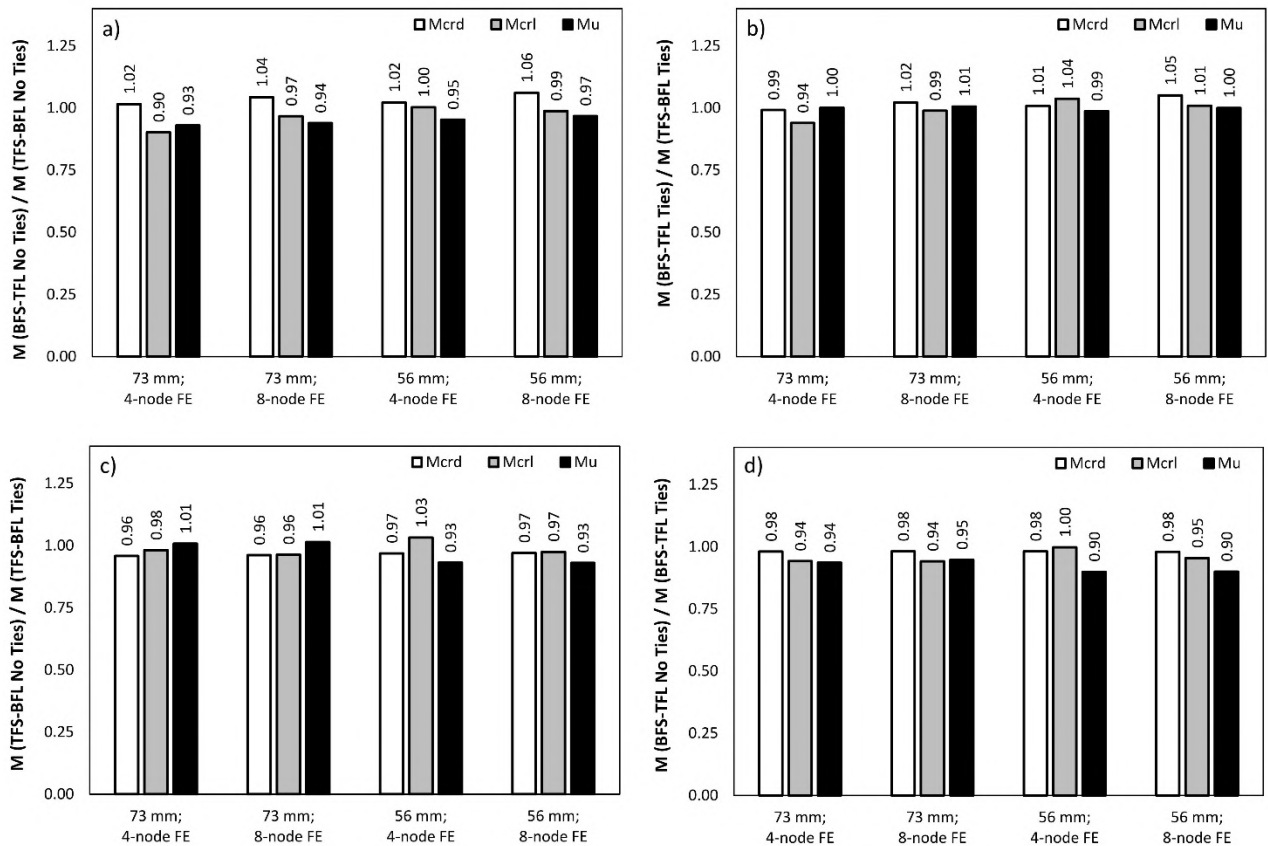


Figure 13. Ratios of elastic buckling and ultimate moments for a) and b) BFS-TFL models to moments for TFS-BFL models without ties and with ties, respectively; c) TFS-BFL models without ties to moments for TFS-BFL models with ties; d) BFS-TFL models without ties to moments for BFS-TFL models with ties.

These results show that addition of the transverse ties generally increases the elastic buckling and ultimate moments of steel deck profiles. The BFS-TFL models are more sensitive to the transverse ties than the TFS-BFL models. The beneficial effects of transverse ties were more pronounced for the thicker deck profiles.

3.6. Effects of loading type

In the physical testing [32], four concentrated loads evenly spaced along the span were applied to the deck. Structural members are also often tested in four-point bending. This loading diagram may be more convenient for FE modeling, because it allows to load the member by imposed displacements, which makes possible obtaining full load-displacement curves with descending branches. In the real life, steel deck is designed for uniformly distributed loads. To study the effects of the different loading types on the elastic buckling and ultimate moments, FE models of the deck with the following additional loading types were analyzed:

- 1) two equal line loads applied as forces along lines parallel to deck supports and located at the distance of $L/3$ (where L is deck span length) from each deck support,
- 2) two equal displacements applied along lines parallel to deck supports and located at the distance of $L/3$ from each deck support, and
- 3) a uniformly distributed load.

Boundary conditions of the models with the different loading types were similar to those shown in Figure 4, except the loads were applied as forces or displacements at the third points or as a uniformly distributed load. The material properties of the deck and corner radii were as those described in Section 3.1. The IGI distribution was based on the distortional elastic buckling of the deck top flanges with the IGI magnitude of $b_{tf}/150$.

Figures 14a, 14b, and 14c show ratios of the elastic buckling and ultimate moments obtained for the models loaded by two line forces, two displacements, and a uniform load, respectively, to those obtained for the models loaded by four line forces. The presented comparisons indicate that all studied loading types resulted in comparable predictions of the elastic buckling and ultimate moments. The differences in the

predictions of the M_{crd} , M_{crl} , and M_u values were within 1, 5, and 5 %, respectively. These results demonstrate that any of the studied loading types can be used for numerical studies of elastic buckling and ultimate moments of corrugated steel deck profiles.

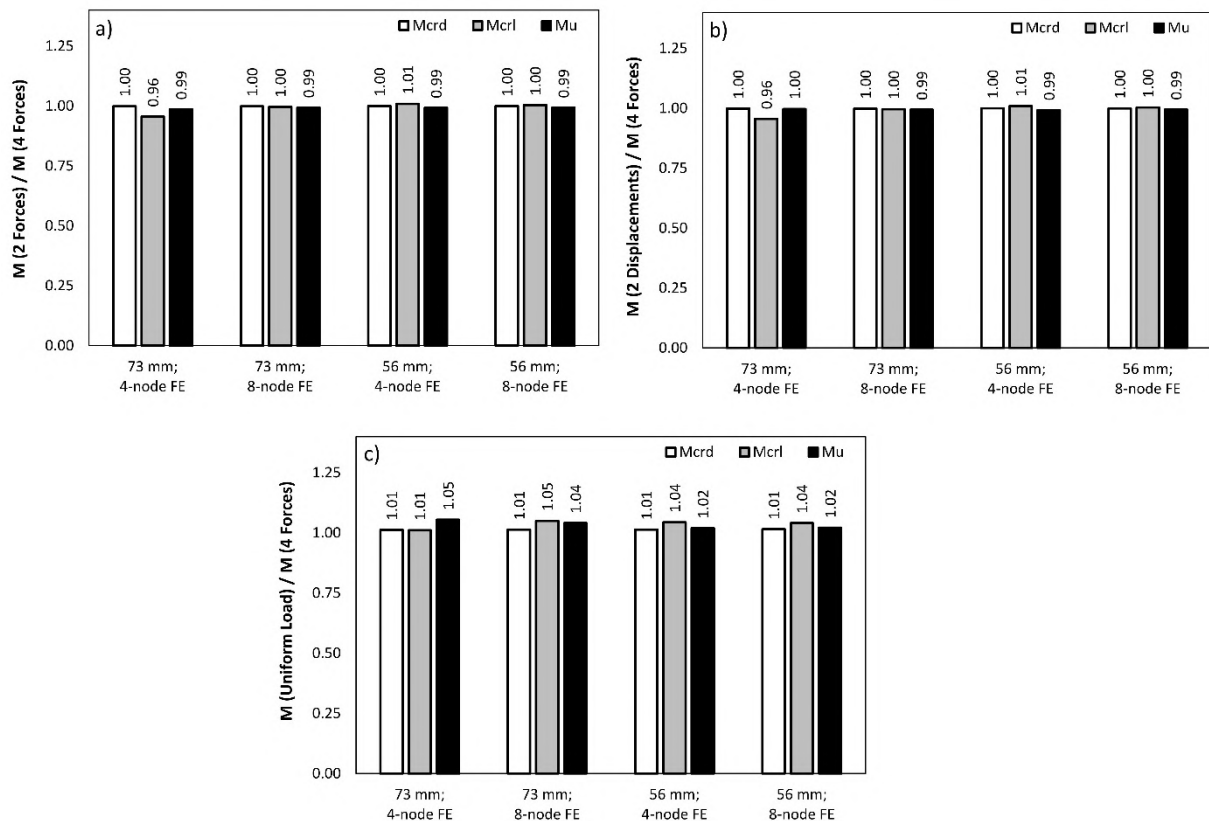


Figure 14. Ratios of elastic buckling and ultimate moments for a) models loaded by two forces, b) models loaded by two displacements, and c) models loaded by uniform load to moments for models loaded by four forces.

3.7. Effects of steel stress-strain diagrams and model validation

All deck models described previously were based on the nonlinear stress-strain curves proposed in [34]. Simplified models, such as elastic-perfectly plastic and bilinear, are also commonly used for modeling the behavior and strength of steel members. To study the effects of different stress-strain diagrams on the structural response, flexural stiffness, and moment capacity of the deck, all solid deck profiles tested in [32] were modeled with the elastic-perfectly plastic, bilinear, and nonlinear stress-strain diagrams shown in Figure 2. The key parameters of the diagrams, such as steel yield stress, f_y , and tensile strength, f_u , were as those reported in [32].

The FE simulation results obtained in this stage were also compared with the experimental data to validate the developed FE models. Overall, 14 physical test results described in [32] were used for the model validation. In addition to the 73-mm deep by 0.75-mm thick and 56-mm deep by 1.00-mm thick profiles described previously, 73-mm deep by 1.00-mm thick and 56-mm deep by 0.75-mm thick profiles were modeled and analyzed. Mesh densities D7 and D5 (see Table 1) were used for deck models with the 4- and 8-node elements, respectively. Corner radii and boundary conditions were as those described in Section 3.1. The IGI distribution was based on the distortional elastic buckling of the deck top flange with the IGI magnitude of $b_{eff}/150$.

Figure 15 shows load-deflection diagrams obtained from the tests [32] and the FE simulations of deck models with different steel stress-strain diagrams and element types. The EPP, BL, and NL abbreviations in Figure 15 stand for elastic-perfectly plastic, bilinear, and nonlinear stress-strain diagrams of steel. Deliveries 1 and 3 shown in Figure 15 refer to deck made from different coils of steel and delivered to the testing lab at different times [32]. The structural response of the 4-node element models with mesh density D7 and the 8-node element models with mesh density D5 were nearly identical. The models based on the elastic-perfectly plastic and bilinear constitutive models did not show noticeable differences in the structural response either. The nonlinear stress-strain diagram resulted in considerably different structural response of the models when compared with the elastic-perfectly plastic and bilinear diagrams due to the plastic deformation of steel at stresses below the yield stress accounted for by the nonlinear model. Figure 15 shows that the nonlinear

stress-strain diagram generally resulted in a better agreement of flexural stiffness of the deck models with the test results for the full range of loading.

Figure 16 compares the ultimate moments of deck models with different constitutive models and element types obtained from the FE simulations with the test results [32]. It can be concluded that the developed FE models with all studied stress-strain diagrams and element types showed good agreements with the experimental data. The nonlinear stress-strain diagrams, however, resulted in slightly better predictions of the ultimate moments when compared with the elastic-perfectly plastic and bilinear diagrams for both the 4- and 8-node shell elements.

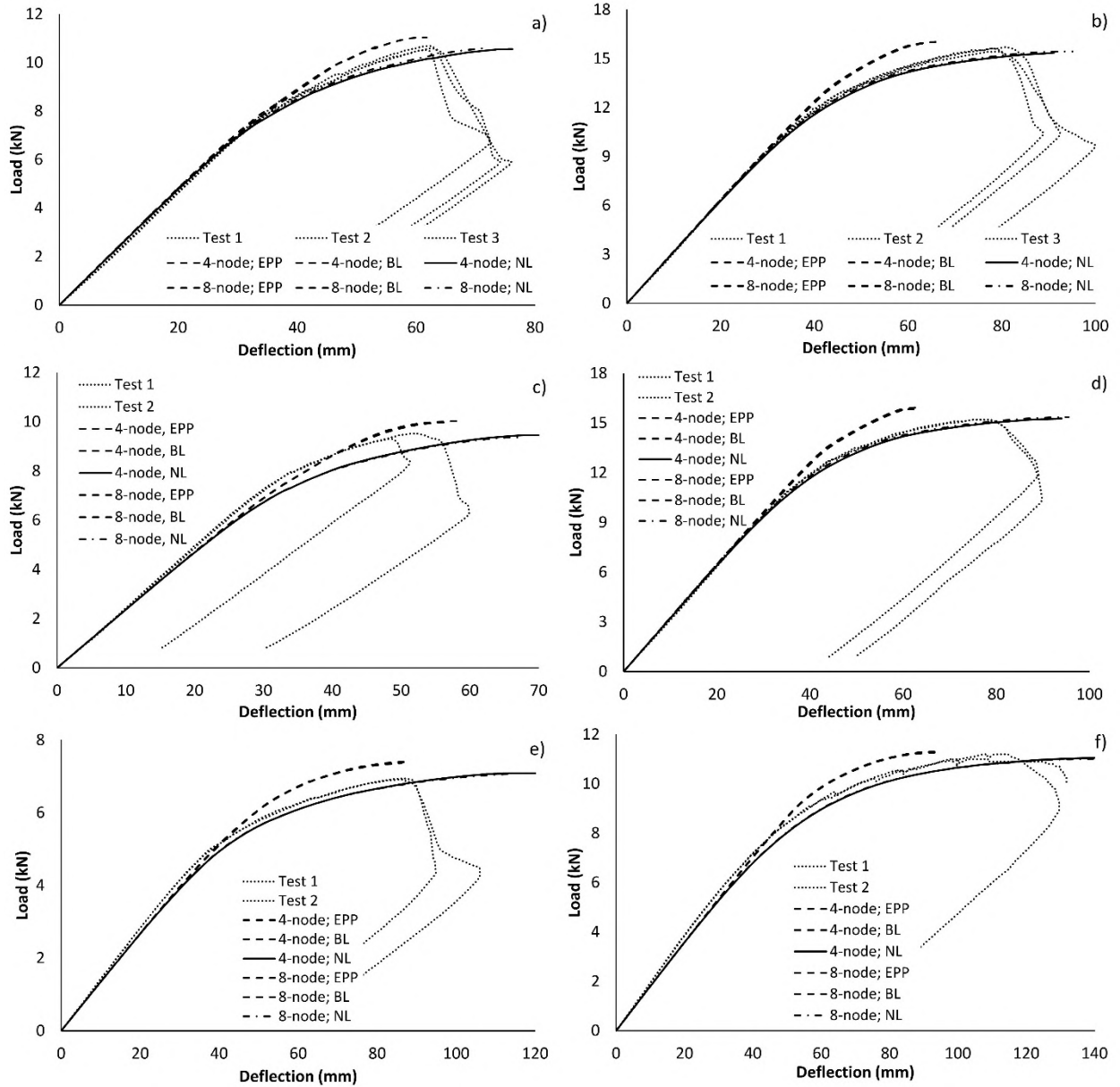


Figure 15. Load-deflection diagrams from tests and FE simulations: a) and c) 73-mm by 0.75-mm deck from delivery 3 and 1, respectively; b) and d) 75-mm by 1.00-mm deck from delivery 3 and 1, respectively; e) and f) 56-mm by 0.75-mm and 1.00-mm, respectively.

Figure 17 compares deck deflections at the maximum moments from the FE simulations and the tests [32]. The FE models with the elastic-perfectly plastic and bilinear stress-strain diagrams slightly underestimated the deck deflections at the maximum moments, whereas the FE models with the nonlinear stress-strain diagram overestimated the maximum deck deflections. The nonlinear diagrams resulted in a smaller scatter of the FEA/Test ratios when compared with the elastic-perfectly plastic and bilinear stress-strain diagrams. The nonlinear stress-strain diagrams of the steel might be adjusted if needed, by reducing the ϵ_u value, to improve predictions of the deck deflection at the maximum moment. This characteristic, however, is not very important for the practical design of steel decks.

A more important characteristic of the deck flexural stiffness is the deck deflection at the service level load, which is compared with the acceptable deck deflection in the structural deck design. The service level

load is commonly assumed to be at 60 % of the ultimate moment. Figure 18 shows comparisons of deck deflections at $0.6M_u$ obtained from the FE simulations with the test results. The FE models with the material behavior of steel described by the nonlinear stress-strain diagram show a better agreement of deflections at the service level loads with the test results when compared with the models based on the simplified stress-strain diagrams. The latter, however, also show reasonably good agreements with the test results.

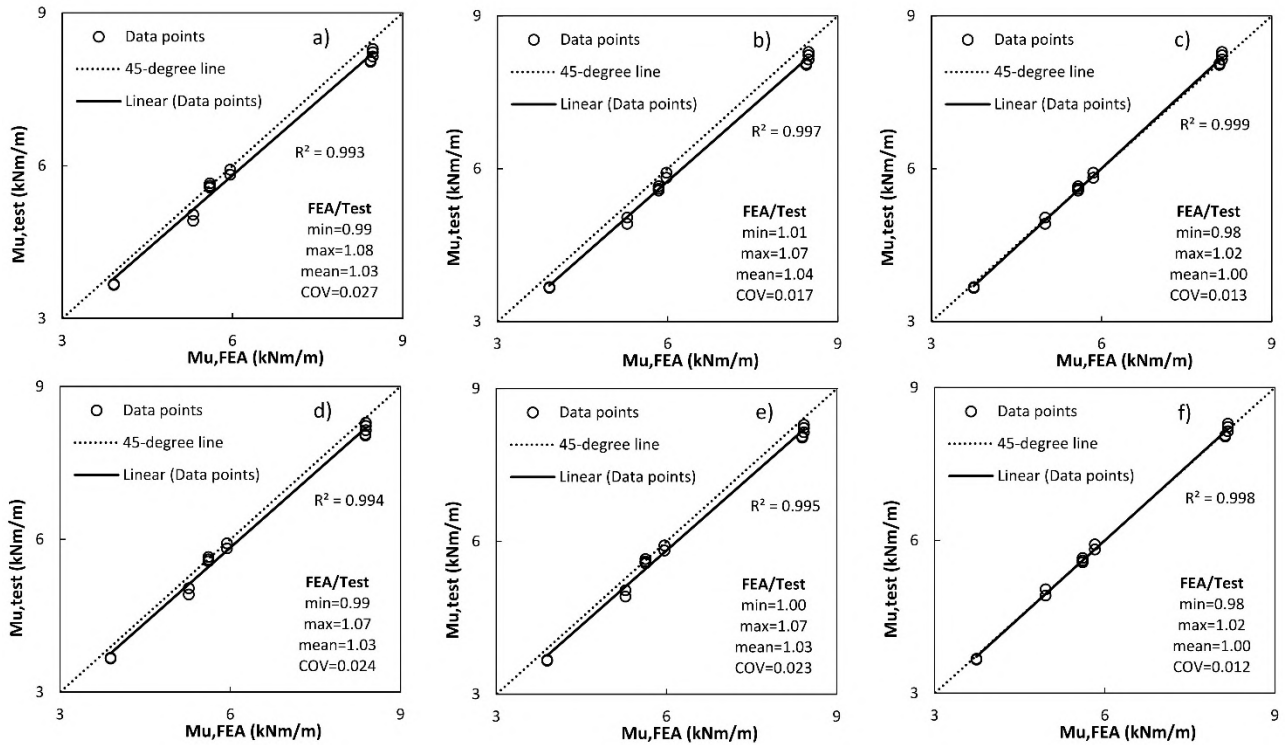


Figure 16. Comparisons of ultimate moments for deck models with different constitutive models and element types from FE simulations with test results: a), b), and c) 4-node FE models with elastic-perfectly plastic, bilinear, and nonlinear stress-strain diagrams, respectively; d), e), and f) 8-node FE models with elastic-perfectly plastic, bilinear, and nonlinear stress-strain diagrams, respectively.

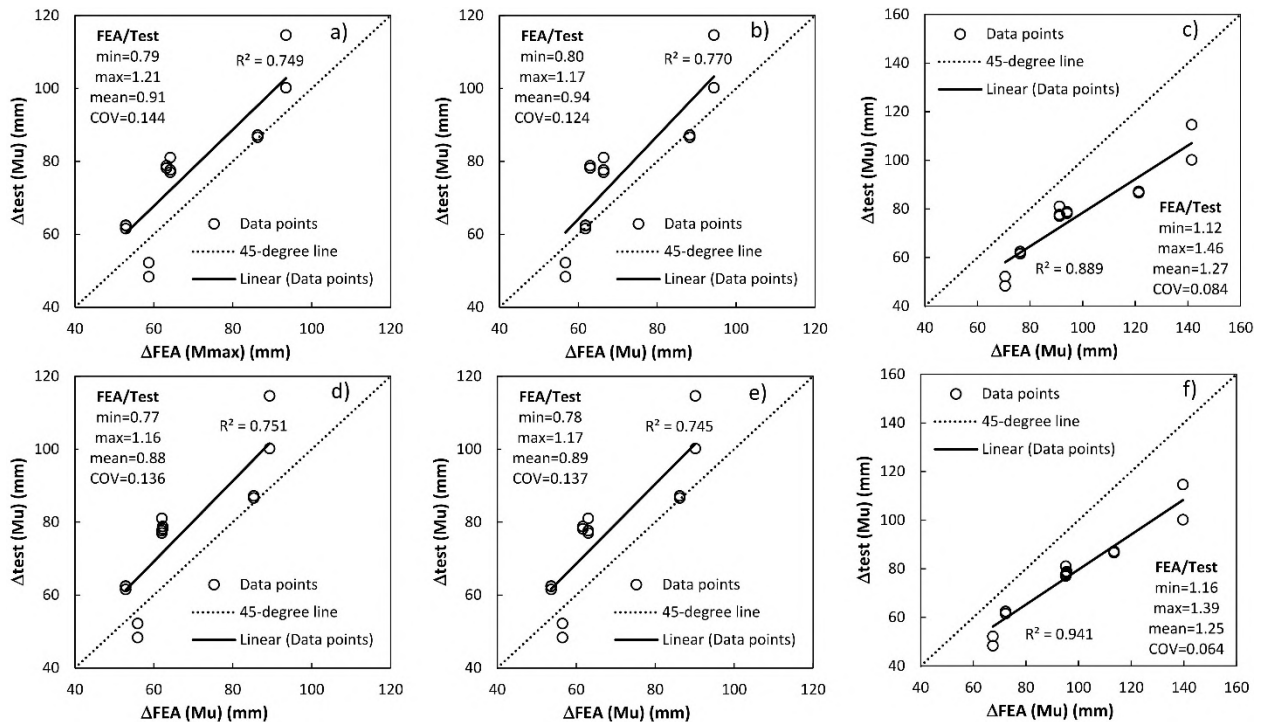


Figure 17. Comparisons of deck deflections at ultimate moments for models with different constitutive models and element types obtained from FE simulations with test results: a), b), and c) 4-node FE models with elastic-perfectly plastic, bilinear, and nonlinear stress-strain diagrams, respectively; d), e), and f) 8-node FE models with elastic-perfectly plastic, bilinear, and nonlinear stress-strain diagrams, respectively.

It can be concluded that the nonlinear stress-strain diagrams used in the FE simulations result in better agreements of strength and flexural stiffness of steel deck with the experimental data than the simplified elastic-perfectly plastic and bilinear models. The developed models can be employed for numerical studies of solid deck profiles and can be used as a basis for the development of FE models of steel deck with openings and acoustical perforations, as well as built-up deck profiles.

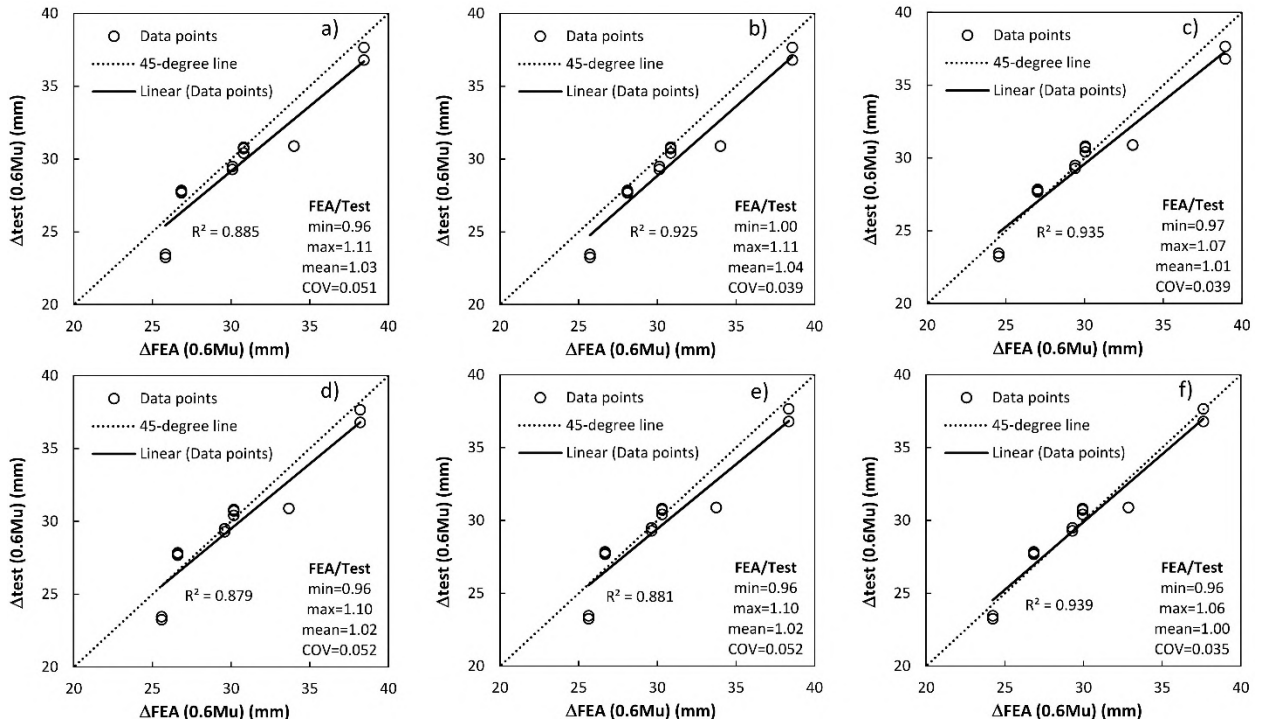


Figure 18. Comparisons of deck deflections at service level moments for models with different constitutive models and element types obtained from FE simulations with test results: a), b), and c) 4-node FE models with elastic-perfectly plastic, bilinear, and nonlinear stress-strain diagrams, respectively; d), e), and f) 8-node FE models with elastic-perfectly plastic, bilinear, and nonlinear stress-strain diagrams, respectively.

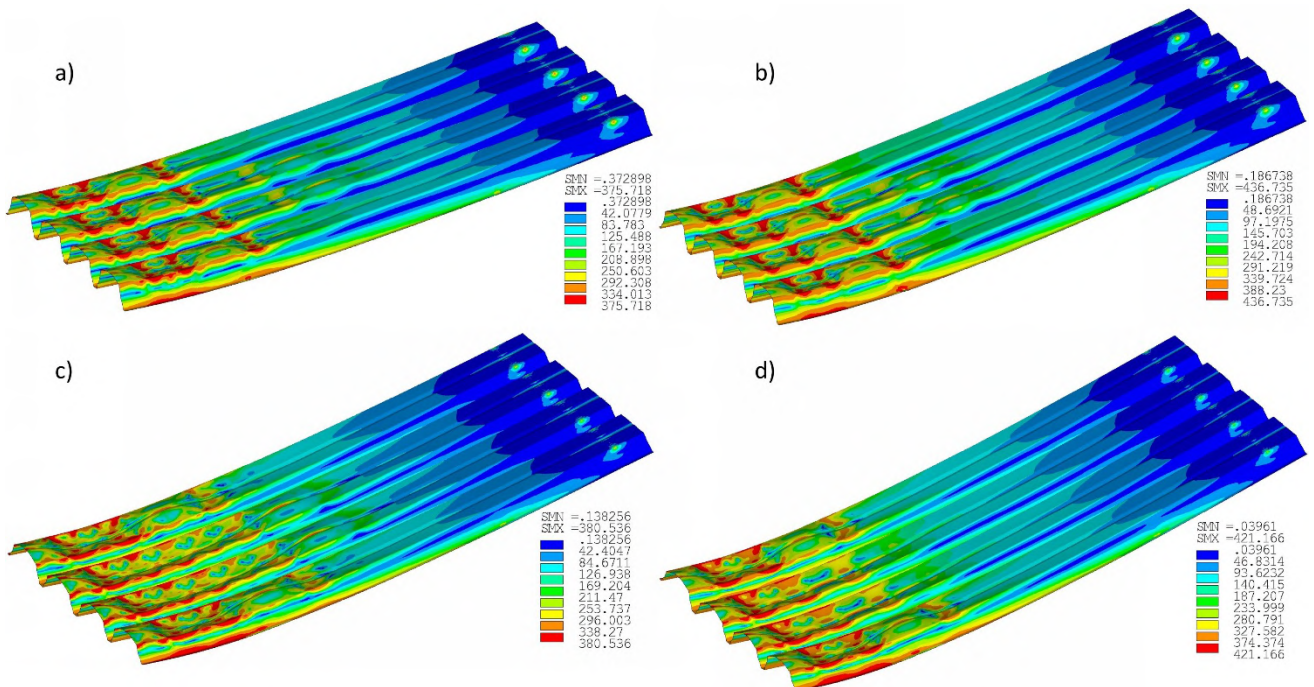


Figure 19. von Mises stresses [MPa] in FE deck models at ultimate moments: a) and b) 73-mm by 0.75- and 1.00-mm deck, respectively; c) and d) 56-mm by 0.75- and 1.00-mm deck, respectively.

Figure 19 shows von Mises stresses in the FE deck models at the ultimate moments. Nonlinear distortional buckling of the deck top flanges can be clearly seen for all studied deck heights and steel thicknesses. This type of buckling was observed in the tests [32] as well. Highly non-uniform von Mises stress distributions along and across the deck top flanges due to the flange nonlinear buckling can be seen in Figure 19. Higher von Mises stresses were observed near the corners and within unbuckled portions of the flanges.

4. Conclusions

1. FE models of corrugated cold-formed steel deck were developed in a commercially available FE simulation software, ANSYS. Steel deck was modeled with linear 4-node and quadratic 8-node structural shell elements. Optimal mesh densities were determined for the deck models with both element types based on a convergence study. The effects of different constitutive steel models on the moment capacity, flexural stiffness, and load-deflection diagrams were considered.

2. The study showed that the deck corner radius had relatively small effects on the moment capacity and the distortional elastic buckling moment, but had a greater effect on the local elastic buckling moment.

3. Reduced-size FE deck models, with only one hat or one-half hat instead of the full-width deck panel with multiple hats, were studied. The reduced-size FE models provided elastic buckling and ultimate moments identical to those predicted by the full-size models.

4. IGI distributions based on the distortional and local elastic buckling modes of the deck top flange with three different IGI magnitudes were studied. The studied IGI distributions and magnitudes had relatively small effects on moment capacities of the FE deck models.

5. Effects of different boundary conditions (with the deck supported at top flanges and loaded through bottom flanges; and with the deck supported at bottom flanges and loaded through top flanges) and transverse ties were studied. The elastic buckling and ultimate moments of the models without transverse ties were more sensitive to the change in the boundary conditions when compared with the models with transverse ties. Addition of the transverse ties resulted in increases in the elastic buckling and ultimate moments, especially for thicker profiles. Deck models supported at bottom flanges and loaded through top flanges were more sensitive to the presence of the transverse ties than the models supported at top flanges and loaded through bottom flanges.

6. Effects of different loading types along the deck span, such as four loads modeled as forces, two loads modeled as forces and imposed displacements, and a uniform load, were considered. The elastic buckling and ultimate moments obtained for the studied loading types showed very small differences.

7. The developed models were validated against available test results. Moment capacities, flexural stiffness values, and load-deflection curves predicted by the models compared well with those obtained from physical testing, especially when nonlinear stress-strain diagrams of steel were used.

8. The developed FE models can be an efficient tool for numerical studies of flexural strength and stiffness of non-perforated steel deck with various geometry under various loading types, which can be useful in development of new efficient profiles and in improving current deck design methods. They may also form a basis for development of FE models of deck with openings and perforations, as well as built-up deck profiles, design methods for which are currently underdeveloped.

References

1. ANSI/SDI RD-2017. Standard for steel roof deck. Steel Deck Institute; 2017.
2. AISI S100-16. North American specification for the design of cold-formed steel structural members. American Iron and Steel Institute. Washington, DC; 2016.
3. AS/NZS 4600:2018. Cold-formed steel structures. Standards Australia/Standards New Zealand. Sidney, Australia; 2018.
4. EN 1993-1-3:2006. Eurocode 3 – Design of steel structures – Part 1–3: General rules – Supplementary rules for cold-formed members and sheeting. European Committee for Standardization. Brussels, Belgium; 2006.
5. SDI MOC3. Manual of construction with steel deck. 3rd ed. Steel Deck Institute; 2016.
6. SDI RDDM1. Roof deck design manual. 1st ed. Steel Deck Institute; 2012.
7. Palisson, A. Guidelines and recommendations for integrating specific profiled steels sheets in Eurocodes (GRISPE). [Online]. D 3.1 Perforated Profiles. Sokol Palisson Consultants. Paris, France, 2018. URL: <http://www.grispeplus.eu/7-families-of-steel-profiles/perforated-and-holed-profiles/>
8. Degtyarev, V.V., Degtyareva, N.V. Elastic stability of uniformly compressed plates perforated in triangular patterns. *Thin-Walled Structures*. 2012. 52. Pp. 165–173.
9. Palisson, A. Guidelines and recommendations for integrating specific profiled steels sheets in Eurocodes (GRISPE). D 3.1 Holed Profiles. Sokol Palisson Consultants. Paris, France, 2018. <http://www.grispeplus.eu/7-families-of-steel-profiles/perforated-and-holed-profiles/>
10. Degtyarev, V.V. A finite element study of corrugated steel deck subjected to concentrated loads. *Proceedings of Wei-Wen Yu International Specialty Conference on Cold-Formed Steel Structures 2018*. St. Louis, Missouri, USA, 2018. Pp. 731–745.
11. Degtyarev, V.V. Concentrated load distribution in corrugated steel decks: A parametric finite element study. *Engineering Structures*. 2020. 206. 110158.
12. Dudenbostel, R.K., Sputo, T. Application of the Direct Strength Method to steel deck. *Proceedings of Wei-Wen Yu International Specialty Conference on Cold-Formed Steel Structures 2016*. Baltimore, Maryland, USA, 2016. Pp. 665–679.
13. Raebel, C., Gwozdz, D. Comparison of experimental and numerical results for flexural capacity of light-gage steel roof deck. *Proceedings of Wei-Wen Yu International Specialty Conference on Cold-Formed Steel Structures 2018*. St. Louis, Missouri, USA, 2018. Pp. 55–67.
14. Schafer, B.W., Li, Z., Moen, C.D. Computational modeling of cold-formed steel. *Thin-Walled Structures*. 2010. 48. Pp. 752–762.

15. Yu, C., Schafer, B.W. Simulations of cold-formed steel beams in local and distortional buckling with applications to the direct strength method. *Journal of Constructional Steel Research*. 2007. 63. Pp. 581–590.
16. Haidarali, M.R., Nethercot, D.A. Finite element modelling of cold-formed steel beams under local buckling or combined local/distortional buckling. *Thin-Walled Structures*. 2011. 49. Pp. 1554–1562.
17. Nazmeeva, T.V., Vatin, N.I. Numerical investigations of notched C-profile compressed members with initial imperfections. *Magazine of Civil Engineering*. 2016. 62(2). Pp. 92–101.
18. Garifullin, M., Nackenhorst, U. Computational analysis of cold-formed steel columns with initial imperfections. *Procedia Engineering*. 2015. 117. Pp. 1073–1079.
19. Salhab, B., Wang, Y.C. Equivalent thickness of cold-formed thin-walled channel sections with perforated webs under compression. *Thin-Walled Structures*. 2008. 46. Pp. 823–838.
20. Pham, C.H., Hancock, G.J. Numerical simulation of high strength cold-formed purlins in combined bending and shear. *Journal of Constructional Steel Research*. 2010. 66(10). Pp. 1205–1217.
21. Pham, C.H., Hancock, G.J. Numerical investigation of longitudinally stiffened web channels predominantly in shear. *Thin-Walled Structures*. 2015. 86. Pp. 47–55.
22. Hui, C., Gardner, L., Nethercot, D.A. Moment redistribution in cold-formed steel continuous beams. *Thin-Walled Structures*. 2016. 98. Pp. 465–477.
23. Keerthan, P., Mahendran, M. Numerical modeling of Lite Steel beams subject to shear. *Journal of Structural Engineering*. 2011. 137(12). Pp. 1428–1439.
24. Keerthan, P., Mahendran, M., Hughes, D. Numerical studies and design of hollow flange channel beams subject to combined bending and shear actions. *Engineering Structures*. 2014. 75. Pp. 197–212.
25. Sundararajah, L., Mahendran, M., Keerthan, P. Numerical Modeling and Design of Lipped Channel Beams Subject to Web Crippling under One-Flange Load Cases. *Journal of Structural Engineering*. 2019. 145(10). Pp. 1–16.
26. Degtyarev, V.V., Degtyareva, N.V. Numerical simulations on cold-formed steel channels with flat slotted webs in shear. Part I: Elastic shear buckling characteristics. *Thin-Walled Structures*. 2017. 119. Pp. 22–32.
27. Degtyarev, V.V., Degtyareva, N.V. Numerical simulations on cold-formed steel channels with flat slotted webs in shear. Part II: Ultimate shear strength. *Thin-Walled Structures*. 2017. 119. Pp. 211–223.
28. Degtyarev, V.V., Degtyareva, N.V. Numerical simulations on cold-formed steel channels with longitudinally stiffened slotted webs in shear. *Thin-Walled Structures*. 2018. 129. Pp. 429–456.
29. Degtyareva, N., Gatheeshgar, P., Poologanathan, K., Gunalan, S., Lawson, M., Sunday, P. Combined bending and shear behaviour of slotted perforated steel channels: Numerical studies. *Journal of Constructional Steel Research*. 2019. 161. Pp. 369–384.
30. Misiek, Th. Tragverhalten dünnwandiger Bauteile aus perforierten Blechen (Load-bearing behaviour of thin-walled building components made of perforated sheets). Dr-Ing. Dissertation. Universität Fridericiana zu Karlsruhe. Karlsruhe, Germany. 2008. 259 p.
31. ANSYS Mechanical APDL, Release 19.2.
32. Fauth, C. Guidelines and recommendations for integrating specific profiled steels sheets in Eurocodes (GRISPE) [Online]. D 3.3 Test report. Karlsruhe Institute of Technology (KIT). Karlsruhe, Germany, 2015 (Rev.4). URL: <http://www.grispeplus.eu/7-families-of-steel-profiles/perforated-and-holed-profiles/>
33. EN 10346:2009. Continuously hot-dip coated steel flat products – Technical delivery conditions. European Committee for Standardization. Brussels, Belgium; 2009.
34. Gardner, L., Yun, X. Description of stress-strain curves for cold-formed steels. *Construction and Building Materials*. 2018. 189. Pp. 527–538.
35. EN 1993-1-5:2006. Eurocode 3 – Design of steel structures – Part 1–5: Plated structural elements. European Committee for Standardization. Brussels, Belgium; 2006.
36. Camotim, D., Silvestre, N. GBT-based analysis of the distortional postbuckling behavior of cold-formed steel z-section columns and beams. *Proceedings of the 4th International Conference on Thin-Walled Structures*. Loughborough, 2004. Pp. 243–250.
37. Schafer, B.W., Peköz, T. Computational modeling of cold-formed steel: characterizing geometric imperfections and residual stresses. *Journal of Constructional Steel Research*. 1998. 47. Pp. 193–210.

Contacts:

Vitaliy Degtyarev, vitaliy.degtyarev@newmill.com

© Degtyarev, V.V., 2020



DOI: 10.18720/MCE.94.12

Micromechanical characteristics of high-performance concrete subjected to modifications of composition and homogenization

P. Bily*, J. Fladr, R. Chylik, V. Hrbek, L. Vrablik

Czech Technical University, Prague, Czech Republic

* E-mail: petr.bily@fsv.cvut.cz

Keywords: high-performance concrete, supplementary cementitious materials, interfacial transition zone, nanoindentation, mechanical pro

Abstract. The paper deals with the effect of various modifications of composition and homogenization procedure on micromechanical characteristics of high-performance concrete (HPC) containing supplementary cementitious materials (SCMs), namely silica fume, fly ash and metakaolin. The main motivation was to characterize the changes of microstructure induced by the type and amount of SCMs, by the time and order of mixing of components and by coarse aggregate washing. The effects of the changes of microstructure on macroscopic mechanical features of the material were also studied. Indentation moduli of particular phases of the material were measured by nanoindentation. Interfacial transition zone (ITZ) thickness was primarily measured by nanoindentation. An alternative method of ITZ thickness determination based on variations in chemical composition was tested for a selected sample with encouraging result. Compressive strength and bulk elastic modulus of concrete were determined by standard loading tests. The results showed that SCMs generally decrease the thickness of ITZ, but no direct relation to compressive strength of concrete was found for mixtures with variable SCMs content. In case of mixtures with optimized SCMs content prepared by different homogenization procedures or with the use of aggregate washing, qualitative dependence between ITZ thickness and compressive strength was found. Aggregate washing proved to be useful for improving both microscopic and macroscopic properties, having positive effect on ITZ thickness, compressive strength, bulk elastic modulus and indentation moduli of particular phases.

1. Introduction

Interfacial transition zone (ITZ) and its properties are one of the most important, but at the same time the least understood phenomena influencing mechanical properties of concrete. ITZ is a thin transitional layer between aggregate grains and cement paste. It is a weak link in the structure of a cementitious composite, where the first microcracks originate and begin to develop into macrocracks. A typical thickness of ITZ in normal strength concrete reaches 30 – 100 μm [1–3], while in high-performance composites, lower values ranging between 10–30 μm are reported [4–7]. Some research works point out a strong relationship between the characteristics of ITZ (mainly its thickness and mechanical properties) and macroscopic properties of concrete, such as compressive and tensile strength, elastic modulus or resistance to deicing chemicals [8–10].

The origin and creation of ITZ is attributed mainly to the wall effect. The phenomenon leading to accumulation of batch water on the surface of aggregate grains and local increase of water-to-binder ratio (w/b) was described by Escadeillas and Maso [11]. The local increase of w/b leads to increased porosity and decreased strength of ITZ. Another important factor is the filtration effect described by Lagerblad and Kjellsen [12]. When more aggregate grains are located close to each other, cement particles get filtrated as fresh cement paste passes through the narrow gap between the grains during concreting. As a result, an area of cement matrix with lower density and higher porosity is created. Microbleeding and syneresis also contribute to ITZ formation. Microbleeding is defined as flocking of microscopic droplets of bleeding water around larger aggregate grains in the course of concrete mixing [13]. During syneresis, cement matrix shrinks and the water is released from the structure of cement gel, leading to the separation of the water rich in cement particles from the solid components of the matrix [14].

Bily, P., Fladr, J., Chylik, R., Hrbek, V., Vrablik, L. Micromechanical characteristics of high-performance concrete subjected to modifications of composition and homogenization. Magazine of Civil Engineering. 2020. 94(2). Pp. 145–157. DOI: 10.18720/MCE.94.12



This work is licensed under a CC BY-NC 4.0

The works cited above identified several ways of efficient reduction of ITZ thickness. The main ones are minimization of w/b, use of superplasticizers and the use of supplementary cementitious materials (SCMs). Other influencing factors are humidity, porosity, absorbability and granulometry of aggregate, cement type, time of homogenization and compaction of the mixture and cleanness of aggregate surface. In case of high-performance concrete (HPC), Portland cement is used, w/b is already minimized to maximum possible extent, superplasticizers are used in high dosages, the aggregates with the best available properties are exploited. Therefore, it makes sense to study the remaining factors – the use of SCMs, technological process of concrete production and cleanness of aggregate surface.

SCMs are nowadays often used to improve various properties of concrete – physical and mechanical characteristics [15–18] or consistence [19]. Fediuk et al. proved that they can also increase the efficiency of grinding of cement [20] or shock resistance of concrete [21].

The positive influence of SCMs on ITZ thickness was observed by Rossignolo [22] who reported that replacing 10 % cement weight by silica fume led to the reduction of ITZ thickness by 36 % compared to reference concrete. When he modified concrete by SBR latex admixture in the dosage of 5 % and 10 % of cement weight, ITZ thickness was reduced by 27 % and 36 % respectively. The best results were obtained by combined use of silica fume (10 % cem. wt.) and SBR latex (10 % cem. wt.) when ITZ thickness was reduced by 64 %.

Duan et al. [23] investigated the effect of slag, metakaolin and silica fume on thickness and microhardness of ITZ and macroscopic compressive strength of concrete. The measurements were performed at the ages of 3, 7, 28 and 180 days for mixtures with 10 % cement weight replacement. The tendency to decrease ITZ thickness in time was evident for all the mixtures including the reference one, but it was more pronounced in the mixtures containing SCMs. In case of reference concrete, ITZ thickness was reduced from 80 μm at 3 days to 60 μm at 180 days. ITZ in concrete containing slag was reduced from 60 μm to 50 μm and in concrete containing silica fume or metakaolin the reduction from 50 μm to 40 μm was observed during the same period. The SCMs also positively influenced the microhardness of ITZ. Microhardness of ITZ constituted 79 % of microhardness of bulk cement paste in case of reference concrete, 83 % in case of concrete containing metakaolin or slag and 86 % in case of concrete containing silica fume. It was also proved that there is a direct linear dependence between microhardness of cement paste and macroscopic compressive strength of concrete.

Nilli and Ehsani [24] focused on the effect of nanosilica and silica fume on ITZ and strength development. Among other results, it was shown that replacing 5 % or 7.5 % cement weight by silica fume increased concrete compressive strength by approximately 10 %.

When studying self-compacting concretes, several researchers [25–27] confirmed that missing vibrations during concrete placement lead to elimination of vibration-induced segregation and microbleeding. The amount of water accumulated on the surface of aggregate grains was also reduced, leading to mitigation of wall effect, reducing porosity of ITZ and permeability of concrete. Yoo et al. [28] proved that the concrete placement method influences the first cracking strength and corresponding toughness of HPC.

Hiremath and Yaragal [29] experimented with the sequence of addition of compounds (microsilica before/after water, aggregate before/after water, water added in two or three steps) into HPC mixture containing 20 % silica fume (20 % cem. wt.). The highest compressive strength of 128 MPa was reached when aggregate was added to wet mortar; the standard mixing procedure (adding water to dry mix of all constituents) led to 105 MPa, i.e. 20 % less.

While some fine fillers are used to optimize the grading curve of aggregate, increase packing density of concrete and increase its compressive strength, the presence of another types of fine particles in concrete is undesirable. These include clay and other fine components (smaller than 0.125 mm) that are formed during the extraction of basalt aggregates and that are trapped on the surface of coarse aggregate grains. These particles can weaken the link between the aggregate and cement matrix and deteriorate mechanical properties of concrete [30, 31]. By increasing the amount of water bonded on the surface of aggregate grains, they locally increase the w/b in the vicinity of these grains. Cepuritis and Mørtzell [32] experimentally verified that the use of washed aggregate improves workability of concrete. However, no studies dealing with the effect of cleanness of aggregate surface (aggregate washing) on mechanical properties of concrete were found.

The paper deals with the effect of various modifications of composition and homogenization procedure on micromechanical characteristics of high-performance concrete (HPC) containing supplementary cementitious materials (SCMs). Silica fume, fly ash and metakaolin were used as partial replacement of cement. The studied modifications consisted in the type and amount of SCMs, the time and order of mixing of components and in coarse aggregate washing. The measured micromechanical characteristics were indentation moduli of individual phases of the material and thickness of interfacial transition zone (ITZ) determined by nanoindentation. Relations between the changes on the microscale and main macroscopic mechanical properties (compressive strength and bulk elastic modulus) were studied.

In their previous study [33], the authors of this paper dealt with the effect of SCMs and homogenization procedure on macroscopic mechanical properties of HPC. A large database of results was obtained, showing the relations between the modifications in composition and homogenization of HPC and a variety of macroscopic mechanical properties of the material. The main motivation of the experimental program presented in this paper was to characterize the changes of properties of the same materials on microscopic level and to study the relations between the microscopic and macroscopic mechanical features of the material. In addition to that, the effect of cleanness of aggregate surface (aggregate washing) was observed in order to evaluate the hypothesis that with cleaner coarse aggregate grains, both microscopic and macroscopic mechanical properties will be improved. As the literature review has shown, there is a very limited number of studies dealing with these topics. The authors of this paper have previously published small sets of data in two preliminary reports [34–35]. This paper provides a systematic and comprehensive study of a wide set of materials and their properties.

In accordance with the previous research study of the authors of this paper [33] and pursuing the studies of other authors cited above, the aims and tasks of the presented experimental program were:

- To determine the effect of the type and amount of SCMs on micromechanical properties of HPC.
- To determine the effect of changes in homogenization procedure, namely various mixing times and sequence of addition of components, on micromechanical properties of HPC.
- To determine the effect of aggregate washing on micromechanical properties of HPC.
- To compare the changes of micromechanical characteristics with the changes of the main macromechanical properties – compressive strength and bulk elastic modulus.

2. Methods

2.1. Investigated materials

In agreement with the preceding study of macroscopic properties [33], ten mixtures described in Table 1 were tested. REF is the reference mixture with no SCMs; MIC are the mixtures containing microsilica; POP are mixtures containing fly ash; and MET are mixtures containing metakaolin. The number 10, 20 or 30 designates the percentage of cement weight replaced by SCMs. The details regarding mixture design, chemical composition and particle size distribution of cementitious materials can be found in [33] and [36].

Table 1. Composition of the mixtures (values in $[\text{kg}/\text{m}^3]$; water-to binder ratio w/b is dimensionless).

Compound	Specification	REF	MIC10	MIC20	MIC30	POP10	POP20	POP30	MET10	MET20	MET30
cement	CEM I 42,5 R	800	720	640	560	720	640	560	720	640	560
admixture	microsilica	0	80	160	240	0	0	0	0	0	0
	fly ash	0	0	0	0	80	160	240	0	0	0
	metakaolin	0	0	0	0	0	0	0	80	160	240
water	-	210	231	252	273	197	185	172	210	210	210
w/b	-	0.26	0.26	0.26	0.26	0.26	0.26	0.26	0.26	0.26	0.26
aggregate (basalt)	8-16 mm	320	320	320	320	320	320	320	320	320	320
	4-8 mm	390	390	390	390	390	390	390	390	390	390
	0-4 mm	730	730	730	730	730	730	730	730	730	730
Superplasticizer	Polycarboxylate	25.0	33.0	33.0	33.0	34.0	32.0	30.0	30.0	30.0	30.0

For the remaining part of the experimental program, just the mixtures with optimal content of SCM from the point of view of macroscopic mechanical properties [33] were selected. Therefore, the effect of homogenization procedure and aggregate washing was measured only for REF, MIC20, POP30 and MET20.

To study the effect of homogenization procedure, four variants of the mixtures were prepared using a pan laboratory mixer with centre shaft (pan fixed, scraper moving) and nominal volume of 80 litres at the speed of 30 rpm. Details are given in Table 2.

- P1: Standard procedure used in the rest of the experimental program
- P2: SCM was added before cement.
- P3: SCM was added as the last component.
- P4: Mixing time of SCM was increased from 180 s to 300 s.

Table 2. Plans of mixing procedures P1 – P4 (the lengths of the steps are given in seconds).

Step no.	P1	P2	P3	P4
1		Aggregate 8/16+4/8 (20)		
2		Aggregate 0/4 (20)		
2	Cement (20)	SCM (180)	Cement (20)	Cement (20)
3	SCM (180)	Cement (20)	Water+SPF (60)	SCM (300)
4	Water+SPF (60)	Water+SPF (60)	SCM (180)	Water+SPF (60)

The effect of aggregate washing was studied by comparing the properties of two types of mixtures. In case of “U” type (unwashed) mixtures, the aggregate was used as received from the quarry; no special processing was carried out. In case of “W” type (washed) mixtures, the coarse fractions of the aggregate (4–8 mm and 8–16 mm) were washed and dried before mixing. To wash the aggregate, it was immersed for 30 seconds into water in running laboratory mixer, then filtered, dried in laboratory dryer and kept in laboratory conditions for 7 days to reach the same natural humidity as the unprocessed aggregate. The efficiency of the applied method of aggregate washing was confirmed by grading test that showed that the content of fine particles smaller than 0.125 mm was lowered by 94 % in 8–16 mm fraction and by 96 % in 4–8 mm fraction.

2.2. Nanoindentation

Micromechanical characteristics of individual phases of the material were obtained by displacement driven grid indentation using Ti 700 series nanoindenter (Hysitron Inc.). The method is based on injection of the tip of the probe into the material. The dependency of the applied force on the depth of penetration is measured. The mechanical properties are then computed using Oliver-Pharr theory [37] from the unloading part of the loading curve. The results of the measurements are microhardness (H) and effective elastic indentation modulus (E_r).

The samples for nanoindentation and microscopic analysis were extracted from macroscopic samples (100 mm cubes) stored in water in laboratory conditions (20–22 °C) for 28 days (identical to samples for macroscopic tests). The extracted samples were treated using grinding and polishing media. Due to mechanical heterogeneity of the material, a method reducing selective abrasivity was applied. This allowed to obtain specimens having both adequate surface roughness and compact ITZ between aggregate and matrix.

Particular indents were driven by loading function with prescribed maximum penetration depth of 150 nm. The loading took 5 seconds. The maximum force was held for 60 seconds which allowed to significantly reduce the effect of creep and viscoelasticity of the material [37]. To obtain statistically relevant set of data regarding indentation moduli of particular material phases and to locate the position of interfacial transition zone (ITZ), a grid of 21×21 indents with spacing of 10 μm was applied on all the samples. Six rows of 100 indents (spacing of 1 μm) were then performed on each ITZ location to determine the thickness of ITZ based on the measured distribution of indentation modulus along the row of indents.

Indentation modulus was derived from spectral deconvolution of measured data (normalized histograms of indentation results). The application of this method is limited by two conditions – identical area of each indent and significantly different mechanical properties of particular phases [38]. The first condition is fulfilled by applying the displacement driven loading function. The second condition is generally not fulfilled considering very similar micromechanical properties of clinker and basalt aggregate ($E_r > 100$ GPa). This problem was solved by dividing the measurements in two levels: the matrix without the aggregate and ITZ between the matrix and the aggregate. The deconvolution procedure was then applied independently on both levels and the final results were obtained by their synthesis.

Contrary to static deconvolution, spectral deconvolution takes into account mutual interactions of phases such as the interaction between matrix and clinker (soft and hard phase). The effective indentation modulus (E_r) was determined with maximum allowed deviation of 2.5 % from experimental measurements considering Gaussian distribution of probability of results.

2.3. Scanning electron microscopy and image analysis

To investigate the phase composition of selected samples, scanning electron microscopy (SEM) in backscattered electron mode (BSE) was performed using microscope Mira II LMU equipped with electron probe microanalyzer (EPMA) from Tescan corp. (Czech Republic). After polishing, 20 nm thick layer of carbon was deposited on the surface of samples to increase electric conductivity. Since grayscale intensity in obtained BSE image depends on atomic mass [39], individual phases could be identified by image analysis using an in-house software PyPAIS [40] based on intensity and entropy thresholding.

An alternative method of assigning ITZ thickness with the use of SEM and energy-dispersive X-ray detector (EDX) based on the work of Kjellsen et al. [41] was examined for one selected sample. EDX probe from Bruker corp. (Germany) was used. In the points along a line, identification of elements and quantification

of each element's concentration was carried out. According to [41], ITZ can be identified based on the ratio of Ca/Si content in hydrated material. Lower values of Ca/Si ratio indicate the presence of ITZ. The motivation for this experiment was the fact that nanoindentation measurements of ITZ thickness are very time consuming in terms of both operator time and computer time required for data processing. The alternative method provides the results relatively quickly.

2.4. Macromechanical characteristics

Macromechanical characteristics were tested according to valid European standards [42–44]. More details regarding the methods as well as complete results and their discussion can be found in [33].

3. Results and Discussion

3.1. The effect of SCM type and amount

Microstructure of the studied HPC samples was influenced by the type and amount of SCMs in many aspects.

The indentation modulus of ITZ (Table 3) was decreased by the addition of metakaolin by approximately 10 %, while the effect of fly ash and silica fume was ambiguous. Relatively strong correlation (correlation coefficient $R = 0.7$) between the change of bulk elastic modulus (E_c) and indentation modulus of ITZ induced by the addition of SCMs was found, see figure 1.

The indentation modulus of LD CSH (low-density calcium-silicate-hydrates) and HD CSH (high-density calcium-silicate-hydrates) was increased by SCMs in all instances and the increase was directly dependent on cement replacement level (Table 3). Fly ash and metakaolin increased the modulus of HD CSH by approximately 20 %; the other changes were less significant. The increase can be explained by the fact that the pozzolanic materials contain large amount of reactive silicon dioxide (SiO_2) that reacts with portlandite ($\text{Ca}(\text{OH})_2$) to form the calcium-silicate-hydrates (CSH) [45]. However, the bulk elastic modulus of all the mixtures was lower than the one of the reference mixture, the reduction reaching up to 20 % for silica fume and metakaolin mixtures and 5–10 % for fly ash containing mixtures.

Volumetric fractions of particular phases were determined for this set of samples (Table 4). In most cases, the amount of HD CSH was lower and the amount of LD CSH was higher in mixtures containing SCMs than in the reference mixture. This partially explains the reduction of bulk elastic modulus.

The indentation modulus of Portlandite (Table 3) was significantly decreased by the addition of silica fume. Fly ash and metakaolin had slightly increasing effect with no clear dependence on the replacement level. No clear relation between SCMs and indentation modulus of clinker was observed. There was no correlation between the bulk elastic modulus and indentation moduli of phases other than ITZ, see Figure 1.

The measured ITZ thickness of all the samples (Table 2) was between 8–23 μm , which coincides with the results obtained by other authors studying high-performance concrete; thickness between 10 and 30 μm was reported [4–7]. Figure 2 shows that SCMs reduced the thickness of ITZ in almost all instances (except MET30), sometimes more than twofold. This is in accordance with results of Rossignolo [22] cited in section 1.2. However, contrary to [24], no clear dependence between ITZ thickness and macroscopic compressive strength of mixtures with varying SCM content was found. In some cases (MIC20, MIC30, MET10), ITZ thickness was significantly reduced, but the compressive strength was decreased at the same time; in another cases, even a small reduction of ITZ thickness lead to noticeable increase of compressive strength (POP20, POP30).

Table 3. Mean values and standard deviations of the indentation moduli E_r [GPa] of individual phases and mean thickness of ITZ [μm] – mixtures with different content of SCMs.

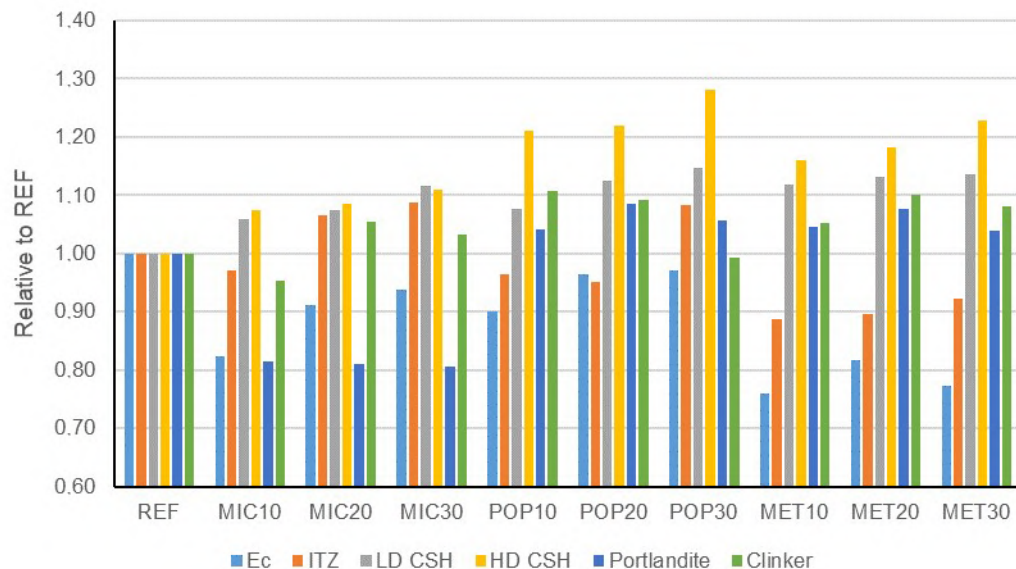
Mixture	ITZ	LD CSH	HD CSH	Portlandite	Clinker	ITZ thickness
REF	17.34±2.38	31.08±4.65	45.07±2.47	81.60±10.36	128.36±14.99	21.3
MIC10	16.82±2.18	32.91±4.16	48.43±5.78	66.55±8.50	122.28±8.50	16.1
MIC20	18.47±2.41	33.37±2.92	48.94±4.24	66.12±11.74	135.49±11.74	10.2
MIC30	18.87±3.91	34.70±3.17	49.98±3.48	65.82±6.51	132.65±6.51	8.2
POP10	16.74±2.42	33.45±5.89	54.54±7.63	84.92±14.07	142.13±13.34	16.9
POP20	16.48±2.12	34.95±5.36	54.99±6.38	88.63±13.16	140.22±12.42	13.8
POP30	18.80±4.40	35.62±5.87	57.72±6.40	86.17±7.59	127.57±16.85	14.9
MET10	15.38±1.98	34.73±4.82	52.32±8.56	85.36±12.06	135.12±18.01	12.1
MET20	15.54±3.24	35.15±6.28	53.27±8.71	87.88±14.55	141.20±18.85	15.9
MET30	16.01±2.25	35.27±5.69	55.40±6.32	84.79±10.26	138.62±14.42	23.0

Table 4. Mean values and standard deviations of volumetric fractions for individual phases – mixtures with different content of SCMs.

Mixture	LD CSH	HD CSH	Portlandite	Clinker	Aggregate
REF	15.82±0.25	15.43±0.35	6.55±0.15	4.18±0.02	56.52±1.39
MIC10	16.09±0.42	16.61±0.44	4.07±0.06	5.43±0.16	57.45±2.44
MIC20	18.30±0.98	14.57±0.17	4.49±0.13	6.48±0.22	55.56±3.31
MIC30	19.33±0.01	13.74±0.38	5.75±0.20	6.76±0.25	56.33±2.79
POP10	19.61±0.31	15.34±0.15	5.77±0.11	6.20±0.18	57.89±2.44
POP20	12.25±0.40	13.96±0.71	8.50±0.03	2.93±0.23	60.78±1.88
POP30	13.48±0.70	13.79±0.50	8.40±0.05	2.81±0.12	59.18±1.93
MET10	18.00±0.21	12.59±0.05	4.65±0.02	6.08±0.18	59.38±1.41
MET20	18.94±0.33	12.90±0.62	3.82±0.21	5.50±0.23	61.26±0.98
MET30	18.78±0.54	12.93±0.53	3.23±0.16	4.81±0.12	60.78±1.03

Table 5. Mean values of macroscopic compressive strength and bulk elastic modulus – mixtures with different content of SCMs.

Mixture	Compressive strength [MPa]	Elastic modulus [GPa]
REF	105.9	51.3
MIC10	109.3	42.2
MIC20	101.3	46.8
MIC30	97.7	48.1
POP10	106.6	46.2
POP20	120.8	49.5
POP30	125.3	49.8
MET10	108.9	39.0
MET20	110.3	41.9
MET30	96.7	39.7

**Figure 1. Bulk elastic modulus (E_c) and indentation moduli of particular phases relative to reference mixture (REF) – mixtures with different content of SCMs.**

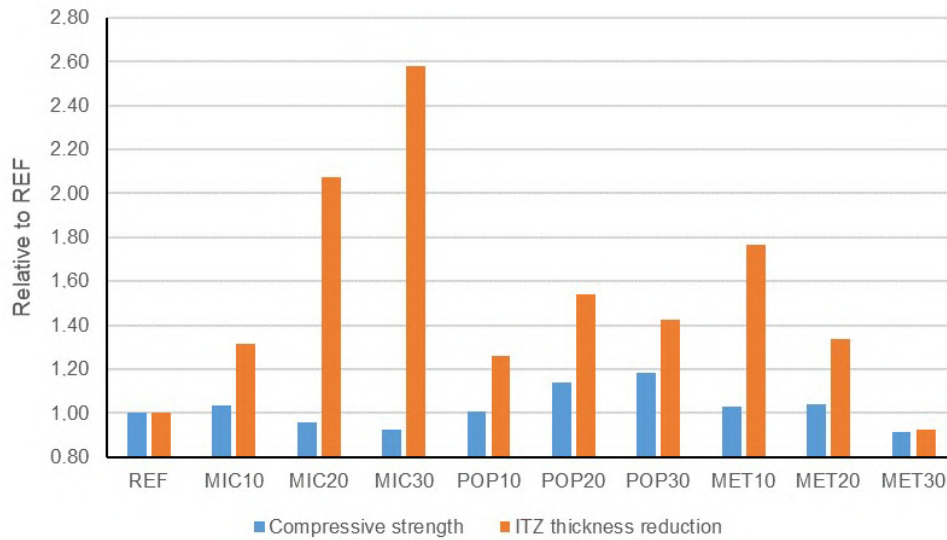


Figure 2. Compressive strength and reduction of ITZ thickness relative to reference mixture (REF) – mixtures with different content of SCMs.

For one selected sample of reference concrete (REF), an alternative method of determination of ITZ thickness was tested. The method is based on the ratio of Ca/Si content in selected points along a line. Figure 3 shows the development of Ca/Si ratio in the analysed area. When we compare the plot with the SEM photograph in figure 4, it can be concluded that points 3–7 are located inside ITZ. This indicates that the ITZ thickness is approximately 23 μm, which is in good agreement with 21.3 μm measured by nanoindentation of REF samples. Finer grid of measuring points would be required to obtain more accurate value, but the method provides very good results in relatively short time.

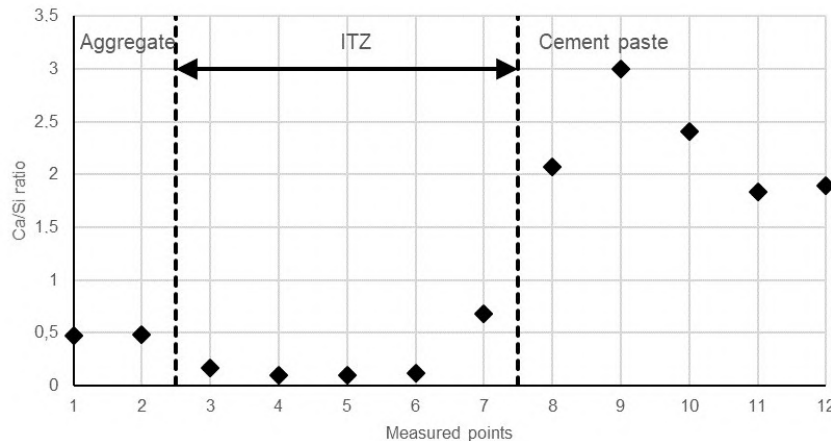


Figure 3. Ca/Si ratio along a line in a sample of reference concrete (REF).

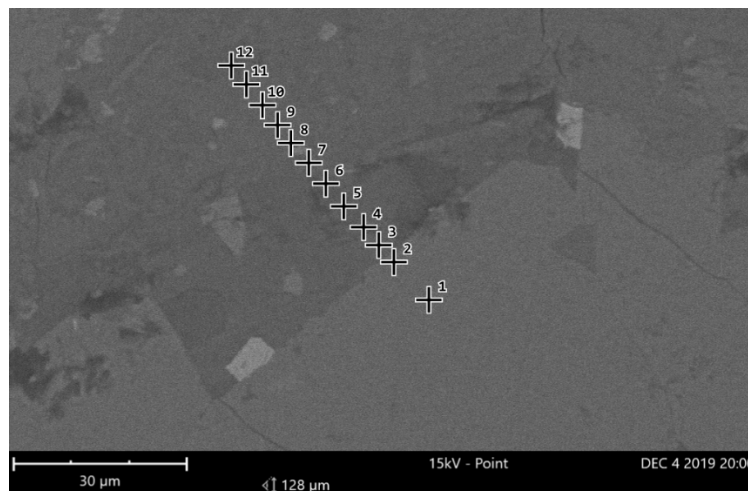


Figure 4. SEM image of the analysed area, showing the transition between an aggregate grain (points 1 and 2), ITZ and cement matrix (200x magnification).

3.2. The effect of homogenization procedure

As Tables 6 and 7 and Figure 5 demonstrate, there was no clear relation between the homogenization procedure applied and indentation moduli of particular phases or bulk elastic modulus of concrete. There was also no correlation between bulk elastic modulus and indentation moduli of any of the phases, but the common feature of mixtures with higher bulk elastic modulus (POP mixtures, MET20-2 and MET20-3) was that they had increased indentation modulus of HD CSH when compared to the reference mixture.

Relatively strong correlation ($R = 0.75$) was found between ITZ thickness and compressive strength of the material. It can be clearly seen in figure 6 that while procedure P2 always increased the ITZ thickness and mostly decreased compressive strength compared to basic procedure P1, procedure P3 lead to the reduction of ITZ thickness and increase of compressive strength. The effect of procedure P4 was ambiguous.

The fact that the homogenization procedure P3, in which the SCM was added as the last component to the wet mix, lead to improvement of the compressive strength, is in agreement with the results of Hiremath and Yaragal [29] cited in section 1.2. No other research works dealing with the effect of homogenization procedure of HPC containing SCMs that could be used for comparison of results were found.

Table 6. Mean values and standard deviations of the indentation moduli E_r [GPa] of individual phases and mean thickness of ITZ [μm] – mixtures prepared by different homogenization procedures (P1 – P4).

Mixture	ITZ	LD CSH	HD CSH	Portlandite	Clinker	ITZ thickness
REF-1	17.19±2.59	32.87±4.39	45.22±4.50	80.08±9.78	127.64±13.82	18.5
MIC20-1	18.26±2.68	33.92±4.34	48.80±4.45	69.02±9.45	134.37±10.67	18.3
MIC20-2	17.43±2.74	32.67±4.39	46.38±4.46	70.29±8.63	132.56±11.74	18.8
MIC20-3	19.81±2.82	35.2±4.42	49.28±4.45	69.57±6.08	133.62±9.56	17.3
MIC20-4	18.91±2.69	34.12±4.43	48.95±4.54	69.25±7.19	134.92±12.27	17.9
POP30-1	15.99±2.74	34.82±4.38	55.85±4.50	79.89±10.14	138.37±12.03	16.1
POP30-2	14.53±2.77	34.00±4.39	53.06±4.53	72.48±8.25	136.36±10.74	19.4
POP30-3	15.18±2.89	34.15±4.38	54.34±4.55	76.53±7.38	137.84±9.98	15.2
POP30-4	15.04±2.77	34.29±4.38	54.46±4.40	77.61±8.80	137.05±10.55	16.1
MET20-1	15.30±2.78	35.31±4.27	53.65±4.44	86.14±12.45	139.71±15.55	14.9
MET20-2	15.82±2.76	35.88±4.27	54.42±4.49	87.26±9.83	136.74±12.38	15.6
MET20-3	16.37±2.70	36.45±4.37	54.91±4.40	87.85±7.36	139.68±9.55	13.7
MET20-4	15.48±2.68	35.56±4.28	54.17±4.48	85.27±8.69	138.12±10.33	18.8

Table 7. Mean values of macroscopic compressive strength and bulk elastic modulus – mixtures prepared by different homogenization procedures (P1 – P4).

Mixture	Compressive strength [MPa]	Elastic modulus [GPa]
REF-1	105.9	51.3
MIC20-1	101.3	46.8
MIC20-2	99.0	39.8
MIC20-3	113.8	41.6
MIC20-4	103.8	40.7
POP30-1	125.3	49.8
POP30-2	95.5	49.5
POP30-3	115.8	51.0
POP30-4	109.0	50.4
MET20-1	110.3	41.9
MET20-2	118.0	52.9
MET20-3	127.7	52.5
MET20-4	115.4	45.5

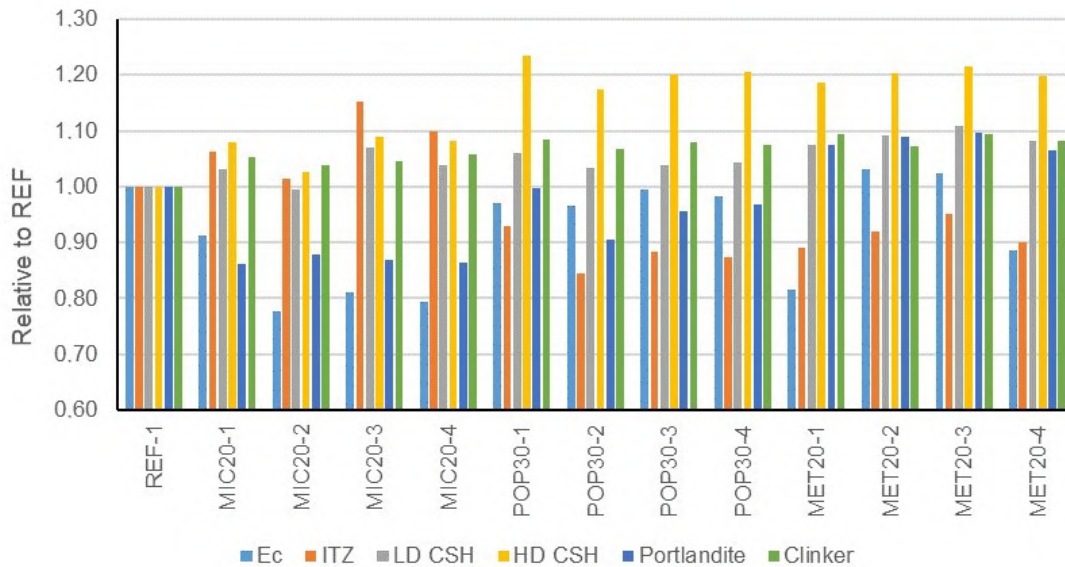


Figure 5. Bulk elastic modulus (Ec) and indentation moduli of particular phases relative to reference mixture (REF-1) – mixtures prepared by different homogenization procedures (P1 – P4).

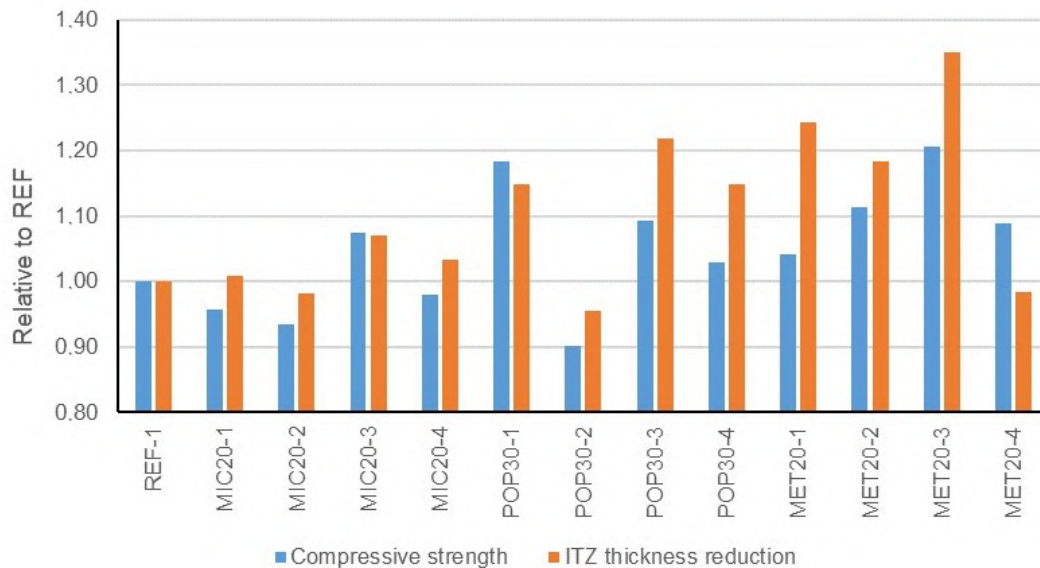


Figure 6. Compressive strength and reduction of ITZ thickness relative to reference mixture (REF-1) – mixtures prepared by different homogenization procedures (P1 – P4).

3.3. The effect of aggregate washing

The results of this part of the experimental program, which studied the effect of washing of coarse fractions of the aggregate (4–8 mm and 8–16 mm), were the clearest ones. When comparing respective mixtures with unwashed (U) and washed (W) aggregate in tables 8 and 9, it is obvious that aggregate washing always had positive effect on ITZ thickness, compressive strength and bulk elastic modulus, even though a mild one (up to 10 % in most cases). The same thing can be said about the effect on indentation moduli of particular phases (Table 8, Figure 7), but the differences are even smaller in this case (smaller than the standard deviation of the results). The positive effect of washing can be related to the fact that due to the removal of detrimental fine particles, the processed coarse aggregate had smaller relative surface area, leading to the elimination of the wall effect described in chapter 1.2.

Figure 8 depicts the relation between compressive strength and the reduction of ITZ thickness of particular mixtures. The trend was clear, when the ITZ thickness was reduced, the compressive strength was increased. However, the changes were not proportional.

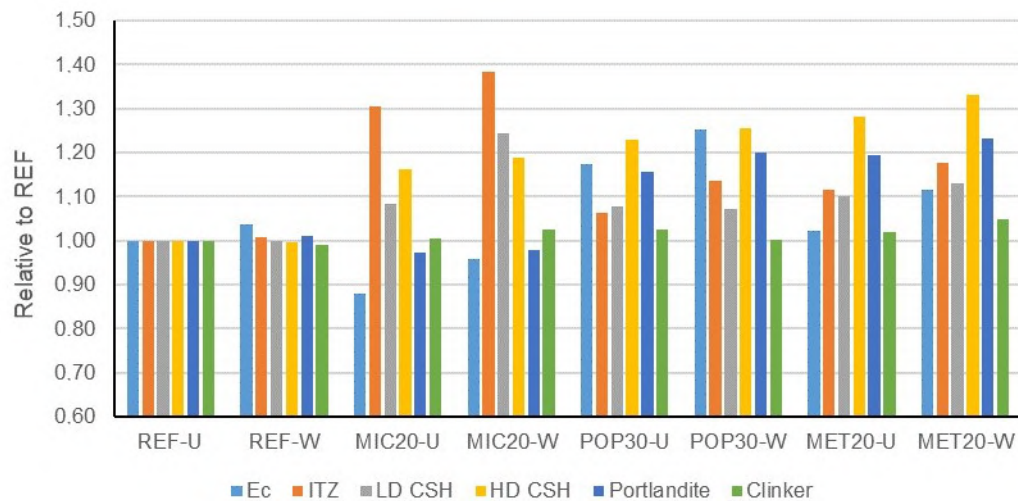
As stated in section 1.2, no studies dealing with the effect of aggregate washing on neither microscopic nor macroscopic properties of concrete were found. Therefore, the comparison of results with other authors is not possible.

Table 8. Mean values and standard deviations of the indentation moduli E_r [GPa] of individual phases and mean thickness of ITZ [μm] – mixtures with unwashed (U) and washed (W) aggregate.

Mixture	ITZ	LD CSH	HD CSH	Portlandite	Clinker	ITZ thickness
REF-U	13.55±3.59	30.96±3.63	41.03±4.04	69.77±6.91	130.55±14.71	21.7
REF-W	13.67±3.55	30.92±4.76	40.93±5.08	70.56±8.32	129.46±15.05	20.4
MIC20-U	17.69±2.46	33.54±2.68	47.73±4.14	67.87±8.58	131.35±12.46	14.1
MIC20-W	18.75±3.53	38.48±4.67	48.77±4.52	68.23±9.00	133.69±14.87	10.5
POP30-U	14.42±3.03	33.37±4.43	50.48±5.02	80.61±7.01	133.97±15.45	15.8
POP30-W	15.40±3.43	33.22±4.43	51.52±4.71	83.72±6.88	130.65±12.13	14.2
MET20-U	15.13±3.86	34.11±3.64	52.59±3.29	83.21±8.99	132.92±11.58	19.3
MET20-W	15.96±2.87	35.00±4.71	54.61±5.41	86.01±10.42	137.03±16.98	15.6

Table 9. Mean values of macroscopic compressive strength and bulk elastic modulus — mixtures with unwashed (U) and washed (W) aggregate.

Mixture	Compressive strength [MPa]	Elastic modulus [GPa]
REF-U	113.7	39.4
REF-W	118.4	40.9
MIC20-U	113.9	34.7
MIC20-W	129.1	37.7
POP30-U	125.8	46.2
POP30-W	131.0	49.3
MET20-U	114.1	40.3
MET20-W	127.3	44.0

**Figure 7. Bulk elastic modulus (E_c) and indentation moduli of particular phases relative to reference mixture (REF-U) – mixtures with unwashed (U) and washed (W) aggregate.**

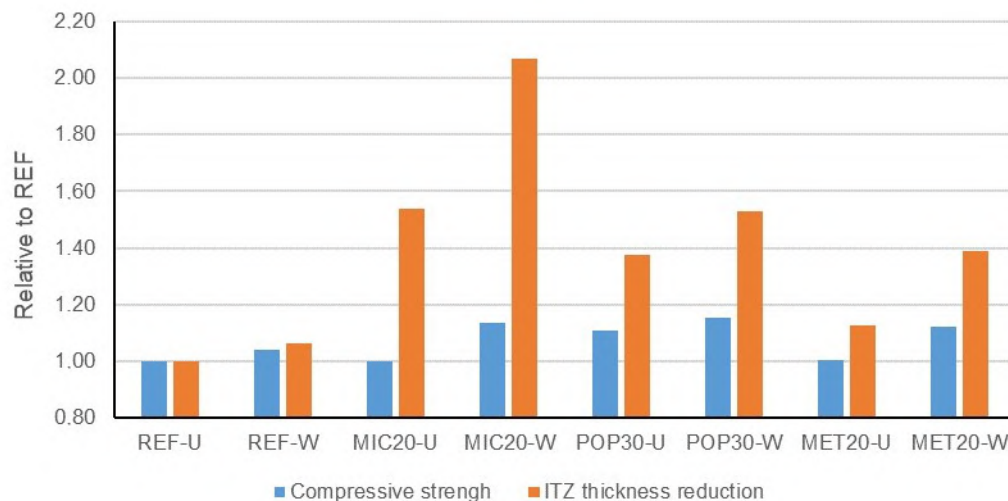


Figure 8. Compressive strength and reduction of ITZ thickness relative to reference mixture (REF-U) – mixtures with unwashed (U) and washed (W) aggregate.

4. Conclusions

The experimental program provided a comprehensive database characterizing the effects of SCM type and content, homogenization procedure and aggregate washing on micromechanical properties of HPC containing SCMs. Several qualitative trends between micromechanical and macromechanical properties of studied concrete were identified. The main conclusions are:

- SCMs increased the indentation modulus of HD CSH. There was a direct dependence on SCM content.
- When varying the SCM content, there was a direct dependence between the change of indentation modulus of ITZ and bulk elastic modulus of concrete.
- The use of SCMs generally had negative effect on bulk elastic modulus of the material. This might be related to the changes of volumetric fractions of LD CSH and HD CSH. The addition of SCMs lead to decrease of HD CSH content and increase of LD CSH content, thus increasing the share of lower-density compounds at the expense of high-density compounds.
- The previous effect was the lowest (only up to 10 %) when fly ash was used. This fact was probably connected with the increase of indentation modulus of HD CSH, which was the highest (up to 20 %) in case of fly ash containing mixtures.
- SCMs generally decreased the thickness of ITZ, in some cases more than twofold. However, there was no clear proportional dependence between ITZ thickness and compressive strength.
- The homogenization procedure of mixtures with optimized SCM content influenced the thickness of ITZ and compressive strength. Adding SCMs to the mixer before cement (P2) had generally negative effect on both, while adding SCM to wet mix (P3) proved to have positive influence. Increased mixing time (P4) had no distinctive effect.
- Aggregate washing was useful for improving both microscopic and macroscopic properties, having positive effect on ITZ thickness, compressive strength, bulk elastic modulus and indentation moduli of particular phases, even though a mild one (up to 10 % in most cases).
- The method of measuring ITZ thickness through variations of Ca/Si ratio was tested with promising results. This method will be further verified on a larger set of specimens. In case of good agreement, it could be used as a faster alternative to nanoindentation method for determination of ITZ thickness.

5. Acknowledgement

The paper was prepared thanks to the support of the Science Foundation of the Czech Republic (GAČR), project no. 17-19463S “Analysis of the relations between the microstructure and macroscopic properties of ultra-high performance concretes”.

References

1. Aitcin, P.C. High-Performance Concrete. CRC Press. London, 1998. DOI: 10.1201/9781420022636
2. Mehta, P.K., Monteiro, P.J.M. Concrete. Microstructure, Properties, and Materials, 3rd Edition. McGraw-Hill. New York, 2006. DOI: 10.1036/0071462899

3. Wang, G., Kong, Y., Sun, T., Shui, Z. Effect of water–binder ratio and fly ash on the homogeneity of concrete. *Construction and Building Materials*. 2013. 38. Pp. 1129–1134. DOI: 10.1016/j.conbuildmat.2012.09.027
4. Wu, K., Shi, H., Xu, L., Ye, G., Schutter, G.D. Microstructural characterization of ITZ in blended cement concretes and its relation to transport properties. *Cement and Concrete Research*. 2016. 79. Pp. 243–256. DOI: 10.1016/j.cemconres.2015.09.018 .
5. Branch, J., Epps, R., Kosson, D. The impact of carbonation on bulk and ITZ porosity in microconcrete materials with fly ash replacement. *Cement and Concrete Research*. 2018. 103. Pp. 170–178. DOI: 10.1016/j.cemconres.2017.10.012
6. Duan, P., Shui, Z., Chen, W., Shen, C. Efficiency of mineral admixtures in concrete: microstructure, compressive strength and stability of hydrate phases. *Applied Clay Science*. 2013. 83–84. Pp. 115–121. DOI: 10.1016/j.clay.2013.08.021
7. Gao, Y., Schutter, G.D., Ye, G., Huang, H., Tan, Z., Wu, K. Characterization of ITZ in ternary blended cementitious composites: experiment and simulation. *Construction and Building Materials*. 2013. 41. Pp. 742–750. DOI: 10.1016/j.conbuildmat.2012.12.051
8. Monteneiro, P.J.M. Microstructure of concrete and its influence on the mechanical properties. PhD dissertation. University of California, Berkeley, 1985.
9. Maso, J.C. Influence of the interfacial transition zone on composite mechanical properties. *Interfacial Transition Zone in Concrete*. E & FN SPON. London, 1996. URL: <http://drbeton.ir/wp-content/uploads/2017/03/Interfacial-Transition-Zone-in-Concrete.pdf#page=131> (date of application: 15.11.2019).
10. Kim, S.S., Qudoos, A., Jakhriani, S.H., Lee, J.B., Kim, H.G. Influence of Coarse Aggregates and Silica Fume on the Mechanical Properties, Durability, and Microstructure of Concrete. *Materials (Basel)*. 2019. 12(20). P. 3324. DOI: 10.3390/ma12203324
11. Escadeillas, G., Maso, J.C. Approach of the initial state in cement paste, mortar, and concrete. *Advances in Cementitious Materials*. 1991. 16. Pp. 169–184. URL: https://www.researchgate.net/publication/288522438_Approach_of_the_initial_state_in_cement_paste_mortar_and_concrete (date of application: 10.10.2019).
12. Lagerblad, B., Kjellsen, K.O. Normal and High Strength Concretes with Conventional Aggregates. *Engineering and Transport Properties of the Interfacial Transition Zone in Cementitious Composites*. RILEM Report 20. RILEM Publications S.A.R.L., 1999.
13. Chandra, S. *Properties of Concrete with Mineral and Chemical Admixtures. Structure and Performance of Cements*. Spon Press. London, 2002. Pp. 140–185 ISBN: 9780419233305.
14. Rooij de, M.R. *Syneresis in Cement Paste Systems*. PhD dissertation. Delft University of Technology, Delft, 2000.
15. Yoo, D.-Y., Banthia, N. Mechanical properties of ultra-high-performance fiber-reinforced concrete: A review. *Cement and Concrete Composites*. 2016. 73. Pp. 267–280. DOI: 10.1016/j.cemconcomp.2016.08.001
16. Yoo, D.-Y., Yoon, Y.-S. A Review on Structural Behavior, Design, and Application of Ultra-High-Performance Fiber-Reinforced Concrete. *International Journal of Concrete Structures and Materials*. 2016. 10(2). Pp. 125–142. DOI: 10.1007/s40069-016-0143-x
17. Fediuk, R.S., Lesovik, V.S., Mochalov, A.V., Otsokov, K.A., Lashina, I.V., Timokhin, R.A. Composite binders for concrete of protective structures. *Magazine of Civil Engineering*. 2018. 82(6), Pp. 208–218. DOI: 10.18720/MCE.82.19
18. Gaifullin, A.R., Rakhimov, R.Z., Rakhimova, N.R. The influence of clay additives in Portland cement on the compressive strength of the cement stone. *Magazine of Civil Engineering*. 2015. 59(7). Pp. 66–73. DOI: 10.5862/MCE.59.7
19. Fediuk, R.S., Lesovik, V.S., Svintsov, A.P., Gladkova, N.A., Timokhin, R.A. Self-compacting concrete using pretreated rice husk ash. *Magazine of Civil Engineering*. 2018. 79(3). Pp. 66–76. DOI: 10.18720/MCE.79.7
20. Fediuk, R., Pak, A., Kuzmin, D. Fine-Grained Concrete of Composite Binder. *IOP Conference Series: Materials Science and Engineering*. 2017. 262(1), 012025. DOI: 10.1088/1757-899X/262/1/012025
21. Fediuk, R.S., Lesovik, V.S., Liseitsev, Y.L., Timokhin, R.A., Bituyev, A.V., Zaiakhanov, M.Y., Mochalov, A.V. Composite binders for concretes with improved shock resistance. *Magazine of Civil Engineering*. 2019. 85(1). Pp. 28–38. DOI: 10.18720/MCE.85.3
22. Rossignolo, J.A. Effect of silica fume and SBR latex on the paste aggregate interfacial transition zone. *Materials Research*. 2007. 10(1). Pp. 83–86. DOI: 10.1590/S1516-14392007000100018
23. Duan, P., Shui, Z., Chen, W. and Shen, C. Effects of metakaolin, silica fume and slag on pore structure, interfacial transition zone and compressive strength of concrete. *Construction and Building Materials*. 2013. 14. Pp. 1–6. DOI: 10.1016/j.conbuildmat.2013.02.075
24. Nili, M., Ehsani, A. Investigating the effect of the cement paste and transition zone on strength development of concrete containing nanosilica and silica fume. *Materials and Design*. 2015. 75. Pp. 174–183. DOI: 10.1016/j.matdes.2015.03.024
25. Skarendahl A, Petersson Ö. Self-compacting concrete – state-of-the-art report. RILEM report 23. Cachan Cedex, France, 2001
26. Hoffmann C, Leemann A. Homogeneity of structures made with selfcompacting concrete and conventional concrete. *Proceedings of 3rd int RILEM symposium SCC*. Reykjavik, Iceland, 2003. Pp. 619–627. e-ISBN: 2912143713
27. Leemann A., Münch B., Gasser P., Holzer L. Influence of compaction on the interfacial transition zone and the permeability of concrete. *Cement and Concrete Research*. 2006. 36. Pp. 1425–1433. DOI: 10.1016/j.cemconres.2006.02.010
28. Yoo, D.-Y., Banthia, N., Zi, G., Yoon, Y.-S. Comparative biaxial flexural behavior of ultra-high-performance fiber-reinforced concrete panels using two different test and placement methods. *Journal of Testing and Evaluation*. 2017. 45(2). Pp. 624–641. DOI: 10.1520/JTE20150275
29. Hiremath, P. N., Yaragal, S. C.: Influence of mixing method, speed and duration on the fresh and hardened properties of Reactive Powder Concrete. *Construction and Building Materials* 141 (2017). Pp. 271–288. DOI: 10.1016/j.conbuildmat.2017.03.009
30. Collepardi, M. *The new concrete*. Tintoretto. Rome, 2006. ISBN: 9788890146947
31. Topçu, İ. B., Uğurlu, A. Effect of the use of mineral filler on the properties of concrete. *Cement and Concrete Research*. 2003. 33. Pp. 1071–1075. DOI: 10.1016/S0008-8846(03)00015-2
32. Cepuritis, R., Mørtzell, E. Possibilities of improving crushed sand performance in fresh concrete by washing: a case study. *Materials and Structures*. 2016. 49(12). Pp. 5131–5146. DOI: 10.1617/s11527-016-0849-x
33. Bílý, P., Fládr, J., Chylík, R., Vráblik, L., Hrbek, V. The effect of cement replacement and homogenization procedure on concrete mechanical properties. *Magazine of Civil Engineering*. 2019. 86(2). Pp. 46–60. DOI: 10.18720/MCE.86.5
34. Hrbek, V., Prošek, Z., Chylík, R., Vráblik, L. The effect of micro-silica on the microscopic features of the UHPC composite and its inter-facial transition zone. *Acta Polytechnica CTU Proceedings*. 201. 15. Pp. 31–35. DOI: 10.14311/APP.2018.15.0031
35. Fládr, J., Bílý, P., Chylík, R., Prošek, Z.: Macroscopic and Microscopic Properties of High Performance Concrete with Partial Replacement of Cement by Fly Ash. *Solid State Phenomena*. 2018. 292. Pp. 108–113. DOI: 10.4028/www.scientific.net/SSP.292.108

36. Chylik, R., Šeps, K: Influence of cement replacement by admixture on mechanical properties of concrete. Proceedings of the 12th fib PhD Symposium in Civil Engineering. Czech Technical University. Prague, 2018. Pp. 1267–1274.
37. Oliver, W. C., Pharr, G. M. Measurement of hardness and elastic modulus by instrumented indentation: Advances in understanding and refinements to methodology. Journal of Material Research. 2004. 19. Pp. 3–20. DOI: 10.1557/jmr.2004.19.1.3
38. Constantinides, G., Chandran, K. R., Ulm, F.-J., Vliet, K.V. Grid indentation analysis of composite microstructure and mechanics: Principles and validation. Material Science and Engineering A. 2006. 430(1–2). Pp. 189–202. DOI: 10.1016/j.msea.2006.05.125
39. Scrivener, K.L., Patel, H.H., Pratt, P.L., Parrott, L.J. Analysis of phases in cement paste using backscattered electron images, methanol adsorption and thermogravimetric analysis. MRS Proceedings 85. Cambridge University Press. Cambridge, 1986. Pp. 321–332. DOI: 10.1557/proc-85-67
40. Nežerka, V., Trejbal, J.: Assessment of aggregate-bitumen coverage using entropy-based image segmentation. Road Material and Pavement Design. 2019. Pp. 1–12. DOI: 10.1080/14680629.2019.1605304
41. Kjellsen, K.O., Wallevik O.H., Fjällberg L. Microstructures and microchemistry of the paste-aggregate interfacial transition zone of high-performance concrete. Advances in Cement Research. 1998. 10(1). Pp. 33–40. DOI: 10.1680/adcr.1998.10.1.33
42. ČSN EN 206+A1 Concrete – Specification, performance, production and conformity. ÚNMZ. Prague, 2018.
43. ČSN EN 12390-3 Testing hardened concrete – Part 3: Compressive strength of test specimens. ÚNMZ. Prague, 2009.
44. ČSN ISO 1920-10 Testing of concrete – Part 10: Determination of static modulus of elasticity in compression. ÚNMZ. Prague, 2016.
45. Ambily, P. S., Umarani, C., Ravisankar, K. Studies on ultra high performance concrete incorporating copper slag as fine aggregate. Construction and Building Materials. 2015. 77. Pp. 233–240. DOI: 10.1016/j.conbuildmat.2014.12.092

Contacts:

Petr Bily, petr.bily@fsv.cvut.cz

Josef Fladr, fladr@fsv.cvut.cz

Roman Chylik, chylik@fsv.cvut.cz

Vladimir Hrbek, hrbek@fsv.cvut.cz

Lukas Vrablok, vrablok@fsv.cvut.cz

© Bily, P., Fladr, J., Chylik, R., Hrbek, V., Vrablok, L., 2020



ПОЛИТЕХ
Санкт-Петербургский
политехнический университет
Петра Великого

Инженерно-строительный институт
Центр дополнительных профессиональных программ

195251, г. Санкт-Петербург, Политехническая ул., 29,
тел/факс: 552-94-60, www.stroikursi.spbstu.ru,
stroikursi@mail.ru

Приглашает специалистов проектных и строительных организаций,
не имеющих базового профильного высшего образования
на курсы профессиональной переподготовки (от 500 часов)
по направлению «Строительство» по программам:

П-01 «Промышленное и гражданское строительство»

Программа включает учебные разделы:

- Основы строительного дела
- Инженерное оборудование зданий и сооружений
- Технология и контроль качества строительства
- Основы проектирования зданий и сооружений
- Автоматизация проектных работ с использованием AutoCAD
- Автоматизация сметного дела в строительстве
- Управление строительной организацией
- Управление инвестиционно-строительными проектами. Выполнение функций технического заказчика

П-02 «Экономика и управление в строительстве»

Программа включает учебные разделы:

- Основы строительного дела
- Инженерное оборудование зданий и сооружений
- Технология и контроль качества строительства
- Управление инвестиционно-строительными проектами. Выполнение функций технического заказчика и генерального подрядчика
- Управление строительной организацией
- Экономика и ценообразование в строительстве
- Управление строительной организацией
- Организация, управление и планирование в строительстве
- Автоматизация сметного дела в строительстве

П-03 «Инженерные системы зданий и сооружений»

Программа включает учебные разделы:

- Основы механики жидкости и газа
- Инженерное оборудование зданий и сооружений
- Проектирование, монтаж и эксплуатация систем вентиляции и кондиционирования
- Проектирование, монтаж и эксплуатация систем отопления и теплоснабжения
- Проектирование, монтаж и эксплуатация систем водоснабжения и водоотведения
- Автоматизация проектных работ с использованием AutoCAD
- Электроснабжение и электрооборудование объектов

П-04 «Проектирование и конструирование зданий и сооружений»

Программа включает учебные разделы:

- Основы сопротивления материалов и механики стержневых систем
- Проектирование и расчет оснований и фундаментов зданий и сооружений
- Проектирование и расчет железобетонных конструкций
- Проектирование и расчет металлических конструкций
- Проектирование зданий и сооружений с использованием AutoCAD
- Расчет строительных конструкций с использованием SCAD Office

П-05 «Контроль качества строительства»

Программа включает учебные разделы:

- Основы строительного дела
- Инженерное оборудование зданий и сооружений
- Технология и контроль качества строительства
- Проектирование и расчет железобетонных конструкций
- Проектирование и расчет металлических конструкций
- Обследование строительных конструкций зданий и сооружений
- Выполнение функций технического заказчика и генерального подрядчика

По окончании курса слушателю выдается диплом о профессиональной переподготовке
установленного образца, дающий право на ведение профессиональной деятельности

